Investigation of Propeller Stall Flutter

Ross John Higgins

Submitted in fulfilment of the requirements for the
Degree of Doctor of Philosophy

James Watt School of Engineering
College of Science and Engineering
University of Glasgow

April 2021

Abstract

Propeller flutter can manifest in a variety of ways. This includes classical bending-torsion flutter, stall flutter and whirl flutter. Classical bending-torsion flutter for propeller blades is driven by the coupling, and excitement, of selected modes of motion. Such flutter problems are often a result of structural coupling and in the linear aerodynamic regime. As a result, low-fidelity, fast calculations can be used to determine boundaries and mitigate the effects via changes in the structural design. Whirl flutter is the most complex and involves the coupling of the aircraft wing modes of motion to the gyroscopic and aerodynamic effects of the propeller. This phenomenon can be highly non-linear due to both the structure and flow-field, and any mitigation involves sophisticated modelling efforts with respect to the airframe. Propeller stall flutter is less complex in terms of the structure, however, involves the highly non-linear aerodynamics associated with detached flow. This phenomena, like classical flutter, is driven by the propeller design and conditions, but due to its nature, the stall flutter boundary significantly reduces the overall flutter boundary of a propeller. Hence, the understanding of this limitation must be known to ensure safe operation.

The development of modern propeller blades utilising high sweep/taper with thin aerofoil sections can result in a change in the flutter boundary. In addition to this, propellers are coming back into focus due to the development of electrically driven Vertical Take-off/Landing (eVTOL) vehicles and, due to the nature of such a vehicle design, the propellers are being pushed into significantly different operating conditions. This motivation, coupled with the increased computational power available in the modern era, requires the need to reassess what is required to understand the stall flutter boundary associated with a modern, in-service, propeller blade. To this end, a numerical investigation using Computational Fluid Dynamics (CFD) and Computational Structural Dynamics (CSD) was conducted on the Commander propeller blade of Dowty Propellers. This blade was selected from the list of experimentally investigated blades due to the availability of geometry, structural data and applicability in real life applications.

A validation procedure was conducted to assess the effects of the computational setup. This included the effects of turbulence, structural modelling and implementation, with a validated process found whilst using Scale-Adaptive-Simulation (SAS) with interpolated structural modes. An attempt was made to extract aerodynamic damping data of the stall flutter phenomenon via the development of a method from the aeroelastic simulations. Such values give

an indication of the stability, with links made to typical two-dimensional modelling. The thesis ends on the parametric study of the validated Commander simulation. This was conducted in order to gain greater detail on the effects of key structural and aerodynamic parameters on the blade stall flutter response.

The key outcome from this investigation is the need for scale-resolving methods in propeller stall flutter investigations. This study utilises a hybrid RANS/LES model to capture the key detached flow content. This detached flow content results in significant pressure fluctuations, not observed in traditional statistical models, which drive the aeroelastic deformations. In addition, the requirement for a well validated structural model is highlighted including the setup of the structural solver for which an interpolated modal response method is used.

It is also found from this investigation that there is a need for a modern experimental test case focusing on propeller stall flutter. The last comprehensive study was conducted in the 1980's and, with improvements in experimental techniques, greater understanding and data can now be extracted. This new data can be used to validate modern CFD efforts.

The novelty of this work lies within the derivation of a method for the extraction of the aerodynamic damping data from three-dimensional simulations. This had previously not be done before and the extracted results correlated with equivalent two-dimensional aerodynamic damping data. Additionally, the development and application of three-dimensional Navier-Stokes based CFD, with a coupled structural model, had not been conducted on propeller stall flutter.

Contents

1 Introduction **1**

1.1 Background and Motivation 1
1.2 Aeroelasticity 2
1.2.1 Static Aeroelasticity 2
1.2.2 Dynamic Aeroelasticity 3
1.3 Unsteady Aerodynamic Modelling for Propellers 5
1.3.1 Two-dimensional Frequency-Domain Theories 7
1.3.2 Two-dimensional Time-Marching Theories 12
1.4 Classical Rotor Flutter 14
1.4.1 Fixed-Wing Derivation 15
1.4.2 Rotor Blade Extension 17
1.5 Stall Flutter 19
1.5.1 Aerofoil Static-Stall 20
1.5.2 Aerofoil Dynamic-Stall 21
1.5.3 Aerodynamic Damping 22
1.6 Propeller Stall Flutter 26
1.6.1 Experimental Studies 26
1.6.2 Numerical Studies 42
1.6.3 Summary 55
1.7 Research Aims and Objectives 59
1.8 Novelty of the Thesis 59
1.9 Thesis Outline 60

2 Time-Marching Aeroelastic Methodology of HMB3 **61**

2.1 Computational Fluid Dynamics 61
2.1.1 Flow Solver Formulation 62
2.1.2 Numerical Methods 64
2.1.3 Turbulence Modelling 64
2.1.4 $k-\omega$ and Shear Stress Transport (SST) Model 65
2.1.5 Hybrid LES/URANS Methods 66

2.1.6 Scale Adaptive Simulation (SAS) . . . 67
2.1.7 Mesh Generation Techniques . . . 68
2.2 Computational Structural Dynamics . . . 69
2.2.1 Computation of Modal Loads and Amplitudes . . . 69
2.2.2 Grid Deformation Procedure . . . 71
2.2.3 Surface Mesh Deformation . . . 72
2.2.4 Deformation of the Volume Mesh . . . 74
2.2.5 Interpolated Modal Response . . . 75
2.2.6 Grid Quality Assessment . . . 76
2.3 Summary . . . 77

3 Verification of the Aerodynamic and Structural Model 79
3.1 Propeller Flow Validation . . . 79
3.1.1 Computational setup . . . 80
3.1.2 Aerodynamic results . . . 81
3.2 Verification of Semi-Span Wing Aerodynamics . . . 81
3.2.1 Computational setup . . . 81
3.2.2 Aerodynamic results . . . 84
3.3 Verification of Semi-Span Wing Aeroelasticity . . . 85
3.3.1 Computational setup . . . 86
3.3.2 Aeroelastic results . . . 88
3.4 Summary . . . 90

4 Aeroelastic Simulations of the Commander Propeller 92
4.1 Full 3D Investigation: Commander Propeller Blade . . . 92
4.1.1 Computational Setup . . . 93
4.1.2 Structural Modelling . . . 95
4.2 Comparison between URANS and SAS for the 3D accelerating blade . . . 97
4.3 Investigating the effect of the blade acceleration . . . 105
4.4 Aeroelastic response with reduced blade stall . . . 108
4.4.1 Examination of stall through rigid computations . . . 108
4.4.2 Aeroelastic results . . . 110
4.5 Influence of supplied mode shape . . . 112
4.5.1 Bungee Structural Modelling . . . 112
4.5.2 Aeroelastic Results . . . 114
4.6 Interpolated Modal Response . . . 117
4.6.1 Supplied Modes . . . 117
4.6.2 Interpolated Four Stage Aeroelastic Results . . . 118
4.6.3 Interpolated Two Stage Aeroelastic Results . . . 123

4.7 Transient Phase Effect . . . 125
4.7.1 Deceleration Computational Setup . . . 126
4.7.2 Deceleration Aeroelastic Results . . . 126
4.8 Conclusions . . . 131

5 Estimation of Three-Dimensional Aerodynamic Damping 134
5.1 Two-Dimensional Aerodynamic Damping . . . 134
5.1.1 2D Aerodynamic Damping Calculation . . . 134
5.1.2 Computational Setup . . . 135
5.1.3 NACA 0012 2D Verification . . . 137
5.1.4 NACA 0012 Quasi-3D Results . . . 138
5.1.5 Commander Aerofoil 2D Aerodynamic Damping Estimation . . . 143
5.1.6 Summary of the Two-Dimensional Aerodynamic Damping Investigation 145
5.2 Three-Dimensional Aerodynamic Damping . . . 145
5.2.1 3D Aerodynamic Damping Calculation . . . 145
5.2.2 Computational Setup . . . 147
5.2.3 Commander Propeller Blade 3D Aerodynamic Damping Estimation . . . 147
5.3 Conclusions . . . 149

6 Parametric Study of the Commander Propeller Blade 152
6.1 Structural Study . . . 152
6.1.1 Centre of Gravity . . . 152
6.1.2 Tip Mass . . . 159
6.1.3 Torsional Stiffness . . . 167
6.1.4 Key Findings . . . 172
6.2 Aerodynamic Study . . . 174
6.2.1 Increase in blade pitch . . . 174
6.2.2 Introduction of Inflow . . . 180
6.2.3 Key Findings . . . 188

7 Conclusions and Future Work 190
7.1 Research Performed and Conclusions . . . 190
7.2 Future Work . . . 194

List of Tables

1.1 Influence of the modal damping and frequency on the simple lifting surface solution . . . 5
1.2 Range of parameters tested in the experimental investigation of Baker [14] . . . 30
1.3 Description of each experimental model propeller for the investigation of Baker [14] . . . 32
1.4 Description of each experimental model propeller for the investigation of Hubbard [71] . . . 34
1.5 Summary of propeller stall flutter experimental test cases. . . . 57
1.6 Summary of propeller stall flutter numerical test cases. . . . 58

2.1 Values of constants used in $k-\omega$ turbulence models. . . . 66
2.2 Values of constants used in SAS model. . . . 68

3.1 JORP propeller blade simulated test conditions . . . 81
3.2 Installed IMPACTA propeller test conditions . . . 84
3.3 Supplied wing mode shapes and frequencies . . . 88
3.4 Average modal response for the wing and blade components . . . 89

4.1 Investigated mesh sizes for the grid convergence study. . . . 94
4.2 Average and change in non-dimensional vertical load using *SAS* for the grid convergence study. . . . 94
4.3 Average and change in non-dimensional vertical load for the time-step convergence study. . . . 95
4.4 Summary of the Commander propeller blade test conditions. . . . 95
4.5 Comparison of the mode shapes and frequencies of the experimental and computational bungee model . . . 113
4.6 Frequencies of each mode for every supplied stage of the interpolated simulation 118
4.7 Frequencies of each mode for every supplied stage of the declerating interpolated simulation . . . 126

5.1 Test Conditions for the Dynamic Stall Computations . . . 136

5.2 Range of tested parameters for the NACA 0012 2D verification 137
5.3 NACA 0012 Aerodynamic Damping 142
5.4 70%*R* Aerodynamic Damping 143
5.5 Aerodynamic Damping 144
5.6 Comparison three-dimensional aerodynamic damping estimates for the 3D *URANS* and *SAS* simulations over the entire simulation. 147

6.1 Frequencies and shape of each mode for the centre of gravity parametric study for every supplied stage of the interpolated simulation 156
6.2 Frequencies and shape of each mode for the tip mass parametric study for every supplied stage of the interpolated simulation 163
6.3 Frequencies and shape of each mode for the reduction in torsional stiffness parametric study for every supplied stage of the interpolated simulation 170

List of Figures

1.1 Summary of the field of aeroelasticity (Collar's Triangle) 3
1.2 Build up of the rotor wake [21] 10
1.3 Influence of the rotor inflow [21] 11
1.4 Typical blade section undergoing bending-torsion flutter 15
1.5 Typical variation of the flutter eigenvalues, fixed wing example of varying store positions for a given mass properties. Simulation of the experimental study of Runyan and Sewall [117] 16
1.6 Typical trends in lift, drag and moment coefficient during static stall [21] 21
1.7 Typical hysteresis trends in lift and moment coefficient during dynamic stall [21] 22
1.8 Pitching moment coefficient trends for each stall regime, as observed by McCroskey for a NACA 0012 aerofoil pitching at $\alpha = \alpha_o + 10^o \sin(2k\tau)$, where $k = 0.10$ [93] 23
1.9 Aerodynamic damping trends across the mean and oscillating magnitude of the angle of attack [29] 25
1.10 Spitfire and Firefly propeller flutter boundaries in static conditions [129] 27
1.11 Spitfire and Firefly blade definitions [129] 28
1.12 The changes found in the flutter boundaries based upon the experiments of Baker [14] 31
1.13 The changes found in the flutter boundaries based upon the experiments of Hubbard [71] 35
1.14 Installed NACA propeller on the Langley dynamometer for the experimental study of Allis and Swihart [8] 35
1.15 Flutter boundary and thrust coefficient changes for each cambered propeller blade [8] 36
1.16 Propeller blade installation and instrumentation for the stall flutter study of Rogallo and Yaggy [114] 37
1.17 Stall flutter results for the experimental investigation of Rogallo and Yaggy, where V_∞=freestream velocity [114] 38
1.18 Strain gauge positioning and SR propeller blade definitions for the experiments of Smith [125] 40

1.19 Total vibratory shear stress results for the two sets of static experiments by Smith [124, 125] 41
1.20 Stress results for the forward-flight and yawed experiments by Smith [124] . . 42
1.21 Estimated stall flutter predictions for the static and forward-flight experiments of Smith [124, 125] 43
1.22 Aeroelastic flow-chart for the numerical study of the SR-2 propeller by Reddy and Kaza [111] 47
1.23 Damping stall flutter boundary plots for the SR-2 propeller for the experimental [125] and numerical studies [22, 111] 48
1.24 Stall flutter boundary comparison for the model propellers of Baker [14] compared against the numerical aeroelastic model of Delamore-Sutcliffe [40] . . . 54

2.1 Illustration of the modal force computation 70
2.2 Illustration of the computational structural dynamics strategy during each CFD time-step, for a fixed mode shape 72
2.3 Surface deformation procedure for linked components 73
2.4 Illustration of the point selection process in order to compute the IDW weights. 75
2.5 Interpolation scaling factor schedule for a single mode computation across two conditions 76
2.6 Example of the grid quality assessment for the aeroelastic method, which focuses on the cell skewness and overall volume differences between a rigid and elastic simulation. Presented is an example of an isolated propeller blade at $70\%R$ undergoing elastic deformation with very little differences is the qualifying criteria. 77

3.1 Propeller geometry used for the aerodynamic and aeroelastic verification process 79
3.2 Isolated JORP propeller blade grid 80
3.3 Aerodynamic results for the isolated JORP propeller 82
3.4 Chimera grid for the installed propeller verification 83
3.5 Semi-span aircraft key aerodynamic loads for the wing and propeller, normalised with respect to twice the freestream dynamic head (q_∞) 85
3.6 Semi-span aircraft aerodynamic solution 85
3.7 IMPACTA propeller blade NASTRAN model 86
3.8 IMPACTA propeller blade spoke diagram 87
3.9 Diagram of the first bending and torsion modes for a cantilever beam 87
3.10 Semi-span wing aeroelastic deflection, non-dimensionalised with respect to the reference chord 89
3.11 Change in surface pressure coefficient between the rigid and elastic solutions for the semi-span wing 91

4.1 Gulfstream American 695A Jetprop 1000 [5] 93
4.2 Commander propeller computational domain and chimera grid. 93
4.3 Commander propeller blade structural properties and resultant frequencies. . . 96
4.4 Comparison of the maximum relative torsional stress, along the blade radius, between the experimental and simulation results. 97
4.5 Modal amplitude response for the Commander blade in static conditions at a pitch angle of $27^{o}40'$ through a rotational velocity acceleration. 98
4.6 FFT of the modal amplitude response for the Commander blade. 99
4.7 Flow visualisation of the non-dimensional tangential velocity using radial slices for the accelerating blade *URANS* calculation. 100
4.8 Flow visualisation of the non-dimensional tangential velocity using radial slices for the accelerating blade *SAS* calculation. 101
4.9 Flow visualisation using vorticity magnitude iso-surface of $|\omega| = 1.0$ for the accelerating blade *URANS* calculation. 102
4.10 Flow visualisation using vorticity magnitude iso-surface of $|\omega| = 1.0$ for the accelerating blade *SAS* calculation. 102
4.11 Visualisation of the surface pressure coefficients for the *URANS* simulation through the transition period. 103
4.12 Visualisation of the surface pressure coefficients for the *SAS* simulation through the transition period. 104
4.13 FFT of the surface pressure coefficient along the upper surface of the blade. . . 104
4.14 Comparison of the maximum relative torsional stress, along the blade radius, between the accelerating and fixed *rpm* simulations. 105
4.15 Comparison of the modal amplitude response between the accelerating blade and fixed *RPM* simulations. 106
4.16 A comparison of the modal amplitude frequency response for the accelerating and fixed *RPM* simulations. 107
4.17 Vorticity magnitude iso-surfaces of the rigid hover formulation solutions over a range of blade pitch angles at 1400 (rpm) 109
4.18 Unsteady normalised thrust coefficients for the standard and reduced pitch *URANS* and *SAS* rigid solutions 110
4.19 Comparison of the modal amplitude response for the reduction in propeller blade stall 111
4.20 Commander propeller blade bungee structural model and tuned properties . . . 113
4.21 Commander propeller blade tuned model spoke diagram 113
4.22 Comparison of the modal amplitude response for the change in structural model for the Commander blade using *SAS* 114

4.23 Comparison of the non-dimensional torsional stress results for the change in structural model for the Commander blade 115
4.24 Difference in bending/torsion for the change in structural model for the Commander blade 116
4.25 Resultant propeller thrust coefficient for the tuned and standard model simulations 117
4.26 Interpolation scaling factor schedule for the tuned model acclerated blade simulation 118
4.27 Comparison of the modal amplitude response for the introduction of interpolated modes to the Commander blade simulation 119
4.28 Comparison of the modal amplitude frequency response, across the full time-history, for the introduction of interpolated modes to the Commander blade simulation 120
4.29 Comparison of the non-dimensional torsional stress results for the introduction of interpolated modes to the Commander blade simulation 121
4.30 Difference in bending/torsion for the introduction of interpolated modes to the Commander blade simulation, along with raw results for the 70%R station . . . 122
4.31 Resultant propeller thrust coefficient for the fixed and interpolated tuned mode simulations 123
4.32 Comparison of the modal amplitude response between the two and four stage interpolated modes 124
4.33 Comparison of the non-dimensional torsional stress results between the two and four stage interpolated simulations 124
4.34 Resultant propeller thrust coefficient for the two and four staged interpolation . 125
4.35 Interpolation scaling factor schedule for the tuned model decelerated blade simulation 126
4.36 Difference between the accelerating and decelerating interpolated modal response for the Commander propeller 127
4.37 Comparison of the accelerating and decelerating interpolated modal frequency response for the Commander propeller 128
4.38 Difference between the accelerating and decelerating interpolated non-dimensional torsional stress response for the Commander propeller 129
4.39 Difference in the bending/torsion of the Commander blade between the accelerating and decelerating simulations 130
4.40 Resultant propeller averaged thrust coefficients for the decelerating and accelerating simulations 131

5.1 Computational grid for the 2D NACA 0012 aerofoil 135

5.2 Pitching moment comparison to the experimental values for the NACA 0012 verification, where the datum case is selected as the middle value for each investigated parameter 138
5.3 Comparison of the NACA 0012 pitching moment coefficient for the 2D and quasi-3D simulations to the experiment, with the flow conditions presented in Table 5.1. 139
5.4 Cycle-to-cycle variations of the NACA 0012 pitching moment coefficient for the quasi-3D *SAS* simulation 140
5.5 Flow visualisation of $|\omega| = [1.0, 5.0, 10.0]$ iso-surfaces during the aerofoil upstroke 141
5.6 Flow visualisation of $|\omega| = [1.0, 5.0, 10.0]$ iso-surfaces during the aerofoil downstroke 142
5.7 Pitching moment response of the $70\%R$ Commander aerofoil section. 143
5.8 Pitching moment response of the $90\%R$ Commander aerofoil section. 145
5.9 Commander propeller sections used for the damping calculations. 146
5.10 Comparison of the change in pitching moment for the *URANS* and *SAS* simulations. 148
5.11 Flow visualisation at $\frac{x}{R} : 0.9$ of the tangential velocity profile for the *SAS* and *URANS* simulations at maximum ΔC_m. 150
5.12 Surface pressure coefficient on the blade upper surface at the 90% radial station through the peak ΔC_m for the *URANS* and *SAS* simulations. 151

6.1 Change in the modal frequencies with the adjustment in centre of gravity position for the Commander propeller blade 153
6.2 Change in the mode shape for adjustment in blade centre of gravity 154
6.3 Influence of the centre of gravity offset on the Commander propeller blade spoke diagram 155
6.4 Comparison of the modal amplitude response for the change in centre of gravity for the Commander blade 157
6.5 Comparison of the torsional stress results for the change in centre of gravity for the Commander blade 158
6.6 Difference in bending/torsion for the change in centre of gravity for the Commander blade 159
6.7 Change in the modal frequencies with the adjustment in additional mass weight for the Commander propeller blade 160
6.8 Change in the mode shape for introduction of a $20\%m_b$ mass to the blade tip . . 161
6.9 Influence of the additional tip mass on the Commander propeller blade spoke diagram 162
6.10 Comparison of the modal amplitude response for the inclusion of a tip mass on the Commander blade 164

6.11 Comparison of the torsional stress results for the the inclusion of a tip mass on the Commander blade . . . 165
6.12 Comparison of the filtered peak torsional stress results for the the inclusion of a tip mass on the Commander blade at select radial stations . . . 166
6.13 Difference in bending/torsion for the inclusion of a tip mass on the Commander blade . . . 167
6.14 Change in the modal frequencies with the reduction in torsional stiffness for the Commander propeller blade . . . 168
6.15 Change in the mode shape for reduction in torsional stiffness by 50% . . . 169
6.16 Influence of a 50% reduction in torsional stiffness on the Commander propeller blade spoke diagram . . . 170
6.17 Comparison of the modal amplitude response for the reduction in torsional stiffness of the Commander blade . . . 171
6.18 Comparison of the torsional stress results for the reduction in torsional stiffness of the Commander blade . . . 172
6.19 Difference in bending/torsion for the reduction in torsional stiffness for the Commander blade . . . 173
6.20 Comparison of the normalised thrust coefficient for all structural parametric studies 174
6.21 Comparison of the modal amplitude response for the increase in blade pitch of the Commander blade . . . 176
6.22 Modal force results for the increased pitch simulation, with the difference from the reference, for the Commander propeller blade . . . 176
6.23 Comparison of the torsional stress results for the the increase in blade pitch of the Commander blade . . . 177
6.24 Difference in bending/torsion for the increase in blade pitch of the Commander blade . . . 178
6.25 Surface pressure coefficient frequency response for the increased pitch simulation of the Commander blade . . . 179
6.26 Rolling average normalised load comparison for the increased pitch simulation of the Commander blade . . . 179
6.27 Rolling average centre of pressure comparison for the increased pitch simulation of the Commander blade . . . 180
6.28 Flow visualisation using iso-surface of vorticity magnitude for the introduction of an inflow velocity to the Commander blade . . . 181
6.29 Unsteady normalised thrust results for the introduction of 20 knots inflow to the Commander blade . . . 183
6.30 Comparison of the modal amplitude response for the introduction of a 20 knots inflow to the Commander blade . . . 184

6.31 Modal force results for the 20 knots inflow simulation, with the difference from the reference, for the Commander propeller blade 184
6.32 Comparison of the torsional stress results for the introduction of a 20 knots inflow to the Commander blade 185
6.33 Difference in bending/torsion for the introduction of a 20 knots inflow to the Commander blade 186
6.34 Rolling average normalised load comparison for the 20 knots inflow simulation of the Commander blade 186
6.35 Surface pressure coefficient frequency response for the 20 knots inflow simulation of the Commander blade 187
6.36 Rolling average centre of pressure comparison for the 20 knots inflow simulation of the Commander blade 188

List of Publications

In Journals

R.J. Higgins, A. Jimenez-Garcia, G.N. Barakos and N. Bown, "High-fidelity computational fluid dynamics methods for the simulation of propeller stall flutter", *AIAA Journal*, Vol. 57, Issue 12, 2019, DOI: 10.2514/1.J058463

R.J. Higgins, G.N. Barakos and E. Jinks, "Estimation of three-dimensional aerodynamic damping using CFD", *The Aeronautical Journal*, Vol. 124, Issue 1271, 2020, DOI: 10.1017/aer.2019.135

R.J. Higgins, A. Zarev, G.N. Barakos and R.B. Green, "Numerical Investigation of a Two-Bladed Propeller Inflow at Yaw", *Journal of Aircraft*, Vol. 57, Issue 2, 2020, DOI: 10.2514/1.C035647

R.J. Higgins, G.N. Barakos and A. Filippone, "A Review of Propeller Stall Flutter", *The Aeronautical Journal*, *Under-review*, 2021

In Conference Proceedings

R.J. Higgins, G.N. Barakos, "Whirl and Stall Flutter Simulation Using CFD", *Proceedings of the 43rd European Rotorcraft Forum, 12-15 September 2017, Milan, Italy*.

R.J. Higgins, A. Jimenez-Garcia, G.N. Barakos, N. Bown, "A Time-Marching Aeroelastic Method Applied to Propeller Flutter", *Proceedings of the 2019 SciTech AIAA Forum, 7-11 January 2019, San Diego, CA, USA*.

In Conferences without Proceedings

R.J. Higgins, G.N. Barakos, "Whirl Flutter Simulation Using CFD", *3rd U.K. Vertical Lift Network Workshop, 22-23 May 2017, Cheshire, U.K.*.

R.J. Higgins, G.N. Barakos, "Investigation of Propeller Stall Flutter", *4th U.K. Vertical Lift Network Workshop, 8-9 April 2019, Cheshire, U.K.*.

Technical Notes

A. Jimenez-Garcia, R.J. Higgins, G.N. Barakos, "Investigation of Propeller Whirl Flutter using HMB3", *Propeller Whirl Flutter Investigation - Internal Report No. 2*, April 2018.

G. Loupy, A. Jimenez-Garcia, R.J. Higgins, G.N. Barakos, "Release and Aeroelastic Computations in HMB", *Techincal Note TN18-001* CFD Laboratory, University of Glasgow, February 2018.

Acknowledgements

Firstly, my greatest thanks must go to Prof. George N. Barakos. Your passion and drive is something I will hold on to throughout my career, and I cannot thank you enough for the words of encouragement, knowledge and opportunities that you have given to me.

It goes without saying that a large amount of appreciation must go to Nicholas Bown and Edward Jinks of Dowty Propellers for their support. Without their collaboration, this project would not be possible. This includes the exchange of geometry and test reports to your patience in allowing me to learn and grow. My great thanks to you both.

I must also thank Dr Rene Steijl and Dr Mark Woodgate for their supervision, guidance and general support throughout my project.

I would like to thank all past and present members of the CFD Laboratory at the University of Glasgow for creating a working environment from which I could thrive. The ability to use this community as a sounding board cannot be underestimated. Of such colleagues, I could like to place a special mention to Blaga Todorova and David Pickles, whom I started the process with, due to their support in key moments of my studies.

Last, but certainly not least, I would like to thank my future wife, Lyndsay Claire Hamilton. Without your love and support, I would not be in this position today.

Declaration

I certify that the thesis presented here for examination for a PhD degree of the University of Glasgow is solely my own work other than where I have clearly indicated that it is the work of others (in which case the extent of any work carried out jointly by me and any other person is clearly identified in it) and that the thesis has not been edited by a third party beyond what is permitted by the University's PGR Code of Practice.

I declare that the thesis does not include work forming part of a thesis presented successfully for another degree.

I declare that this thesis has been produced in accordance with the University of Glasgow's Code of Good Practice in Research.

I acknowledge that if any issues are raised regarding good research practice based on review of the thesis, the examination may be postponed pending the outcome of any investigation of the issues.

April 2021

.....

Ross John Higgins

1000262

Nomenclature

Latin symbols

c_{ref}	Reference chord (m)
C_m	Pitching moment coefficient (-)
C_m^D	Pitching moment coefficient during the aerofoil downstroke (-)
C_m^U	Pitching moment coefficient during the aerofoil upstroke (-)
ΔC_m	Change in pitching moment coefficient (-)
C_p	Surface pressure coefficient (-)
ΔC_p	Change in the surface pressure coefficient between elastic and rigid simulations (-)
C_T	Thrust coefficient (-)
$\mathbf{C}_A$	Centroids of the shared points at the original position, A (m)
$\mathbf{C}_B$	Centroids of the shared points at the secondary position, B (m)
e	Specific Internal Energy ($(m/s)^2$)
E	Total energy of the fluid per unit mass ($(m/s)^2$)
E	Young's modulus (N/m^2)
f_i	i-th component of the body force acting on the fluid (N/kg)
f_m^s	Modal force on solid, s, for the m-th mode ($N/m\dot{k}g$)
$\mathbf{F}^i$	Inviscid flux vector in the x-direction (-)
$\mathbf{F}^v$	Viscous flux vector in the x-direction (-)
$\mathbf{G}^i$	Inviscid flux vector in the y-direction (-)
$\mathbf{G}^v$	Viscous flux vector in the y-direction (-)
$\mathbf{H}$	Covariance matrix (m)
$\mathbf{H}^i$	Inviscid flux vector in the z-direction (-)
$\mathbf{H}^v$	Viscous flux vector in the z-direction (-)
I	Rayleigh-Ritz wing moment of inertia (m^4)
i, j, k	Spatial indicies the curvilinear coordinate system (-)
k	Turbulent kinetic energy ($(m/s)^2$)
k_h	Heat transfer coefficient (-)
ℓ	Turbulent length scale (m)
ℓ_{vk}	von K*á*rm*á*n turbulent length scale (m)
L	Wing semi-span length/Length of the Rayleigh-Ritz beam (m)
m	Number of modes (-)
m	Rayleigh-Ritz mass per unit length (kg/m)
m_m	Generalised mass of the m-th mode (kg)
$\mathbf{M}$	Structural mass matrix (kg)
n_s	Number of CFD mesh points on solid, s (-)
n_{sp}	Number of shared points (-)

n_m^s	Number of modes, m, for solid, s (-)
N	Number of inner time-steps for the structural solver (-)
p	Fluid pressure (Pa)
$p(p,t)$	Solid pressure vector at point, p, and time, t (N/m^2)
$\tilde{p}$	Unsteady surface pressure (Pa)
$\mathbf{P}$	Position vector (m)
P_k	Turbulent kinetic energy turbulence production term ($kg/(ms^3)$)
P_ω	Specific dissipation rate turbulence production term ($kg/(ms^3)$)
$\mathbf{q}$	Heat flux vector (W/m^2)
q_j	Rayleigh-Ritz generalised coordinate for the j-th mode
q_∞	Freestream dynamic head (kg/ms^2)
Q_{SAS}	Additional source term for ω in the SAS turbulence model ($kg/(m^3s^2)$)
r/R	Non-dimensional radial position (-)
R	Blade radius (m)
R/c	Blade Aspect Ratio (-)
$\mathbf{R}$	Residual vector (-)
$\mathbf{R}$	Rotation matrix (-)
R_{sp}	Specific gas constant ($J/(kg\dot{K})$)
Re	Reynolds number (-)
R/c	Blade aspect ratio (-)
$\mathbf{S}$	Navier-Stokes source term vector (-)
$\mathbb{S}$	Scalar invariant of the strain rate tensor (1/s)
S_{ij}	Strain rate tensor (1/s)
t	Time (s)
$\mathbf{t}$	Translation vector (m)
Δt	CFD time-step (s)
Δt_i	Inner time-step for the structural solver (s)
T	Temperature (K)
$\mathbf{u}$	Fluid velocity vector (m/s)
$\vec{u}$	Local displacement velocity (m/s)
V	Cell volume ($grid\ units^3$)
$w_i(\mathbf{x})$	IDW interpolation weight at position, $\mathbf{x}$ (-)
W_{aero}	Aerodynamic Work (J)
$\mathbf{W}$	Vector of conserved variables (-)
$\mathbf{x}$	Position vector (m)
y/L	Non-dimensional semi-span station (-)
Y^+	Non-dimensional wall distance (-)
$z(y,t)$	Rayleigh-Ritz bending deformation across radius, y, and time, t (m)

Greek symbols

α_m^s	Modal amplitude for the m-th mode of solid, s (-)
α_h	Harmonic angle of attack (^{o})
γ	Gas specific heat capacity ratio (-)
γ_j	Rayleigh-Ritz assumed torsional mode shape for the j-th mode
δ_{ij}	Kronecker delta (-)
Δ	Change in variable (-)
ε	Rate of dissipation of the turbulent kinetic energy (m^2/s^3)
ζ_m	Structural damping coefficient for the m-th mode (-)
η_m	Eigenvector of the m-th mode
$\theta(y,t)$	Rayleigh-Ritz torsional deformation across radius, y, and time, t (^{o})
θ_{cycle}	Aerodynamic Damping (-)
κ	von K*á*rm*á*n constant (-)
μ	Molecular dynamic viscosity ($Pa\dot{s}$)
μ_t	Turbulent Eddy viscosity ($Pa\dot{s}$)
ρ	Fluid Density (kg/m^3)
τ_{ij}	Viscous stress tensor (Pa)
υ_t	Turbulent kinematic viscosity (m^2/s)
$\phi^b(p)$	Displacement of the point, p, due to the parent body (m/kg)
ϕ^p	Displacement due to the parent body, p (m/kg)
$\phi^s(t)$	Normalised displacement of solid, s, at time, t (m/kg)
ϕ_0^s	Undeformed shape of solid, s (m/kg)
$\phi_m^s(p)$	Normalised m-th mode displacement of point, p, on solid, s (m/kg)
ψ_j	Rayleigh-Ritz assumed bending mode shape for the j-th mode
Ψ	Azimuthal position (^{o})
ω	Specific dissipation rate of the turbulent kinetic energy (1/s)
$\lvert\omega\rvert$	Vorticity Magnitude (1/s)
ω_m	Modal frequency for the m-th mode (Hz)
ω_{1b}	Rayleigh-Ritz 1st bending mode natural frequency (Hz)
Ω_{CV}	control volume size (m^3)

Acronyms

ADT	Alternating Digital Tree
BEMT	Blade Element Momentum Theory
BILU	Block Incomplete Lower-Upper
CFD	Computational Fluid Dynamics
CFL	Courant-Fridrichs-Lewy condition
CG	Centre of gravity

CSD	Computational Structural Dynamics
FFT	Fast-Fourier-Transform
HMB3	Helicopter Multi-Block 3
IDW	Inverse Distance Weighting
IMPACTA	Improving the Propulsion Aerodynamic and aCoustics of Turboprop Aircraft
JORP	Joint Open Rotor Propeller
LES	Large-Eddy Simulation
MLS	Moving Least Square
MPI	Message Passing Interface
MUSCL	Monotone Upstream-centred Schemes for Conservation Laws
NACA	National Advisory Committee for Aeronautics
NASA	National Aeronautics and Space Administration
NASTRAN	NAsa STRucture ANalysis
PBEAM	NASTRAN Properties of BEAM element
RANS	Reynolds-Averaged Navier-Stokes
RBARS	NASTRAN Rigid Bar
RK4	Four-stage Rugge-Kutta
SAS	Scale-Adaptive Simulation
SOL	NASTRAN Solution
SST	Shear Stress Transport
SVD	Singular Value Decomposition
URANS	Unsteady Reynolds-Averaged Navier-Stokes
UTRC	United Technologies Research Centre

Chapter 1

Introduction*

1.1 Background and Motivation

The focus of the thesis is on propeller flutter, which can manifest in a variety of different ways. This includes classic, stall and whirl flutter. These types of flutter, particularly whirl and stall, require detailed modelling of the aerodynamics and structural response of a propeller. For stall flutter, the non-linear aerodynamics is a result of the detached flow-field which triggers the aeroelastic excitation.

Successful capture of such aerodynamic interactions allows for increased accuracy in surface loads, and increased accuracy in predicting the resultant flutter boundary. From this base, and with the development of faster computing power, a time-marching aeroelastic method has been developed which couples Computational Fluid Dynamics (CFD) and Computational Structural Dynamics (CSD). Flutter of any type is a result of a fluid-structure interaction and the method was derived based on this assumption.

In order to understand the requirement for this project, it is important to recognise the context for which propeller design and use currently resides. Propeller blades are coming back into fashion due to their high efficiency across short- to medium-range flight [118, 123]. However, their acoustic emissions dictated a need for a re-design to limit such factors [10, 38]. This led to the IMPACTA investigation [1, 26] for which a significant change to the standard design was implemented [31]. This included high sweep and taper, with non-typical twist profiles. Such alterations to the propeller design can result in a change to the propeller flutter boundary, particularly stall flutter due to the change in aerodynamics. In addition, stall flutter is one of the main limiting factors in propeller aeroelasticity due to the pronouced reduction in flutter boundary.

This change in propeller design is coupled with the novel research into electrical Vertical Take-off/Landing (eVTOL) [100,142] vehicles which utilise propellers for their multi-directional

*This chapter is submitted for publication in R.J. Higgins *et al.* "A Review of Propeller Stall Flutter", *The Aeronautical Journal*, *Under review*, 2021

thrust. Such a design was unvieled by Rolls-Royce in 2018 and utilises multi-rotor electrically-driven propulsion with a tiltwing airframe [3, 4]. The idea behind the concept was to use the tiltwing capability with the front propellers to vertically take-off/land. The front propellers would then be folded following the completion of the transition phase. Such a design pushes the propeller into non-typical operating conditions, hence there is a need to re-examine what is required to numerically investigate propeller stall flutter.

1.2 Aeroelasticity

Propeller flutter, or flutter in general, is a branch of aerospace research termed aeroelasticity. The field of aeroelasticity encompasses the study of aerodynamics and its interaction with the given structure. The overall response can be categorised based upon the combination of forces, with the forces being aerodynamic, inertial and elastic. This is summarised by Figure 1.1 (Collar's Triangle) where the combination of each force is categorised. The combination of the inertial and elastic forces follows the study of classic structural dynamics and does not consider any load effect due to the given flow. The introduction of aerodynamic forces with inertial results in the study of flight mechanics. This tends towards classic flight mechanics theory and the associated modes of motion. For a standard airframe, this includes the phugoid and short period longitudinal modes and the roll and dutch roll lateral modes. The final category involves the coupling of the aerodynamic and elastic forces, and is termed static aeroelasticity. Within this area of study, focus is given to understanding the deformation of a given structure based upon its elastic properties due to a load driven by the flow conditions. Any alteration to the shape can result in significant change to the flow-field conditions changing the applied load. This is a direct coupling of forces and requires the thorough investigation of both components. The addition of inertial forces to the study of static aeroelasticity results in a dynamic response. Such a dynamic response includes the study of aerodynamic instabilities, which can be driven by a multitude of factors.

1.2.1 Static Aeroelasticity

Some of the basic principles of aeroelasticity can be found within the understanding of static aeroelasticity. Described by Wright and Cooper [149], static aeroelasticity considers the non-oscillatory effects of aerodynamic loads on a flexible structure. For example, the overall deflection of a blade due to the steady hover loads. Any change in shape, whether it is driven by aerodynamics or the material, results in a change of the applied loads and their distribution. This is important to consider during the design process as a subsequent loss of performance may be induced.

The typical aeroelastic problems associated with static aeroelasticity are control surface reversal and divergence. The phenomenon of control surface reversal typically occurs when the

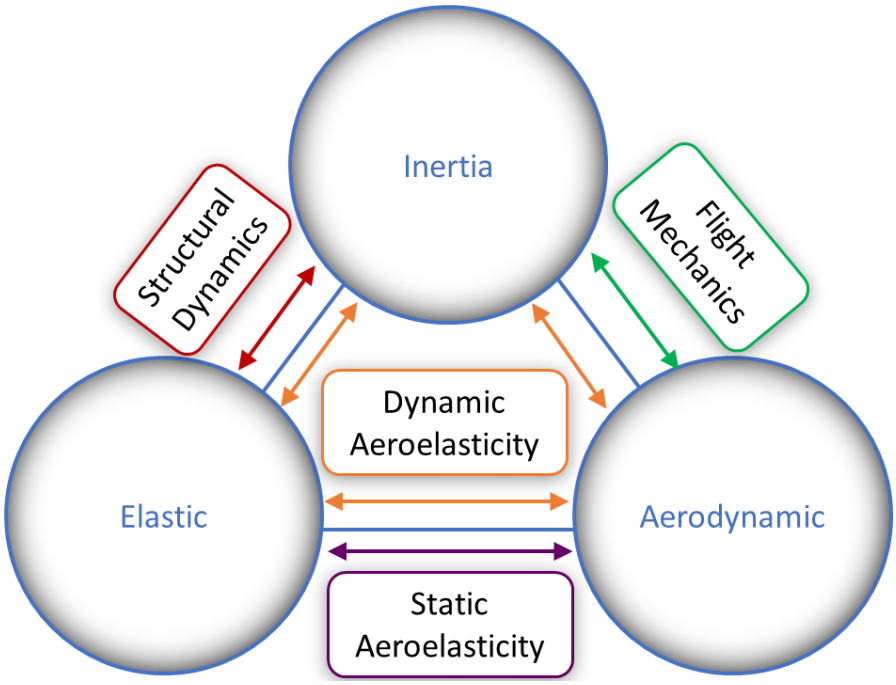

Figure 1.1: Summary of the field of aeroelasticity (Collar's Triangle)

generated hinge pitching moment is negated by the change in twist due to the static aeroelastic deflection. Control surface reversal studies are often conducted on fixed wing aircraft, with the focus on the effectiveness of the aileron, flaps and slats. In recent times, studies on the introduction of Gurney flaps to helicopter rotor blades have been conducted [65] and therefore the understanding of potential flap reversal would have to be considered during the design process.

Divergence is a catastrophic aeroelastic phenomenon where the deflection of the structure continues to increase until destruction. It is often seen as the twist of a fixed wing aircraft reaching a theoretically infinite value and is driven by the aerodynamic pitching moment exceeding the structural restoring moment. Divergence boundaries for propeller blades have been investigated by Liu and Young with the study utilising an aeroelastic model inspired by classical aeroelasticity [88]. This study was driven by the composite design of the marine propeller blades.

As per the study by Liu and Young, the modelling of divergence and control reversal phenomena can be undertaken by classical aeroelasticity. Such models are derived from one dimensional aerofoil analysis where the eigenvalues of the equations are computed to determine the subsequent boundaries. Classic models, such as this, are described by Dowell [44] using classic aerodynamic theory [11] and beam structural models [70]. Although such models can be effective, the non-linearity associated with unsteady aerodynamics is not accounted for.

1.2.2 Dynamic Aeroelasticity

Static aeroelasticity takes into account the non-oscillatory effects of elasticity and aerodynamics, combining this with the inertial effects of the structure can introduce oscillatory motion and this is termed as dynamic aeroelasticity. Dynamic aeroelasticity encompasses a variety of research areas including dynamic load prediction, gust analysis and fatigue. However, one of the key areas of study is the instability known as flutter. Classical flutter involves the unstable coupling of at least two modes of motion due to the combined effects of elasticity, aerodynamics and inertia [149]. An unstable flutter condition would typically involve the aerodynamics supplying energy to the structure and thus, overpowering the internal structural damping effects.

The most common, and likely catastrophic, flutter category is lifting surface flutter. This can include every lifting surface associated with the vehicle and therefore all surfaces must be investigated for such effects [67]. If the airflow separates during any stage of the elastic oscillation, the instability is known as stall flutter. It is typical for a one degree of freedom response to be found in a structure undergoing the effects of stall flutter. This degree of freedom is commonly found in torsion due to the introduction of a pitching moment which oscillates the structure in and out of stall. Due to the introduction of stalled flow, the aeroelastic equations of motions become non-linear. One of the critical factors in modelling dynamic aeroelasticity is capturing the non-linearity associated with unsteady aerodynamics. Many years of study have gone into the understanding and prediction of unsteady forces and moments. This is typified by the study of dynamic stall where some of the earliest experiments were conducted in the early 1950's [63] to the latest modelling efforts in 2019 [140].

A simple representation of a lifting surface flutter problem is described by Hodges and Pierce [67]. Using a modal representation, a lifting surface flutter analysis can be represented as a set of ordinal differential equations, with the generalised equations of motion presented in Equation 1.1.

$$M_i \left(\ddot{\xi}_i + \omega_i^2 \xi_i \right) = \Xi_i \qquad (i = 0, 1, \ldots n) \tag{1.1}$$

Here, M_i, ξ_i and Ξ_i are the generalised mass, coordinate and force terms, respectively, with the natural frequency represented by ω_i for the $i-th$ mode. Within this analysis, structural damping is neglected however typical values for propellers range from 6% to 0.1% and are dependent upon the root-hub connection. Expansion of generalised force and mass terms results in equations of motion which can be solved as an eigenvalue problem for ν_i, the complex column matrix for each mode (Equation 1.2). Each complex number determines the modal damping (Γ_i) and frequency (Ω_i) of the general solution, where the sign and value of both determine the response. Typical responses based upon this analysis is highlighted in Table 1.1.

$$\nu_i = \Gamma_i \pm i\Omega_i \qquad (i = 0, 1, \ldots n) \tag{1.2}$$

Γ_i	Ω_i	Type of Motion	Stability Characteristics
< 0	$\neq 0$	Convergent Oscillations	Stable
$= 0$	$\neq 0$	Simple Harmonic	Stability Boundary
> 0	$\neq 0$	Divergent Oscillations	Unstable
< 0	$= 0$	Continuous Convergence	Stable
$= 0$	$= 0$	Time Independent	Stability Boundary
> 0	$= 0$	Continuous Divergence	Unstable

Table 1.1: Influence of the modal damping and frequency on the simple lifting surface solution

Although such analyses can provide insight, they neglect the effects of unsteady aerodynamics. Such effects can only be determined via a classical flutter analysis and the introduction of additional modelling such as Theodorsen's thin aerofoil theory. As the focus of this thesis is on rotating wing aeroelasticity, the discussion of unsteady aerodynamics will continue within the context of a propeller.

1.3 Unsteady Aerodynamic Modelling for Propellers

To understand some of the challenges associated with propeller aeroelasticity, it is important to know the aerodynamic characteristics that are associated with propellers. Some of the propeller flow characteristics share some similarities with helicopter rotor with these described by Bielawa [21].

- In helicopter forward/edgewise flight, the tangential velocity fluctuates around the azimuth resulting in a zeroth, first and second order fourier component of the dynamic pressure. This variation in tangential velocity is driven by the respective freestream velocity contribution either side of the rotor revolution. Taking the tangential velocity due to the blade rotation as the nominal value, this is then supplimented on the advancing side via the addition of the freestream edgewise velocity. Therefore creating an overall tangential velocity above the nominal value. The opposite then occurs on the retreating side where the freestream edgewise and blade tangential velocities oppose one another, resulting in a tangential velocity below the nominal value. Such variations increase in complexity at high helicopter forward/edgewise flight speeds with the introduction of compressibility and stall effects on the advancing and retreating sides, respectively. This can often lead to secondary responses such as the introduction of shock waves or the development of dynamic stall vorticies. For a propeller in traditional forward/axial flight, such variations in the velocity components only occur with a freestream velocity at incidence. When at incidence, the typical uniform inflow profile is skewed resulting in similar additions/substractions on the advancing/retreating sides.

- In rotating wing aerodynamics, the local section angle of attack is comprised of the geometric pitch, the freestream inflow factor and the induced velocity effects. Both helicopter and propeller induced velocity effects are a result of the produced thrust and are therefore dependent upon the overall blade design. For helicopters, the geometric pitch is influenced by the required azimuthal control angles which ensure roll trim in forward/edgewise flight. Such angles are limited to collective controls in propellers due to the fact they primarily operate in uniform inflow conditions. Additionally, the inflow effects are typically larger in propellers due to operating in axial flight when in cruise. However during take-off, this inflow effect is reduced resulting in an overall larger effective angle of attack. This can potentially lead to the detachment of flow across the propeller.

- Depending on the rotor condition and configuration, blade vortex interaction, or simple vortex disturbances, can be seen in the blade loads. This is due to the wake generated behind the blade. This can be present in a helicopter rotor depending on the ratio between the normal airflow velocity through the disc and the tangential velocity generated due to the blade rotation. This ratio is often heavily biased towards the tangential velocity and, hence, the blade vortex projection downstream may not be great enough to ensure it is out of the influence of the oncoming blade. This ratio is not as biased towards the tangential velocity for a propeller blade, with the freestream inflow velocity and generated thrust of greater importance to any potential blade vortex interaction.

All of the above characteristics assume a rigid blade and, therefore, any oscillation in propeller loads will induce secondary blade bending and torsion which introduced further fluctuations.

Such characteristics highlight the complexity associated with the modelling of the aerodynamics around a rotating wing. This fact has often been the limiting factor in the development of a universal theory for rotorcraft aeroelasticity. In the past, aerodynamic theory driven from fixed-wing applications have been adapted and applied. However, significant factors limit its applicability due to some of the basic assumptions. These include: two-dimensionality; the effect of reduced frequency and the subsequent response; heavily variable flow and aerofoil motion; and the near- and far-field effects associated with shed vorticity.

These factors have led to a range of proposed rotor airload theories which can be categorised based upon their aim. Such categorises take into account the purpose, complexity, mathematical principle, the treatment of the rotor wake and its method of implementation. For example, the purpose of the theory could be to determine the steady-state harmonic loads using a two-dimensional lifting line code based upon aerofoil theory with no wake model to determine the blade response in the frequency domain. This represents a basic framework from which to examine rotor aerodynamics. Something more complex would look to determine the unsteady harmonic loads using the Navier-Stokes equations to apply such derived loads to a time-marching aeroelastic method.

In the context of a flutter analysis, the aerodynamic methods can be split into frequency domain and time-marching methods with a two-dimensional assumption. Three key frequency-based theories have been developed from fixed-wing applications and subsequently modified for the rotating wing. Two time-marching theories are presented with the first building on a well known frequency method. Each model is described for the context of a rotor blade classical bending-torsion analysis.

1.3.1 Two-dimensional Frequency-Domain Theories

For each of the three frequency domain theories, the following assumptions are made:

1) The aerofoil section consists of a thin flat plate under the condition of a small angle of attack. Wake is shed from the trailing edge rearward to infinity with no downward velocity or vertical distortion.

2) The flow is inviscid and incompressible.

3) The flow is governed by linear potential flow with the non-linearity associated with stall neglected.

4) All disturbances in aerofoil motion and airflow are assumed to be harmonic.

Theodorsen's theory. One of the most popular theories is that derived by Theodorsen [131, 133] and covers the modelling of a plunging (h) and pitching (θ) aerofoil in static conditions. Taking the expressions for lift (L) and moment (M) on an aerofoil with unit span:

$$\begin{aligned} L &= \pi\rho b^2\left[\ddot{h}+U\dot{\theta}-ba\ddot{\theta}\right]+2\pi\rho UbC(k)\left[\dot{h}+U\theta+b(0.5-a)\dot{\theta}\right], \\ M &= \pi\rho b^3\left[a\ddot{h}-U(0.5-a)\dot{\theta}-b(0.125+a^2)\ddot{\theta}\right] \\ &\quad +2\pi\rho Ub^2(0.5+a)C(k)\left[\dot{h}+U\theta+b(0.5-a)\dot{\theta}\right], \end{aligned} \tag{1.3}$$

where b is the aerofoil semi-chord, ba is the distance between the aerofoil leading edge and the axis of rotation, a being the difference between the semi-chord and axis of rotation, U is the freestream velocity and $C(k)$ is the Theodorsen function. This function is complex and defined as:

$$C(k) = F(k) + iG(k) = \frac{H_1^{(2)}(k)}{H_1^{(2)}(k) + iH_0^{(2)}(k)}, \tag{1.4}$$

where $H_n^{(2)}$ are Hankel functions of the second kind, which are Bessel functions of the first and second kinds. To modify this fixed wing theory for rotorcraft, the following assumptions are made:

- The term 2π is replaced by the true aerofoil lift curve slope, c_{l_α}
- The distance from the leading edge to the rotation axis, ba, is replaced by the distance between the aerodynamic center and axis of rotation $(x_a - c/4)$, where c is the aerofoil chord
- The freestream velocity, U, is taken as the blade tangential velocity due to the rotation (Ω) at the given radial position (r), Ωr
- The reduced frequency (k), which characterises the unsteadiness of the flow, is taken with respect to the tangential velocity at the 75% radial station. Hence, $k = \frac{b\omega}{0.75\Omega R}$, where ω is the circular frequency, Ω the blade rotational velocity and R the blade radius.
- The semi-chord b is replaced by $c/2$ with the aerofoil plunging notation h replaced by blade bending z.

Taking the differential across the blade radius, the equivalent lift and moment equations are derived (Equation 1.5). Although such a theory would appear restrictive to the Theodorsen function, by substituting different lift-deficiency functions in place of the Theodorsen function the unsteady airloads for other assumed conditions can be expressed. Their substitutions are described in the following sections.

$$\begin{aligned}
\frac{dL}{dr} &= -\frac{\pi}{4}\rho c^2\Omega^2\left[\frac{\ddot{z}}{\Omega^2} - \frac{r\dot{\theta}}{\Omega} + \frac{(x_a - c/4)\ddot{\theta}}{\Omega^2}\right] + \frac{1}{2}\rho c_{l_\alpha} c r\Omega^2 C(k)\left[-\frac{\dot{z}}{\Omega} + r\theta + \frac{(c/2 - x_a)\dot{\theta}}{\Omega}\right] \\
\frac{dM}{dr} &= -\frac{\pi}{4}\rho c^2\Omega^2\left[\frac{(x_a - c/4)\ddot{z}}{\Omega^2} + \frac{r(c/2 - x_a)\dot{\theta}}{\Omega} + (\frac{3}{32}c^2 - \frac{c}{4}x_a + x_a^2)\ddot{\theta}/\Omega^2\right] \\
&\quad + \frac{1}{2}\rho c_{l_\alpha} c x_a r\Omega^2 C(k)\left[-\dot{z}/\Omega + r\theta + \frac{(c/2 - x_a)\dot{\theta}}{\Omega}\right]
\end{aligned} \tag{1.5}$$

Sears Function. The formulation of the Sears function [121] is similar in its framework to the Theodorsen function, however, the assumption of a pitching and plunging aerofoil is no longer applied with the aerofoil motionless. The unsteadiness is therefore assumed to be driven by a sinusoidal variation in the airflow vertical direction.

With the double derivative terms neglected due to the lack of aerofoil motion, the remaining terms of the equations can be represented by a vertical velocity distribution ($w(x,t)$) of the following form:

$$w(x,t) = We^{i\omega(t - x/U)}, \tag{1.6}$$

where W is the effective downward velocity, t is time, x the aerofoil coorindate position, U the freestream velocity and the frequency, ω, with which the waves passes the aerofoil is given by:

$$\omega = \frac{2\pi U}{\ell_w} \tag{1.7}$$

where ℓ_w is the wavelength of the gusts. This results in the following formulation using the Sears function ($\phi(k)$):

$$\begin{aligned} L &= \pi\rho c U W e^{i\omega t}\phi(k) \\ M_{c/2} &= L(c/4) \end{aligned} \tag{1.8}$$

The Sears function is again calculated using Bessel functions, or alternatively, a combination of Bessel and Theodorsen functions:

$$\phi(k) = [J_0(k) - iJ_1(k)]C(k) + iJ_1(k) \tag{1.9}$$

The Loewy Problem. One of the key factors in rotor aerodynamics is the influence of trailing vorticity. The Loewy model takes this into account via a modification of the Theodorsen theory [89]. In this model, the lift-deficiency function used in Equation 1.5 is modified to give a more accurate representation of the rotor airloads. As a result, increased accuracy flutter calculations can be conducted.

To understand the changes in the lift-deficiency function, the characteristics associated with the rotor wake must be discussed. Assuming a hovering or vertical flight rotor, the axial component of the velocity through the rotor disc (u) is proportional to the rotor thrust (T) and axial freestream velocity (V_z). Assuming a constant inflow and using momentum theory, the axial velocity through the rotor is given by:

$$u = \frac{V_z}{2} + \sqrt{\frac{V_z^2}{4} + \frac{T}{2A\rho}}, \tag{1.10}$$

where A is the rotor disc area and ρ the air density. As presented by Bielawa [21], the rotor wake can be built up based upon levels of different complexity with each level highlighted in Figure 1.2. The main feature of the rotor wake is the blade tip vortex (Figure 1.2(a)). This is driven by the roll up of vorticity at the tip and, due to the rotation, creates a contracting helix which is projected downstream at a velocity, u. The contraction is caused by the blade motion driving the airflow. An extracting helix is found in wind turbines due to the energy being extracted from the wind. In Figure 1.2(b), the location of the local airstreams which detach from the trailing edge of the rotor are highlighted. Such airstreams combine with the blade tip vortex to create a helical surface. As explained earlier, fluctuations in loads due to the change in conditions on the retreating and advancing sides of the rotor are found. Such fluctuations cause changes in the vorticity present along the blade span and, as a result, shed vorticity will be produced and gathered in the rotor wake (Figure 1.2(c)). Due to the three-dimensionality of

rotor aerodynamics, unsteady trailing edge vorticity is produced adding greater complexity to the rotor wake (Figure 1.2(d)).

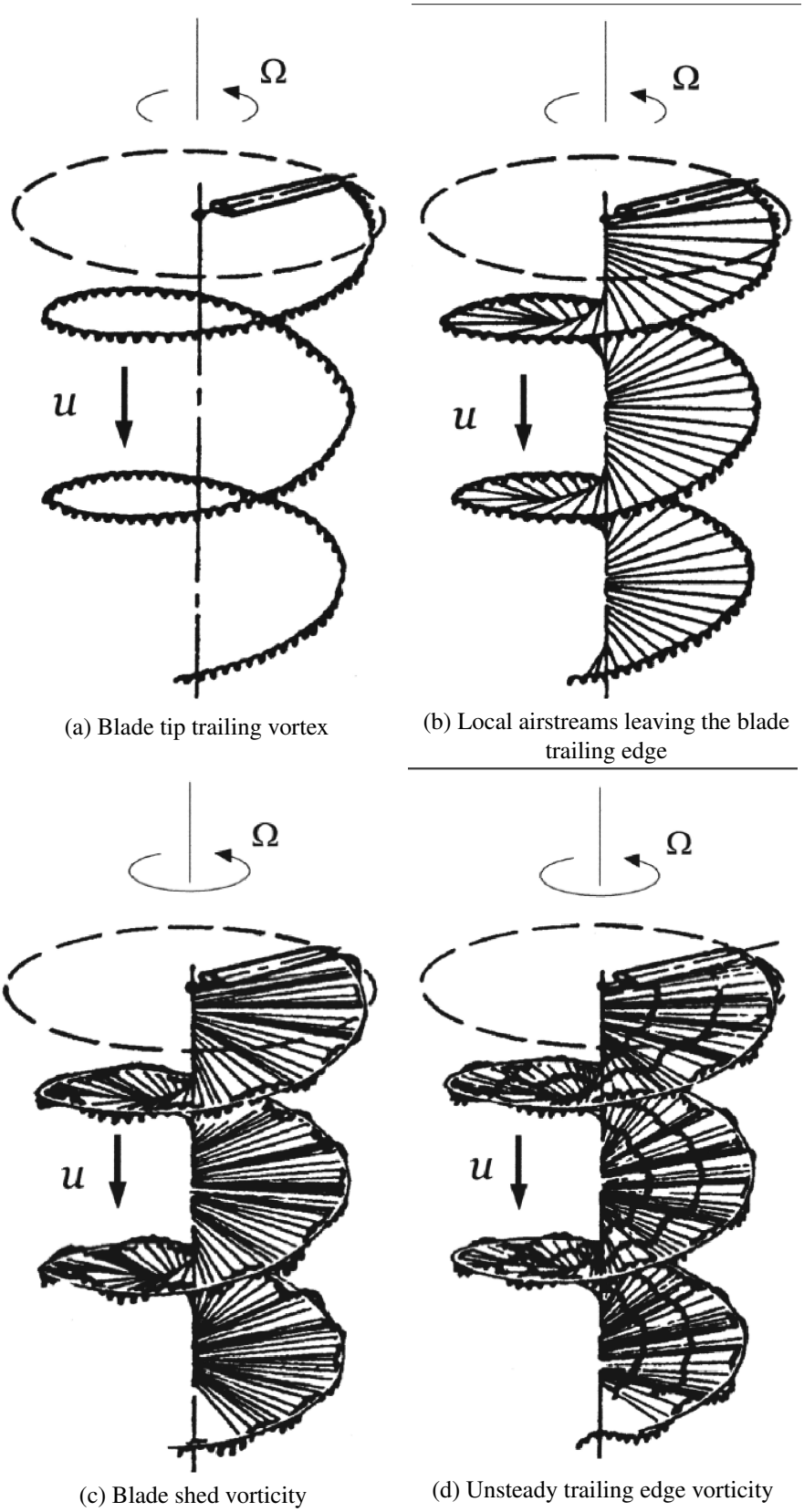

(a) Blade tip trailing vortex

(b) Local airstreams leaving the blade trailing edge

(c) Blade shed vorticity

(d) Unsteady trailing edge vorticity

Figure 1.2: Build up of the rotor wake [21]

These schematics indicate the complexity of the rotor flow, however, one factor that has not been discussed is the axial velocity at which the wake convects downstream. At high values of the inflow velocity, the distance between the subsequent wake surfaces are large. A schematic of this condition is shown in Figure 1.3(a). If the distance between the surfaces equals $2\pi u/Q\Omega$, where Q is the number of blades, u is the axial velocity and Ω is the rotational speed, the wake effect can be ignored and the standard Theodorsen function used for the blade airloads.

If the opposite is true, and a low inflow velocity is seen (Figure 1.3(b)), the influence of the helical wake surface increases. Depending on the distance, the vorticity present several surface iterations downstream can become more influential on the blade airloads than the vorticity produced directly behind the blade trailing edge. In such a condition, the accuracy of the standard Theodorsen function decreases, and an update to the lift-deficiency function is required to include this effect.

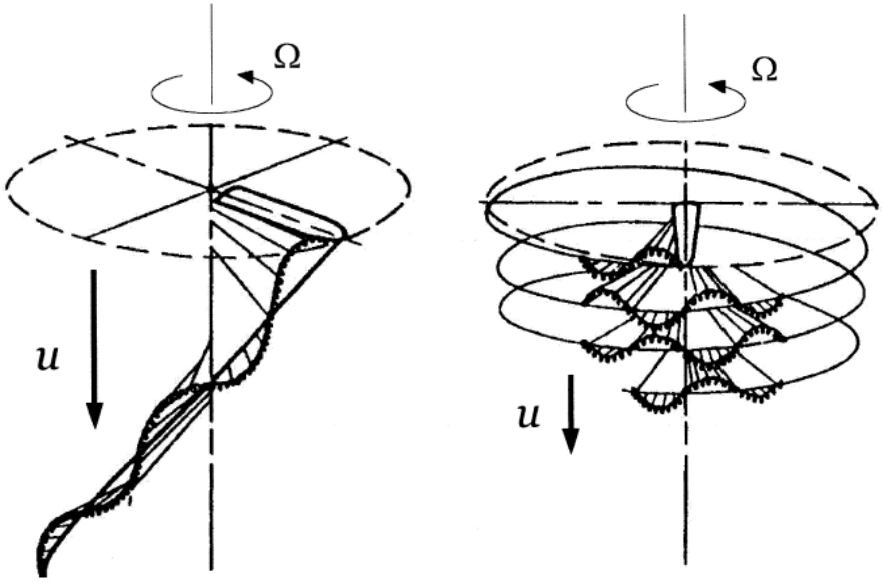

(a) High inflow velocity (b) Low inflow velocity

Figure 1.3: Influence of the rotor inflow [21]

The Loewy model [89] describes the lift-deficiency function as shown in Equation 1.11. Again, a combination of Bessel functions and a new parameter, $\mathscr{W}$, which accounts for the total effect of the returning wake, is used to determine the lift-deficiency. This parameter, and the lift-deficiency function itself, is a function of several factors including reduced frequency (k), the spacing between the returning wakes (h_{rw}), the number of blades (Q), the phasing between the blades (ψ) and the frequency ratio ($m_{fr} = \omega/\Omega$). The total effect of the returning wake, $\mathscr{W}$, is determined via Equation 1.12. As $\mathscr{W}$ approaches zero, the lift-deficiency function returns to the standard Theodorsen function, $C(k)$.

$$C'(k, m_{fr}, h_{rw}, Q, \psi) = \frac{H_1^{(2)}(k) + 2J_1(k)\mathscr{W}(k, m_{fr}, h_{rw}, Q, \psi)}{H_1^{(2)}(k) + iH_0^{(2)}(k) + 2\left[J_1(k) + iJ_0(k)\right]\mathscr{W}} \tag{1.11}$$

$$\mathscr{W} = \frac{1 + \sum_{q=1}^{Q-1} \left(e^{kh_{rw}Q} e^{i2\pi m_{fr}}\right)^{(Q-q)/Q} e^{i\psi}}{e^{kh_{rw}Q} e^{i2\pi m_{fr}} - 1} \tag{1.12}$$

Although the Loewy theory is seen to be a substantial achievement in rotorcraft aerodynamic modelling, four key limitations remain:

1) The theory does not account of oscillations in the streamwise air velocity and is therefore invalid in helicopter forward/edgewise flight and propeller forward/axial flight at incidence conditions.

2) Due to the two-dimensional framework, interactional characteristics in spanwise phenomena are neglected.

3) The Theodorsen assumption of small amplitude motions results in the relatively large motions of flapping rotors being ignored.

4) The theory can only be treated in the frequency domain for aeroelastic problems.

1.3.2 Two-dimensional Time-Marching Theories

The above frequency-based theories paved the way for the aeroelastic analysis of rotor blades. However, designers pushing the boundary in terms of the blade design and operating conditions, increased fidelity models using time-marching frameworks are required. For such methods, two theories are discussed by Wagner and by Leishman and Beddoes.

Wagner Functions. Returning to the standard Theodorsen function, the secondary term for the fixed wing lift (composed as the product of the lift-deficiency function, $C(k)$) in deemed the circulatory terms. Removing the outside product, the remaining terms are the vertical velocity at the three quarter chord point, $w_{0.75c}$. Using this velocity, the transform from the frequency to the time domain is conducted via the use of the Fourier integral transform, $f(\omega)$, where the variables used below are defined as per the Theodorsen function in Section 1.3.1.

$$\begin{aligned} w_{0.75c}(t) &= \left[\dot{h} + U\theta + b(0.5-a)\dot{\theta}\right] \\ f(\omega) &= \int_{-\infty}^{+\infty} w_{0.75c} e^{-i\omega t} dt \end{aligned} \tag{1.13}$$

Wagner assumed a step angle in angle of attack (α_0):

$$w_{0.75c}(t) = \begin{cases} 0 & t < 0 \\ U\alpha_0 & t \geq 0 \end{cases} \tag{1.14}$$

and this leads to the inversed-Fourier transformed circulatory lift (L_c):

$$L_c(s) = \rho b U^2 \alpha_0 \int_{-\infty}^{+\infty} \frac{C(k)e^{iks}}{ik} dk = 2\pi\rho b U^2 \alpha_0 \phi_w(s) \tag{1.15}$$

where s is the aerodynamic time variable given by $s = Ut/b$. Following this, use of the Duhamel integral and Wagner function ($\phi_w(s)$) enables the full airloads to be computed whilst under the influence of any arbitrary angle of attack change, with the lift and moment given in Equation 1.16.

$$\begin{aligned} L &= \pi\rho b^2 \left[\ddot{h} + U\dot{\theta} - ba\ddot{\theta}\right] + 2\pi\rho b U W_\phi \\ M &= \pi\rho b^2 \left[ba\ddot{h} - Ub(0.5-a)\dot{\theta} - b^2(0.125+a^2)\ddot{\theta}\right] + 2\pi\rho U b(0.5+a)W_\phi \end{aligned} \tag{1.16}$$

where,

$$W_\phi = w_{0.75c}(0)\phi(s) + \int_0^s \frac{dw_{0.75c}(\sigma)}{d\sigma}\phi(s-\sigma)d\sigma. \tag{1.17}$$

Although such a function is seen as a first step, it is often used in transient load calculations where the aerofoil motion is known. Using such methods in a flutter analysis, where the exact direction of the motion is unknown, may be too complex.

Leishman-Beddoes Theory. To include true unsteady effects, it is often seen as desirable to use quasi-steady descriptions. Leishman defined an effective angle of attack for use with the quasi-steady formulation and, in turn, this effective angle of attack produces the lift-deficiency effects which characterise unsteady aerodynamics. The effective angle of attack is made up of an *unsteady decay parameter* which acts to modify the quasi-steady model to include unsteady fluctuations. The method begins with the evaluation of the circulatory lift (L_c) for an arbitrary quasi-steady angle of attack (α_{QS}):

$$L_c = 2\pi\rho b U^2 \left[\alpha_{QS}(0)\phi_w(s) + \int_0^s \frac{d\alpha_{QS}(\sigma)}{d\sigma}\phi_w(s-\sigma)d\sigma\right] \tag{1.18}$$

Replacing the lift curve slope, 2π, with the true value (c_{l_α}), the semi-chord length (b) with $c/2$, and defining the square bracket terms as the effective angle of attack (α_E), results in a condensed version for the circulatory lift.

$$L_c = 0.5\rho c c_{l_\alpha} U^2 \alpha_E \tag{1.19}$$

Taking the effective angle of attack and performing an integration by parts, a final solution and unsteady decay parameter (α_W) is derived.

$$\begin{aligned}\alpha_E &= 0.5\alpha_{QS} + \int_0^s \alpha_{QS}(\sigma)\phi_w'(s-\sigma)d\sigma \\ &= \alpha_{QS} - \left[0.5\alpha_{QS} - \int_0^s \alpha_{QS}(\sigma)\phi_w'(s-\sigma)d\sigma\right] \\ &= \alpha_{QS} - \alpha_W\end{aligned} \tag{1.20}$$

As part of this theory, Beddoes [17] suggested a compressibility correction in the form of an adjusted Wagner function ($\phi_w(s)$). Using the Prandtl-Glauert correction factor β (where $\beta = \sqrt{(1-M_a^2)}$ and M_a the Mach number) and an approximation to the Wagner function (ϕ_a), the following correction is derived:

$$\phi_c(s,M) = \frac{1}{\beta}\left(1 - 0.165e^{-0.0455\beta^2 s} - 0.355e^{-0.3\beta^2 s}\right) \tag{1.21}$$

where the approximation was originally given by:

$$\phi_a(s) = 1 - 0.165e^{-0.0455s} - 0.355e^{-0.3s} \tag{1.22}$$

This results in an updated unsteady decay parameter (α_W) that accounts for compressibility. Note, in this framework the true lift curve slope is used and, hence, the division by β is omitted from the corrected Wagner function.

$$\alpha_W = 0.5\alpha_{QS} - \int_0^s \alpha_{QS}(\sigma)\beta\phi_c'(s-\sigma)d\sigma \tag{1.23}$$

This expression for the effective angle of attack, and unsteady decay parameter, serves as a definition and starting point for the formulation of practical time-marching engineering tools to study rotorcraft aeroelasticity. The principle advantage is that it allows for the inclusion of unsteady effects in a convenient manner. One of the methods in which this framework is utilised is through the use of aerofoil look-up tables for the lift, drag and moment coefficients. Such coefficients are often derived from wind tunnel experiments and allow for the inclusion of compressibility effects. Using such techniques, low-frequency airloads needed for trim calculations or low-frequency aeroelastic analysis can be performed at a high level of accuracy.

1.4 Classical Rotor Flutter

In spite of the fact that the reduced frequency range for a rotor undergoing bending-torsion flutter requires the use of unsteady aerodynamics, the mechanism from which the flutter point is reached can be independent of unsteady airloads. Therefore, in order to gain some insight into classical rotor flutter, aerodynamics using an incompressible quasi-steady formulation for a blade in hover is used.

A blade undergoing flutter is driven by the interactions between the out-of-phase bending motion (z) and the torsional motion (θ). An inherent coupling between both bending and torsion exists and, hence, the chordwise offsets between the aerodynamic and mass centres to the shear centre (y_{AC} and y_{CG}, respectively) must be taken into consideration. These offsets are highlighted in the typical flutter blade section in Figure 1.4.

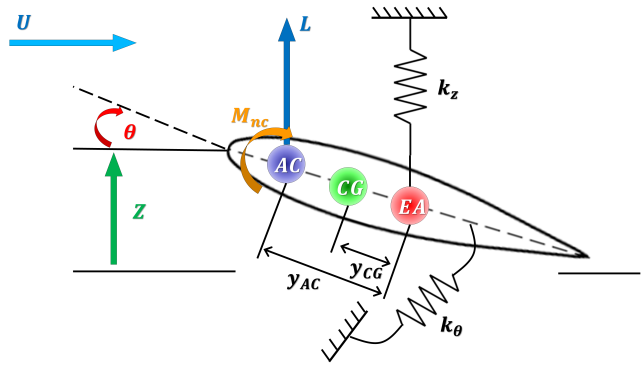

Figure 1.4: Typical blade section undergoing bending-torsion flutter

1.4.1 Fixed-Wing Derivation

For classical rotor flutter, the derived equations of motion are extensions of classical beam theory used for fixed wing applications. Therefore, for background, a basic flutter analysis for a two-dimensional fixed wing is derived. For a wing of effective length (ℓ_e), mass (m) and based upon the typical section shown in Figure 1.4, the resultant equations of motion for the vertical (z) and pitching (θ) motions are:

$$\begin{aligned} L &= m\ddot{z} + my_{CG}\ddot{\theta} + k_z z \\ Ly_{AC} + M_{\theta_{nc}} &= my_{CG}\ddot{z} + (I_\theta + my_{CG}^2)\ddot{\theta} + k_\theta \theta \end{aligned} \tag{1.24}$$

where k_z and k_θ are the plunge and pitch stiffness, the pitching inertia is given by I_θ and the lift (L) and non-circulatory moment ($M_{\theta_{nc}}$) are defined as:

$$\begin{aligned} L &= \ell_e \langle \frac{\pi\rho c^2}{4} U\dot{\theta} + c_{l_\alpha}\rho U \frac{c}{4} C(k)\left[-\dot{z} + U\theta + (0.5c - y_{AC})\dot{\theta}\right]\rangle \\ M_{\theta_{nc}} &= -\ell_e \langle \frac{\pi\rho c^2}{8} Uc\dot{\theta}\rangle \end{aligned} \tag{1.25}$$

The circulatory term in the expression can be treated as a frequency based lift-deficiency factor or as a Laplace transformed function using the approximate Wagner function. Using the

Laplace transform variable approach, the flutter equations of motion are expressed in Equation 1.26.

$$\begin{aligned}&\left[\begin{bmatrix} m & my_{CG} \\ my_{CG} & (I_\theta + my_{CG}^2) \end{bmatrix} p_\ell^2 + \pi\rho U \ell_e \frac{c^2}{4} \begin{bmatrix} 0 & -1 \\ 0 & c/2 \end{bmatrix} p_\ell + \begin{bmatrix} k_z & 0 \\ 0 & k_\theta \end{bmatrix} \right. \\ &+ c_{l_\alpha} \rho U \frac{c}{2} \ell_e \frac{0.5p_\ell^2 + 0.281(U/b)p_\ell + 0.01365(U/b)^2}{[p_\ell + 0.3(U/b)][p_\ell + 0.0445(U/b)]} \\ &\left.\times \left[\begin{bmatrix} 1 & -(c/2 - y_{AC}) \\ y_{AC} & -y_{AC}(c/2 - y_{AC}) \end{bmatrix} p_\ell + \begin{bmatrix} 0 & -1 \\ 0 & -y_{AC} \end{bmatrix}\right]\right] \begin{bmatrix} \bar{z} \\ \bar{\theta} \end{bmatrix} = 0\end{aligned} \tag{1.26}$$

In order to solve for the final flutter solution, a variety of methods are available. The Laplace variable domain formulation fits neatly into an eigenvalue solution that yields two eigenvectors with eight eigenvalues. Four of these eigenvalues relate to the unsteady aerodynamics, with an additional four formed as two complex conjugate pairs relating to the flutter damping and frequency for the bending and torsional modes [21].

A typical plot of these with respect to the freestream velocity is presented in Figure 1.5 where the results of a K-method* simulation of the experiments of Runyan and Sewall are made for certain mass properties and spanwise location. Here, the flutter velocity is driven by the damping and a positive damping value finds an unstable solution. This is found at the lower velocity of 68.3 m/s for *Mass 5* compared to 92.3 m/s for *Mass 7*.

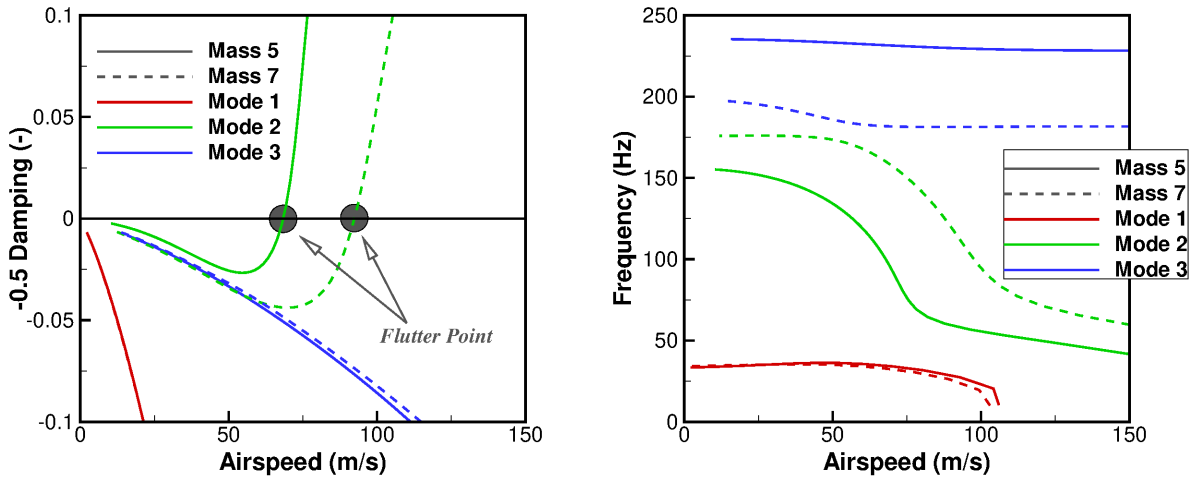

(a) Damping (b) Frequency

Figure 1.5: Typical variation of the flutter eigenvalues, fixed wing example of varying store positions for a given mass properties. Simulation of the experimental study of Runyan and Sewall [117]

*This method varies the reduced frequency (k) to find the point at which the artificial structural damping is zero, indicating the flutter point [67, 119].

1.4.2 Rotor Blade Extension

With the fixed-wing flutter application now defined, a transition is made to the flutter analysis of a flexible rotor blade. A modal approach is used where the physical motions of bending and torsion are applied via the natural modes $\gamma_w(r)$ and $\gamma_\theta(r)$, respectively.

$$\begin{aligned} z &= \sum_i \gamma_{w_i}(r) \cdot q_{w_i}(t) \\ \theta &= \sum_j \gamma_{\theta_j}(r) \cdot q_{\theta_j}(t) \end{aligned} \tag{1.27}$$

where q_{w_i} and q_{θ_j} are the bending and torsional generalised coordinates, respectively. With this approach, and assuming the control collective (θ_0) and coning (β_0) are negligible, the following general equations are derived for bending (Equation 1.28) and torsion (Equation 1.29) [21, 64, 98]:

$$\begin{aligned} m'\gamma_{w_m}\ddot{q_{w_m}} + m' y_{CG}\gamma_{\theta_k}\ddot{q_{\theta_k}} + \left[EyI\gamma''_{w_m}\right]'' q_{w_m} \underbrace{-\Omega^2\left[\gamma'_{w_m}\int_r^R m' r_1 dr_1\right]' q_{w_m}}_{1} \\ \underbrace{-\Omega^2\left[m' r y_{CG}\gamma_{\theta_k}\right]' q_{\theta_k}}_{2} = \frac{dL}{dr} \end{aligned} \tag{1.28}$$

$$\begin{aligned} m' y_{CG}\gamma_{w_m}\ddot{q_{w_m}} + m'(k_\theta^2 + y_{CG}^2)\gamma_{\theta_k}\ddot{q_{\theta_k}} \underbrace{+\Omega^2 m' r y_{CG}\gamma_{w_m} q_{w_m}}_{3} - [GJ + \underbrace{Tk_a^2}_{4}]'\gamma_{\theta_k} q_{\theta_k} \\ + \underbrace{\Omega^2 m' k_z^2 \gamma_{\theta_k} q_{\theta_k}}_{5} = y_{AC}\frac{dL}{dr} + \frac{dM_{\theta_{nc}}}{dr} \end{aligned} \tag{1.29}$$

where m is the sectional mass, y_{CG} is the section centre of gravity position, Ey is the bending Young's modulus, I is the blade section moment of inertia, Ω is the blade rotational velocity, r_1 and r are the spanwise position, k_θ is the torsional stiffness, GJ is the torsional rigidity, Tk_a is the axial tension, k_z is the bending stiffness and y_{AC} is the distance to the aerodynamic centre.

The highlighted terms represent new terms not included within the fixed-wing formulation and relate to rotorcraft specific effects. Starting with the bending terms, and these effects are caused by the introduction of the centrifugal force. The first term represents the natural flapwise bending stiffening that occurs with the centrifugal force. The second term is due to a moment which is generated between the centrifugal force and a moment arm created due to a torsional deflection. Focusing on the torsional equation terms, the third term represents a torsional moment about a deflected elastic axis where the deflection is driven by the flapwise bending. The

fourth term represents additional torsional stiffening is a result of the blade torsion and subsequent non-alignment of the tensile stress filaments. The fifth, and final, term is a propeller moment torsional stiffening effect caused by the centrifugal forces that has a component in the rotor plane direction, with any torsional deflection creating the moment arm from the elastic axis.

In order to complete the equations of motion, the differential lift (L) and non-circulatory moment (M_{nc}) across the blade radius is required. With quasi-steady airloads used, the effective angle of attack is seen as a summation of the pitch, inflow, and the blade section vertical velocity, the following equations define the required lift and moment terms:

$$\begin{aligned}\frac{dL}{dr} &= \pi\rho\frac{c^2}{4}\Omega r\gamma_{\theta_k}\dot{q_{\theta_k}} + 0.5\rho c_{l_\alpha} c\Omega r C(\bar{k})\left[-\gamma_{w_m}\dot{q_{w_m}} + \Omega r\gamma_{\theta_k}q_{\theta_k} + (0.5c - y_{AC})\gamma_{\theta_k}\dot{q_{\theta_k}}\right],\\ \frac{dM_{nc}}{dr} &= -\pi\rho\frac{c^3}{8}\Omega r\gamma_{\theta_k}\dot{q_{\theta_k}},\end{aligned} \tag{1.30}$$

where $C(\bar{k})$ equals the lift-deficiency function derived at $75\%R$ and all other terms are as per the Theodorsen theory in Section 1.3.1. Following the completion of the equations of motion for a flexible rotor blade, a reduction process is conducted to transform these equations into easily solvable ordinal differential equations. This is done by multiplying the bending equation by $\gamma_{w_m}dr$, the torsional equation by $\gamma_{\theta_k}dr$ and integrating both equations over the blade span. The resulting equations of motion are given as following in tensor notation:
ith bending mode:

$$S_{10_i}\left(\ddot{q_{w_i}} + \omega_i^2 q_{w_i}\right) + A_{1_{im}}\dot{q_{w_m}} + S_{31_{ij}}\ddot{q_{\theta_j}} - A_{2_{ij}}\dot{q_{\theta_j}} + \left(-A_{3_{ij}} + S_{38_{ij}}\right)q_{\theta_j} = 0 \tag{1.31}$$

jth torsional mode:

$$S_{31_{ij}}\ddot{q_{w_i}} + A_{4_{ji}}\dot{q_{w_i}} + S_{38_{ij}}q_{w_i} + S_{78_j}\left(\ddot{q_{\theta_j}} + \omega_{\theta_j}^2 q_{\theta_j}\right) + A_{5_{jm}}\dot{q_{\theta_m}} - A_{6_{jm}}q_{\theta_m} = 0 \tag{1.32}$$

where the following structural integrals are defined as:

$$\begin{aligned}S_{10_i} &= \int_0^R m'\gamma_{w_i}^2 dr,\\ S_{31_{ij}} &= \int_0^R m' y_{CG}\gamma_{w_i}\gamma_{\theta_j} dr,\\ S_{38_{ij}} &= \int_0^R m' r y_{CG}\gamma'_{w_i}\gamma_{\theta_j} dr,\\ S_{78_j} &= \int_0^R m'\left(k_\theta^2 + y_{CG}^2\right)\gamma_{\theta_j}^2 dr,\end{aligned} \tag{1.33}$$

and the aerodynamic integrals:

$$
\begin{aligned}
A_{1_{im}} &= 0.5\rho\Omega c_{l_\alpha} C(\bar{k}) \int_0^{BR} cr\gamma_{w_i} dr \\
A_{2_{ij}} &= 0.5\rho\Omega \int_0^{BR} \left[0.5\rho c^2 + c_{l_\alpha} cC(\bar{k})(0.5c - y_{AC})\right] \gamma_{w_i}\gamma_{\theta_j} dr \\
A_{3_{ij}} &= 0.5\rho\Omega c_{l_\alpha} C(\bar{k}) \int_0^{BR} cr^2\gamma_{w_i}\gamma_{\theta_j} dr \\
A_{4_{ji}} &= 0.5\rho\Omega c_{l_\alpha} C(\bar{k}) \int_0^{BR} cy_{AC} r\gamma_{w_i}\gamma_{\theta_j} dr \\
A_{5_{jm}} &= 0.5\rho\Omega \int_0^{BR} (0.5c - y_{AC}) \left[0.5\pi c^2 + c_{l_\alpha} cC(\bar{k})\right] r\gamma_{\theta_j}\gamma_{\theta_m} dr \\
A_{6_{jm}} &= 0.5\rho\Omega c_{l_\alpha} C(\bar{k}) \int_0^{BR} cy_{AC} r^2\gamma_{\theta_j}\gamma_{\theta_m} dr
\end{aligned}
\tag{1.34}
$$

A variety of solutions methods are available for these equations and they depend on the selection of the lift-deficiency and the overall objective. For a standard flutter boundary extraction, frequency-based airloads are ideal. However, if additional parameters, such as damping are required, more complex airloads may be needed. The range of solutions methods include the following:

Characteristic-equation: This method can be used when the equations of motion are easily Laplace transformable and that the system is simple enough for the characteristic equation to be formed. For this, it must be a low-order polynomial [21, 52].

Eigenvalue-solution: The use of Laplace transformed space eigenvalues gives rise to damping estimates along with flutter boundaries. For this method, the equations of motion must be re-written in canonical form [21, 53].

Nyquist criterion: This analysis focuses on the re-construction of the equations of motion to determine the locus of the characteristic multipliers with respect to the frequency. This is done via splitting off the unsteady airloads from the standard equations and computing two additional **X** matrices to determine a final form. This technique is ideal for the analysis of rotors due to the fact the airloads are typically formed in the frequency domain [21, 149].

Although complex, this section gives an introduction into the analysis of the flexible rotor.

1.5 Stall Flutter

In Section 1.3, one of the characteristics associated with rotorcraft aerodynamics, the stall effects on the retreating side, is discussed as part of the aerodynamic environment. Combine this with an elastic rotor blade and there is a potential for further blade oscillations due to the presence of stall. A blade under the presence of detached flow experiences pressure fluctuations which can alter the active moments acting on the blade. This is typically the pitching moment which,

if large enough, alters the overall blade collective, with the sign of the moment determining the direction of the pitch change. For example, a blade undergoing light stall may induce a pitch-up moment that increases the overall collective and, in turn, the amount of stall. This increase in stall results in an alteration to the centre of pressure which flips the pitching moment direction to a pitch-down. This pitch-down moment would likely overshoot the restoring fluctuation, bypassing the light stall condition to a more attached solution. The resulting increase in load due to the attached solution would then generate the original pitch-up moment at an increased magnitude.

It is this type of fluctuation and flutter that is classed as stall flutter and, due to the combination of non-linear aerodynamics and structure, is a highly complex phenomena from which to study/model. As we have seen from a classical rotor flutter point-of-view, elementary modelling can be achieved via the adaption of fixed-wing techniques. This becomes trickier for stall flutter due to the fact that a fixed-wing application rarely encounters a dynamic-stall-*like* occurrence during its standard operation.

The presence of stall on a rotor blade due to the control pitch oscillations is termed as dynamic stall and can be studied in the form of a two-dimensional aerofoil. The inclusion of dynamic stall on an aerofoil introduces a unique set of characteristics not found in standard static stall. In terms of rotor airloads, the use of quasi-static look-up tables for lift, drag and moment have their applications in hovering or low-speed forward-flight. These have been verified with rotor load studies and are justified due to the relatively low angle of attack change during the revolution. At high speeds, however, such quasi-static tables cannot be used and investigations such as those of Kufield and Bousman [80] highlight this where the airloads of the UH-60A helicopter rotor in flight were measured. The airloads indicate a significant alteration from the expected two-dimensional aerofoil results. To understand this, an examination of both the standard static-stall and dynamic stall effects on an aerofoil are discussed.

1.5.1 Aerofoil Static-Stall

With the range of angle of attack significant for rotorcraft analysis, the typical trends in lift, drag and moment coefficient are examined from attached flow to deep stall, with the typical trends for each presented in Figure 1.6. These trends are highlighted by Bielawa [21], with correlation to previous experimental [34, 105] and numerical studies [87, 126].

Focusing on the lift coefficient (Figure 1.6(a)), a linear increase is lift is found during the initial stages and this remains up until a static stall angle (α_s). This angle is defined based upon the location of the maximum lift coefficient ($c_{\ell_{max}}$) and is accompanied by the presence of detached flow. After the static stall angle, the lift coefficient decreases in value for a short range before gradually increasing towards a secondary peak. This secondary peak is typically under the presence of deep stall where three-dimensional detached flow effects introduce pressure reductions causing the increase in lift. It is often within this range that fighter aircraft operate

due to the highly dynamic nature of the aerodynamics. Typical angle of attack values for this secondary peak is seen around $\sim 45^{o}$.

During the linear range in lift, the drag coefficient (Figure 1.6(b)) and moment coefficient (Figure 1.6(c)) remain fairly constant up until the static stall angle. At this point, both the drag and moment sharply increase in magnitude with the moment experiencing a sharp nose-down moment resulting from a rearward shift in the centre of pressure. Both continue to increase until high angles of attack with the drag coefficient reaching a maximum at 90^{o}, when the aerofoil is perpendicular to the flow.

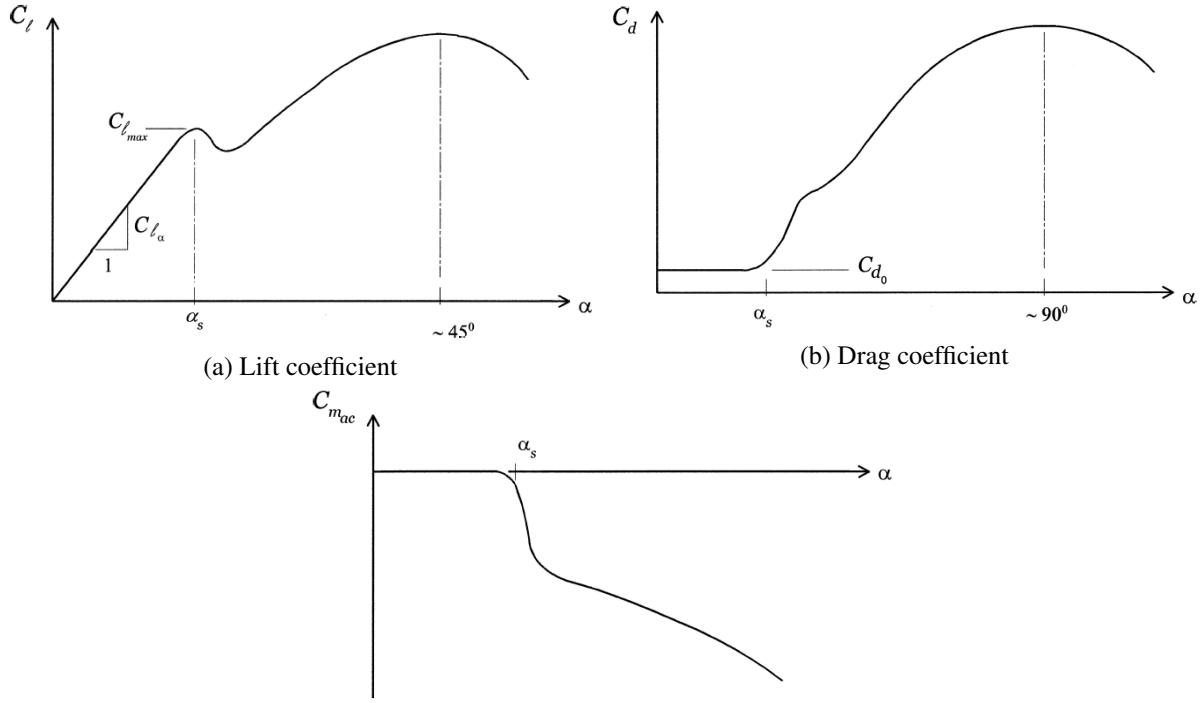

(a) Lift coefficient

(b) Drag coefficient

(c) Moment coefficient

Figure 1.6: Typical trends in lift, drag and moment coefficient during static stall [21]

1.5.2 Aerofoil Dynamic-Stall

The common feature among dynamic stall aerofoils is the introduction of a hysteresis effect. This hysteresis effect changes with the given conditions and level of detached flow. To illustrate some of the key features, the typical trends are shown in Figure 1.7 for the lift and moment coefficient. One of the effects of a dynamically oscillating aerofoil is the increase in maximum lift coefficient and stall angle (Figure 1.7(a)). This gives an indication as to the difference in airloads between the low-angle-of-attack look-up tables and what is observed in the true blade. This is potentially beneficial in terms of the blade operation as momentary increases in lift can be obtained at lower angles of attack. However, an increased load can potentially lead to an increase in blade deflection thus pushing the blade towards a potential stall flutter boundary.

In terms of the moment coefficient (Figure 1.7(b)), a similar hysteresis loop can be obtained in the moment profile. A similar increase in moment above the static estimate is found and is related to the increase in lift. The number of loops included within the profile depends on the angle at which the aerofoil is oscillating around and the amount of detached flow associated with the condition. These loops have an effect on the stability of the aerofoil along with each individual loops direction. This stability is categorised in terms of aerodynamic damping with a clockwise moment loop introducing negative damping.

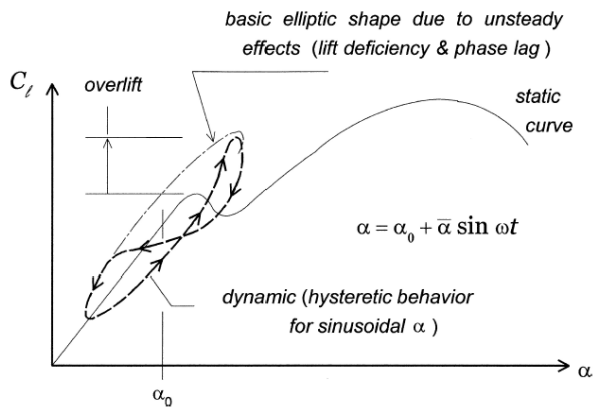

(a) Lift coefficient

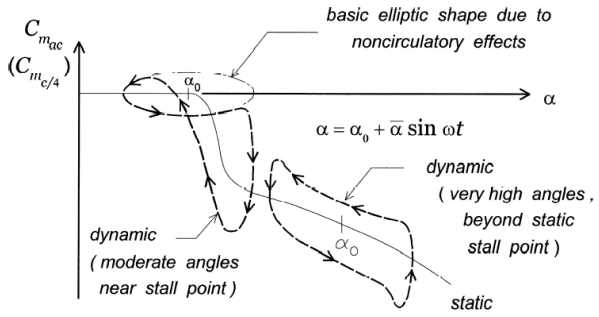

(b) Moment coefficient

Figure 1.7: Typical hysteresis trends in lift and moment coefficient during dynamic stall [21]

In order to further develop the understanding of such aerodynamic damping, a fuller description associated to stall flutter and the moment hysteresis loops is presented.

1.5.3 Aerodynamic Damping

Aerodynamic damping is the result of forces and moments exerted on to a structure due to aerodynamics. Aerodynamic damping often opposes structural damping, and can potentially result in aeroelastic instabilities. Aerodynamic damping is often critical to the flutter characteristics of a structure. Above the flutter velocity, the structure is seen to be negatively damped due to the work applied via the aerodynamics. Thus, the structure's oscillatory motions tend to increase with time.

Stall flutter originates from separated flow and is found to be present in helicopter rotors, propellers and other rotating wings. A stall flutter instability can only be corrected via positive structural damping or a change in the aerodynamic conditions. As a result, an investigation into stall flutter can begin from the aerodynamic damping of a system. Damping estimation is often performed for aerofoils and full three-dimensional calculations are rare.

Early investigations of stall flutter were two-dimensional and experimental [30, 91, 93]. These investigations focused on determining the aerodynamic coefficients during dynamic stall phenomena for the purpose of improving helicopter performance in forward flight. Such 2D investigations of oscillating aerofoils highlighted the trends seen during differing stall regimes.

These regimes are highlighted in Figure 1.8 where the pitching moment coefficient trends are presented for a NACA 0012 aerofoil oscillating at $\alpha = \alpha_o + 10^o \sin(2k\tau)$, where α and α_o are the overall and mean angles of attack, respectively, k is the reduced frequency and τ is non-dimensional time given by $\tau = t\ (time) \times U\ (velocity)/c\ (chord)$.

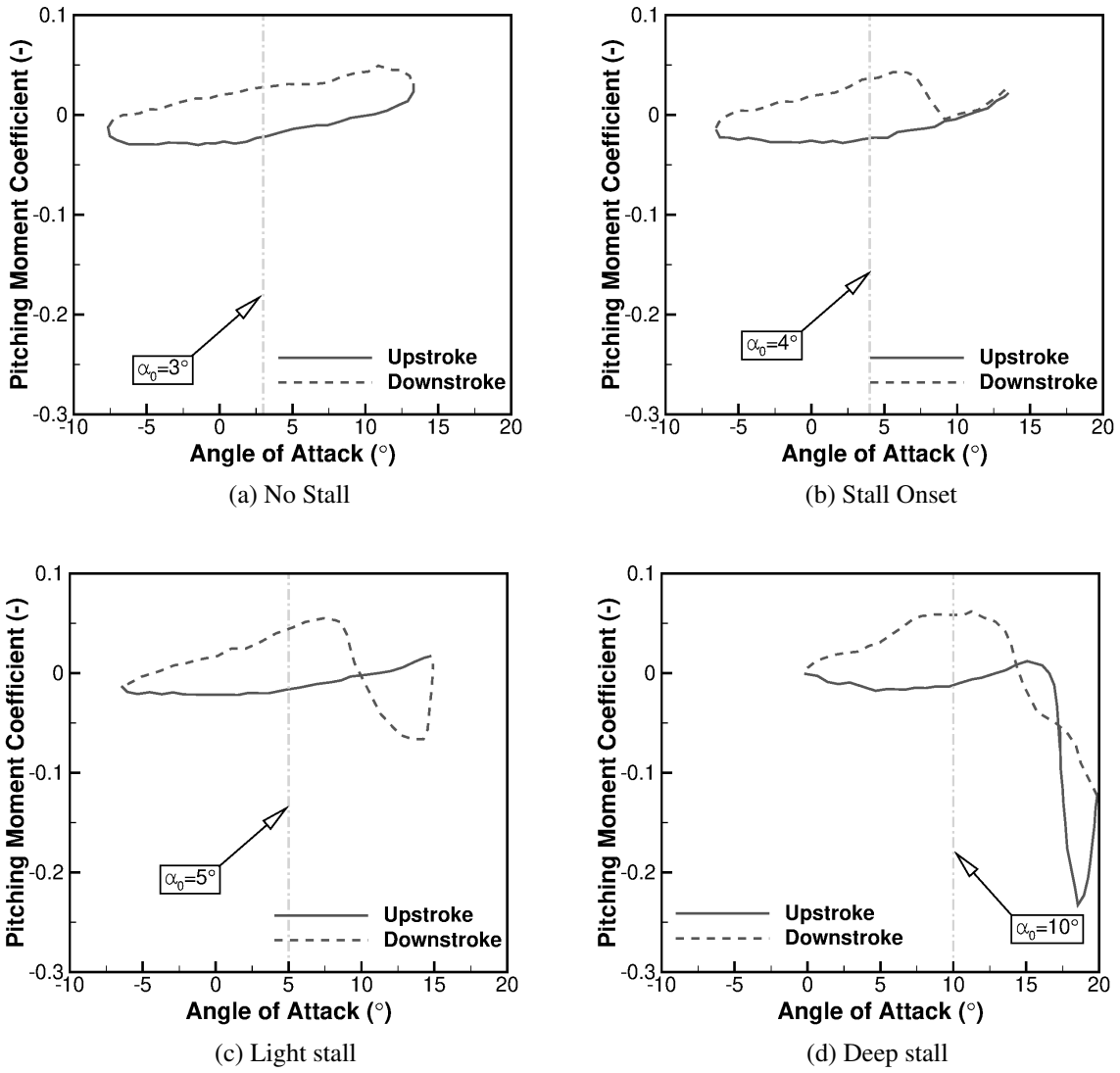

(a) No Stall

(b) Stall Onset

(c) Light stall

(d) Deep stall

Figure 1.8: Pitching moment coefficient trends for each stall regime, as observed by McCroskey for a NACA 0012 aerofoil pitching at $\alpha = \alpha_o + 10^o \sin(2k\tau)$, where $k = 0.10$ [93]

No Stall: Within the no stall regime, the aerofoil motion remains below the static stall angle and the use of quasi-steady aerodynamic is sufficient enough to predict the aerofoil loading. Both the lift and pitching moment coefficients are found to circle in an anti-clockwise manner with no crossing of the downstroke and upstroke profiles.

Stall Onset: During this regime, the aerofoil motion reaches the static stall angle. There is often found a slight reduction within the area of the anti-clockwise loop, however, no crossing of

the profiles are seen and therefore quasi-steady aerodynamic can be used to estimate the loads.

Light Stall: It is within this regime that dynamic stall vortices are present. For this regime, the aerofoil motion reaches values higher than the static stall angle, with the aerofoil loads characterised by a hysteresis effect. The development of separated flow regions are found to be sensitive to the aerofoil geometry, freestream Reynolds number and Mach number, reduced frequency of the aerofoil oscillation, and the mean and harmonic angles of attack. It is also within the regime that there is the highest tendency towards negative aerodynamic damping.

Deep Stall: For this regime, the aerofoil motion is often found to pitch entirely beyond the static stall angle and it is where the strongest effects of the dynamic stall vortex are seen. The aerofoil loading is characterised by a strong hysteresis effect, with significantly larger peak lift and moment coefficients.

The general trend in aviation, following the initial propeller stall flutter studies, involved a transition from propeller driven aircraft to turbo-fan engines. In addition to this, there was a greater need to understand the aerodynamics associated with dynamic stall of a helicopter rotor. Hence, the large amount of research conducted. The above description of dynamic stall is focused on helicopter applications, and as such, involves large amplitude variations in pitch. In propeller dynamic stall, significantly smaller oscillations in pitch are found around the static stall angle, and therefore the mechanism which triggers the stall flutter phenomena must be taken from the context of aerodynamic damping.

Following some of the initial experimental propeller stall flutter investigations [14] (described in Section 1.6.1), attempts were made to better understand the stall flutter boundaries with respect to aerodynamic damping. This included the experiments of Fanti *et al.* [50] and Lemnios [86]. However, as described by Carta and Lorber [29], such estimations were seen to be inadequate for design and deeper understanding of the mechanism due to the insensitive instruments. To this end, Carta and Lorber conducted an experimental investigation into the variation in aerodynamic damping due to small amplitude oscillations in pitch of a propeller aerofoil section [29]. This study followed the successful demonstration of the damping extraction for a cascade environment [51].

Experiments were conducted in the United Technologies Research Centre (UTRC) wind tunnel. Sinusoidal oscillations of the Sikorsky SC1095 aerofoil section were conducted over a range of amplitudes and mean angles. Pitch amplitudes ranged from 0.5^{o} to 4^{o}, with the mean angle selected between 8^{o} and 10.5^{o}. From initial static results, it is shown that the static stall angle is $\sim 9.5^{o}$ for this section. Pressure transducers were installed on the section in order to determine surface pressure and load profiles.

The presented results indicated a significant influence of the mean and oscillating magnitude angle of attack. The static derivative results are shown to be sensitive to the mean angle of attack when oscillating at low magnitudes. The derivatives are found to significantly vary once the mean angle approaches the static stall. This variation is seen to be random, with this random

nature also present within the load time-histories at low oscillating amplitudes.

Standard pitching moment hysteresis loops (similar to Figure 1.8) are presented which determine the aerodynamic damping estimations. The amount of aerodynamic damping is dependent on the direction of the individual loops are their total area. A clockwise loop is shown to have negative damping, with an anti-clockwise loop resulting in positive. The ratio of such gives an indication to the stability. For this experiment, low amplitude oscillations are found to induce a dominant clockwise loop when the mean angle is defined as above the static stall. The trend of aerodynamic damping from these given profiles are presented in Figure 1.9, where negative damping indicates an unstable condition. As shown, although the entire mean angle of attack range is seen to be negative for the highest amplitude, the greatest variation comes from the lower values with the destabilising range being dependent on the mean angle. An overall negative damping result can be mitigated via the blade design, however, the variation is harder to design for and therefore, the lower amplitudes become more critical.

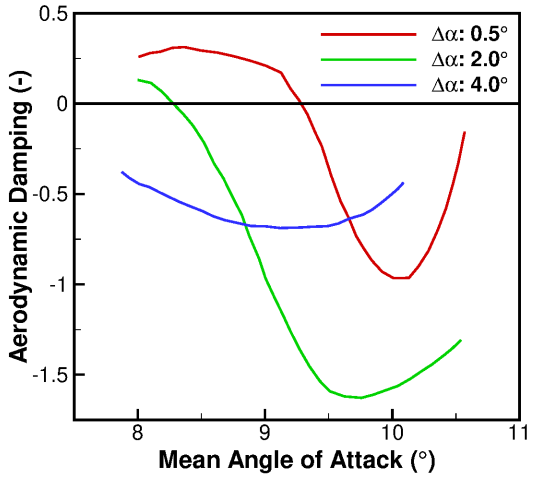

Figure 1.9: Aerodynamic damping trends across the mean and oscillating magnitude of the angle of attack [29]

.

Using the data gained from experimental investigations, such as Carta and Lorber [29] and McCroskey [93], validation of aerodynamic models could be undertaken with respect to dynamic stall and aerodynamic damping. This involved theoretical and semi-empirical models with a review conducted by Ericsson and Reding [47] in 1987. However, with the need for experimental parameters to ensure the accuracy of semi-empirical formulations, a review was conducted by Ekaterinaris and Platzer [46] in 1997 which focused on the use of the Navier-Stokes equations. This was brought on by the development of the numerical methods and increased computational power to allow for Navier-Stokes methods to be used in dynamic stall modelling.

The use of Navier-Stokes based modelling can not only assist in the extraction of damping estimations but also steady airloads for the semi-empirical formulations should no experimental

data exist. This was conducted by Beedy *et al.* [18] in 2003 who utilised the ONERA aerodynamic model with CFD coefficients for the study of aerofoil stall flutter.

Returning to the review of Ekaterinaris and Platzer [46], discussions were made on the effects of numerical schemes, turbulence modelling and effect of transition, with the turbulence and transition modelling seen to have a significant effect on the experimental correlation. They concluded that compressibility, transition, and flow reattachment were key flow effects limiting the correlation between the experiments and CFD results. Compressibility effects are driven by the partially supersonic profile observed across the aerofoil section. This is typically seen in the advancing side of the helicopter rotor due to the combination of freestream and rotational velocities combining. The use of transition models was seen to have a significant effect on the leading edge separation, and with the transition models of the time utilising empirical coefficients, an improvement was required in the modelling to enhance the correlation.

The final factor was related to flow reattachment and this was seen during the aerofoil downstroke where poor agreement was shown. This is often found in the light and deep dynamic stall regimes where the influence of the three-dimensional detached flow effects become important. Two-dimensional CFD cannot capture this effect, and therefore, an increase to the computational expense is required. This comes in the form of three-dimensional calculations and/or resolved flow modelling. Resolved flow modelling allows for the shedding process associated with dynamic stall process to be captured, potentially improving the downstroke performance.

From this basis, for highly stalled cases such as stalled aerofoils or propellers, high fidelity three-dimensional aerodynamic modelling is required. An insight can be gained via the understanding of the aerodynamic damping, however, high fidelity modelling will again be required to ensure accurate capture of the detached flow process.

1.6 Propeller Stall Flutter

In order to understand sources of data, typical trends and past numerical studies, a thorough examination of the current literature on propeller stall flutter is required. This is presented below for the experimental (Section 1.6.1) and numerical studies (Section 1.6.2), with a summary given in Section 1.6.3.

1.6.1 Experimental Studies

Propeller stall flutter research began during World War II and was primarily motivated by the use of propeller driven aircraft such as the Spitfire and Mustang. This research began with two studies: one from the U.S.A and another by the U.K. The U.K. study was conducted by Sterne and focused on the flutter analysis of the 4-bladed Spitfire propeller [129]. The U.S.A. investigation was conducted by Theodorsen and Regier and utilised a range of wind-tunnel designed propellers [134].

Focusing on the U.K. study [129], static experiments were conducted to determine the flutter boundary of the propeller, with the boundary presented in the form of the blade pitch versus blade rotational velocity (Figure 1.10). The blade was spun at 19 different pitch angles ranging from 8° to 32° with this value taken from the 70%R station. Note, that for the employed blade, a reference pitch of 8° at 70%R results in a 0° pitch angle at the blade tip. As observed from Figure 1.10(a), the experiment found that the blade would flutter at a much lower velocity within a specific pitch region. This region ranged from 20° to 28° with a 24% reduction in flutter velocity found.

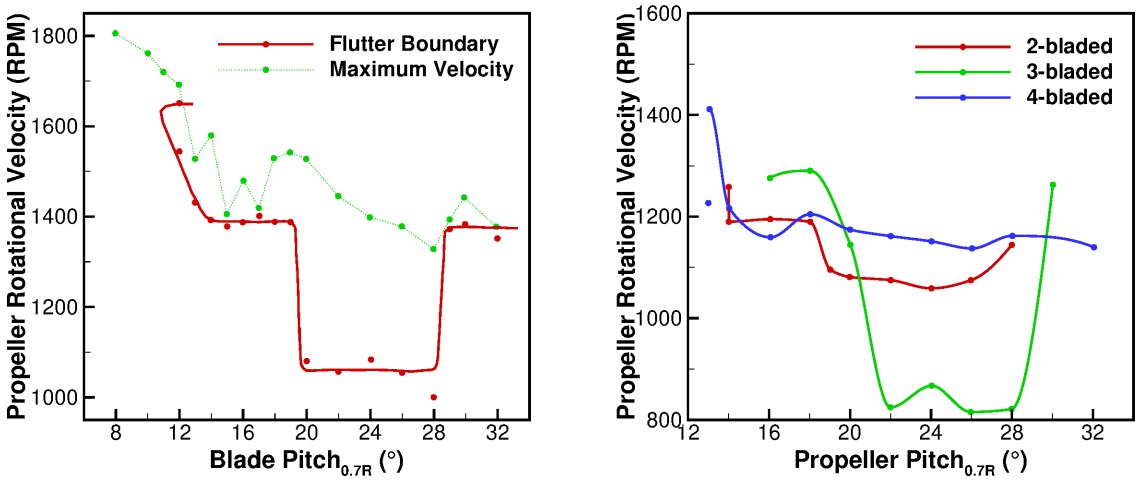

(a) Spitfire (b) Firefly

Figure 1.10: Spitfire and Firefly propeller flutter boundaries in static conditions [129]

Sterne came to the conclusion that the distinct decrease in velocity between 20° and 28° was the result of the presence of stall, hence stall flutter oscillations. The remaining pitch angles were conducted to be a result of classical flutter. This observation was also found by the work of Stüder who found a similar drop in velocity across a model wing due to stall and theorised it to be a result of negative aerodynamic damping [130].

In addition to this standard spin test on the Spitfire propeller, Sterne conducted an experiment to investigate the influence of the number of blades on the flutter characteristics. Those tested include a 2-, 3- and 4-bladed Firefly propeller. The Firefly blade is constructed in the same manner as the Spitfire, using compressed wood, however, with a slightly larger diameter of $13ft$ compared to $10ft\ 9in$. A comparison of the *thickness/chord* ratio and the solidity for the 4-bladed cases is presented in Figure 1.11.

Examining the flutter results in Figure 1.10(b) it was shown that the number of blades appears to have an influence on the flutter boundary. In the classical flutter boundary range, the 2- and 4-bladed propellers produced similar results with the 3-bladed propeller producing a higher velocity of $\sim 90(rpm)$. One slight difference in the experimental setup between the 2-/4-bladed propeller and the 3-bladed was a slightly different hub. It is expected then that such a difference

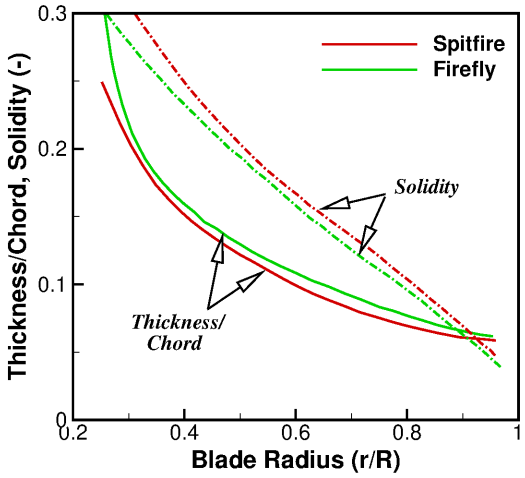

Figure 1.11: Spitfire and Firefly blade definitions [129]

will have an influence on the flutter boundary and, hence, the increase within the classical range could be explained via this difference. In terms of the stall flutter range, a significant reduction in stall flutter boundary was observed in the 3-bladed propeller compared to the 2- and 4-bladed. Sterne conducted that the reduction in stall velocity could be a result of the greater influence of the preceding blade stall upon the oncoming blade. With the experiment conducted in static conditions, and no thrust data known, the blade wake could very well interact with a subsequent blade.

Returning to the experimental investigation of Theodorsen and Regier (the U.S.A. wartime report on propeller flutter) [134] and as previously stated, a range of experiments were conducted on model propellers for examination, and use, in the wind-tunnel. This investigation was conducted in connection with the construction of the Langley, Ames and Cleveland blades for use within the tunnels. In this study, two propeller blades were presented. In a similar manner to the Spitfire/Firefly blades, both were made of laminated wood (spruce) with flat bottom Clark Y aerofoil sections. The first propeller (Propeller A) was designed as a 6-bladed propeller with a 45*inch* diameter. The second propeller (Propeller B) was designed as single bladed with a reduction in the chord length and *thickness/chord* ratio of one third. This reduction in size was to reduce the flutter velocity in order to examine the results.

The experiments were conducted in an open wind tunnel in static conditions, with only the induced velocity present at the tunnel exit. For Propeller B, this induced velocity was enhanced by a booster fan at the rear of the motor due to being of single blade design. A stroboscope was used at the blade tip in order to measure the bending and torsion, with strain gauges also used. With the blade pitch fixed, the rotational velocity was increased until flutter was determined for a range of propeller lift coefficients. These lift coefficients were adjusted through the change in the wind tunnel exit area, i.e. essentially compressing or expanding the wake area. The change

in lift coefficient was confirmed via pitot tubes.

It was observed from the experiment that at the lowest flutter velocities, the oscillations were found to be pure torsional fluctuations. This was determined from the strain gauges of Propeller B. It was concluded from this experiment, in a similar manner to the Sterne experiments, that the stall flutter velocities are much lower than the classical boundary. In order to mitigate this effect, Theodorsen and Regier concluded that the design blade angle should be such that the lift coefficient produces zero blade twist. Equations were presented to determine such angles, with the effect of addition twist seen as inducing further detached flow. Approaching the classical flutter boundary, less and less detached flow is required to excite the blade.

Although both studies provide a clear insight into propeller stall flutter, the construction of the blades make it difficult to study numerically. The compressed wood construction has the potential to introduce manufacturing inconsistencies and, therefore, make the understanding of the blade structural properties potentially difficult. From this basis, the Spitfire, Firefly and model NASA blades could not be used for a numerical study.

Following this observation of classical and stalled flutter within the working range of the wooden Spitfire and Firefly propellers, Ewing *et al.* conducted an experiment on the duralumin blades of the Tempest 5-bladed aircraft [48]. This experiment was conducted in the spinning tower of the Royal Aircraft Establishment, with strain gauges applied to the blades to measure the vibratory stress. Each propeller was pitched below and above the stalling region with only stall flutter found during the runs.

The experiments found a heavy dependence of the stress results on the phase differences between subsequent blades. This phase difference (ψ) is given by $\psi = 2\pi p/Q$, where Q is the number of blades and $p = 0, 1, 2 \ldots$. As p changed value, there was a change in the phase relationship and wave-form. The experiments found the value of p to increase with blade rotational velocity at a given pitch angle. Due to this influence of phase, an exact comparison of the stress values for the number of blades could not be made, hence general stresses are compared. For the three-, four- and five-bladed propellers, the greatest stress values occurred at 24^{o}. This reduced to 20^{o} for the two-bladed case. Either side of 24^{o}, the four- and five-bladed propellers stress values drop rapidly with a progressively lower gradient for the three- and two-bladed propellers. It was concluded from this experiment that the examination of the number of blades of the same design can only provide a rough indication of stress level.

In 1955 [14], Baker conducted a static experimental investigation into the effects of various parameters on the flutter boundary of a model propeller blade to determine the minimum stall flutter condition. These parameters included the effects of the blade structure, the blade geometry, and the freestream flow conditions, with the full list and range presented in Table 1.2. Due to the change in certain parameters, a range of blades were manufactured. For the construction, a *16-series* NACA aerofoil was used with the material selected as aluminum alloy, steel or maple, depending on the model and test case. All propeller blades were tested across the full pitch angle

range.

Table 1.2: Range of parameters tested in the experimental investigation of Baker [14]

Parameters studied	Range of values
Torsional stiffness ($lb - ft^2$)	12 - 101
Taper ratio (-)	0.5 - 1.0
Blade twist$_{100\%R}$ (^{o})	0 & 17
Length/Chord ratio (-)	2.6 - 5.4
Density ($slug/ft^3$)	0.0006 - 0.0024
Thickness ratio (*%chord*)	3 - 9
Sweep (^{o})	0 - 20
Centre-of-gravity location (*%chord*)	34.0 - 48.5
Mach number (-)	0.0 - 1.3
Blade pitch$_{80\%R}$ (^{o})	5 - 35

The experiments were conducted in the Langley vacuum sphere to allow for the use of Freon-12 to achieve more realistic Reynolds numbers during the density and Mach number studies. Strain gauges were attached to the blades to measure the bending and torsion oscillations with the rotational velocity gradually increased until flutter was observed.

The experimental results showed very little difference in the boundaries for the torsional stiffness, blade taper, blade twist, *length/chord* ratio and density studies. Substantial changes were found for the centre-of-gravity, sweep, thickness and Mach number runs with the non-dimensional flutter velocity results presented in Figure 1.12 for each. The models used for the results shown are described in Table 1.3. The most significant change in the stall flutter boundary was found in the centre-of-gravity results (Figure 1.12(a)), where a 14.5% shift in CG results in a 44% reduction in the minimum flutter boundary. Very little difference in the thickness ratio results (Figure 1.12(b)) was found between the 3% and 6% plots with the 9% model resulting in a $\sim 25\%$ increase in the boundary. Although a benefit was found using a thicker aerofoil section, propeller performance dictates thin aerofoils.

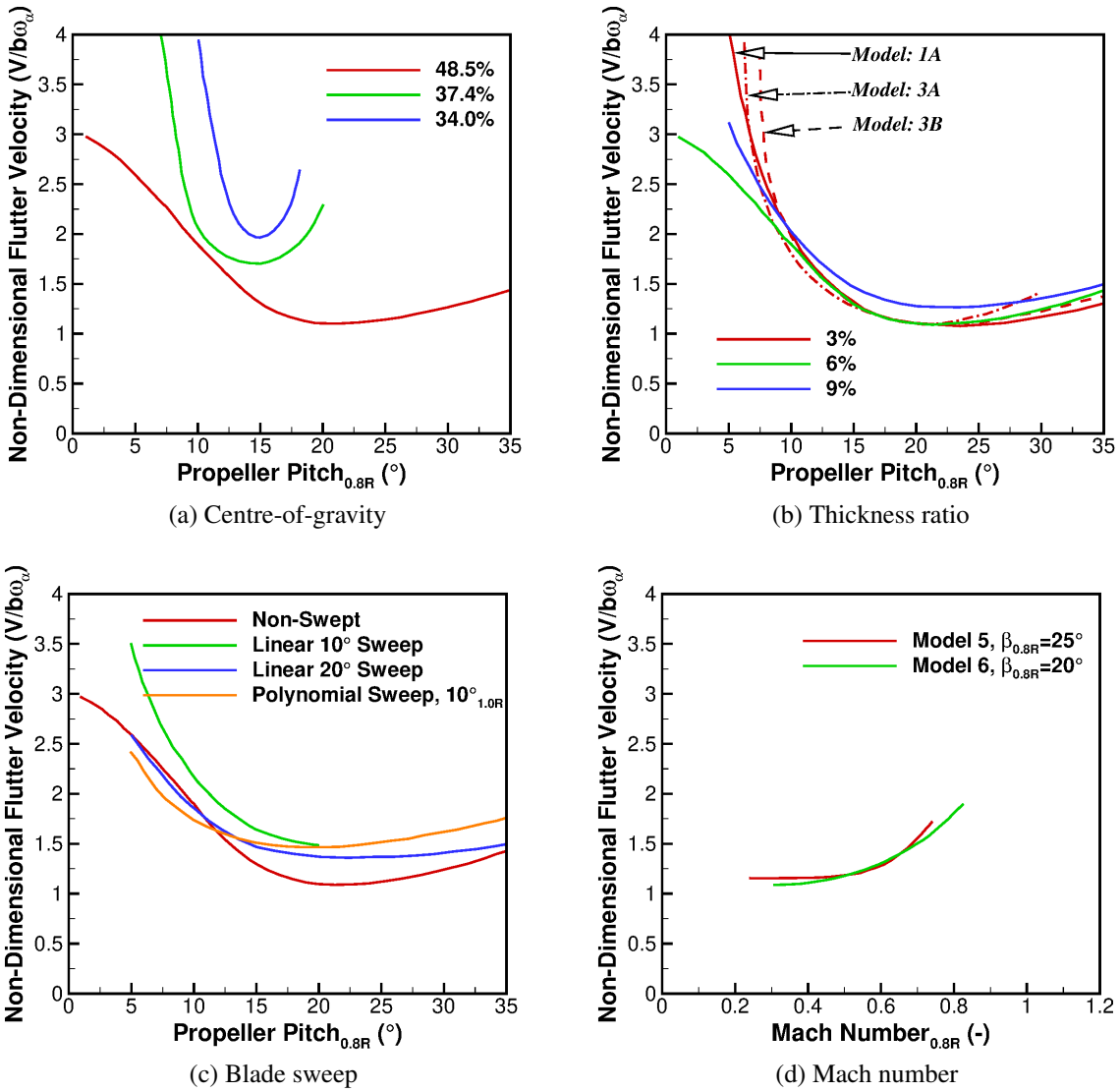

(a) Centre-of-gravity

(b) Thickness ratio

(c) Blade sweep

(d) Mach number

Figure 1.12: The changes found in the flutter boundaries based upon the experiments of Baker [14]

Table 1.3: Description of each experimental model propeller for the investigation of Baker [14]

Model	1A	3A	3B	4	5	6	7	8	9	10	11	13
Blade material	Aluminium	Steel	Steel	Maple	Aluminium	Aluminium	Maple*	Maple*	Maple	Maple	Maple	Maple
t/c (*%chord*)	3	3	3	6	6	3	6	6	6	6	6	6
$c_{80\%R}$ (ft)		0.167			0.250	0.199			0.167			
R (ft)			1.788			1.750			1.788			
f_h (cps)	7.6	7.2	7.6	13.4	20.6	43.7	11.3	10.5	13.5	13.7	13.9	19.0
f_α (cps)	91.4	90.5	95.0	81.2	176.0	280.5	63.5	56.2	73.0	78.6	96.9	113.0
y_{CG} (*%chord*)				48.5			37.5	34.0		48.5		
y_{EA} (*%chord*)	45	47	46	47	44	46	42	40	65	65	62	44
GJ (ln/ft^2)	36	101	101	12	1400	-	18	20	12	12	12	40
γ (-)			-			0.57			-			
Λ (°)					-				10	20	10**	-

Where t/c=thickness ratio, c=chord, R=radius, f_h=1st bending frequency, f_α=1st torsion frequency, y_{CG}=centre of gravity position,...
y_{EA}=elastic axis position, GJ=torsional stiffness, γ=taper ratio and Λ=blade sweep
**Brass insert at leading edge for CG offset*
***At tip, polynomial sweep*

The introduction of sweep (Figure 1.12(c)) to the blade design had a significantly positive influence on the stall flutter boundary, with all sweep configurations seeing an increase in the flutter velocity of greater than 25%. Examining the results from a pitch angle of 10^{o} to 35^{o}, the quadratic polynomial sweep had the greatest continual increase in the boundary across this region. The final positive observation from the investigation was the increase in flutter boundary for a Mach number greater than 0.6 (Figure 1.12(d)). The Mach number influence was tested across two models at different pitch angles. The second test (Model 6), is seen to have a more gradual increase in the boundary, with the first (Model 5) having a steeper gradient above 0.6.

Baker did note that the resultant flutter boundaries were not within the normal operating cruise conditions for typical propellers, and it was only during take-off *like* conditions that the blades were found to suffer from stall flutter. Following the experiment of Sterne, greater insight into several aerodynamic and structural influences on the stall flutter boundary were found due to this investigation. Although some details are available for the blade used (Table 1.3), further information would be required to map the blade inertias along the radius for a numerical study.

In 1956, Hubbard *et al.* followed on from the work conducted by Baker [71] by focusing on three specific parameters. The primary aim was to determine the effect of Mach number, structural damping and built-in twist on the flutter boundary. For these parameters, four model propellers were constructed (one each for the Mach number and twist study with the final two for the structural damping). Each blade was defined in a similar manner to the Baker propellers [14] with Table 1.4 presenting the blade descriptions and each blade using *16-series* aerofoil sections. Model 3B was constructed using laminated steel in order to change the internal structural damping. In the same manner as the Baker experiments, the propeller models were tested in the Langley vacuum sphere in static conditions. During the experiment, strain gauges were used to measure the vibratory stress levels with runs conducted at a fixed pitch angle, only varying the rotational velocity.

Presented in Figure 1.13 is the experimental results for the twisted blade, Mach number and structural damping studies. Focusing on the twisted blade result (Figure 1.13(a)) and using the strain gauges, the type of blade oscillations across the examined pitch range was determined. Through the low pitch range (-8^{o} to 8^{o}), the blade oscillations are dominated by bending-torsion or pure bending oscillations. In addition to this, the higher flutter velocities are found during this region with an average value 228% above the minimum velocity. The reduction of the pitch angle to higher-magnitude negative angles results in the activation of the torsional mode, reducing the flutter velocity. At high positive angles, the traditional shape expected from the Baker [14] and Sterne [129] experiments is found. Due to the detached flow present at these angles, the flutter velocity was reduced significantly with the torsional mode active.

The effect of Mach number (Figure 1.13(b)) on the propeller flutter velocity mirrors that found by Baker [14]. As the speed of sound is decreased, thus increasing the Mach number, the extent of the flutter region was reduced. In terms of structural damping (Figure 1.13(c)),

Table 1.4: Description of each experimental model propeller for the investigation of Hubbard [71]

Model	1	2	3A	3B
	Twist	*Mach*	*Structural Damping*	
Blade material	Aluminium Alloy	Aluminium Alloy	Steel	Laminated Steel
t/c ($\%chord$)	2	6	3	3
$c_{80\%R}$ (ft)	0.265	0.25	0.25	0.25
R (ft)	2.67	1.792	1.775	1.775
f_h (cps)	8.8	20.0	11.3	11.4
f_α (cps)	124.0	183.0	93.3	96.5
y_{CG} ($\%chord$)	48.2	48.5	48.3	48.2
y_{EA} ($\%chord$)	-	44.0	50.0	49.8
GJ (ln/ft^2)	-	1400	521	511
Λ (^{o})	31	0	0	0

Where all symbols are the same as Table 1.3

an increase in the internal damping was shown to increase the flutter velocity. This was to be expected and therefore any oscillations due to a negative aerodynamic damping are mitigated by the increase in structural damping.

The combined works of Baker [14] and Hubbard *et al.* [71] allowed for a detailed understanding of propeller stall flutter due to the volume of parameters investigated. However, the blades used in these experiments do not represent a realistic modern blade and this has a significant effect on the observed flutter boundary.

Similarly, in 1956, Allis and Swihart conducted a static experimental investigation to determine the effect of blade-section camber [8]. This work followed on from the experiments of Wood and Swihart [146] who found an increase in stall flutter boundary due to an increase in camber at one specific pitch angle. This pitch angle was extended to test over a range from 16^o to 38^o. Three 2-bladed NACA propellers, of varying camber, were tested in the Langley dynamometer with the blades fitted with strain gauges. Figure 1.14 presents the installed blades on the dynamometer. At a fixed pitch angle, the propeller rotational velocity was slowly increased until flutter was encountered.

Presented in Figure 1.15 is the non-dimensional flutter velocity and thrust coefficient results for the range of cambered propellers. Focusing on the flutter boundary result (Figure 1.15(a)), it was shown that at 16^o an increase in flutter velocity of 45% was achieved with the highest cambered propeller compared to the symmetrical blades. This difference slowly reduces with increased pitch angle until 30^o where the flutter velocity values are approximately the same. Above 30^o, an increase in the flutter velocity was seen by all, with the symmetrical propeller having the highest value at the largest pitch angle. Allis and Swihart observe that at 16^o, only the inboard radial stages were stalled and this increased to the entire blade at 30^o.

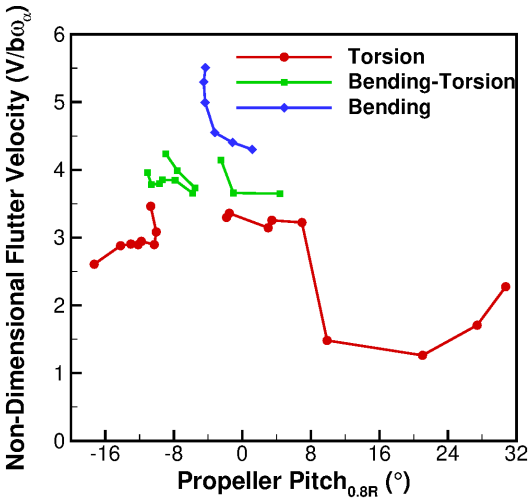

(a) Twist

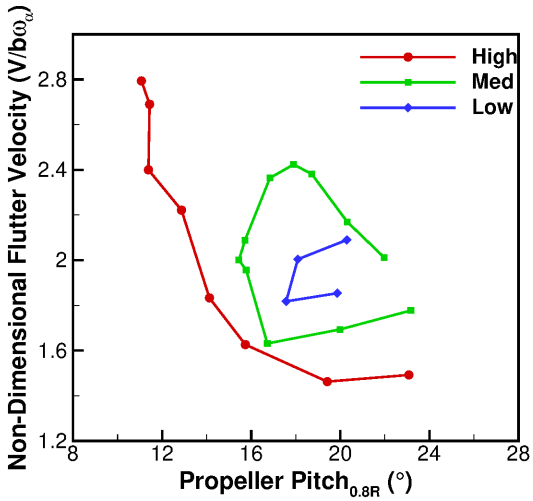

(b) Mach number

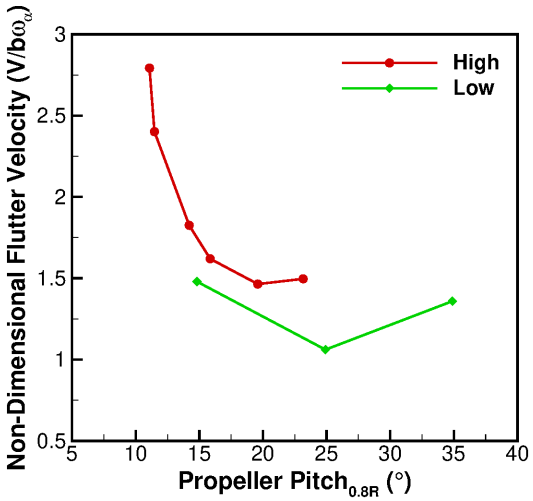

(c) Structural damping

Figure 1.13: The changes found in the flutter boundaries based upon the experiments of Hubbard [71]

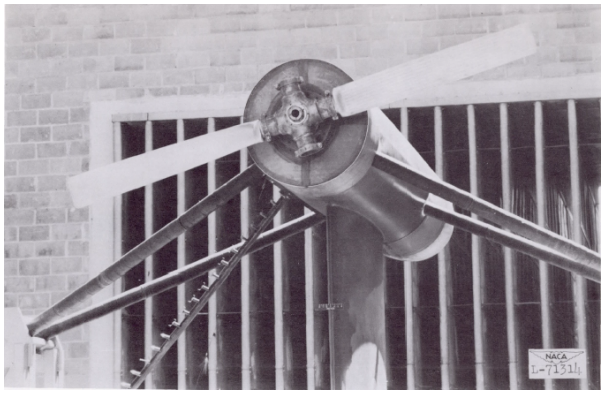

Figure 1.14: Installed NACA propeller on the Langley dynamometer for the experimental study of Allis and Swihart [8]

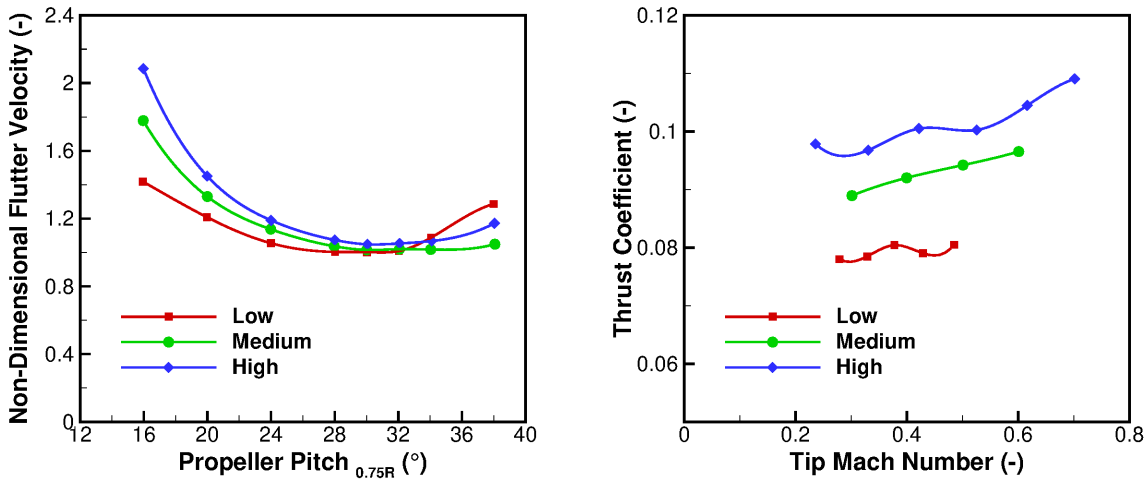

(a) Flutter-vs-Pitch (b) Thrust-vs-Mach

Figure 1.15: Flutter boundary and thrust coefficient changes for each cambered propeller blade [8]

One of the key observations from the experiment was the significant difference at 16°. The flutter boundary was not only driven by the combination of detached flow and structural damping, but also the total airloads applied to the blade. At higher thrust, higher fluctuations in blade deformation is expected. This is what was observed at the 16° pitch angle, with this confirmed in Figure 1.15(b) where the highest camber blade is shown to have a 36% increase in thrust in comparison to the symmetrical blade. With greater thrust comes greatest induced velocity and therefore a reduced effective angle of attack at a given rotational velocity. In order to assess the true effect of blade-section camber, a trimming process would be required to ensure the same thrust is generated from the blade.

In 1959, Rogallo and Yaggy conducted an experimental campaign on a 3-bladed $10ft$ propeller to determine the effect of positive/negative thrust and thrust axis inclination on the stall flutter characteristics [114]. The experiments were conducted in the 40-by-80 foot NASA Ames wind tunnel facility, with the installed blades presented in Figure 1.16(a). The blades were instrumented with strain gauges to determine the torsional and bending stresses. The positioning of the strain gauges, and definition of the blade profiles, shown in Figure 1.16(b). These gauges were accompanied by flow-field rakes upstream and downstream of the propeller, with the rakes shown in Figure 1.16(a).

In order to capture positive and negative thrust conditions, the blade pitch angle was varied throughout the experiment from $-17.5°$ to $+42°$. The exact range was dependent on the desired condition and also the freestream velocity. The freestream velocity was varied from zero to $183.5ft/s$. This maximum velocity represents 50% of the maximum achieved tip velocity. For the majority of the tests, the rotational velocity was fixed with the blade pitch angle varied until stall flutter was encountered. When examining the effect of the thrust axis inclination, the

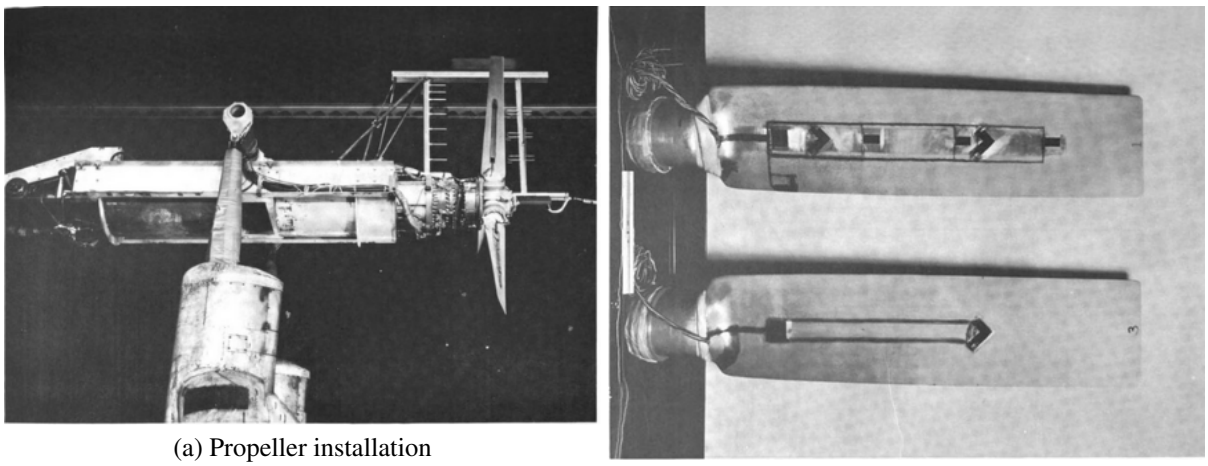

(a) Propeller installation

(b) Blade instrumentation

Figure 1.16: Propeller blade installation and instrumentation for the stall flutter study of Rogallo and Yaggy [114]

positive thrust pitch range was examined along with the inclusion of a freestream velocity. The axis angle was varied by 10^o and 15^o, with only the 15^o tilt at the highest velocity presented in the report.

Presented in Figure 1.17 is a selection of the stall flutter results for the Rogallo and Yaggy experimental investigation [114]. For the positive thrust runs, similar trends were found in the shear stress results with varying freestream velocity. To highlight this trend, the results in static conditions are shown in Figure 1.17(a). With increasing rotational velocity, lower pitch angles are required before entering stall flutter. For rotational velocities between 1800 and 1200 (rpm), a sharp rise in stress was captured at a given pitch with very few additional angles tested before reaching the stain gauge limits. This sharp rise trend transitions at 1000 (rpm), in static conditions, to a more gradual gradient with the lower velocity runs able to reach the full pitch angle range.

This transition velocity, from very high to lower stress gradients, reduces with increasing freestream. Overall, the effect of increasing freestream is presented in Figure 1.17(b) where the stall flutter boundary in terms of pitch and rotational velocity is shown for the positive thrust cases. As observed, an increasing freestream velocity pushes the stall flutter boundary further, i.e. a greater pitch and rotational velocity is required before encountering stall flutter.

In terms of the negative thrust study, very similar trends and values were found for all tested freestream velocities. Unlike the positive thrust cases, no coupling between the pitch angle and rotational velocity was found at a given freestream, with increases in stress observed at similar pitch angles. With the sharp rise in shear stress occurring around 0^o, the stress values remained fairly stable before slowly decreasing at the lowest pitch angles.

One of the final investigations was the effect of axis tilt on the stall flutter boundary. This effect is shown in Figure 1.17(c) where the highest freestream velocity results are presented for a tilt angle of 15^o over a range of rotational velocities. As observed, the introduction of a tilt

angle has very little effect on the shear stress results. To understand this, the thrust and torque coefficients are obtained along the blade radius from the rake data. The thrust values indicated only the outer section of the blade to be stalled with a small magnitude found in the change of angle of attack. With the change in angle of attack, driven from the axis tilt, too small, the detached flow dominates resulting in similar stress results.

In order to understand the trend between generated thrust and the stall flutter boundary, Rogallo and Yaggy extracted the thrust coefficient results along the blade radius and compared them to the values indicated from the shear stress plots when above ± 1000 *psi*. Presented in Figure 1.17(d) is the thrust coefficient results for the $90\%R$ radial station at the highest freestream velocity in positive thrust. It was shown that the stall flutter boundary appears to coalesce with the drop-off in thrust coefficient. This gave further indication to the dominance of the detached flow.

A similar investigation was conducted by DOWTY Propellers in 1979 at the spinning tower of the Royal Aircraft Establishment Farnborough [28]. The aim was to determine the torsional stress levels, and subsequently the flutter characteristics, of the Commander propeller blade when spun at fixed pitch over a range of rotational velocities. The torsional stress levels were measured via strain gauges placed along the propeller radius.

During the first stage of the test, high levels of torsional stress were seen for a given pitch angle, with the test terminated due to excessive oscillations. Upon examination of the propeller apparatus, the propeller crosshead had failed and hence a redesign of the crosshead was required. Following this, overspeed and 30 minute power run tests were completed at lower blade pitch angles, without further attempts to probe the stall flutter boundary. From the torsional stress results, a clear stall flutter boundary was observed with a sharp increase in stress seen around 1650 *rpm*.

In 1985, Smith conducted a static experimental investigation into three prop-fan model propellers [125]. These models were designated SR-2, SR-3 and SR-5, with the blades featuring increasing levels of sweep from the unswept, SR-2, design to the highly swept, SR-5. In a similar manner to the DOWTY tests, for a fixed pitch angle, the propeller rotational velocity was increased to maximum before returning to its baseline value. Vibratory stress levels were measured via strain gauges. The positioning of the strain gauges and the blade profiles are presented in Figure 1.18. This study was motivated by the transition to thin and highly swept blade designs, conclusions that were drawn from past studies, with the aim to ensure the structural stability of the blades.

Each propeller was installed on an isolated nacelle in the UTRC large subsonic wind tunnel where previous in-house tests had been conducted [57]. The SR-2 propeller was an 8-bladed rotor constructed of steel. The SR-3 and SR-5 were both made using aluminum with the SR-5 having an additional two blades. All configurations were derived from the full scale designs at an intended operating Mach number of 0.8. A reduction to $1/8^{th}$ scale was required due to the

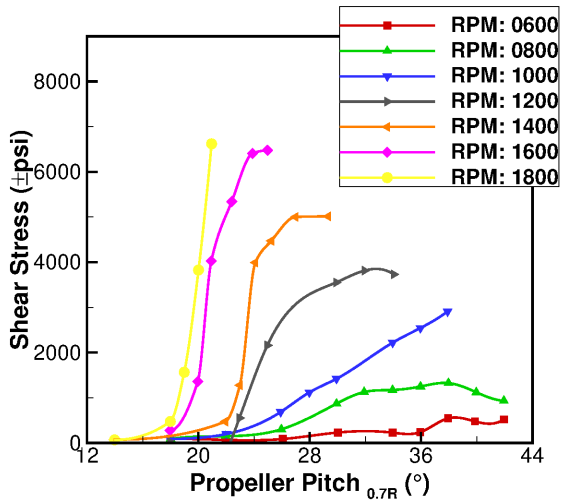

(a) Shear stress boundary for $V_\infty = 0.0 ft/s$ at zero tilt

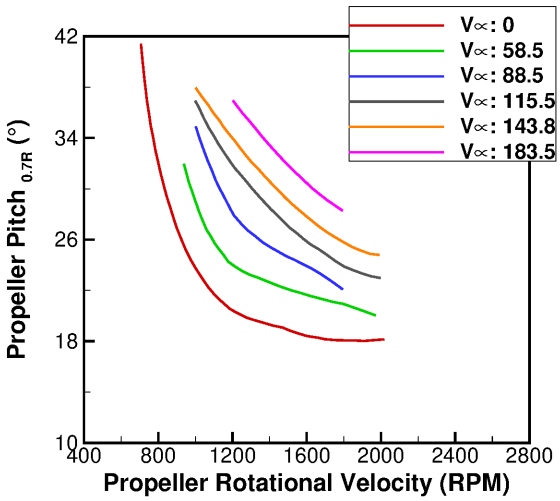

(b) Stall flutter boundary

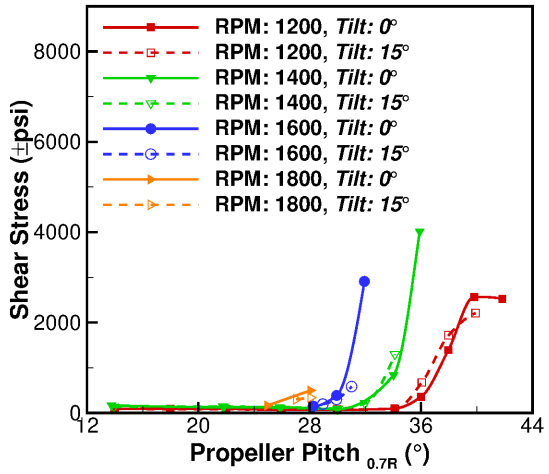

(c) Tilt effect on shear stress boundary

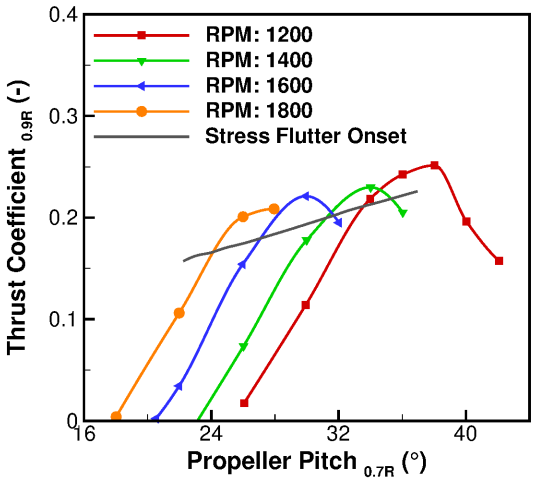

(d) Thrust coefficient at $90\%R$ for $V_\infty = 183.5 ft/s$ at zero tilt

Figure 1.17: Stall flutter results for the experimental investigation of Rogallo and Yaggy, where V_∞=freestream velocity [114]

wind tunnel constraints.

In addition to the results of this experiment, the total vibratory stress results were compared against previous experiments of Smith in the NASA-Lewis Research Center [124]. The additional tests of Smith [124] not only looked into static conditions, but also introduced a forward velocity and yaw angle to the freestream to determine its effect. Focusing on the static results, plots of the total vibratory shear stress are presented in Figure 1.19 for each blade. Outputs were also presented for the mid and tip blade bending, with shear only presented here due to stall flutter typically being active in the torsional mode.

For each propeller blade, results are presented for a pitch angle of 32^o and a subsequent higher value. This higher value was selected as 40^o, 60^o and 50^o for the SR-2, SR-3, and SR-5 propellers, respectively. Focusing on the comparison between the experiments (Figure 1.19(a-

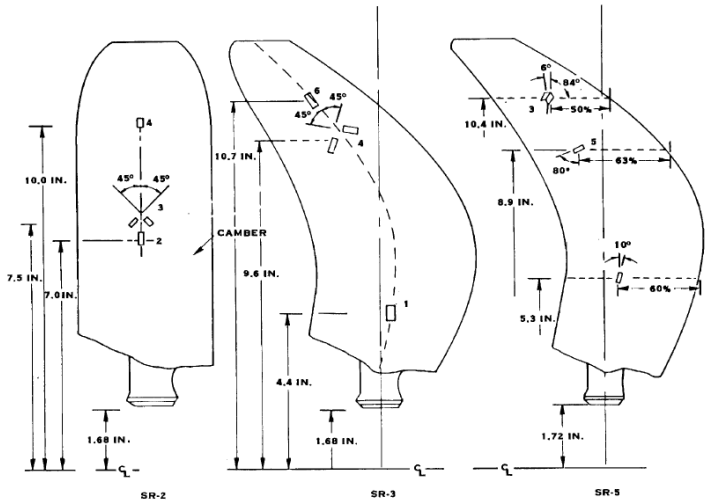

Figure 1.18: Strain gauge positioning and SR propeller blade definitions for the experiments of Smith [125]

c)), good correlation is found between the UTRC and NASA-Lewis investigations. The UTRC results at the critical speeds were found to be higher in all blades with this theorised to be the effect of turbulence.

Figure 1.19(d) presents the results for the 32^{o} pitch runs only for each propeller. It is observed that during the lower velocity range, similar trend and gradients were seen between the blades. The results start to deviate around $6000(rpm)$. At this stage, the SR-2 propeller was stopped due to excessive vibration with the maximum speed of $9000(rpm)$ not reached. At this point, the SR-2 propeller was seen to have the highest stress values. As the stress levels are lower during this stage for the SR-3 and SR-5 propellers, the runs continue towards the maximum velocity. Upon reaching the maximum velocity, the SR-3 propeller was seen to have a greater stress value, with the SR-5 results dropping following $7000(rpm)$. This overall trend mirrors previous experiments in that an increase in blade sweep results in a decrease in the stall flutter boundary.

As previously stated, in addition to the static experiments, Smith conducted a similar range of tests on the SR-2, SR-3 and SR-5 propellers in low forward-flight conditions in axial and yawed conditions [124]. A maximum forward-flight Mach number of 0.35 was selected with a yaw range of -2^{o} to $+15^{o}$. Presented in Figure 1.20 is the total stress results for the Mach number and yawed inflow effects on the SR-3 propeller. In Figure 1.20(a) the total vibratory stress results are presented with Figure 1.20(b) showing the total stress per excitation factor (deemed *stress sensitivity*). The excitation factor (EF) was used by Smith due to its linear dependence on tilt and was defined as:

$$EF = \psi_i (V_{eq}/348)^2 \tag{1.35}$$

where ψ_i is the inflow angle and V_{eq} the equivalent airspeed. Focusing on the inflow effect

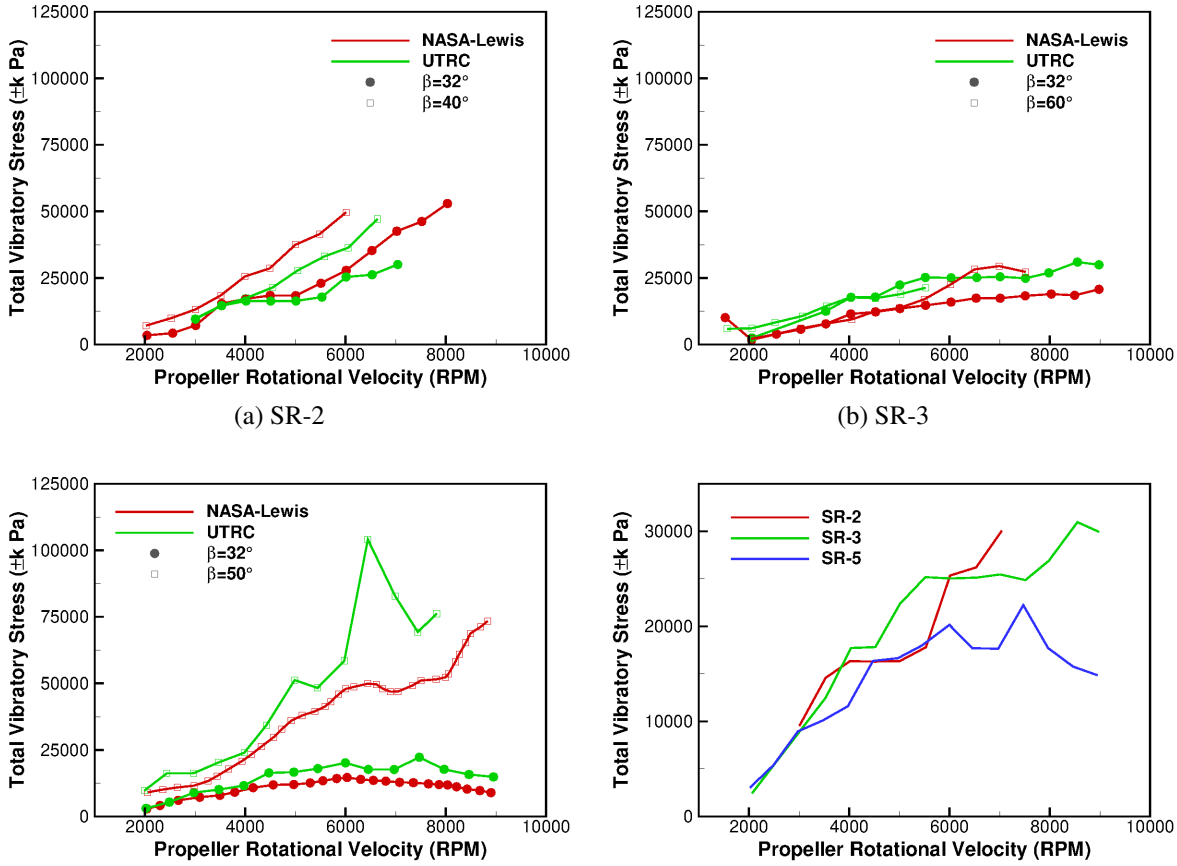

(a) SR-2 (b) SR-3

(c) SR-5 (d) Pitch=32°

Figure 1.19: Total vibratory shear stress results for the two sets of static experiments by Smith [124, 125]

(Figure 1.20(a)) and the results presented are for a pitch angle of 35° over a range of inflow velocities. As is shown, a significant decrease in the stress values was seen with the introduction of an inflow velocity. The reduction in stress was mainly observed for the lowest forward-flight speed (Mach number of 0.1), with similar trends observed during the higher velocities. A comparable profile was also shown for the SR-2 and SR-5 blades with these profiles presented in the experimental article. In addition to these trends, an increase in stress was also observed with an increase in blade pitch. This is to be expected, further pushing the propeller towards highly detached flow, and was observed across all tested Mach numbers.

The secondary factor analysed by Smith was the introduction of an angle to the inflow velocity. With this in mind, Smith presented the results for the 15° yawed inflow for all blades, with the SR-3 at a Mach number of 0.1, across a range of blade pitch angles, this is shown in Figure 1.20(b). The introduction of a yawed inflow results in a $1/revolution$ fluctuation in the stress. This was seen as the main component and therefore resulted in a linear increase in stress with yawed inflow angle. A resonance-*like* effect was found when the $1/revolution$ frequency equals the rotational velocity seeing a spike in the stress values. This spike was mitigated with the introduction of greater sweep. As observed from Figure 1.20(b), the stress sensitivity

increased with increasing blade pitch and rotational velocity.

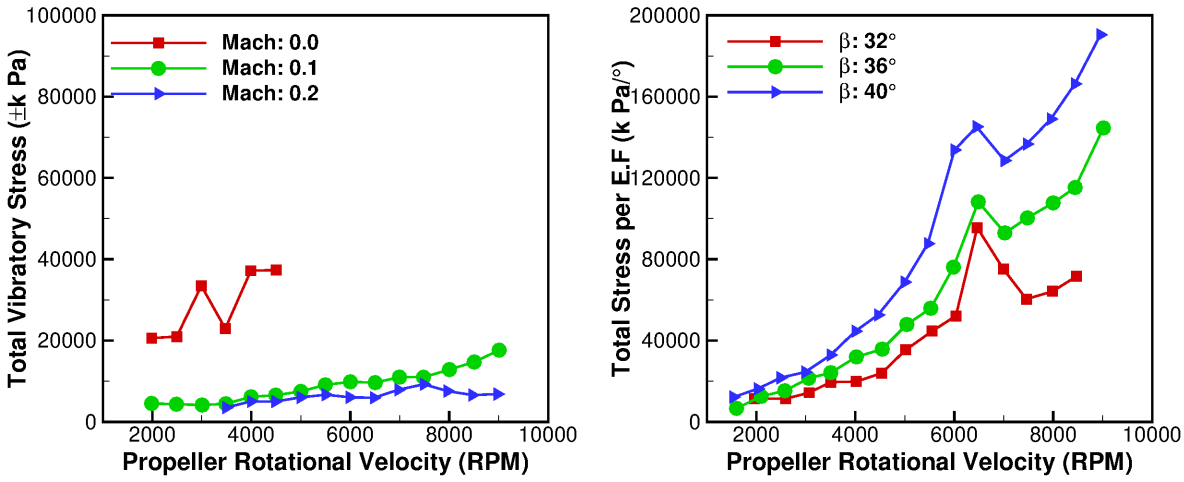

(a) Mach number (b) 15° yaw

Figure 1.20: Stress results for the forward-flight and yawed experiments by Smith [124]

Due to the amount of data available and the publicly available blade definitions, a numerical study could be conducted using these blades. The structural properties would need to be defined with a clear flutter boundary not present within the test range. Smith also acknowledged the effect of the highly-stiff titanium model propellers used for this study. The full discreprancy between model- and full-scale would need to be examined.

1.6.2 Numerical Studies

In addition to the experiments, Smith [124, 125] conducted numerical simulations of the SR propellers with a comparison made to the wind tunnel results. Both investigations utilise the F203 stability analysis code developed by Turnberg [136]. This code requires the supply of the blade mode shapes and frequencies, along with the aerodynamic loads, to determine an eigenvalue solution.

The mode shapes and frequencies are derived via a finite element analysis, with a beam based method (H025/H027) used for the SR-2 propeller and NASTRAN for the SR-3 and SR-5 blades. The H025 code determines the bending modes of a straight blade acting under the influence of a centrifugal force, with H027 determining the torsional modes. These codes are limited to long, slender, isotropic blades. Due to the sweep, offset and large chord lengths of the SR-3 and SR-5 blades, the H025 and H027 codes would fail and, hence, finite element grids were derived in NASTRAN to utilise its non-linear static analysis method. The grids for these blades used a combination of quadrilateral and triangular elements. These results are then transformed into the required coordinate system using code F214. This code essentially splits the displacements into radial sections with two translational and one rotational degree of freedom. This was done in

order to linearise the aerodynamics during the stability analysis. For the unsteady aerodynamics, the H444 code was utilised and this was derived from a Goldstein-*type* [58] performance strip analysis to determine the steady-static sectional lift and moment curves. These were derived for each aerofoil section in the coordinate system derived by F214.

Presented in Figure 1.21(a) is the estimated stall flutter predictions of the static experiments of Smith [125], with the prediction assumed to be at the point where the damping goes negative. As shown, the stall flutter predictions mirror the experiments in that the introduction of greater sweep was shown to increase the stall flutter boundary. At this current condition (7000 (rpm)), the highly swept SR-5 propeller did not suffer from stall flutter and required the velocity to be increased towards the maximum value to induce the instability.

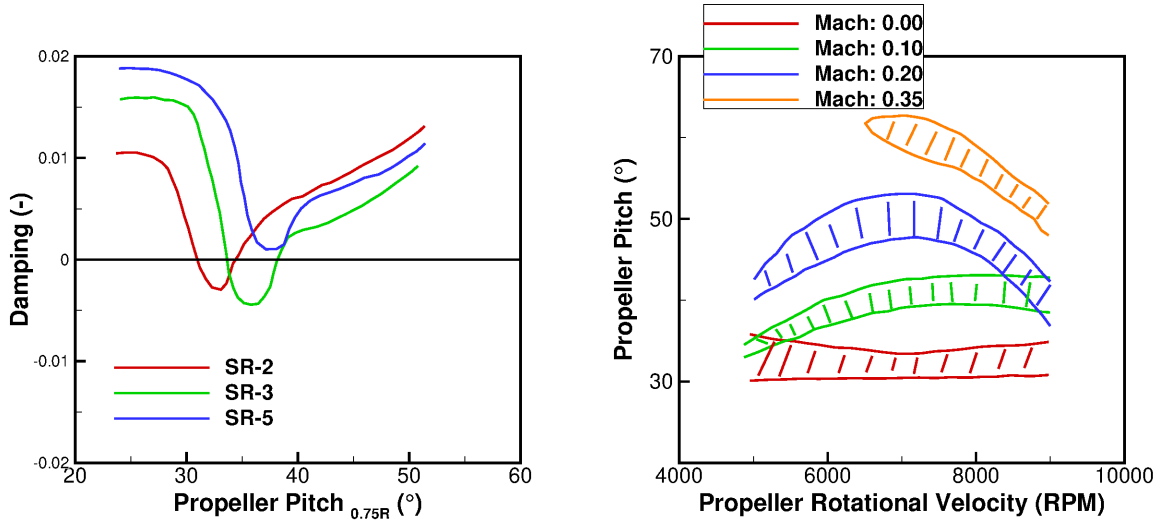

(a) Static (b) Forward-flight

Figure 1.21: Estimated stall flutter predictions for the static and forward-flight experiments of Smith [124, 125]

In a similar manner to the static simulations, the forward-flight results (Figure 1.21(b)) predicted the same trend as the experiments. With increasing freestream velocity, higher blade pitch angles and velocities were required to induce stall flutter. Although the trend was captured through the numerical method, less correlation was found in terms of the exact boundary. This was primarily a result of the aerodynamic modelling and, hence, greater effort is required to model the unsteady flow.

Based upon the static experimental results of Smith [125], Reddy and Kaza in 1989 conducted a numerical investigation into the SR-2 propeller [111]. Due to the findings of the Smith analytical models, Reddy and Kaza sought to improve on the numerical methods used. In particular the aerodynamic modelling. As was described in Section 1.5.3, the instability of stall flutter can be derived from the understanding of dynamic stall and such a study was conducted by Reddy and Kaza in 1987 [110]. This study compared three semi-empirical dynamic stall models in terms of their lift and moment hysteresis loop predictions for a sinusoidally oscillating

aerofoil.

The three semi-empirical models include the Gormont model [61, 62], the Gangwani model [54, 55] and the ONERA model [135]. The Gormont model requires only one empirical parameter, with a large number of stall parameters required for the Gangwani and ONERA models. A short description is given for each modelling method:

Gormont Model: In a similar manner to the Leishman-Beddoes model described in Section 1.3.2, the angle of attack is corrected to obtain an effective angle (α_E). The lift and moment coefficients are then obtained from static aerofoil data. This correction for the effective angle of attack is a function of the rate and is based on oscillating aerofoil test data. The correlation between the true (α) and effective angles is given by:

$$\alpha_E = \alpha - K_1 \Delta\alpha_{DS}, \tag{1.36}$$

where $\Delta\alpha_{DS}$ is an incremental dynamic stall angle given by:

$$\Delta\alpha_{DS} = \gamma_g \sqrt{|\,\frac{\dot{\alpha}c}{2U}\,|}. \tag{1.37}$$

Here, U is the resultant velocity, c the aerofoil chord, $\dot{\alpha}$ the rate of angle of attack and γ_g the non-dimensional empirical function derived from experimental tests. This empirical parameter is determined by:

$$\gamma_g = \sqrt{|\,Ar\,|}, \tag{1.38}$$

where, Ar is the non-dimensional rate of angle of attack. This parameter is a function of Mach number and *thickness/chord*. The final parameter K_1 is given by:

$$K_1 = 0.75 + 0.25\sin(\dot{\alpha}) \tag{1.39}$$

Gangwani Model: This synthesised approach is development by Gangwani [54, 55]. The model utilises semi-empirical obtained analytical expressions representing the qualitative physical features of dynamic stall. The model is seen to capture the formation and streamwise travel of the dynamic stall vortex.

In this model, three stages of dynamic stall are defined: the stall onset; the trailing edge vortex; and the reattachment. Each of these stages are related empirically by the static stall angle, α_s, the non-dimensional rate of angle of attack, Ar, and the unsteady decay parameter, α_W. This decay parameter was previously defined as part of the findings of Beddoes and is described in Section 1.3.2, specifically Equation 1.23.

Stall onset: The angle at which the dynamic stall vortex (α_{Dm}) is initiated is given based upon the instance of moment stall (since moment stall occurs before lift) and this is represented as:

$$\alpha_{Dm} = (1 + \varepsilon_{gw} + C_{Am}Ar + C_{Wm}\alpha_W)\,\alpha_s, \tag{1.40}$$

where the empirical parameters ε_{gw}, C_{Am} and C_{Wm} are obtained from curve fitted experimental data.

Trailing edge vortex: Following the stall onset, the moment coefficient increases significantly in magnitude and this increase is a result of the vortex travel across the aerofoil. The point at which the moment coefficient reaches its maximum value is seen as the point at which the vortex reaches the trailing edge of the aerofoil. The time at which the vortex detaches from the trailing edge is given by:

$$s_{mt} = \frac{1}{C_{At}Ar + C_{\alpha t}\alpha_{Dm}}, \tag{1.41}$$

where C_{At} and $C_{\alpha t}$ are again the empirical parameters defined using experiments.

Reattachment: The point at which the flow reattaches to the aerofoil depends on the freestream Mach number. For a Mach number less than 0.4, the reattachment occurs at an angle which is less than the static stall angle. When the Mach number is greater than 0.4, the reattachment angle occurs at an angle greater than the static stall. Using the empirical parameters ε_{gw}, C_{AR} and C_{wR}, this reattachment angle (α_{re}) is defined as:

$$\alpha_{re} = (1 - \varepsilon_{gw} + C_{AR}Ar + C_{wR}\alpha_W)\,\alpha_s. \tag{1.42}$$

Using these equations for the dynamic stall events, the lift and moment coefficients can be derived alongside additional empirical parameters.

ONERA Model: The ONERA model defines the lift and moment coefficients as a set of ordinary differential equations [135]. When attached, the equations are first order with this increasing to third order for the detached flow regime. A total of eleven empirical parameters are required for the differential equations (six for lift and five for moment) with both lift (c_ℓ) and moment at the quarter-chord point ($c_{m,0.25c}$) containing a linear (C_1) and non-linear (C_2) expression resulting in the following simple equations:

$$\begin{aligned} c_\ell &= C_{L1} + C_{L2}, \\ c_{m,0.25c} &= C_{M1} + C_{M2}, \end{aligned} \tag{1.43}$$

where each linear and non-linear expression is given as follows:

$$\begin{aligned} \dot{C_{L1}} + \lambda_{on} C_{L1} &= \lambda_{on} C_{L\ell} + \lambda_{on} s_{on} \dot{\theta} + \sigma_{on} \dot{\alpha} + s\ddot{\theta} \\ \ddot{C_{L2}} + a_{on} \dot{C_{L2}} + r_{on} C_{L2} &= -\left(r_{on} \Delta C_L + E_{on} \dot{\alpha}\right) \\ C_{M1} &= C_{M\ell} + s_{on} \dot{\theta} + \sigma_{on} \dot{\alpha} + s_{on} \ddot{\theta} \\ \ddot{C_{M2}} + a_{on} \dot{C_{M2}} + r_{on} C_{M2} &= -\left(r_{on} \Delta C_M + E_{on} \dot{\alpha}\right) \end{aligned} \tag{1.44}$$

The total aerodynamic angle of attack (α) is a summation of the angles due to the pitching (θ) and plunging ($\dot{h}/b$) motions. $C_{L\ell}$ and $C_{M\ell}$ represent the static lift and moment coefficients in the linear region, with ΔC_L and ΔC_M the difference between the extended linear curve and the true static curve. The operators $\dot{()}$ and $\ddot{()}$ represent derivatives with respect to the non-dimensional time, $\tau = Ut/b$. This leaves the empirical parameters λ_{on}, s_{on}, a_{on}, σ_{on}, r_{on} and E_{on} which are derived from wind tunnel data.

In addition to the pitching aerofoil study of Reddy and Kaza [110], this model has been used to obtain the dynamic response of a typical helicopter blade section [115] and the entire helicopter blade [103]. For the dynamic stall study [110], all models were used across a range of test cases for the NACA 0012 aerofoil. For the lift coefficient, all models correlated well, across the range of test conditions, to the experimental data. The moment coefficient was not presented for the NACA 0012 test cases using the ONERA model, however, it is seen to predict the moment coefficient well for a reference OA212 aerofoil section. The moment coefficient was not predicted well for the Gormont model, with very good agreement for the Gangwani. The results from the Gangwani model were expected due to the empirical data taken from the experimental results.

Reddy and Kaza [110] concluded from this initial dynamic stall investigation that the Gormont and ONERA models can be used for propeller flows in typical operating conditions due to the blade being primarily within the light stall regime. The ONERA model involves fewer experimental parameters than the Gangwani, with the Gormont only requiring one. This could potentially be a factor in the choosing of an aerodynamic model as it depends on the availability of static aerofoil data of the blade sections. This situation was found in the propeller stall flutter study [111] and, hence, the Gormont model was used due to the lack of blade sectional data. This model was used to provide the stall effects with quasi-steady, incompressible two-dimensional strip theory used to calculate the generalised aerodynamic forces across a range of sections along the blade.

The structural modelling used by Reddy and Kaza [111] involved the derivation of the static-displacement and normal modes and frequencies from a non-linear finite element analysis which was then supplied to the standard modal equations of motion for a propeller blade [77]. The final equations are derived as:

$$\ddot{q}_i + 2\zeta_i \omega \dot{q}_i + \omega_i^2 q_i = \frac{Q_i}{m_i} \qquad i = 1, 2 \ldots n, \tag{1.45}$$

where m_i is the generalised mass, ω_i is the natural frequency, ζ_i is the critical damping, Q_i is the generalised force terms and q_i the normal coordinate for the i^{th} mode where n modes are supplied. These equations are solved within the time-domain using the *Wilson-*θ method [145]. This method is an implicit integration method that assumes a linear variation in acceleration between time-steps. The static-displacement and modal displacements were derived using NASTRAN, with four normal modes supplied. The aeroelastic flow chart used by Reddy and Kaza is presented in Figure 1.22.

The experimental results of Smith [125] presented the stall flutter boundaries in terms of stress across the blade. Using the Gormont dynamic stall model, qualitative correlation was found between the experiment and numerical study, however, the quantitative comparison of the damping plots showed a conservative estimation of the boundary using this model. This conservative estimation may be acceptable from a design point of view if the boundary is outside the normal operating range of the propeller.

Due to the fact that only a qualitative comparison could be made to the experimental results, a numerical comparison of the modal amplitude results is conducted against the study of Bielawa [22]. The investigation of Bielawa utilised the Gangwani dynamic stall model with a non-linear beam model for the structural modelling. The use of a non-linear beam model for the unswept SR-2 is acceptable due to the design of the blade. However, for a more complex structure, such as the swept SR-5, the more general finite element analysis of Reddy and Kaza [111] is more suitable. The modal amplitude predictions of both the Gormont and Gangwani models agree well. A slight improvement on the damping-boundary plots is found in the Bielawa study whilst using the Gangwani model with the predictions shown in Figure 1.23.

In 2007, Delamore-Sutcliffe [40] conducted a numerical investigation into propeller stall flutter with a comparison made to the experiments of Baker [14]. The investigation involved the development of an unsteady aerodynamic model, coupled with the Brookes and Houbolt equations of motion for a rotating beam, to determine the stall flutter boundaries. The main objective of this work was to transition from the empirical models still used by industry to a more advanced formulation without penalising the fast prediction characteristics of such methods.

Delamore-Sutcliffe built-up the aerodynamic model from the linear to non-linear regime in two-dimensions, with experimental tests conducted to ensure a validated model was derived. Three fundamental models were tested for the attached flow (linear) regime, with this involving two established models and a third derived in the time-domain. The experiments used to validate the attached flow model were those of Piziali in 1994 [104]. Details such as the pressure distribution over a semi-span wing and oscillating aerofoil were presented, thus ensuring an extensive range of data from which to compare.

The first model was defined as the indicial response model and considers the instantaneous

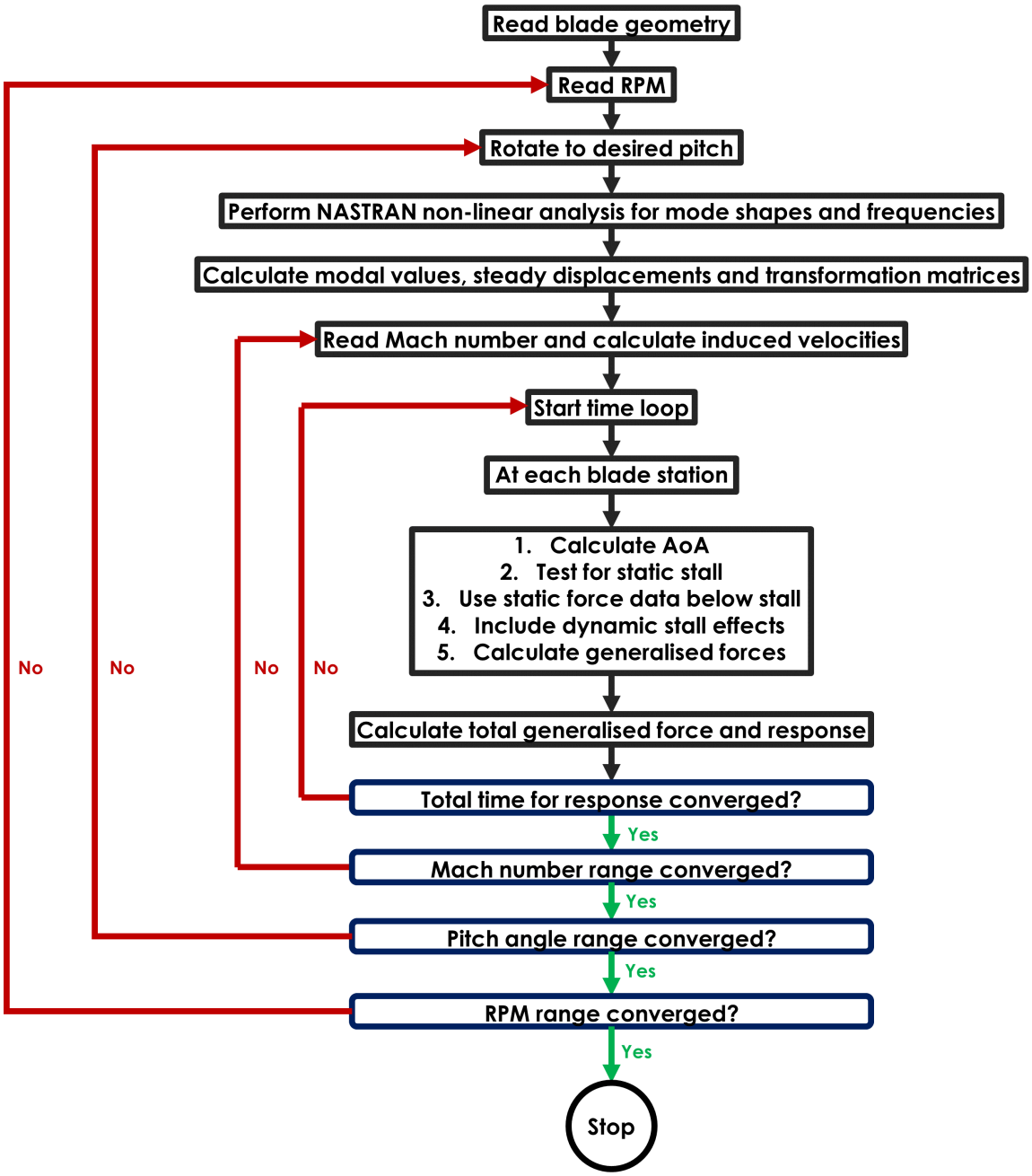

Figure 1.22: Aeroelastic flow-chart for the numerical study of the SR-2 propeller by Reddy and Kaza [111]

changes between two steady states. A review of this method was conducted by Beddoes [16]. With an indicial response function defined for the circulatory and non-circulatory terms as a function of semi-empirical coefficients, the total force coefficient is seen as a sum of the subsequent parts. These semi-empirical coefficients have been discussed by Leishman in which a method for obtaining [83] and validating [82] was presented. Using a finite difference approximation to Duhamel's integral [24], as used in Section 1.3.2, is it possible to determine the response to an arbitrary time-history. A full derivation is presented by Leishman [84].

The second model used was the Theodorsen model [131, 133] described in Section 1.3.1.

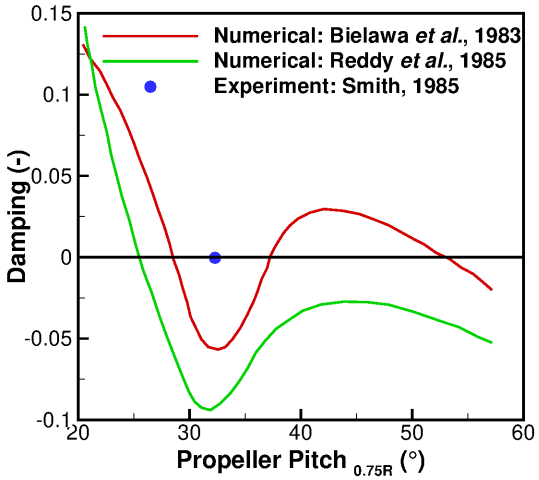

Figure 1.23: Damping stall flutter boundary plots for the SR-2 propeller for the experimental [125] and numerical studies [22, 111]

Due to the fact that the Theodorsen model is constructed within the frequency domain, an ideal coupling to a time-marching aeroelastic model remains tricky. This leads on to the third model which was a time-domain approximation of the Theodorsen model derived by Dowell [43]. Here, it was found that a link between the frequency and time-domain can be obtained via a Fourier transform pair. This results in an updated Theodorsen function with coefficients λ_1 and λ_2, which can be substituted into the full lift and moment equations (Equation 1.3) before converting to the final time-domain differentials by using the inverse of the differential rule for Laplace transforms.

$$C(k) = \frac{\lambda_2 ik + \lambda_1}{ik + \lambda_1} \tag{1.46}$$

All attached flow models were tested and provided satisfactory correlation with the experimental results [104]. The third model was chosen as the basis for the full aerodynamic model due to the lack of empirical data and formulation within the time-domain.

Following the derivation of the linear aerodynamic model, an extension was required to include the dynamic stall effects. Using a state-space approach, a non-dimensional parameter was introduced in order to provide the detached flow mechanism. This parameter was the static upper surface separation point (x_s) and this was combined with the Kirchoff and Helmholtz theory [148] to determine the equations for the normal force and moment coefficients. The separation point was defined as $x_s \in [0,1]$, where $x_s = 0$ corresponds to detached flow at the aerofoil leading edge and $x_s = 1$ to fully attached flow. The normal force coefficient (C_N) was given by:

$$C_N = c_{l_\alpha} \left(\frac{1 + \sqrt{x_s}}{2} \right)^2 \alpha, \tag{1.47}$$

where c_{l_α} is the lift curve slope and α the aerofoil angle of attack. For the moment coefficient, a reference to the work of Khrabrov and Ol was made as they produced a theory which combined thin aerofoil theory and Kirchoff concepts to determine a closed solution for the pitching moment coefficient at high angles of attack [78]. However, a small angle assumption was made and therefore the work of Leishman and Beddoes is cited [85] for the ratio equation between the normal force and moment coefficients (C_M), due to the fact it utilised the separation point. The ratio was given as:

$$\frac{C_M}{C_N} = k_0 + k_1(1 - x_s) + k_2 \sin(\pi x_s^2), \tag{1.48}$$

where $k_0 = (0.25 - x_{ac})$ is the non-dimensional aerodynamic centre offset from the quarter chord. The remaining two parameters, k_1 and k_2, are semi-empirical coefficients derived from experiments. To estimate the separation point, further semi-empirical coefficients were required depending on the current state of the flow and the static stall angle. Leishman and Beddoes stated that the static stall angle (α_s) corresponds closely to the point where $x_s = 0.7$. This fact was utilised alongside experimental data to determine the static stall angle. The separation point was then given by:

$$x_s = \begin{cases} 1 - 0.3exp\left[s_1(\alpha - \alpha_s)\right] & \alpha \leq \alpha_s \\ 0.04 + 0.66exp\left[s_2(\alpha_s - \alpha)\right] & \alpha > \alpha_s \end{cases} \tag{1.49}$$

where s_1 and s_2 are semi-empirical coefficients chosen to define the shape of the state variable curve pre- and post-stall. In order to model the unsteady effects of detached flow, an effective angle of attack (α_E) was introduced:

$$\alpha_E = \alpha - \tau_2 \dot{\alpha}, \tag{1.50}$$

where τ_2 defines the time delay associated with quasi-steady effects. The model was completed by modelling the transient aerodynamics associated with the relaxation process following detached flow. These effects were determined via a first order differential equation for the effective separation point x_{s_E}:

$$\tau_1 \frac{dx_{s_E}}{dt} + x_{s_E} = x_s, \tag{1.51}$$

where τ_1 was the semi-empirical relaxation time constant.

This dynamic stall model was validated against the experiments of Jumper *et al.* from 1987 [76]. Jumper *et al.* conducted wind tunnel tests of the pitching NACA 0015 aerofoil over a range of constant pitch rates. The aerodynamic model was tested over a range of the experimental rates with the semi-empirical parameters s_1, s_2 and α_s determined from the data. Initial estimates of the two dynamic coefficients (τ_1 and τ_2) were sourced from the studies of Goman

and Khrabrov [59] and Khrabrov and Ol [78]. These estimates were then adjusted to provide improved correlation. Excellent correlation was found across all pitch rates.

To combined the attached and detached flow effects, a similar summation as the linear model was utilised. This involved the addition of the zero-angle (C_{L_0}), circulatory (C_{L_c}) and non-circulatory ($C_{L_{nc}}$) lift coefficients, with the high angle of attack effects included via an unsteady factor (LF).

$$C_L = C_{L_0} + (C_{L_c} \times LF) + C_{L_{nc}} \tag{1.52}$$

This unsteady factor was multiplied by the circulatory lift and was derived in the Kirchoff/Helmholtz theory [148] as:

$$LF = \left(\frac{1 + \sqrt{x_{s_E}}}{2} \right)^2 . \tag{1.53}$$

A similar process was found for the pitching moment term. An additional unsteady pitching moment factor (PF) was introduced and this was multiplied by the unsteady lift factor and circulatory lift. This term was then included in the summation of the zero-angle (C_{M_0}), circulatory (C_{M_c}) and non-circulatory ($C_{M_{nc}}$) moment coefficients.

$$\begin{aligned} C_M &= C_{M_0} + (C_{L_c} \times LF \times PF) + C_{M_c} + C_{M_{nc}} \\ PF &= k_0 + k_1(1 - x_{s_E}) + k_2 \sin(\pi x_{s_E}^2) \end{aligned} \tag{1.54}$$

The full aerodynamic model was verified against the pitching aerofoil experiments of Piziali [104], with pre-requisite testing used to determine the semi-empirical coefficients. Good correlation was found in static and dynamic tests, with some small deficiencies at high static angles of attack and the dynamic overshoot of the lift and pitching moments.

To verify the aerodynamic model for the stall flutter phenomena, Delamore-Sutcliffe conducted a range of wind tunnel experiments of a two-dimensional aerofoil with a single degree of freedom in pitch. This verification was conducted via a time-marching and eigenvalue stability analysis through the coupling of the aerodynamic and structural models. The structural model was derived using Lagrange's equations of motion [23]. Due to the motion of the aerofoil, the potential remains for the aerofoil to stall at a negative angle of attack. As a result, the equations for the separation point had to be updated to include the negative range with respect to the negative static-stall angle (α_{s_n}):

$$x_s = \begin{cases} 1 - 0.3exp\left[s_{1_n}(\alpha_{s_n} - \alpha)\right] & 0 > \alpha > \alpha_{s_n} \\ 0.04 + 0.66exp\left[s_{2_n}(\alpha - \alpha_{s_n})\right] & \alpha \leq \alpha_{s_n} \end{cases} \tag{1.55}$$

where the semi-empirical parameters s_{1_n} and s_{2_n} were updated for the negative range. The equa-

tions were coupled in a second order matrix equation including the mass, damping and stiffness matrices. A Runge-Kutta scheme was utilised for the time-marching formulation and a linearised solution in the form of an exponential was assumed in order to obtain eigenvalues for the stability analysis. Further details are presented by Delamore-Sutcliffe *et al.* [42]. A comparison of the experimental and numerical results showed a good correlation, with the numerical results from both the stability and time-marching methods slightly below the experiment.

In preparation for the transition to the propeller test cases, the aeroelastic model developed for the two-dimensional aerofoil was extended to look at a three-dimensional cantilever wing. The wing was structurally modelled using strip theory and assumed modes with two degrees of freedom in pitch and heave. A key benefit to using this method was the limitation of two-dimensional aerofoil characteristics and the computational solution time. Disadvantages included the lack of three-dimensional crossflow modelling and the requirement for empirical data.

As per the structural model, the aerodynamic model was updated to compute the spanwise lift and moment coefficients in both attached and detached conditions. With the use of strip theory, the aerodynamic model was applied at each spanwise location with a station-by-station update required for the semi-empirical coefficients and lift curve slope. Experiments [104] were again used for the coefficients, along with curve fitting, to determine the spanwise distribution of the values. Theoretical expressions used to convert the two-dimensional slope to three-dimensions with a quintic power distribution over the span was assumed for the lift curve slope with a value of zero applied at the tip. In addition to this, the effect of cantilever wing twist was taken into account. This was conducted via lifting-line theory and Prandtl's integral equation for circulation [69].

These expressions for aerodynamics and structure were combined in a similar manner to the two-dimensional aerofoil equations. The structural equations were generalised with respect to the assumed modes and then integrated over the span. Two bending and a single torsional mode were included, with higher modes having a minimal effect on the accuracy. A similar process was conducted for the aerodynamic terms including the circulatory and non-circulatory coefficients. The solution to these equations were obtained via a time-marching and eigenvalue analysis. Due to the increase in matrix terms, the time-marching calculations were limited due to the increase in computational cost. These were subsequently compared to the eigenvalue analysis which was conducted across the entire test case range.

This three-dimensional wing method was compared against the experiment of Dunn and Dugundji [45]. Good correlation between the experimental and numerical calculations was found. For the first test case examined, the time-marching method appeared to produce an improved correlation of the flutter frequency in comparison to the stability analysis. However, the flutter velocity was under-predicted at high initial pitch angles. Only the stability analysis was used for the second test case with an under-prediction of the flutter velocity at low and high

initial angles, and an under-prediction of the frequency across the full range.

Following the verification of the three-dimensional wing aeroelastic model, the aerodynamic model was extended and utilised with the Brookes and Houbolt equations of motion for a rotating beam [68] to conduct a propeller stall flutter investigation. The structural model derived by Brookes and Houbolt included several assumptions made to reduce the complexity of the equations without losing accuracy. There were:

1) The chordwise bending was assumed to be very small, and hence negligible, in comparison to the flapwise bending. This is due to the fact that the chordwise bending stiffness is much greater than the flapwise stiffness when the *thickness/chord* ratio is less than 15%. This is acceptable with modern propellers due to their need to utilise thin aerofoil sections for performance. This assumption may fail for tiltrotor blades where thicker sections are used.

2) The blade was assumed to have no set twist distribution in the spanwise direction. This was applicable within this study due to the fact that the experimental blades have zero twist. For more complex, highly twisted blades, this assumption would fail and the terms associated would need to be included.

3) The final assumption was that the tensile and rotational axis of the blade align with the elastic axis. This was, again, driven by the experimental data were no information was supplied regarding these offsets from the elastic/mass axis.

These equations resulted in the following structural equations for the propeller blade:

$$\begin{aligned} L &= \frac{\partial^2}{\partial y^2}(EI_1\frac{\partial^2 w}{\partial y^2}) - \frac{\partial}{\partial y}(T\frac{\partial w}{\partial y}) - \frac{\partial}{\partial y}\left(\Omega^2 m(y+R_{hub})e_d\alpha\right) + m\left(\frac{\partial^2 w}{\partial t^2} + e_d\frac{\partial^2\alpha}{\partial t^2}\right) \\ M &= -\frac{\partial}{\partial y}\left((GJ+Tk_y^2)\frac{\partial\alpha}{\partial y}\right) + \Omega^2 m(y+R_{hub})e_d\frac{\partial w}{\partial y} \\ &+\Omega^2 m(k_{zz}^2-k_{xx}^2)\alpha + I_y\frac{\partial^2\alpha}{\partial t^2} + me_d\frac{\partial^2 w}{\partial y^2} \end{aligned} \tag{1.56}$$

where E is the Young's modulus, I_1 is the vertical area moment of inerta, w is the plunge motion, T is the axial tension defined as $T = \int_y^L \Omega^2 m(y+R_{hub})dy$, Ω is the blade rotational velocity, m is the blade mass, R_{hub} is the blade hub radius, e_d the distance between the elastic (x_{ea}) and mass axes (x_{cg}) given by $e_d = (x_{ea} - x_{cg})c$, α is the overall angle of attack, GJ is the torsional stiffness, k_y is the blade area radius of gyration, k_{zz} and k_{xx} are the blade mass radii of gyration and I_y is the mass moments of inerta.

An important point to note is the reduction of the above equations from propeller to wing configurations is possible via the setting of Ω and R_{hub} to zero. This provided continuity in the aeroelastic modelling.

The strip theory aerodynamic model, used in the cantilever wing, was updated to include the spanwise variation in induced velocity. A factor of rotorcraft aerodynamic modelling is the wake influence on the preceding blade. This effect can be captured by methods such as Loewy [89] and was previous discussed in Section 1.3.1. It was assumed that such an effect is minimal in comparison to the overall load results obtained via Theodorsen's method. This is true in high thrust/inflow condition were the propeller wake is induced far away from the disc.

In order to update the aerodynamic model for the rotorcraft environment, the effect of the induced incidence was taken into account. The induced incidence is the effect of the blade rotation and inflow velocity, and was modelled via Blade Element Momentum Theory (BEMT) [92]. This model was used for each section with an iterative process conducted to obtain the induced velocity effect.

Both the structural and aerodynamic terms were combined as the previous versions, in state-space form of stiffness, damping and mass matrices. In the cantilever wing model, the structural damping (C) was set to zero. This was not the case for the propeller model due to the fact it was taken into account in the experimental studies [14] and, hence, must be included within the equations. To include this, the theory of Theodorsen [133] was again applied where the structural damping was seen as a function of the generalised stiffness matrix (K), i.e.:

$$[C] = ig[K] \tag{1.57}$$

where g is the structural damping coefficient. In order to solve the equations of motion, the stability analysis conducted for the aerofoil and cantilever wing was used. Due to the increased computational cost, the time-marching method was not used for this analysis. Further details regarding the aeroelastic modelling was presented by Delamore-Sutcliffe *et al.* [41].

A comparison to the experimental data of Baker [14] was made with three test cases selected and presented in Figure 1.24. Good correlation between the experiment and numerical analysis was found. The trend of lowering velocity with increased pitch angle was seen in both results with the minimum flutter velocity well captured. Differences at higher angles of attack are seen within the comparison and these are determined to be an effect of the high angle of attack detached flow modelling. However, the pitch angles where this was seen are outside the blades operational regime and, hence, a good correlation was concluded.

Ognev in 2011 investigated different unsteady aerodynamic models and their influence on the determined flutter boundary [101]. These unsteady aerodynamic models include Theodorsen's model [132], three *cascade* models [75, 127, 141] and a detailed three-dimensional model [72]. The *cascade* models take into account the effect of the returning wake. Something which is neglected in the Theodorsen model. However, they are limited by their two-dimensionality with the effect only applied from equivalent cross sections. This was mitigated by the use of the three-dimensional model by Isoilevskii *et al.* [72] where bound, trailing and shed vortices are included. For all models, the viscous effects are neglected and this resulted in the loss of

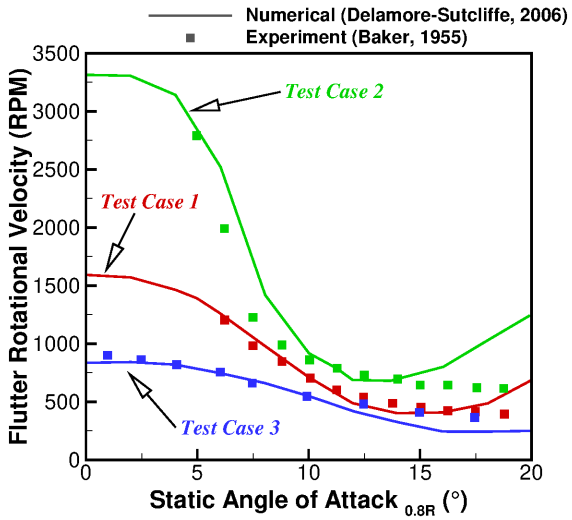

Figure 1.24: Stall flutter boundary comparison for the model propellers of Baker [14] compared against the numerical aeroelastic model of Delamore-Sutcliffe [40]

detached flow modelling, not ideal for a stall flutter analysis. To combat this, the Delamore-Sutcliffe model [40] was included within this analysis.

A finite element approach with ANSYS [90] was utilised for the structural modelling. The blade was defined by shell elements with the blade divided into several spanwise segments and each segment into chordwise elements. To linearise the equations of motion, a steady state calculation was conducted followed by an analysis using small perturbations on this steady state. Aerodynamic coupling was included for multiple blades, with structural coupling neglected. With the equations of motion linearised, an eigenvalue analysis was conducted to determine the flutter boundaries.

A comparison was made to the experiments of Hubbard *et al.* [71] with various parameters tested for each aerodynamic model. This included the effect of compressibility for the Theodorsen model, and the variation in induced velocity with respect to the propeller disc for the *cascade* and three-dimensional models. All tested models predicted a drop in the propeller flutter boundary at very low and high pitch angles. This trend was also seen within the experimental data, but due to the lack of detached flow modelling the agreement between the results can only be seen to be satisfactory due to the captured trend. In terms of the classical flutter range, fair agreement was found between all models and the experiments. The inclusion of compressibility was seen to have a beneficial effect on the agreement with this dominating over the wake effects in the three-dimensional model.

Following this, a test of the number of blades was conducted. This involved two of the *cascade* models [127, 141] (due to the similar results captured between the Smith [127] and Jones [75] models) along with the Theodorsen and Isoilevskii formulations. In addition to the number of blades, these test cases were conducted at low and high advance ratios. At low advance ratios, the effect of the blade wake increased and this was highlighted by the use of the

cascade and three-dimensional model. This inter-blade aerodynamic interaction also increased with the number of blades. At high advance ratio, the propeller wake was projected further from the blade sections and, therefore, the Theodorsen model can be applied to provide acceptable results.

In addition to these full propeller stall flutter investigations, many studies have been conducted in recent times which focused on two-dimensional aerofoils. Such investigations made use of pitch and plunge rigid models [109, 139, 150], cyber-physical models (where the structural response of the aerofoil was given based upon a known set of derived equations of motion) [36, 37], or if numerical, utilised dynamic stall based aerodynamic models [9, 27]. The use of such studies can only provide fundamental analysis into aerofoil stall response, with conservative boundaries when applied to true test cases. This was highlighted by the full propeller studies described.

1.6.3 Summary

As observed from literature, a range of experimental investigations have been conducted. Due to the heavy use of propeller driven aircraft between 1945 and 1960, a high number of experiments were conducted to understand blade flutter. This included a number of wooden propeller investigations during World War II. The use of laminated wood can result in variations in the structural properties during manufacturing and, therefore, such blades remain non-ideal for a numerical simulation. Following this in the 1950's, a range of model blades were designed for wind tunnel investigations. Such blades were made of a modern alloy to allow for a reduction in the variability of the manufacturing process. As a result of this, a range of parameters could be investigated and the greatest insight into stall flutter was found during this period. However, due to the specific design, the blade was not fully defined within the reports and therefore results in non-ideal test cases.

With the aerospace transition from propeller driven aircraft to turbo-fan engines, interest was lost in propeller stall flutter and therefore very few studies were conducted after the 1950's. A private-sector test was conducted by Dowty Propellers in 1979 using a modern, in-service blade. Although the primary aim of the test was not specifically for stall flutter understanding, stall flutter was encountered due to the pitch angle range. In addition to this, interest within prop-fans grew in the 1980's and this resulted in new studies to understand the blade flutter boundaries.

For each described experimental investigation, the structural properties are unknown, resulting in an estimation of these properties. A summary of the pros and cons associated with each experimental test case is presented below in Table 1.5.

With the minimal development in aeroelastic models during the 1950's, interest in numerical stall flutter investigations only began with the development/study of the SR Prop-fans. These studies, conducted in the 1980's, involved both eigenvalue and time-marching modal methods

with semi-empirical aerodynamic models. The use of the eigenvalue analysis was selected to ensure a fast calculation and this trend continued into the modern propeller stall flutter studies. With the availability of faster computing power, more complex finite element models could be used and greater time-marching analysis was utilised. However, the focused still remained on the use of the semi-empirical dynamic stall models and therefore conservative boundaries were achieved. A summary of the numerical studies can be found in Table 1.6.

Table 1.5: Summary of propeller stall flutter experimental test cases.

Test Case	Pros	Cons	Conditions
Spitfire/Firefly Propellers [129]	*1:* Clear stall flutter boundary *2:* Known geometry	*1:* Wooden blade *2:* Structural properties	*rpm:* $800-1800$ *Pitch:* $8^{o}-32^{o}$
Theodorsen Models [134]	*1:* Clear stall flutter boundary	*1:* Wooden blade *2:* Blade definition *3:* Experimental setup	*Non-dimensionalised*
Tempest Propeller [48]	*1:* First non-wooden blade *2:* Stress traces across range	*1:* Coarse pitch range *2:* Multi-blade setup *3:* Blade definition	*rpm:* $900-1600$ *Pitch:* 12, 16, 20, 24, 28, 30^{o}
Baker/Hubbard Models [14, 71]	*1:* Dimensionless boundary *2:* Extensively analysed	*1:* Structural properties *2:* Non-realistic blades (model only)	*Pitch:* $5^{o}-35^{o}$
NACA Propellers [8]	*1:* Extensively analysed *2:* Blades defined	*1:* Experimental setup *2:* Blade trim	*Pitch:* $16^{o}-38^{o}$ *rpm:* $\sim 400-1700$
Rogallo Models [114]	*1:* Extensively analysed *2:* Experimental setup	*1:* Blade definition *2:* Axis tilt range	*Pitch:* -17.5^{o} to $+42^{o}$ *rpm:* $550-2200$
Commander Propeller [28]	*1:* Torsional stress boundary *2:* Known geometry *3:* Realistic blade (in-service) *4:* Trusted by manufacturers	*1:* Structural properties estimated	*rpm:* $1400-1800$ *Pitch:* $26^{o}-28^{o}$
SR Blades [124, 125]	*1:* Presented data *2:* Blade configurations *3:* Extensively analysed	*1:* Structural properties *2:* Full boundary	*rpm:* $2000-10000$ *Pitch:* $20^{o}-50^{o}$ *Scale:* $^{1}/_{8}$

Table 1.6: Summary of propeller stall flutter numerical test cases.

Test Case	Summary	Conditions	Date
Smith	Eigenvalue analysis	*rpm:* $5000, 7000, 9000$	1985
[124, 125]	2D strip theory aerodynamics	*Pitch:* $20^{\circ} - 50^{\circ}$	
SR Propellers	Finite element model		
	Conservative results		
Bielawa *et al.*	Eigenvalue & Time-marching	*rpm:* $2000, 8500$	1983
[22]	Gangwani dynamic stall	*Pitch:* $20, 25, 30, 32^{\circ}$	
SR-2 Propeller	Non-linear beam		
	Conservative boundaries		
Reddy and Kaza	Time-marching, modal	*rpm:* $2000, 5000, 8500$	1989
[111]	Gormont dynamic stall	*Pitch:* $30^{\circ}, 50^{\circ}$	
SR-2 Propeller	Finite element model		
	Conservative results		
Delamore-Sutcliffe	Theodorsen unsteady strip theory	*Pitch:* $0^{\circ} - 20^{\circ}$	2007
[40]	Validated via 2D experiments		
Baker/Hubbard Models	Coupled with rotating beam equations of motion		
	Eigenvalue & Time-marching analysis		
	Deviations from experiment at high pitch angles		
Ognev	Eigenvalue analysis	*rpm:* $500 - 2500$	2011
[101]	Various unsteady inviscid aerodynamic models	*Pitch:* $-20^{\circ} - 10^{\circ}$	
Baker/Hubbard Models	Finite element model		
	Fair agreement to experiments		

1.7 Research Aims and Objectives

Based upon the motivation described in Section 1.1, the following research aims and objectives are derived:

- An examination of the current literature must be undertaken to understand the sources of data and past numerical studies. This has been conducted and presented in Section 1.6. A key outcome from this is the need for a modern experimental test case from which numerical methods can be validated. The last study was conducted in the 1980's and, with improvements in experimental technqiues, greater insight and data can be extracted.
- There is a need to develop a modern understanding of the modelling requirements for a propeller stall flutter study. This includes both aerodynamic and structural modelling, with a range of techiniques previously used for the structural model presented in Section 1.6.2.
- Time-marching aeroelastic calculations are expensive. Therefore, in order to mitigate this, a method is required which can allow for an estimation of potential instability at a reduced computational cost.
- Using the derived method and based upon the key factors that have previously been investigated (Section 1.6), there is a need to develop an understanding of propeller stall flutter, and its factors, within a modern blade.

1.8 Novelty of the Thesis

The novelty of the work lies within three key areas and these are as follows:

- The novelty of this work lies within the application and development of the Navier-Stokes based CFD with a coupled structural model. This includes the development of a structural interpolation technique that allows for the improvement in the standard modal method to account for transient effects. To this date, no fully three-dimensional, elastic, CFD computations have been conducted which focus on propeller stall flutter, thus improving on the aerodynamic modelling previously used.
- Due to the implementation of the improved aerodynamic modelling techinique, greater insight into the mechanisms and parameter influence has been gained. This includes the effects of structural and aerodynamic changes which followed trends from past studies.
- As part of the improved insight, a method was derived which extracted aerodynamic damping estimates from three-dimensional computations. This was linked to the objective which aimed to provide stability estimations at a reduced computational cost. Such estimations had previously not been conducted before.

1.9 Thesis Outline

The thesis is outlined as follows:

Chapter 2 details the time-marching aeroelastic method of the in-house code Helicopter Multi-Block 3 (HMB3). This includes details on the aerodynamic and structural modelling.

This is followed by Chapter 3 which looks into the aerodynamic and structural validation and verification. Full rigid aerodynamic simulations of isolated and installed propellers are presented, before a verification process is conducted on the installed propeller using the coupled CFD and CSD.

Chapter 4 presents the results of the aeroelastic validation of the Commander propeller test case. This chapter examines details such as turbulence modelling, blade aerodynamic transient effects and structural setup. The structural setup investigation involves the use of different structural models and their utilisation.

Due to the use of expensive time-marching calculations, a method is presented in Chapter 5 to estimate the amount of aerodynamic damping from three-dimensional simulations. This includes an initial comparison of pitching aerofoils before a focus on the full propeller.

The final results are presented in Chapter 6 and this includes the structural and aerodynamic parametric study. Three structural and two aerodynamic parameters are investigated with comparisons made to the validated result. Insight is gained into potential changes to the blade design which could benefit its stall flutter response.

The thesis concludes with Chapter 7 where the research conclusions are presented along with potential future work.

Chapter 2

Time-Marching Aeroelastic Methodology of HMB3*

For this investigation, a time-marching aeroelastic method was developed. The method uses the in-house flow solver HMB3, and couples Computational Fluid Dynamic (CFD) and Computational Structural Dynamics (CSD). The core functionality of HMB3 is CFD, however its use has been extended in recent years to include whole engineering applications, including helicopter rotor aeroelasticity [39], propeller aeroacoustics [31], flight mechanics [35] and missile trajectory prediction [13].

There remains a possibility to utilise the frequency-based harmonic balance method of HMB3 [147]. This method represents the flow and residuals as truncated fourier series of order N_H, where N_H is the number of harmonic balance modes. This conversion to the frequecy domain allows for a significant reduction in computational cost due to the fact unsteady aerodynamics can be obtained through a series of snapshots, negating the need for time-marching. This reduction in computational cost is in spite of a significant increase to the allocated memory. However, due to an expected change in the blade rotational velocity (as observed within the selected test case [28]), the focus of this thesis will remain in the time domain.

2.1 Computational Fluid Dynamics

Previous investigations using HMB3 have provided propeller flow validation in both installed and isolated conditions, by comparison with the experimental results of the JORP propeller [120] and the IMPACTA wind tunnel tests [60, 79]. These results were compared in 2016 [15] and 2018 [31], respectively, with good agreement found in terms of aerodynamics and acoustics.

*The methodology presented in this chapter is published in R.J. Higgins *et al.* "High-Fidelity CFD Methods for the Simulation of Propeller Stall Flutter", *AIAA Journal*, Vol. 57, Issue 12, doi: 10.2514/1.J058463, 2019

2.1.1 Flow Solver Formulation

HMB3 solves the compressible Navier-Stokes equations in three-dimensions. The complete system of the Navier-Stokes equations involves the fluid conversation laws along with the two thermodynamic equations of state for pressure and temperature. These are:

- Conservation of mass
- Conservation of momentum
- Conservation of energy
- Equations of state (*pressure, temperature)*

The two equations of state are used to close the system of Navier-Stokes equations, with two scalar terms and one vector remaining as unknowns. These are: fluid density ρ, velocity $\mathbf{u}$ and specific internal energy e.

The first conversation law states that mass must be conserved or remain constant over time. Known as the continuity equations, it is expressed in Cartesian coordinates as:

$$\frac{\partial \rho}{\partial t} + \frac{\partial (\rho u_i)}{\partial x_i} = 0 \tag{2.1}$$

Newton's 2^{nd} Law states that linear momentum must be conserved, and is expressed as:

$$\frac{\partial (\rho u_i)}{\partial t} + \frac{\partial (\rho u_i u_j)}{\partial x_j} = \rho f_i - \frac{\partial p}{\partial x_i} + \frac{\partial \tau_{ij}}{\partial x_j}, \tag{2.2}$$

where f_i represents any acting body force, and τ_{ij} is the viscous stress tensor. Using the assumption of a Newtonian fluid [*], along with Stokes's hypothesis [†], the viscous stress tensor can be expressed as:

$$\tau_{ij} = \mu \left[\left(\frac{\partial u_i}{\partial x_j} + \frac{\partial u_j}{\partial x_i} \right) - \frac{2}{3} \delta_{ij} \frac{\partial u_k}{\partial x_k} \right], \tag{2.3}$$

where μ is the molecular viscosity and δ_{ij} the Kronecker delta.

The 1^{st} Law of Thermodynamics states that the total energy of an isolated system is constant. This can be written as:

$$\frac{\partial \rho E}{\partial t} + \frac{\partial}{\partial x_j} \left[u_j (\rho E + p) \right] - \frac{\partial}{\partial x_j} \left(u_i \tau_{ij} - q_{ij} \right) = 0, \tag{2.4}$$

where E is the total energy of the fluid per unit mass, and $\mathbf{q}$ is the heat flux vector. The total energy per unit mass is defined as:

[*] In a Newtonian fluid the viscous stress are proportional to the rates of change of the fluid velocity vector

[†] The Stokes's hypothesis implies that the bulk viscosity is zero

$$E = \left[e + \frac{1}{2} u_i u_i \right], \tag{2.5}$$

where $\frac{1}{2}u_i u_i$ represents the kinetic energy per unit mass. The heat flux vector is calculated using Fourier's Law:

$$q_i = -k_h \frac{\partial T}{\partial x_i}, \tag{2.6}$$

where k_h is the heat transfer coefficient. An ideal gas approximation is assumed and is used to relate pressure and density. By default dry air is considered, with a specific gas constant, R_{sp}, of 287.058 $\frac{J}{KgK}$.

$$p = \rho R_{sp} T \tag{2.7}$$

Sutherland's law is also used to determine the molecular viscosity of air.

$$\mu = \mu_0 \left(\frac{T}{T_0} \right)^{\frac{3}{2}} \left(\frac{T_0 + 110}{T + 110} \right) \tag{2.8}$$

The combination of the three conservation laws allows for the derivation of the Navier-Stokes equations for viscous flows. These equations are shown and are written in vector notation in order to be concise.

$$\frac{\partial \mathbf{W}}{\partial t} + \frac{\partial \left(\mathbf{F}^i + \mathbf{F}^v \right)}{\partial x} + \frac{\partial \left(\mathbf{G}^i + \mathbf{G}^v \right)}{\partial y} + \frac{\partial \left(\mathbf{H}^i + \mathbf{H}^v \right)}{\partial z} = \mathbf{S}, \tag{2.9}$$

where $\mathbf{W}$ is the vector of conserved variables:

$$\mathbf{W} = \left(\rho, \rho u, \rho v, \rho w, \rho E \right)^T, \tag{2.10}$$

with u, v and w being the three velocity components. The flux components in the x-, y-, and z-direction are denoted by $\mathbf{F}$, $\mathbf{G}$ and $\mathbf{H}$, respectively, with superscripts i and v used to denote the inviscid and viscous terms. The flux terms are presented below for the inviscid and viscous components:

$$\begin{aligned}
\mathbf{F}^i &= \left(\rho u, \rho u^2 + p, \rho uv, \rho uw, u\left(\rho E + p\right) \right)^T & \mathbf{F}^v &= \tfrac{1}{\mathrm{Re}} \left(0, \tau_{xx}, \tau_{xy}, \tau_{xz}, u\tau_{xx} + v\tau_{xy} + w\tau_{xz} + q_x \right)^T \\
\mathbf{G}^i &= \left(\rho v, \rho uv, \rho v^2 + p, \rho vw, v\left(\rho E + p\right) \right)^T & \mathbf{G}^v &= \tfrac{1}{\mathrm{Re}} \left(0, \tau_{xy}, \tau_{yy}, \tau_{yz}, u\tau_{xy} + v\tau_{yy} + w\tau_{yz} + q_y \right)^T \\
\mathbf{H}^i &= \left(\rho w, \rho uw, \rho vw, \rho w^2 + p, w\left(\rho E + p\right) \right)^T & \mathbf{H}^v &= \tfrac{1}{\mathrm{Re}} \left(0, \tau_{xz}, \tau_{yz}, \tau_{zz}, u\tau_{xz} + v\tau_{yz} + w\tau_{zz} + q_z \right)^T
\end{aligned}$$

The term $\mathbf{S}$ represents source terms and is often used as part of the hover formulation of HMB3 [128]. For this work, all source terms are set to zero.

2.1.2 Numerical Methods

HMB3 solves the Navier-Stokes equations in integral form using the Arbitrary Lagrangian Eulerian (ALE) formulation, first proposed by Hirt [66], for time-dependent domains, which may include moving boundaries. The Navier-Stokes equations are discretised using a cell-centred finite volume approach on a multi-block grid. The spatial discretisation of these equations leads to a set of ordinary differential equations in time,

$$\frac{d}{dt}(\mathbf{W}_{i,j,k}V_{i,j,k}) = -\mathbf{R}_{i,j,k}(\mathbf{w}) \tag{2.11}$$

where i, j, k represent the cell index, $\mathbf{W}$ and $\mathbf{R}$ are the vector of conservative variables and flux residual respectively and $V_{i,j,k}$ is the volume of the cell i, j, k. The upwind scheme of Osher and Chakravarthy [102] is used to discretise the convective terms in space, whereas viscous terms are discretised using a second order central differencing spatial discretisation. The Monotone Upstream-centred Schemes for Conservation Laws (MUSCL) by Leer [138] is used to provide third order accuracy in space. The HMB3 solver uses the alternative form of the van Albada limiter [137] in regions where large gradients are encountered mainly due to shock waves, avoiding non-physical spurious oscillations. An implicit dual-time stepping method is employed to performed the temporal integration, where the solution is marching in pseudo-time iterations to achieve fast convergence, which is solved using first-order backward differences.

The linearised system of equations is solved using the Generalised Conjugate Gradient method with a Block Incomplete Lower-Upper (BILU) factorisation as a pre-conditioner [12]. Because implicit schemes require small Courant-Friedrichs-Lewy (CFL) value during early iterations, some explicit iteration using the forward Euler method or the four stage Runge-Kutta method (RK4) by Jameson [73] should be computed to smooth out the initial flow. Multi-block structured meshes are used with HMB3, which allow an easy sharing of the calculation load for parallel job using the Message Passing Interface MPI tool for communication.

2.1.3 Turbulence Modelling

The Navier-Stokes equations allow for the capturing of all the turbulent scales, however at high Reynolds numbers[‡], the successful resolution of all temporal and spatial scales requires a significantly large computational cost. As a result, the Navier-Stokes equations are time-averaged in order to reduce the number of unknown turbulence scales. This lead to the Reynolds-Averaged Navier-Stokes equations (RANS). This is a statistical formulation which model all turbulence scales, with the mean flow quantities predicted at a modest computational cost. However, by construction, the RANS formulation cannot provide the unsteady data that is required for some applications, i.e., the capturing of the detached flow associated with stall flutter prediction.

[‡]When $Re > 10^5$ resulting in a fully turbulent wake [106]

A higher fidelity method known as Large-Eddy Simulation (LES) is based on resolving scales larger than the grid cells while modelling the smaller ones with a sub-grid model. This ensures that the majority of the turbulent kinetic energy k is resolved, with most of the dissipation ε modelled. This approach bears less modelling uncertainties and gives unsteady data by its constitutive nature, yielding to more accurate results than RANS in the case of complex phenomena like flow separation, re-attachment or vortex shedding. However, LES is computationally expensive because it requires a very fine grid and time-step. Coupling of LES with time-dependent RANS (URANS) models become therefore the main strategy to make LES affordable for a wide range of industrial applications.

Several turbulence models, of both URANS and hybrid LES/URANS families, are available in the HMB3 solver. The idea and the equations behind the models used in this work are described below.

2.1.4 $k-\omega$ and Shear Stress Transport (SST) Model

In 1988, Wilcox [143] developed the popular $k-\omega$ turbulence model to close the RANS equations with two transport equations for k and ω, where k is the local turbulent kinetic energy and ω the specific dissipation rate of the turbulent kinetic energy. Turbulence transport equations used in the formulation of the $k-\omega$ models are given by:

$$\begin{aligned}
\frac{\partial}{\partial t}(\rho k)+\frac{\partial}{\partial x_j}(\rho U_j k) &= \frac{\partial}{\partial x_j}\left[\left(\mu+\frac{\mu_t}{\sigma_k}\right)\frac{\partial k}{\partial x_j}\right]+\rho\left(P_k-\beta^*_{k\omega}\omega k\right) \\
\frac{\partial}{\partial t}(\rho \omega)+\frac{\partial}{\partial x_j}(\rho U_j \omega) &= \frac{\partial}{\partial x_j}\left[\left(\mu+\frac{\mu_t}{\sigma_\omega}\right)\frac{\partial \omega}{\partial x_j}\right]+\rho\left(\frac{\alpha_{k\omega}}{\upsilon_t}P_\omega-\frac{\beta_{k\omega}}{\beta^*_{k\omega}\omega^2}\right)+\rho S_l
\end{aligned} \tag{2.12}$$

Since the introduction of the $k-\omega$ model by Wilcox, the other notable modification to the model came from Menter in 1994 [95] who proposed the hybridisation of the $k-\omega$ and $k-\varepsilon$, where ε represents the specific dissipation rate of turbulence. This was termed the $k-\omega$ - Shear Stress Transport (SST) two-equation model. In the transport equation for k and ω, the production of turbulence, P_k, and the dissipation rate specific to k, P_ω, is defined by:

$$\begin{aligned}
P_k &= \tau_{ij}\frac{\partial u_i}{\partial x_j} \\
P_\omega &= \rho\frac{\alpha_{k\omega}}{\upsilon_t}P_k
\end{aligned} \tag{2.13}$$

The values of the coefficients used for both the standard $k-\omega$ model, along with the $k-\omega$ SST variant, are presented below in Table 2.1.

Menter's models [95] are constructed as a 'blend' of the $k-\omega$ and $k-\varepsilon$ models, hence the values for the coefficients $\alpha_{k\omega}$, $\beta_{k\omega}$, σ_k and σ_ω are blended as such that:

Table 2.1: Values of constants used in $k-\omega$ turbulence models.

Wilcox [143]					
$\beta^*_{k\omega}$	$\alpha_{k\omega}$	$\beta_{k\omega}$	σ_k	σ_ω	S_l
$\frac{9}{100}$	$\frac{5}{9}$	$\frac{3}{40}$	2	2	0
Wilcox [144]					
$\beta^*_{k\omega}$	$\alpha_{k\omega}$	$\beta_{k\omega}$	σ_k	σ_ω	S_l
$\frac{9}{100}\left(\frac{\frac{5}{18}+\frac{R_\omega}{8}^4}{1+\frac{R_\omega}{8}^4}\right)$	$\frac{5}{9}\left(\frac{\frac{1}{10}+\frac{R_\omega}{2.7}}{1+\frac{R_\omega}{2.7}}\right)$	$\frac{3}{40}$	2	2	0
Menter (*BSL) [95]*					
$\beta^*_{k\omega}$	$\alpha_{k\omega}$	$\beta_{k\omega}$	σ_k	σ_ω	S_l
$\frac{9}{100}$	$B\begin{pmatrix}0.553\\0.440\end{pmatrix}$	$B\begin{pmatrix}0.075\\0.083\end{pmatrix}$	$\frac{1}{B\begin{pmatrix}0.5\\1.0\end{pmatrix}}$	$\frac{1}{B\begin{pmatrix}0.5\\0.856\end{pmatrix}}$	$B\begin{pmatrix}0\\\frac{1.71}{\omega}\nabla k.\nabla\omega\end{pmatrix}$
Menter (*SST) [95]*					
$\beta^*_{k\omega}$	$\alpha_{k\omega}$	$\beta_{k\omega}$	σ_k	σ_ω	S_l
$\frac{9}{100}$	$B\begin{pmatrix}0.553\\0.440\end{pmatrix}$	$B\begin{pmatrix}0.075\\0.083\end{pmatrix}$	$\frac{1}{B\begin{pmatrix}0.85\\1.0\end{pmatrix}}$	$\frac{1}{B\begin{pmatrix}0.5\\0.856\end{pmatrix}}$	$B\begin{pmatrix}0\\\frac{1.71}{\omega}\nabla k.\nabla\omega\end{pmatrix}$

$$B\begin{pmatrix}a\\b\end{pmatrix} = F_1 a + (1-F_1)b, \tag{2.14}$$

where the blending function, F_1 is defined as:

$$F_1 = \tanh(arg_1^4), \tag{2.15}$$

with the blending argument expressed as:

$$arg_1 = \min\left[\max\left(\frac{k^{0.5}}{\beta^*_{k\omega}\omega y}, \frac{500\upsilon}{y_n^2\omega}\right), \frac{2k\omega}{y_n^2\max(\nabla k.\nabla\omega, 0.0)}\right]. \tag{2.16}$$

2.1.5 Hybrid LES/URANS Methods

As previously described, the use of LES models can significantly increase the computational accuracy, when compared to RANS, however this is at the expense of computational cost. Due to the similarity of the structure of the governing and turbulence equations for LES and RANS, it is natural to assume that a hybrid version of these techniques may be beneficial in ensuring computational accuracy without an increase in cost. A variety of hybrid methods have been developed which couple LES/URANS using different strategies:

A: A pure LES model is used in some regions of the domain, with RANS used in the remain-

ing - *Segregated/interfacing models*;

B: the two models can be added together in a weighed manner via local mixing coefficients - *Blending models*;

C: the selected model can be altered to include the behavior of the other, usually a RANS model is adapted to LES capability - *Second generation URANS models*.

2.1.6 Scale Adaptive Simulation (SAS)

The Scale Adaptive Simulation (SAS) is an improved URANS approach able to generate spectral content in unsteady flows thanks to its ability to operate as a scale-resolving mode [97]. Under specific conditions, the model naturally balances the contribution of modelled and resolved part of the turbulent stress tensor by adjusting the turbulent length scale to local flow inhomogeneities. SAS models comply with the following characteristics:

- a second mechanical scale, dependent on the second (or higher) velocity derivatives, is introduced in the selected RANS model;
- the model must provide a RANS solution in stationary flows while allowing the break-up of the large unsteady structures like LES in flow regions with transient instabilities - this without explicit dependency of the model on grid size or time step;
- damping of resolved turbulence must be introduced at high wave numbers depending on the grid resolution limit.

Menter and Egorov derived the first "scale-adaptive" model, named as K-Square-root K L (KSKL) where k is the turbulent kinetic energy and L is an integral length scale [97], by introducing the second derivative of the velocity field, and consequently the von K*á*rm*á*n length scale, κ in Rotta's KL model [116]. The motivation of this modelling choice originates from the analysis of the third derivative term of the exact transport equation of the quantity kL, L_R being a turbulent integral length scale, derived by Rotta. In this way, the model reduces the eddy viscosity according to the locally resolved vortex size represented by κ in unsteady flow regions, by resolving the turbulent spectrum up to the grid limit and avoiding single-mode vortex structure typical of RANS. The KSKL model was then transformed by the authors to other variables, thus to include its scale-adaptive capability in existing two-equations turbulence models.

The turbulent transport equations of the SAS model [96] differ from those of the SST model only by the introduction of an additional source term, Q_{SAS}, for the specific dissipation rate, ω, of the form:

$$Q_{SAS} = \max\left[\rho\xi_2\kappa\mathbb{S}^2\left(\frac{\ell}{\ell_{vk}}\right)^2 - C_{SAS}\frac{2\rho k}{\sigma_\phi}\max\left(\frac{1}{k^2}\frac{\partial k}{\partial x_j}\frac{\partial k}{\partial x_j}, \frac{1}{\omega^2}\frac{\partial \omega}{\partial x_j}\frac{\partial \omega}{\partial x_j}\right), 0\right], \qquad (2.17)$$

where ℓ is the length scale of the modelled turbulence:

$$\ell = \frac{\sqrt{k}}{\sqrt[4]{\beta_{k\omega}^{8}\omega}}, \tag{2.18}$$

and ℓ_{vk} is the von K*á*rm*á*n length scale derived from a 3D generalisation of the basic boundary layer definition, lowerly bounded to provide adequate damping for high wave numbers:

$$\ell_{vk} = \max\left(\frac{\kappa\mathbb{S}}{\mid \nabla^2\mathbf{u} \mid}, C_s\sqrt{\frac{\kappa\xi_2}{\frac{\beta_{k\omega}}{\beta_{k\omega}^{*}} - \gamma}}\sqrt[3]{\Omega_{CV}}\right), \tag{2.19}$$

Here, $\mid \nabla^2\mathbf{u} \mid = \sqrt{(\nabla^2 u)^2 + (\nabla^2 v)^2 (\nabla^2 w)^2}$ is the magnitude of the velocity Laplacian, C_s is the Smagorinsky coefficient properly tuned on the adopted discretisation scheme, and Ω_{CV} is the control volume size. $\mathbb{S}$ is a scalar invariant of the strain rate tensor, S_{ij}:

$$\mathbb{S} = \sqrt{2S_{ij}S_{ij}}, \tag{2.20}$$

which in this model is also used to compute the turbulent production term as:

$$P_k = \mu_t\mathbb{S}^2. \tag{2.21}$$

Finally, the constant coefficients of the model are shown below in Table 2.2

Table 2.2: Values of constants used in SAS model.

ξ_2	3.51
C_{SAS}	2
σ_ϕ	$\frac{2}{3}$

2.1.7 Mesh Generation Techniques

Despite the geometric complexity of the 3D test cases , block-structured hexagonal meshes were chosen to ensure an orthogonal and flow-aligned mesh, thus to keep the numerical errors to a minimum. This choice benefits from the higher efficiency and lower memory requirements of a structured code.

As prevously stated, the focus on this investigation is on propeller aeroelasticity and therefore, there is a need for blade deformation and relative motion. In order to achieve this, the chimera grid method was employed. The chimera method is based on composite grids, consisting of independently generated, overlapping non-matching sub-domains. Each of these subdomains are referred to as Levels and are sorted hierarchically, with higher levels having priority.

The exchange of information between sub-domains is achieved through interpolation and by following a hierarchy of mesh levels [74]. This allows for a mesh level to be defined around the propeller blade, thus applying the pure aeroelastic deformation to the blade level, before adjusting the entire domain, propeller blade foreground and background, in terms of the required relative motion.

2.2 Computational Structural Dynamics

The aeroelastic framework of HMB3 is based on the modal method [13]. This method uses externally computed structural modes and a mesh deformation module based on the inverse distance weighting interpolation. This is a weak/loosely coupled method and it was selected in order to reduce computational cost as it expresses solid deformations as functions of the structure's eigenmodes.

A NASTRAN finite element model is created in order to obtain the structural mode shapes and frequencies. The finite element model uses non-linear PBEAM elements to model the structure's mass and inertia distribution along the span, with rigid bars (RBAR) elements used to connect the PBEAM node to each of the fluid mesh points at the given section. The rigid bars were used to ensure the aerofoil shapes were preserved and the interpolation between the CFD and CSD grids can be conducted accurately. The single node of the PBEAM element would not be enough on it's own to transfer the modal displacement across the full span/chordwise length of the blade.

The blade mode shapes and frequencies were computed using the non-linear static analysis (SOL 106). This solves for the static displacement to provided loads along with a modal analysis under the influence of a centrifugal force. Both the centrifugal and static loads were provided, with the static loads determined from rigid CFD calculations prior to any full aeroelastic simulation.

At the beginning of each computation, the structural modes are interpolated from the CSD-NASTRAN grid to the CFD mesh. The interpolation is performed with the Moving Least Square method (MLS), where the interpolation weights are stored for each solid. This method is accurate as loads integrations and displacement computations are carried out on the CFD mesh without interpolation. In addition to this, the relative deflection of a given solid in contact to another must be computed to ensure any deflection is transferred correctly.

2.2.1 Computation of Modal Loads and Amplitudes

The CFD computation is performed on the deformed mesh to obtain the solution at $t + \Delta t$. The pressure is then summed over the undeformed mesh points to compute the modal loads $f_m^s(t)$ on the solid (s) for the m-th mode at time t:

$$f_m^s(t) = \sum_{p=1}^{n_s} \mathbf{p}(p,t).\phi_m^s(p) \tag{2.22}$$

with n_s the number of CFD points on the solid s, $\mathbf{p}(p,t)$ the pressure at a point p in N/m^2, and $\phi_m^s(p)$ the mode displacement at the point p for the m-th mode of the solid, s. This process is highlighted in Figure 2.1, with the final modal load value having units of $N/m.kg$.

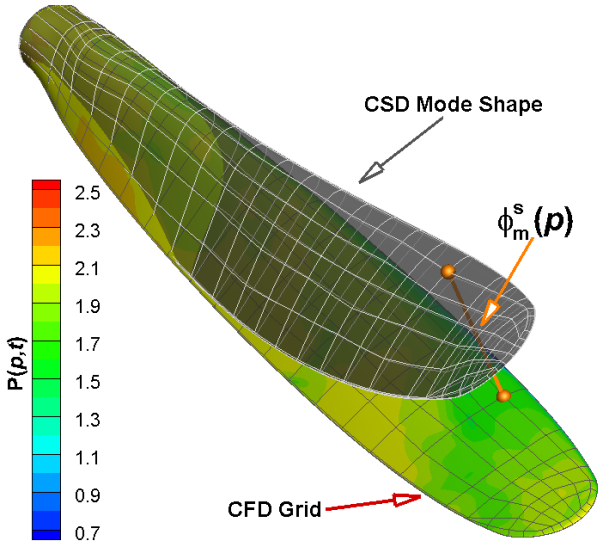

Figure 2.1: Illustration of the modal force computation

During the modal shape and frequency calculation from NASTRAN, mass scaling is applied with a generalised mass (m_j) of 1 kg. This generalised mass is defined as:

$$m_m = {\eta_m}^T [\mathbf{M}] \eta_m, \tag{2.23}$$

where η is the eigenvector/mode shape of the $m-th$ mode and $\mathbf{M}$ is the mass matrix [99].

The shape of the solid (s), $\phi^s(t)$, is described as a sum of eigenvectors ϕ_m^s :

$$\phi^s(t) = \phi_0^s + \sum_{m=1}^{n_m^s} \alpha_m^s(t)\phi_m^s \tag{2.24}$$

with n_m^s the number of modes on the solid s, and ϕ_0^s the undeformed shape. The problem is then reduced to solving for the coefficient α_m^s.

In the modal approach, the coefficient can be obtained by solving the following differential equation:

$$\frac{\partial^2 \alpha_m^s}{\partial t^2} + 2\zeta_m \omega_m \frac{\partial \alpha_m^s}{\partial t} + \omega_m^2 \alpha_m^s = f_m^s(t) \tag{2.25}$$

For stability purposes, the analysis is initiated with a strong damping coefficient of $\zeta_m = 0.2$ across the initial 180^o of the first propeller revolution for each mode. This high structural

damping is used to control the oscillations created during the initial steps of the simulation, due to the sudden change in the forces applied to a second order system. Once the solid reaches an acceptable level of deformation, the damping is then gradually brought to its final value of $\zeta_m = 0.01$, with the starting and final value taken based upon previous studies (see Section 1.6).

Equation 2.25 is explicitly solved using the leap-frog method [19, 108], which is presented below. To ensure stability of higher modal frequencies, each time-step is solved in N inner time-steps of size $\Delta t_i = \Delta t/N$ (where i is the counter to N). The modal force at the time $t_i = t + i\Delta t_i$ is :

$$f_m^s(t_i) = f_m^s(t) + \frac{i(f_m^s(t+\Delta t) - f_m^s(t))}{N} \tag{2.26}$$

The m-th amplitude α_m^s is then assessed for inner time-step t_{i+1} :

$$[\alpha_m^s]_{t_{i+1}} = [\alpha_m^s]_{t_i} + \left[\frac{\partial \alpha_m^s}{\partial t_i}\right]_{t_i} \Delta t_i + \frac{1}{2}\left[\frac{\partial^2 \alpha_m^s}{\partial t_i^2}\right]_{t_i} \Delta t_i^2 \tag{2.27}$$

The time derivative of the amplitudes are then computed as:

$$\begin{aligned} \left[\frac{\partial^2 \alpha_m^s}{\partial t_i^2}\right]_{t_{i+1}} &= [f_m^s]_{t_i} - \omega_m^2 [\alpha_m^s]_{t_i} - 2\zeta\omega_m \left[\frac{\partial \alpha_m^s}{\partial t_i}\right]_{t_i} \\ \left[\frac{\partial \alpha_m^s}{\partial t_i}\right]_{t_{i+1}} &= \left[\frac{\partial \alpha_m^s}{\partial t_i}\right]_{t_i} + \frac{1}{2}\left(\left[\frac{\partial^2 \alpha_m^s}{\partial t_i^2}\right]_{t_i} + \left[\frac{\partial^2 \alpha_m^s}{\partial t_i^2}\right]_{t_{i+1}}\right)\Delta t_i \end{aligned} \tag{2.28}$$

A flow chart showing the different stages of the method is shown in Figure 2.2, for a fixed mode shape.

2.2.2 Grid Deformation Procedure

There is a need for flexibility within the aeroelastic process to ensure a wide range of test cases can be computed. This can range from a simple single-blade deformation to the more complex fully installed 8-bladed propeller with a wing and nacelle. With the complex case, the effect of the wing and nacelle deformation must be taken into account in the positioning of the propeller. For example, if the nacelle/spinner was to pitch up 10^o due to the wing deformation, the propeller centre of rotation will no longer be in its rigid position, hence the rotations and translations must be transferred. In order to achieve this, the grid deformation is split into three stages. Firstly, each individual solid surface is deformed based upon the calculated modal amplitudes. This allows for the rotation and translation matrix to be computed. Following this, the shared points between any linked bodies are computed with the parent and child sections defined (see Figure 2.3). The deformation due to the parent component is then applied to the child. The effect of the full surface deformation is then implemented in the volume mesh via an inverse distance weighting technique. The individual surface and volume mesh procedures are explained in

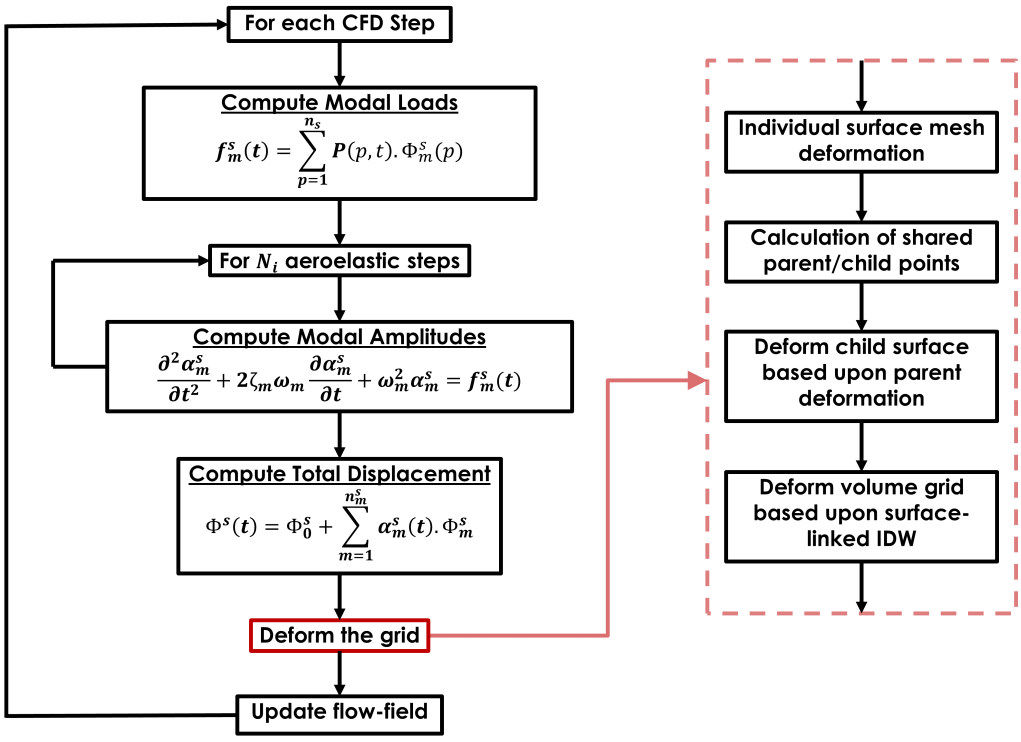

Figure 2.2: Illustration of the computational structural dynamics strategy during each CFD time-step, for a fixed mode shape

Sections 2.2.3 and 2.2.4, respectively.

2.2.3 Surface Mesh Deformation

The displacement of the surface of each solid is computed using equation 2.24. The surface mesh is deformed then for each solid body, where the displacement due to the body is computed as:

$$\phi^p = \mathbf{RP} + \mathbf{t} \tag{2.29}$$

with **R** and **t**, respectively, being the mean rotation matrix and the translation vector of the shared points between the parent solid and its child, and $\mathbf{P} = [x, y, z]$ the position of the points of body, s.

The translation vector is the mean displacement of the n_{sp} shared points between the parent body and its child:

$$\mathbf{t} = \frac{1}{n_{sp}} \sum_{p=1}^{n_{sp}} \phi^b(p) \tag{2.30}$$

with $\phi^b(p)$ the displacement of the point p imposed by the parent body. The centroids of

the shared points are computed at the original position (A), and at the secondary position (B) imposed by the parent body:

$$\begin{aligned} \mathbf{C}_A &= \frac{1}{n_{sp}} \sum_{p=1}^{n_{sp}} \mathbf{P}(p) \\ \mathbf{C}_B &= \frac{1}{n_{sp}} \sum_{p=1}^{n_{sp}} (\mathbf{P}(p) + \phi^b(p)) \end{aligned} \tag{2.31}$$

The optimal solid rotation to go from position A to position B is computed with the Singular Value Decomposition technique (SVD). This method is fast and easy to implement [2]. The centres of both A and B are sent to the origin. Then, a covariance matrix $\mathbf{H}$ is computed:

$$\mathbf{H} = \sum_{p=1}^{n_{sp}} (\mathbf{P}(p) - \mathbf{C}_A)(\mathbf{P}(p) + \phi^b(p) - \mathbf{C}_B)^T \tag{2.32}$$

The singular value decomposition of the matrix is computed as:

$$[\mathbf{U}, \mathbf{S}, \mathbf{V}] = SVD(\mathbf{H}) \tag{2.33}$$

Using this result, the rotation matrix is then given by:

$$\mathbf{R} = \mathbf{V}\mathbf{U}^T \tag{2.34}$$

Finally, the computed displacement with equation 2.29 and the displacement due to the structural modes are applied to the body. This full procedure is highlighted in Figure 2.3.

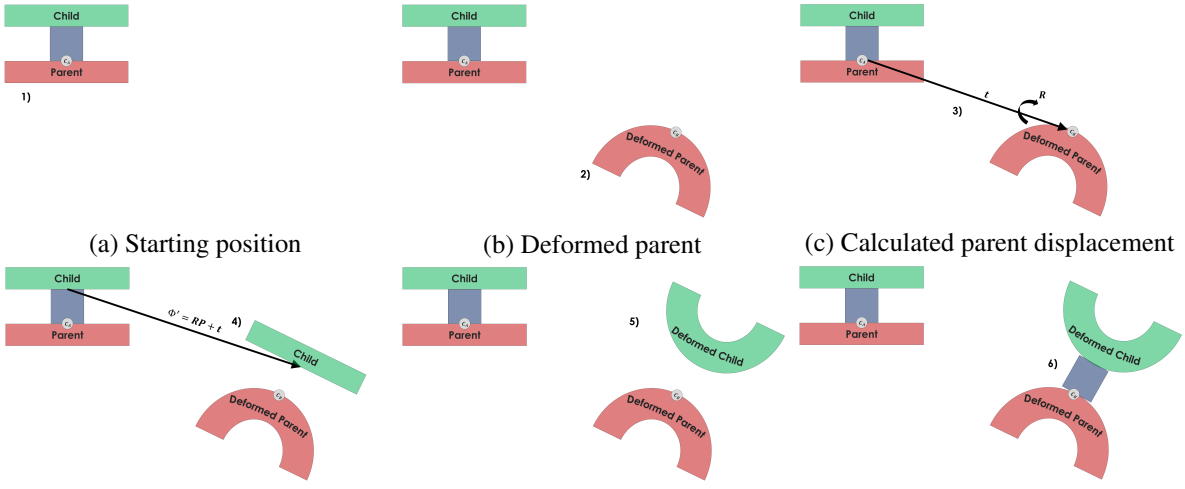

(a) Starting position

(b) Deformed parent

(c) Calculated parent displacement

(d) Re-position child based upon parent displacement

(e) Deformed child

(f) Interpolated patch

Figure 2.3: Surface deformation procedure for linked components

2.2.4 Deformation of the Volume Mesh

To adapt the volume mesh to the surface of the deformed solid, a mesh deformation algorithm has been implemented in HMB3 based on Inverse Distance Weighting (IDW) [122]. IDW interpolates the values at given points with a weighted average of the values available at a set of known points. The weight assigned to the value at a known point is proportional to the inverse of the distance between the known and the given point. Biava *et al.* [20] used this method to optimise rotor blade shapes in HMB3, and obtained good quality mesh after mesh deformations.

Given N samples $\mathbf{u}_i = u(\mathbf{x}_i)$ for $i = 1,2,...,N$, the interpolated value of the function $\mathbf{u}$ at a point $\mathbf{x}$ using IDW is given by:

$$\mathbf{u}(\mathbf{x}) = \begin{cases} \dfrac{\sum_{i=1}^{N} w_i(\mathbf{x})\mathbf{u_i}}{\sum_{i=1}^{N} w_i(\mathbf{x})}, & \text{if } d(\mathbf{x},\mathbf{x_i}) \neq \mathbf{0} \text{ for all } \mathbf{i} \\ \mathbf{u_i}, & \text{if } d(\mathbf{x},\mathbf{x_i}) = \mathbf{0} \text{ for some } \mathbf{i} \end{cases} \tag{2.35}$$

where

$$w_i(\mathbf{x}) = \frac{\mathbf{1}}{\mathbf{d}(\mathbf{x},\mathbf{x_i})^{\mathbf{p}}} \tag{2.36}$$

In the above equations, p is any positive real number (called the *power parameter*) and $d((\mathbf{x}),(\mathbf{y}))$ is the Euclidean distance between $(\mathbf{x})$ and $(\mathbf{y})$.

The method in its original form becomes expensive as sample data sets get larger. An alternative formulation of the Shepard's method, which is better suited for large-scale problems, has been proposed by Renka [112] where the interpolated value is calculated using only the k nearest neighbours within an R-sphere shown in green in Figure 2.4. The weights are slightly modified in this case:

$$w_i(\mathbf{x}) = \left(\frac{\max(\mathbf{0}, \mathbf{R} - \mathbf{d}(\mathbf{x},\mathbf{x_i}))}{\mathbf{R}\mathbf{d}(\mathbf{x},\mathbf{x_i})} \right)^{\mathbf{2}}, \quad \mathbf{i} = \mathbf{1},\mathbf{2},...,\mathbf{k}. \tag{2.37}$$

If this interpolation formula is combined with a fast spatial search structure for finding the k nearest points, it yields an efficient interpolation method suitable for large-scale problems [122]. The power parameter (p), number of nearest neighbours (k) and sphere radius (R) are supplied and fixed variables, with these values being problem specific.

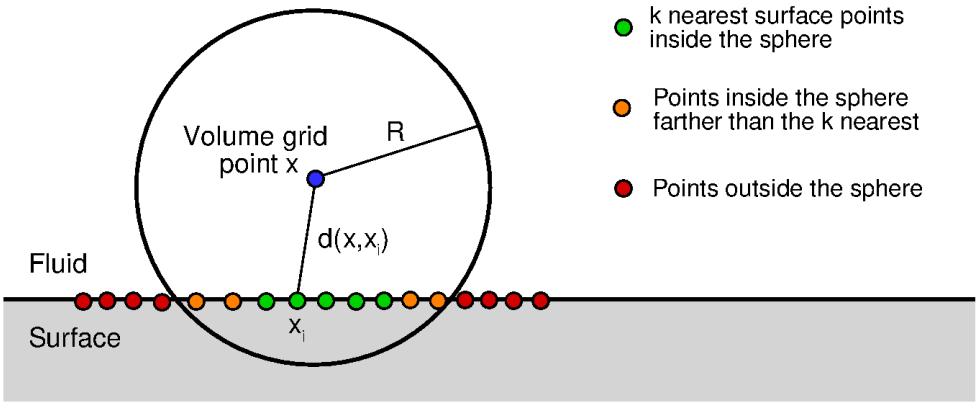

Figure 2.4: Illustration of the point selection process in order to compute the IDW weights.

The modified IDW interpolation formula is used in HMB3 to implement mesh deformation in an efficient and robust way. The known displacements of points belonging to solid surfaces represent the sample data, while the displacements at all other points of the volume grid are computed using Equation 2.35 with the weights of Equation 2.37. For fast spatial search of the sample points, an Alternating Digital Tree (ADT) data structure [25] is used. A blending function is also applied to the interpolated displacements, so that they smoothly tend to zero as the distance from the deforming surface approaches R.

2.2.5 Interpolated Modal Response

An adjustment in flow conditions results in a change in modal response from the structure. To this end, in order to improve the accuracy of the modal method, an interpolation functionality is included in the structural method. This function will ensure the correct modal frequencies and mode shapes are selected at a given time-step with the intermediate reponse selected as blend of the two stages. The interpolation is calculated based upon inverse distance weighting to calculate a scaling factor which is multiplied by the modal amplitude. An example of the interpolation scaling factor is presented in Figure 2.5 for a single mode computation across two conditions. This method is utilised for the changing of the blade rotational velocity, where the stiffening effect due to the centrifugal force adjust the mode shapes and frequencies.

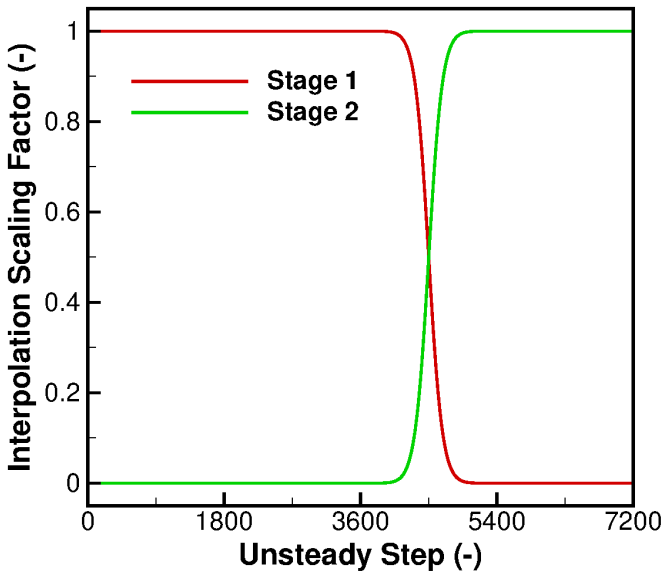

Figure 2.5: Interpolation scaling factor schedule for a single mode computation across two conditions

2.2.6 Grid Quality Assessment

In order to ensure the quality of the grid is preserved throughout the aeroelastic deformation, two key factors are assessed. This includes the cell volume and cell skewness, and by preserving both of these factors this ensures the continued convergence of the simulation. The cell skewness is calculated based upon the dot product of the face normals, with the maximum value presented per cell. An example of the change in cell volume and skewness between an elastic and rigid simulation is presented in Figure 2.6. A slice is taken at the blade tip section with the focus remaining on the deforming foreground grid. The values of the cell volume and skewness are also presented with respect to the maximum value in the rigid slice, hence a relative scale is shown.

Focusing on the cell volume (Figures 2.6(a) & (b)), very similar profiles are observed with larger cells ahead and behind the blade. In terms of average and maximum cell values, only a slight change is observed in terms of the maximum cell volume for the elastic blade. This maximum is found ahead of the blade and therefore will have a minimal effect on the solution. More critically however, there is almost no change in volume within the boundary layer section of the blade.

The relative skewness ratio is presented in Figures 2.6(c) and (d) for the rigid and elastic simulations, respectively. Although similar profiles are observed, a lower value of skewness is seen downstream of the upper surface trailing edge. This leads to a slight reduction in the average value. A slight increase in skewness is observed at the section leading edge indicating a

smoothing effect due to the deformation.

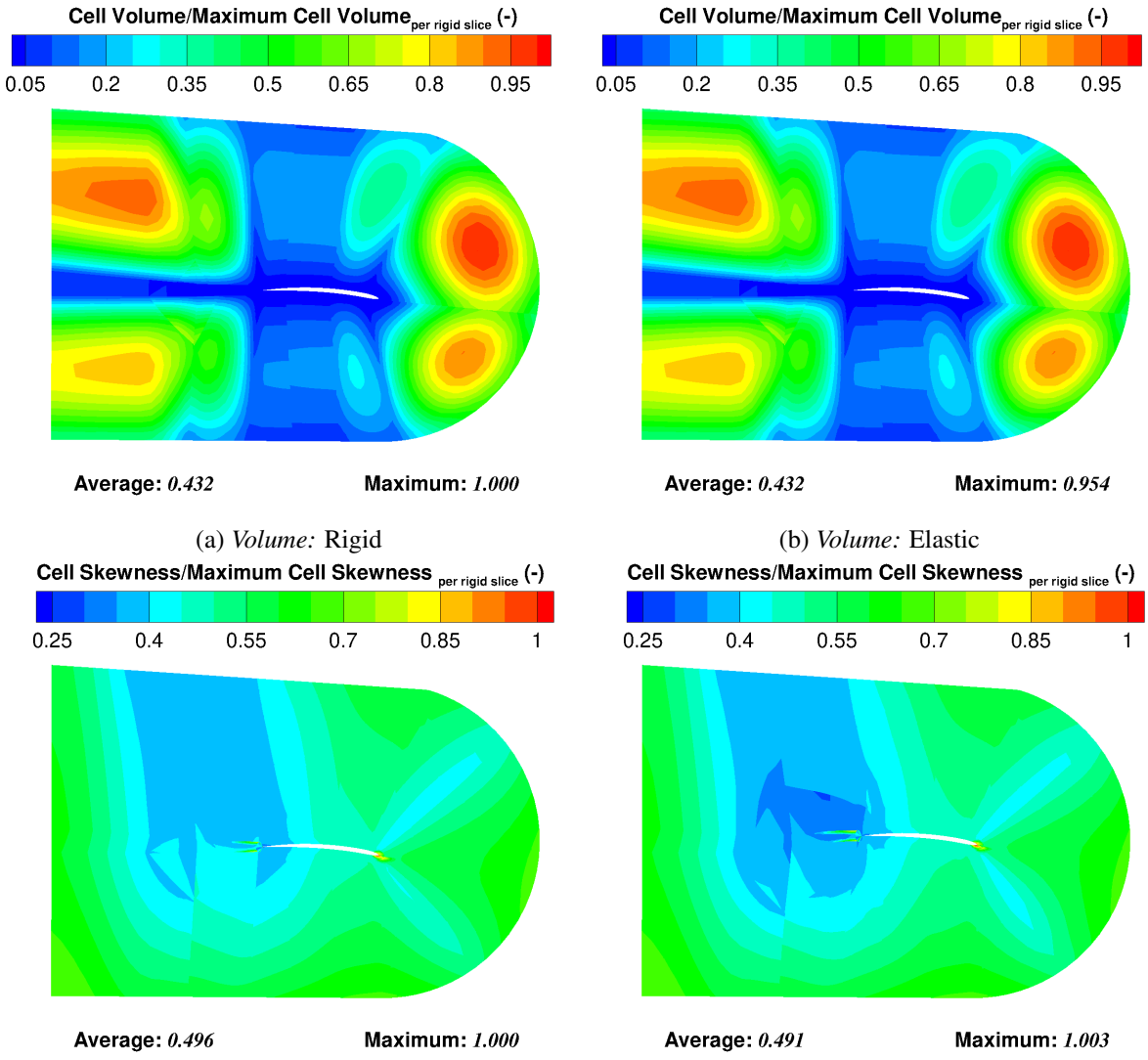

(a) *Volume:* Rigid

(b) *Volume:* Elastic

(c) *Skewness:* Rigid

(d) *Skewness:* Elastic

Figure 2.6: Example of the grid quality assessment for the aeroelastic method, which focuses on the cell skewness and overall volume differences between a rigid and elastic simulation. Presented is an example of an isolated propeller blade at 70%R undergoing elastic deformation with very little differences is the qualifying criteria.

2.3 Summary

This chapter presented the computational method used in this investigation. A Navier-Stokes based computational solver is used as this allows for a combination of statistical and hybrid statistical/resolved aerodynamic models to be used. Under the presence of detached flow, the ability to resolve certain flow structures could become critical in the assessment of propeller stall flutter.

In terms of the structural solver, an interpolated modal method has been developed and is coupled in a loose/weak fashion to the aerodynamic solver. The modal method has been shown in the past to correlate well with experimental data (see Section 1.6), with the interpolated version allowing for the change in mode shape/frequency to be implemented in the calculation.

With this method development, a verification process is conducted on the aerodynamic and structural solvers in Chapter 3, before validating against a known stall flutter case in Chapter 4.

Chapter 3

Verification of the Aerodynamic and Structural Model

This chapter will validate and verify the application of the aerodynamic and structural models used within the study of propeller stall flutter. This chapter will first confirm the validation of propeller flow simulation using HMB3 on the JORP blade [15, 120] (Figure 3.1(a)) before transitioning from isolated to installed conditions using the IMPACTA propeller. Following this, the structural model will be verified via the simulation of the installed IMPACTA propeller [32, 60, 79] (Figure 3.1(b)). These propellers were selected based upon the availability of geometry, structural models and experimental data.

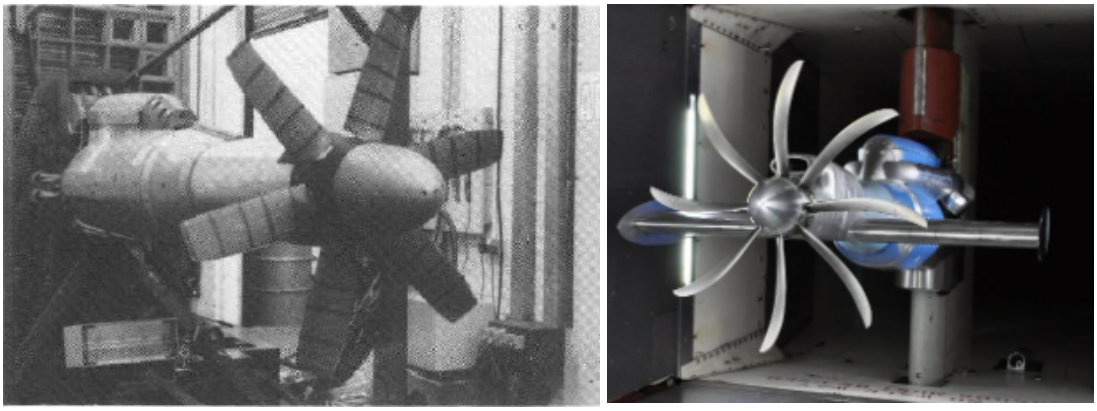

(a) JORP Propeller [120] (b) IMPACTA Propeller [60]

Figure 3.1: Propeller geometry used for the aerodynamic and aeroelastic verification process

3.1 Propeller Flow Validation

In 1994 [120], Scrase and Maina conducted an investigation into the aerodynamic and acoustic performance of the Joint Open Rotor Propeller (JORP). The aim of the investigation was to obtain a database of aerodynamic and acoustics results for a high speed blade design. Through

pressure taps, contours of surface pressure coefficient across the blade chord were captured and as such will be used to validate the aerodynamic performance of HMB3.

3.1.1 Computational setup

For this study, the rigid JORP propeller blade is simulated in isolation allowing the use of the hover formulation of HMB3. The hover formulation includes an additional source term in the Navier-Stokes equations to account for the inertial effects of the rotation [128]. This allows for a steady simulation to be conducted, reducing the computational cost associated with an unsteady simulation.

Grid generation

For this investigation, a matched multi-block topology of 482 blocks is derived (Figure 3.2). Solid boundary conditions are applied to the blade and hub with the hub geometry extended to the domain outflow. Periodic boundary conditions are applied to the vertical faces with the remaining boundaries defined as far-field. The vertical outflow and inflow far-field boundaries are selected to be 22 and 10 radial distances away from the blade, with the radial far-field boundary extended by 4 lengths. A total of 127 nodes are distributed across the blade radius with 152 nodes in the chordwise direction. These nodes are distributed via the hyperbolic expansion law. A solid wall distance of $1 \times 10^{-5}\ c_{ref}$ is defined to ensure a Y^{+} value of < 1.0. Based upon these parameters, a grid size of $7,982,088$ cells is derived.

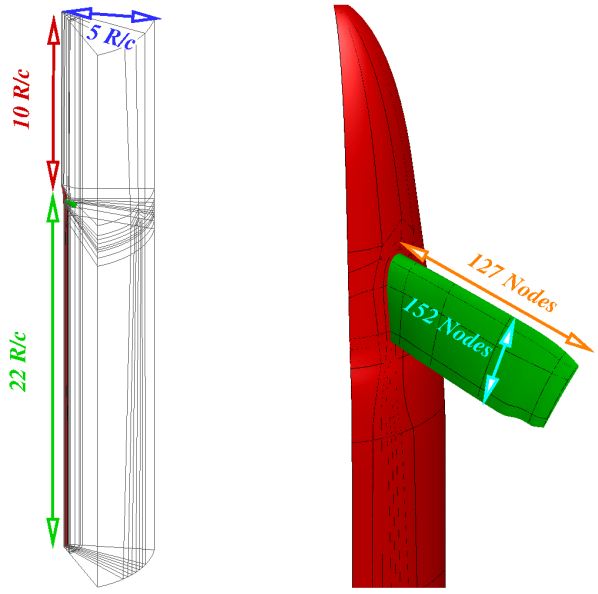

Figure 3.2: Isolated JORP propeller blade grid

Test Conditions

Presented in Table 3.1 are the simulated test conditions for the JORP propeller blade, with these conditions selected based upon the experimental data [120]. The blade is spun at a rotational speed of 3760 (rpm) with an axial freestream Mach number of 0.692. The reference length is taken as the root chord, with sea-level conditions.

Table 3.1: JORP propeller blade simulated test conditions

Tip Reynolds Number (-)	1.163×10^6
Tip Mach Number (-)	0.529
Freestream Mach Number (-)	0.692
Propeller Rotational Velocity (*rpm)*	3760
Advance Ratio (-)	4.12
Blade pitch $_{70\%R}$ ($^{\circ}$)	60.2
Reference Chord Length (*m)*	0.114
Blade Radius (*m)*	0.456

3.1.2 Aerodynamic results

Presented in Figure 3.3 are the aerodynamic results for the isolated JORP propeller. In Figure 3.3(a-e), a comparison between experiment and simulation is seen in terms of surface pressure coefficient from root to tip sections. Overall, good agreement in the pressure coefficient trends are found in terms of the suction peak and upper surface profile. Some discreprancies are found in the lower surface profile and stagnation pressures, however these remain within an acceptable range with suspicious variations in the experimental stagnation pressure trend across the blade radius. Figure 3.3(f) presents the flow-field visualisation using iso-surface of Q-criterion value 0.001 with the propeller wake captured well below the blade.

3.2 Verification of Semi-Span Wing Aerodynamics

Following on from the isolated propeller validation, verification of installed aerodynamics is required to ensure the capture of the propeller flow. To this end, the IMPACTA propeller [32, 60, 79] was installed on a high-lift semi-span wing and simulated in forward flight. No current experimental data is available for this test case and is therefore, only a verification simulation.

3.2.1 Computational setup

Due to the installation of the propeller, the full rotor is required with rigid body motions and the Unsteady Reynolds-Averaged Navier-Stokes (URANS) equations. This results in an increase in

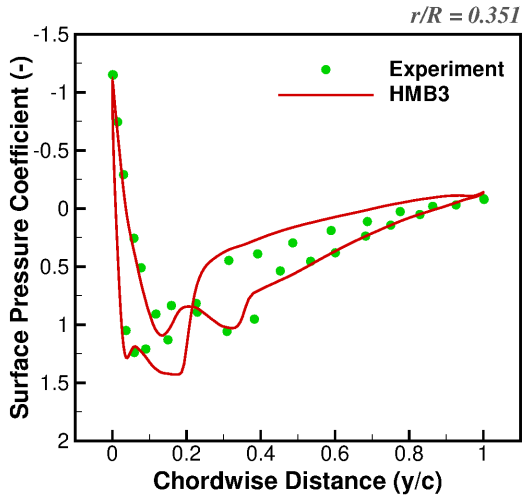

(a) C_p at 35.1%R

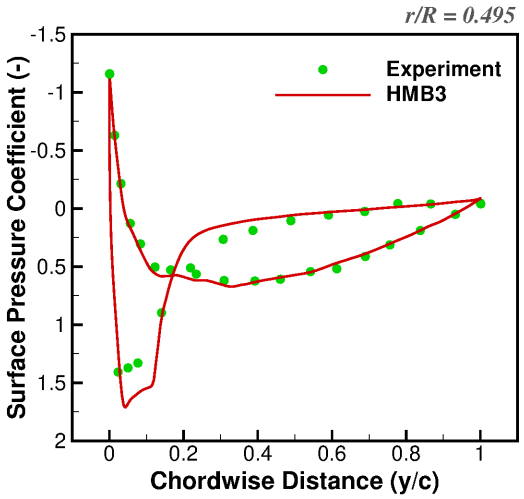

(b) C_p at 49.5%R

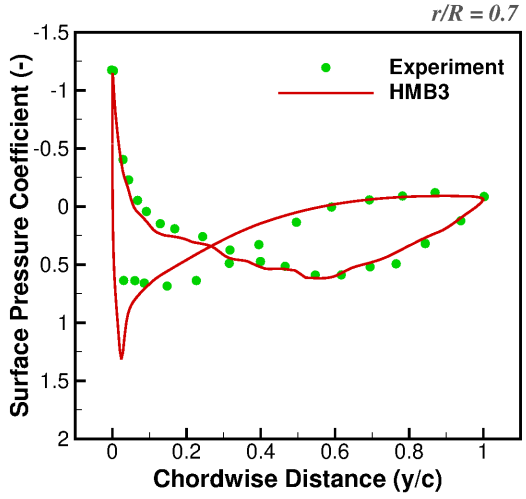

(c) C_p at 70%R

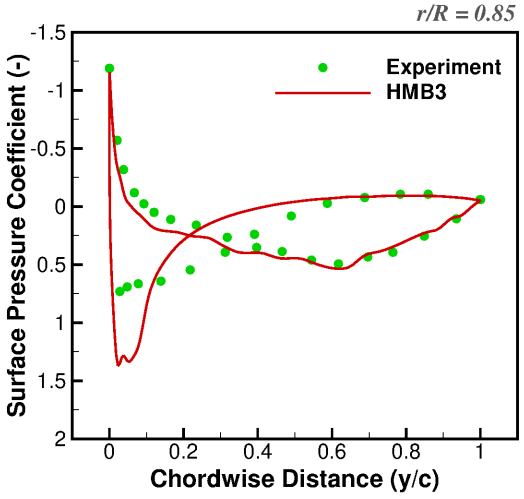

(d) C_p at 85%R

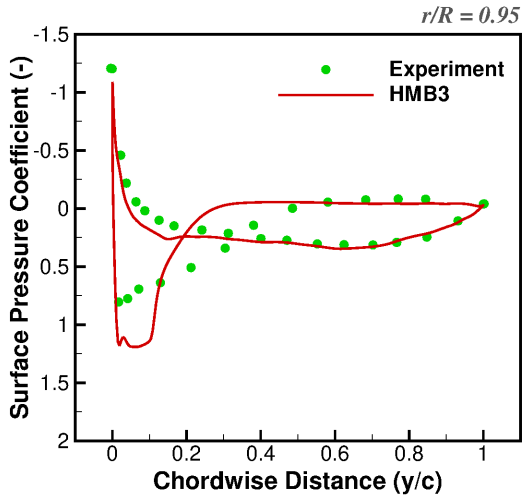

(e) C_p at 95%R

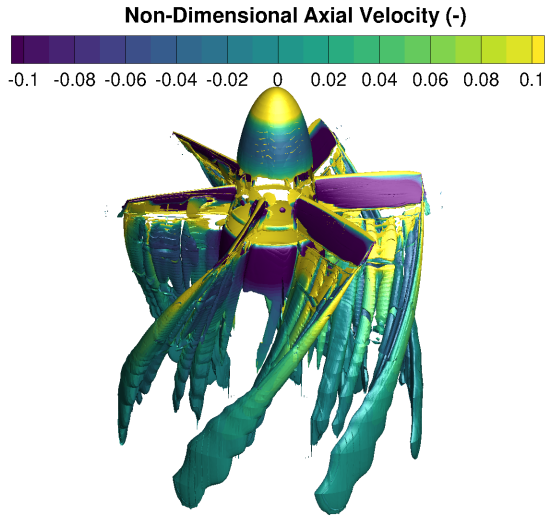

(f) Flow-field visualisation

Figure 3.3: Aerodynamic results for the isolated JORP propeller

computational cost with respect to the isolated propeller.

Grid generation

In order to simplify the rigid body motions of the propeller, the chimera grid method is used. This allows for the propeller blades to be placed within their own rotating sub-domain with subsequent interpolation into a background grid. This background grid contains the aircraft wing, including a nacelle and spinner, and extends to far-field boundary conditions. Symmetry boundary conditions are applied to the centre plane in order to simulate the semi-span configuration. Presented in Figure 3.4 is the derived chimera grid. As observed, individual foreground domains are defined for each blade with a C-grid topology used. The remaining solids are placed in the background with the far-field boundary conditions extending outwards of the wing by $50R$ in all directions. As per the isolated propeller simulation, a wall distance of $1 \times 10^{-5} c_{ref}$ is selected to ensure a Y^+ value of < 1.0. A grid size of $1,623,496$ cells is derived for each blade resulting in a total rotor grid of $12,987,968$ cells. To ensure sufficient interpolation between the foreground and background, a background grid of $32,123,264$ cells is created with the majority of cells clustered around/downstream of the propeller.

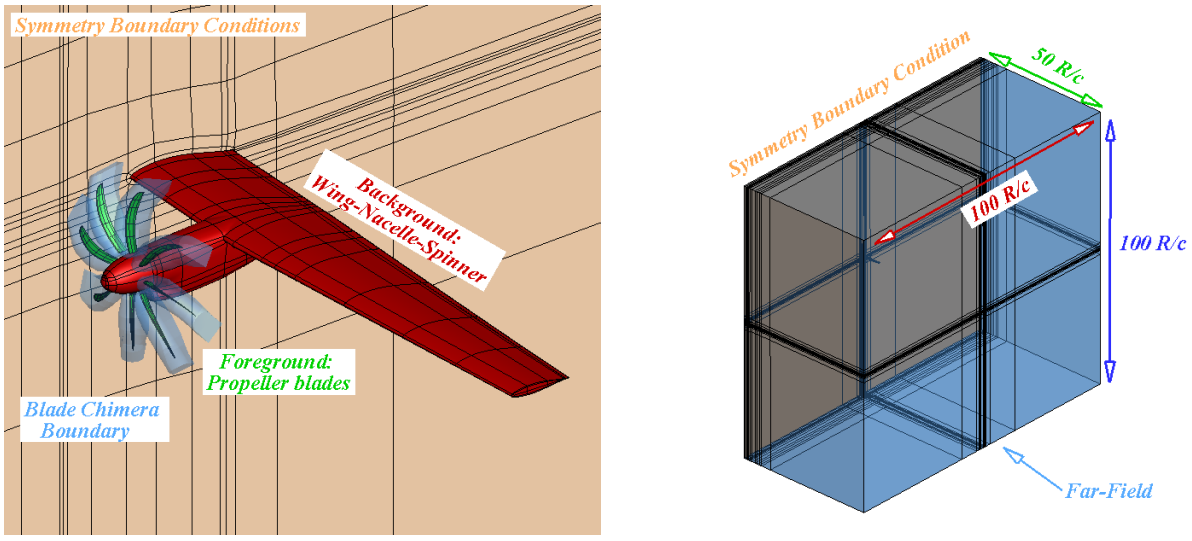

(a) Foreground chimera

(b) Background far-field

Figure 3.4: Chimera grid for the installed propeller verification

Test conditions

As previously discussed, the installed propeller was simulated in forward-flight with the test conditions for this simulation presented in Table 3.2. Some details such as the reference blade chord, pitch angle and rotational velocity are not shared due to confidentiality reasons, however reference non-dimensional values are given. The freestream Reynolds and Mach numbers are used as reference with an incidence angle of -2.0° applied to the freestream conditions. The

propeller rotates at a rate corresponding to a tip Mach number of 0.626, resulting in an advance ratio of 2.51. For this unsteady simulation, the standard $k-\omega$ turbulence model is used with 1^{o} time-steps. This is seen as sufficient to capture the aerodynamic interactions based upon past studies [32].

Table 3.2: Installed IMPACTA propeller test conditions

Freestream Reynolds Number (-)	0.99×10^6
Freestream Mach Number (-)	0.5
Tip Mach Number (-)	0.626
Wing Angle of Attack (^{o})	-2.0
Number of blades (-)	8
Advance Ratio (-)	2.51
Turbulence Model	$k-\omega$
Time-Step ($^{o}/step$)	1.0

3.2.2 Aerodynamic results

Presented in Figure 3.5 is the key aerodynamic loads for the semi-span wing and individual propeller blade. All loads were scaled with respect to twice the freestream dynamic head (q_∞). Figure 3.5(a) presents the wing drag and lift force. Due to the presence of the freestream velocity, the lifting force has the greater magnitude. Oscillation's in wing loading are found due to the influence of the blade tip vortex. Across the propeller revolution, eight peaks in both lift and drag are seen. This corresponds to the passing of the blades. A similar oscillation in blade thrust coefficient is observed in Figure 3.5(b). As the blade passes the wing, increased blockage is seen downstream. This influences the propeller wake by reducing the final standard streamtube value to zero. Thus, creating a ground effect response in the blade thrust, resulting in an increased blade load [49, 81].

Presented in Figure 3.6 is the aerodynamic solution for the installed propeller simulation. Figure 3.6(a) presents the instantaneous flow-field visualisation via the iso-surface of Q-criterion of value 0.001. As observed, the blade tip vortices are preserved well across the wing ensuring the correct influence of the propeller rotation. The revolution average surface pressure coefficient is presented in Figure 3.6(b). The influence of the top-in rotation of the propeller can be seen on the upper surface of the wing with a pocket of negative pressure seen on the port side of the nacelle.

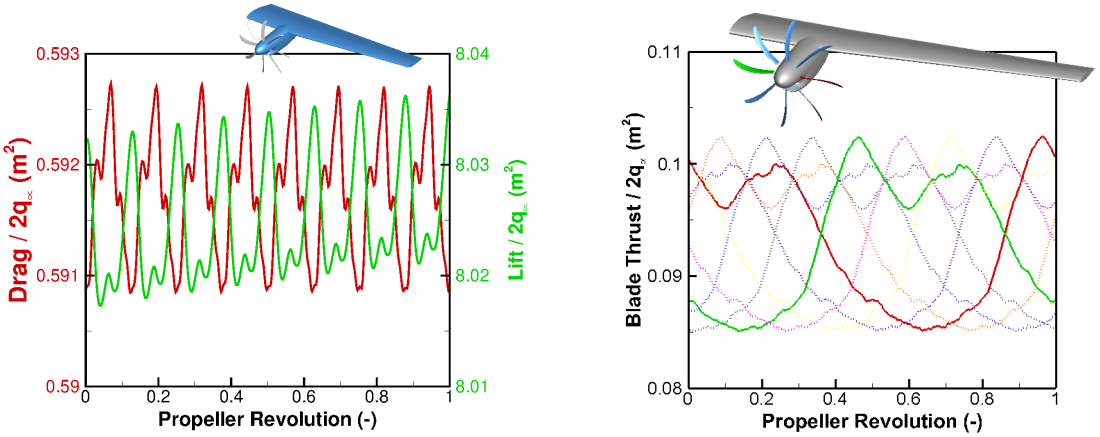

(a) Semi-span wing (b) Propeller blade

Figure 3.5: Semi-span aircraft key aerodynamic loads for the wing and propeller, normalised with respect to twice the freestream dynamic head (q_∞)

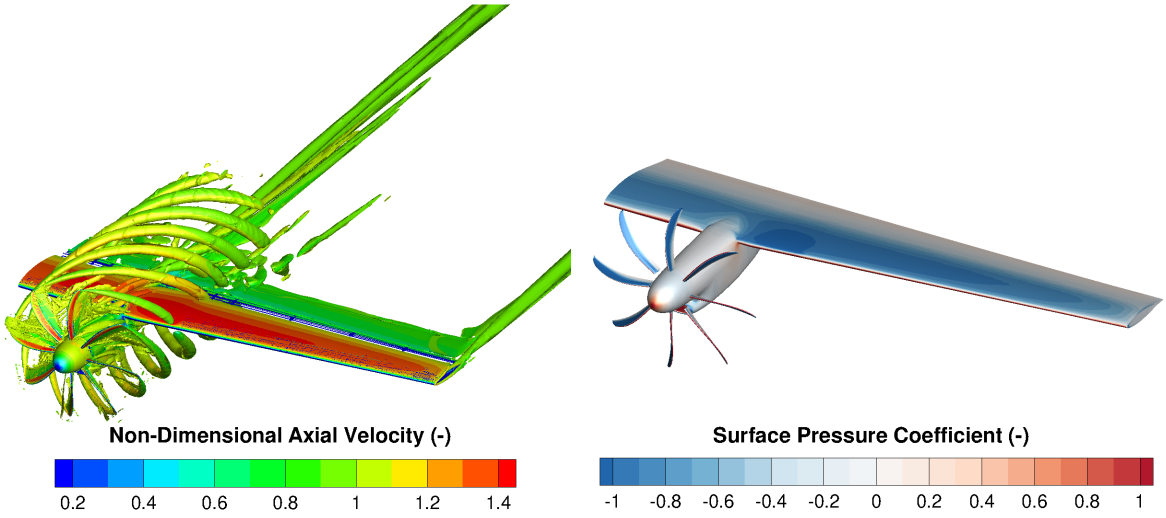

(a) Instantaneous flow visualisation (b) Average surface pressure

Figure 3.6: Semi-span aircraft aerodynamic solution

3.3 Verification of Semi-Span Wing Aeroelasticity

The CFD-solver HMB3 was previously validated and verified for the study of isolated and installed propeller aerodynamics. As this investigation is focused on the aeroelastic study of propeller blades, the fluid-structure interaction method described in Chapter 2 must be verified. To this end, the installed IMPACTA propeller will be studied in terms of aeroelasticity. This test case as selected as it allows for the verification of wing bending/torsion adjustments being transferred to the blade structure. As per the aerodynamic verification study (Section 3.2), no experimental data exists for this test case and is, therefore, only used as a verification calculation.

3.3.1 Computational setup

For this verification process, the same test conditions (Table 3.2) and grid (Figure 3.4) will be used. For this simulation, all solids are structurally active.

Structural model

As previously described in Chapter 2, the aeroelastic method requires the mode shapes and frequencies of the wing and propeller blade. For the propeller blade, the structural model consists of 15 elements of the CBEAM type of NASTRAN located through the spanwise of the blade. For each element, the quarter-chord line is selected as centre of elastic axis. Likewise, rigid bar elements (RBAR) are used to link the chord nodes to the aerofoil surface and these elements contain no structural properties. The element attached to the spinner is modelled with zero lead-lag, flapping, and pitch motions. Figure 3.7(a) shows the structural model build for the scale-model propeller. The blade is assumed to be of solid Titanium-Ti-6Al-4V (Grade 5) AMS-4911 material with the moments of inertia derived based upon the integration of the aerofoil shape. The sectional properties are presented in Figure 3.7(b), with the inertia's and non-structural mass non-dimensionalised.

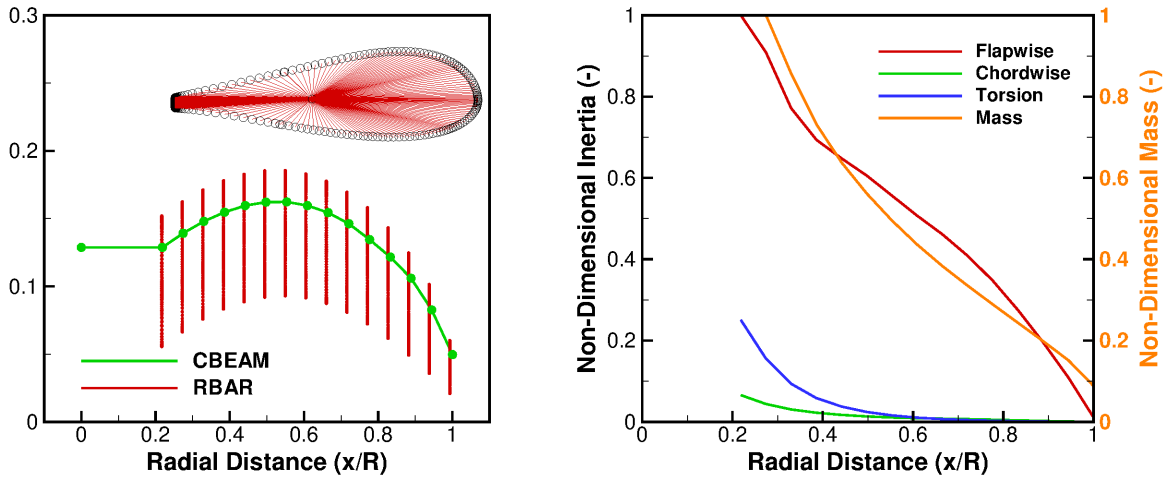

(a) Element structure

(b) Properties

Figure 3.7: IMPACTA propeller blade NASTRAN model

Using the non-linear NASTRAN solver (SOL 106) [99], which is described in Section 2.2, the mode shapes and frequencies of the blade were obtained. The spoke diagram for the blade is presented in Figure 3.8, where a comparison is made to the numerical estimations of Dowty. A good correlation between the methods is found. For the elastic simulation of the blades, the 1^{st} flapwise bending and 1^{st} torsion mode are selected. This correlates to Modes 1 and 3 on Figure 3.8.

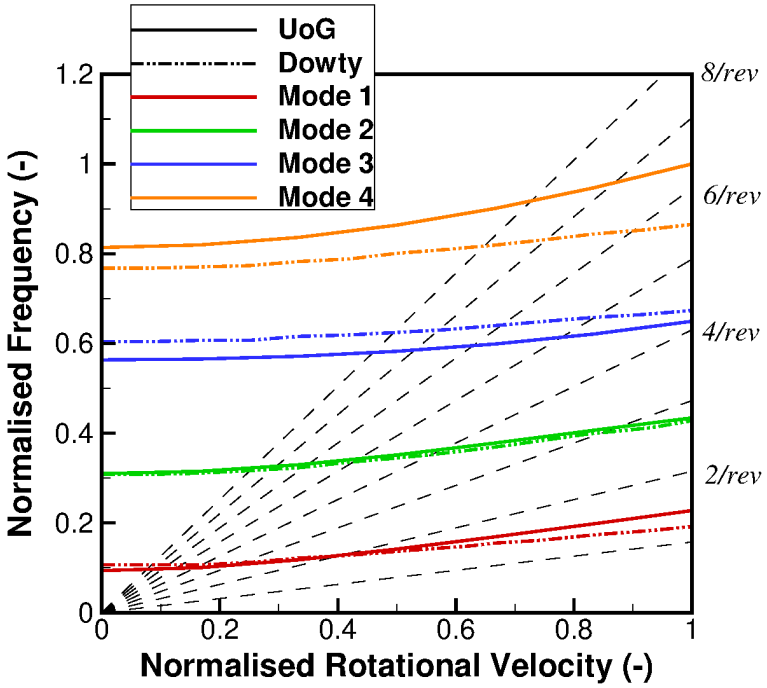

Figure 3.8: IMPACTA propeller blade spoke diagram

Due to the lack of information on the frequencies and shapes modes for the wing-nacelle-spinner component, Rayleigh-Ritz method was employed. It assumes that deformation varies in only one dimension (bending or torsion). The bending deformation z(y,t), can be written as:

$$z(y,t) = \sum_{j=1}^{N} \psi_j(y) q_j(t) \tag{3.1}$$

where $\psi_j(y)$ is the j-th assumed deformation shape and $q_j(t)$ is the j-th unknown coefficient also called generalised coordinate. N is the number of assumed shapes. The selection of the assumed shapes is restricted to polynomials or trigonometric functions and they must satisfy the kinematic boundary conditions of the system. If we idealised the wing-nacelle-spinner component as a cantilever beam (no transverse deformation at the root and zero load at the tip), the bending deformation z(y,t) can be approximated as $z(y,t) = \psi_1(y)q_1(t) = (\frac{y}{L})^2 q(t)$ (see Figure 3.9(a)).

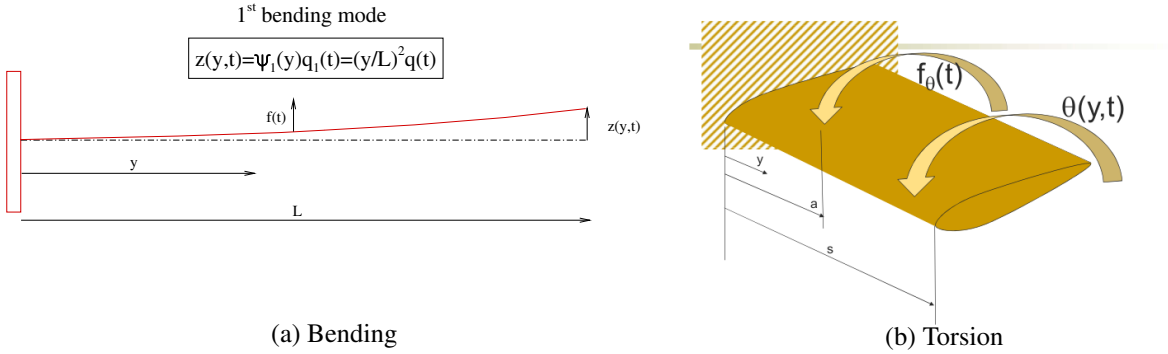

(a) Bending (b) Torsion

Figure 3.9: Diagram of the first bending and torsion modes for a cantilever beam

The real natural frequency (1st bending mode) of this system (Figure 3.9(a)) is:

$$\omega_{1b} = (1.875)^2 \sqrt{\left(\frac{EI}{mL^4}\right)} \tag{3.2}$$

where E is modulus of elasticity of the material in N/m^2, I is the moment of inertia of the system in m^4, m represents the mass per unit span of the beam and L the length of the beam. In addition to bending, torsion has also been considered in this study. Like the bending mode, the same boundary conditions are considered here (clamped root and free tip in torsion). The assumed shapes describes the twist θ along the y axis (see Figure 3.9(b)) as follows:

$$\theta(y,t) = \gamma_j(y) q_j(t) = \left(\frac{y}{x}\right) q \tag{3.3}$$

Using this method, the mode shapes and frequencies presented in Table 3.3 were supplied to the simulation for the deforming wing.

Table 3.3: Supplied wing mode shapes and frequencies

Bending Mode	0.6 Hz
Torsional Mode	2.8 Hz

3.3.2 Aeroelastic results

Presented in Table 3.4 are the average modal amplitude and forces for the wing and blade components. In terms of magnitude, the largest modal forces are found on the wing. This is to be expected based upon the configuration of the test case and the rigid results shown in Figure 3.5. Additionally, the forces for the respective torsional modes on the wing and blade solids have differing signs, thus indicating a pitch-down response for the wing and a pitch-up response for the blades.

The overall modal amplitude response depends on two factors: the modal force and supplied frequency. The difference in modal force for the bending and torsional modes are 38% and 55% respectively, between the wing and blade. The difference in the amplitudes, however, are significantly higher with over 100% differences in both bending and torsional modes. This indicates that the supplied modal frequency has a significant effect on the overall amplitude. In terms of the differences in supplied frequencies for each comparitative mode, differences of $> 3000\%$ and $> 800\%$ are found. Thus indicating that the lower frequency wing modes have the greatest effect on the overall geometry deformation.

In order to visualise the total deformation, the average aeroelastic response of the semi-span wing and propeller is presented in Figure 3.10. Here, the average deformation are non-

Table 3.4: Average modal response for the wing and blade components

Solid & Mod		Modal Amplitude	Modal Force
Wing	*Bending Mode*	22.62	391.76
	Torsion Mode	-0.96	-311.55
Blade	*Bending Mode*	-0.01724	-242.57
	Torsion Mode	0.00603	138.93

dimensionalised with respect to the reference chord. As observed in Figure 3.10(a), the greatest deformation is found at the wing tip with deflections greater than 2 c_{ref}. This is driven by the high modal amplitudes shown in Table 3.4 and the tip-dominant modes supplied to the calculation.

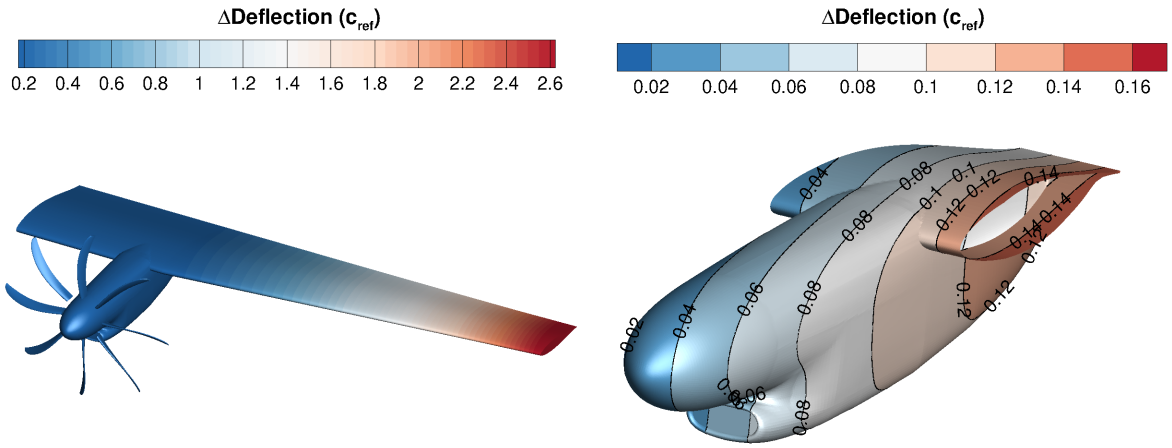

(a) Wing

(b) Nacelle

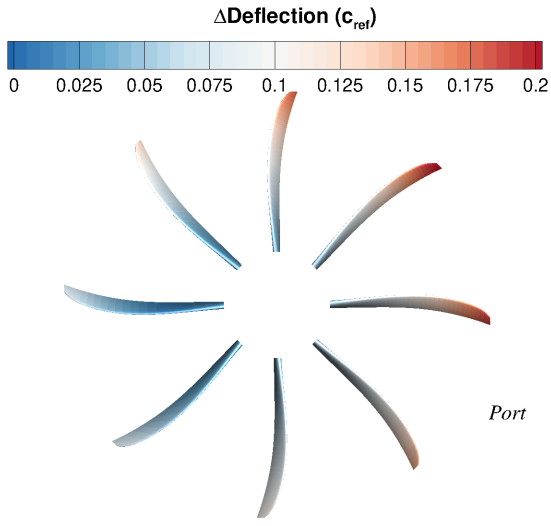

(c) Propeller

Figure 3.10: Semi-span wing aeroelastic deflection, non-dimensionalised with respect to the reference chord

One of the key factors in the aeroelastic method is the transfer of respective deflections between parent and child components. In this case, this refers to the wing and propeller, respectively. Focusing on the nacelle deflection in Figure 3.10(b), it is observed that the full nacelle deflects between 0.02 c_{ref} and 1.4 c_{ref}, with an average value of 0.074 c_{ref}. Focusing on the parent surfaces which are linked to the propeller, this average reduces to 0.04 c_{ref} due to being nearer the wing root and nacelle stagnation point.

With the propeller deflection presented in Figure 3.10(c), the root surface faces have an average deflection of 0.046 c_{ref}. This confirms the nacelle deflections have been transfered to the blades as very little deflection is seen at the blade root in the supplied structural modes, therefore this is dominated by the nacelle deflection. It is slightly larger than the nacelle average due to the fact that the blade is elastic, hence, although minimal, will deflect. Overall, the propeller deformation is driven by an azimuthal harmonic with the greatest deflection at the tip. This is expected based upon the rigid load results presented in Figure 3.5 in which an azimuthal harmonic due to the wing blockage is generated. Additionally, the blade mode shapes are tip dominant, hence the greatest deflection coming at the tip.

In order to understand how the change in blade shape effects the overall loading, the change in surface pressure coefficient between the average rigid and elastic solutions is presented in Figure 3.11. The introduction of the elastic deformation sees a decrease in surface pressure on the leading edge of the wing surface. This is a result of the reduction in pitch angle along the wing with an average reduction of 0.9^{o}. In line with the azimuth variation in thrust and deflection, an oscillation in surface pressure is seen on the propeller between the elastic and rigid solutions, with the maximum deflection correlating with the maximum increase in pressure.

From this aeroelastic verification process, it has been shown that the derived method can handle complex aeroelastic phenomena allowing the high-fidelity aerodynamics to influence the solution. The derived method allows for a range of tests to be conducted focusing on the principle of a fluid-structure interaction.

3.4 Summary

This chapter presented the validation for the aerodynamic model and the verification procedure for the aeroelastic solver. The valdation of the aerodynamic model was conducted against known experimental data for an isolated propeller. Good agreement was found in terms of the surface pressure coefficients across a range of stations from root to tip. In terms of this investigation's focus on propeller stall flutter, greater aerodynamic validation may be required against a detached flow case. However, such data does not currently exist for the investigated geometry.

The aeroelastic verification procedure was conducted on an installed propeller blade. A change to the selected blade was made due to the availability of accompaning wing/nacelle geometry from previous studies. It has been shown that the combined aerodynamic and structural

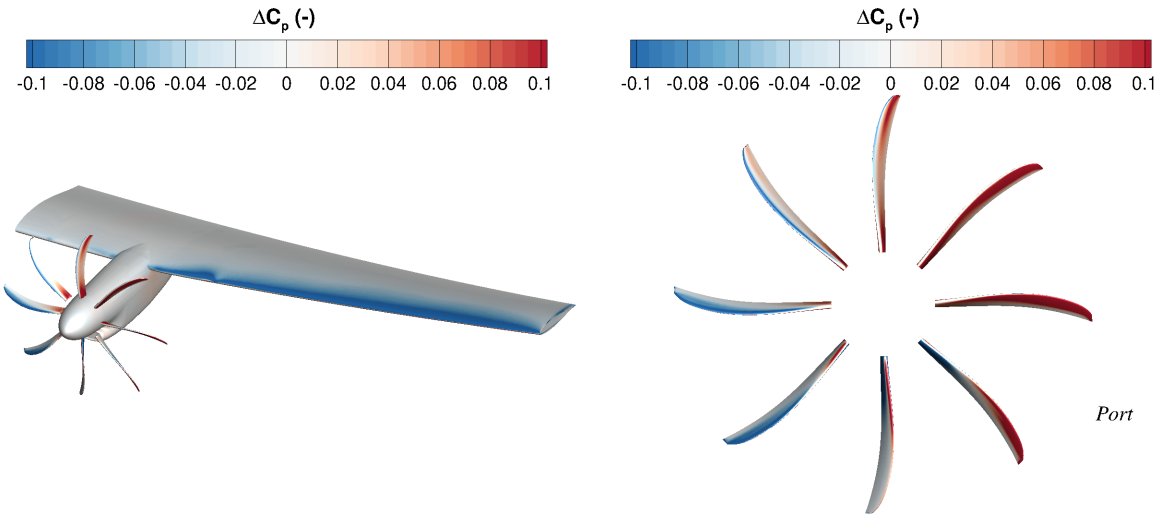

(a) Wing (b) Propeller

Figure 3.11: Change in surface pressure coefficient between the rigid and elastic solutions for the semi-span wing

models perform as expected, with the aerodynamics preserved well past the wing and the structural solver deforming the wing and propeller, with the respective wing deformations applied to the propeller centre of rotation. As no experimental data was currently available for these test cases, no comparison could be made. However, the aim of model verification was achieved.

Chapter 4

Aeroelastic Simulations of the Commander Propeller*

4.1 Full 3D Investigation: Commander Propeller Blade

Using the derived time-marching method, the Commander [6] blade was modelled in isolation. During model implementation, simulations were conducted utilising the full propeller, nacelle, wing combination. However, due to the large computational cost associated with such a simulation, and due to the fact that it is the detached flow associated with the reference blade that triggers the aeroelastic excitation (the excitation is then propagated to the additional blades via the nacelle connection with a phase difference seen within the excitation between blades), periodicity in space was assumed. This allows for the reduction of the computational domain to one propeller blade.

The structural model for the Commander blades are based upon the assumption of a solid material blade due to the fact the key data regarding the internal structure was unknown. The linear mass distribution was calculated as a function of the cross-section area, with the blade inertia based upon the variation in cross-section area.

The Commander propeller of Dowty was utilised within the Jetprop variants of the Aero Commander aircraft, the most advanced variants of the twin-engine turboprop [7], and the 695A Jetprop 1000 is presented in Figure 4.1. The baseline propeller design consisted of three blades with variable pitch and constant speed, each with an aspect ratio of ~ 11.0 and a chord of $\sim 0.13\ m$.

*The results presented in this chapter is published in R.J. Higgins *et al.* "High-Fidelity CFD Methods for the Simulation of Propeller Stall Flutter", *AIAA Journal*, Vol. 57, Issue 12, doi: 10.2514/1.J058463, 2019

Figure 4.1: Gulfstream American 695A Jetprop 1000 [5]

4.1.1 Computational Setup

Based upon the blade geometry, a computation domain of 120^{o} was created with a radial distance from the origin of 5 R/c. The inflow was selected to be also 5 R/c with the outflow 8 R/c from the origin in the vertical direction. These values are dervied based upon previous rotor blade studies [128]. A solid cylindrical hub was created from the inflow to outflow.

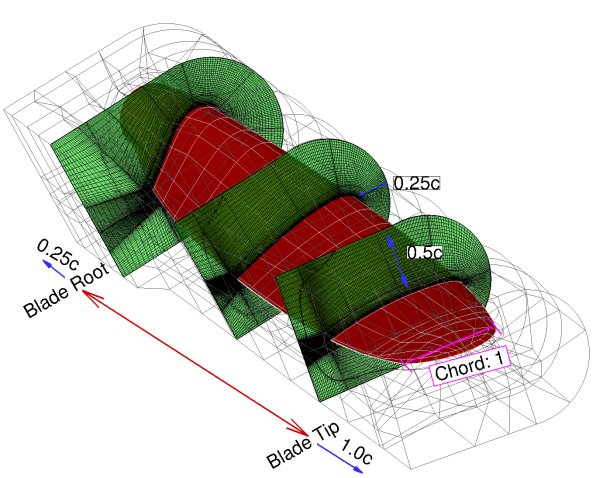

(a) Foreground Grid

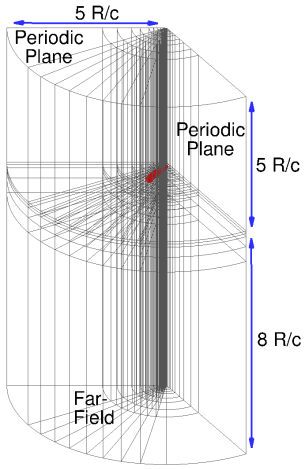

(b) Background Grid

Figure 4.2: Commander propeller computational domain and chimera grid.

The chimera technique was used for the aeroelastic computations and was selected to allow for the deflection of only the blade grid. An O-grid was used for the foreground mesh and this was due to the blunt trailing edge and blade tip design. This was accompanied by a conventional cylindrical background mesh. Presented in Table 4.1 is the grid sizes used for the mesh convergence study. Similar levels of mean thrust and load oscillations were seen between the three grids from *SAS* rigid simulations (Table 4.2), therefore the baseline grid was selected for this study.

A time-step comparison was conducted using 1^{o}, 0.5^{o} and 0.25^{o} steps per propeller revo-

Table 4.1: Investigated mesh sizes for the grid convergence study.

Grid level	**Coarse**	**Baseline**	**Fine**
Total Grid Size (*volume cells)*	1,597,508	12,780,064	18,857,888
Foreground	441,508	3,532,064	9,609,888
Background	1,156,000	9,248,000	9,248,000

Table 4.2: Average and change in non-dimensional vertical load using *SAS* for the grid convergence study.

		Grid		
		Coarse	*Baseline*	*Fine*
Pressure Force	*Average*	5.508	3.14	5.77
	Δ *Average (%)*	5.340	-	9.03
	Δ *Amplitude (%)*	5.499	2.97	8.83
Shear Force	*Average*	-2.27×10^{-4}	2.85	1.81
	Δ *Average (%)**	-2.51×10^{-3}	-	4.09
	Δ *Amplitude (%)**	-4.18×10^{-3}	1.98	2.94

*Scaled by pressure component

lution, with the change in pressure and shear vertical load presented in Table 4.3. The average vertical load for the pressure component is seen to be within 2% for the 0.5^{o} and 0.25^{o} simulations to the baseline time-step. The average amplitude variation of the vertical pressure load is found to be less than 8% for all simulations, with instantaneous maximum values of similar levels. The viscous load is seen to be less than 0.05% of the pressure component for all simulations, therefore the change in average and average amplitude is scaled by the pressure component. Very little change in seen between the average viscous loads with all simulations showing similar amplitude levels. In addition to this, three clear frequency peaks were observed between all simulations, thus ensuring that all simulations are able to capture the same content. Due to the match of vertical load levels and captured frequencies, the $1^{o}/step$ simulation will be used for this study as this balances the computational cost to level of resolved content.

The baseline test conditions for this propeller were based upon the initial starting conditions of the static wind tunnel test [28]. Sea-level conditions were assumed, with the reference velocity and length selected as the tip Mach number at 1400 (rpm) and tip chord length, respectively. Following the convergence of the rigid flow-field at 1400 (rpm), the aeroelastic module was introduced.

A single revolution was used to settle the structural response, with this found to be enough to settle the initial spike in deformation along with the selected damping coefficients. The blade rotational velocity was then accelerated from 1400 to 1750 (rpm) over 5 revolutions. This

Table 4.3: Average and change in non-dimensional vertical load for the time-step convergence study.

		Time-step		
		$1^o/step$	$0.5^o/step$	$0.25^o/step$
Pressure Force	*Average*	5.832	-	4.28
	Δ *Average (%)*	5.932	1.71	7.34
	Δ *Amplitude (%)*	5.854	0.38	6.53
Shear Force	*Average*	-2.75×10^{-3}	-	0.013
	Δ *Average (%)**	-2.27×10^{-3}	0.007	0.012
	Δ *Amplitude (%)**	-2.47×10^{-3}	0.004	0.012

*Scaled by pressure component

acceleration mirrors the process conducted during the experiment. To determine the effect of the blade acceleration on its qualitative aeroelastic response, an additional simulation at the final rotational velocity value of 1750 (rpm) was conducted. Table 4.4 details the flow computational parameters.

Table 4.4: Summary of the Commander propeller blade test conditions.

Reynolds Number (-)	1.65×10^6
Starting Propeller Velocity (*rpm)*	1400
Final Propeller Velocity (*rpm)*	1750
Blade Pitch Angle $(^o)_{0.70R}$	$27^o40'$
Altitude *(m)*	*Sea-level*
Inflow Velocity *(m/s)*	0.0 *(Static conditions)*
Tip Velocity *(m/s)*	197.36
Tip Chord Length *(m)*	0.122
Turbulence Model	*URANS* $k-\omega$ *& SAS*

4.1.2 Structural Modelling

The blade was assumed to be of solid 1100 grade aluminum alloy, with a Young's Modulus of 6.9×10^{10} *Pa*, shear modulus of 2.6×10^{10} *Pa* and mass density of 2710 kg/m^3. The cross-sectional area, linear mass and blade inertia's are presented in Figure 4.3(a). The derived structural model includes the effects of the blade rotational force, with this varied to determine the Spoke diagram shown in Figure 4.3(b). The derived mode shapes match those seen within the experiment and are found to be of order bending-bending-torsion for modes 1-3. The structural model frequencies compare well to the experimental excitations presented in Figure 4.3(b) for the second and third mode, with the first being higher than the experiment. In addition to the ex-

perimental excitation frequencies, the investigated range and flutter boundary are also presented within the Spoke diagram.

For the aeroelastic simulations, the structural model focuses on, and uses, the first three modes. This was due to the fact that only the first three modes are reported as part of the experiment. HMB3 has the ability to update the the active eigenmode through an interpolation feature. This is particularly useful when stiffening effects due to increasing rotational force are significant. However, looking at the Spoke diagram (Figure 4.3(b)), the stiffening effects are seen to be marginal for this blade. As a result, the modes shapes at the starting velocity of 1400 (rpm) are initially selected and kept constant throughout the simulation.

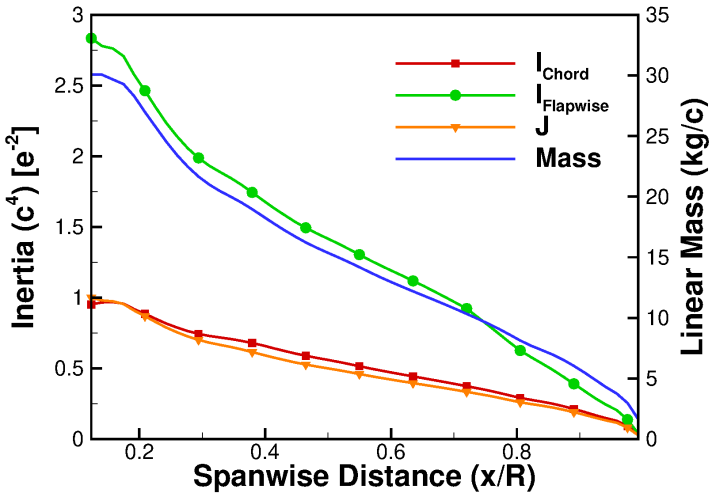

(a) Blade Structural Properties

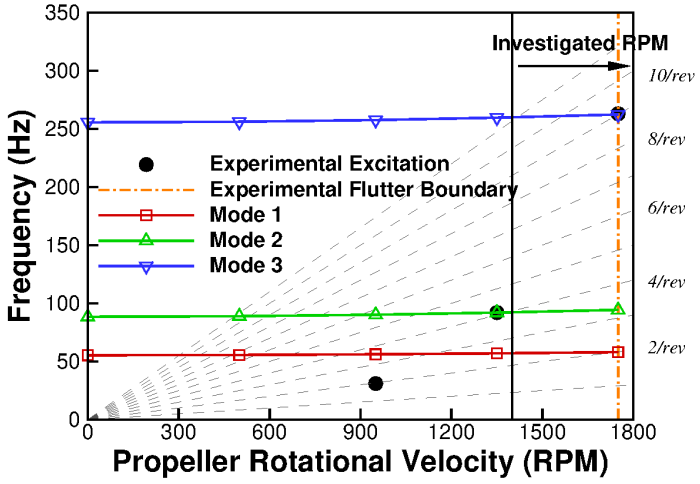

(b) Blade Spoke Diagram

Figure 4.3: Commander propeller blade structural properties and resultant frequencies.

4.2 Comparison between URANS and SAS for the 3D accelerating blade

Presented in Figure 4.4 is a comparison of the maximum relative torsional stress between the simulations and the experimental results. Both experiments and simulation results provide a simple quadratic response across the blade radius. The maximum stress value for the experiment is seen at the 75% *R* station. For both simulations, the maximum values are seen slightly outboard at 80% *R*. Comparing the relative values of the *URANS* and *SAS* simulations, the *SAS* simulation achieves larger torsional stress values, thus being closer to the experimental values. Although the absolute values do not match exactly, the trend across the blade radius are very well captured. This indicates similar loading patterns are observed between the experiments and simulations.

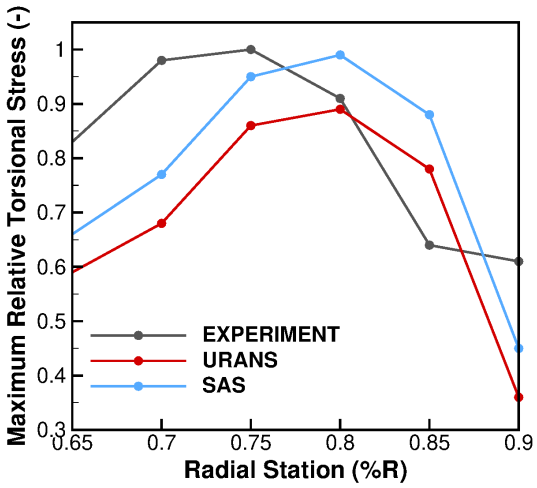

Figure 4.4: Comparison of the maximum relative torsional stress, along the blade radius, between the experimental and simulation results.

In addition to the torsional stress levels, an analysis can be conducted on the structural response of the modal method. As the aeroelastic technique assumes the blade deflection is a combination of the supplied eigenmodes, modal amplitudes and forces are generated for each mode. Figure 4.5 presents the modal amplitudes for the three modes supplied. Looking at the first mode (chord-wise bending mode) an oscillating response of 2.54 $/revolution$ around a linearly increasing mean value is observed for the *URANS* simulation. A similar response is found for the *SAS*, with a frequency of 2.46 $/revolution$, however, the periodic amplitude increases for the *SAS* computation by 20% during the transition phase. This increases to a factor of 3 by the final revolutions.

During the transition phase for the second mode, a decrease in periodic amplitude is found for the *SAS* simulation. This is a result of the current mode being of flap-wise bending type.

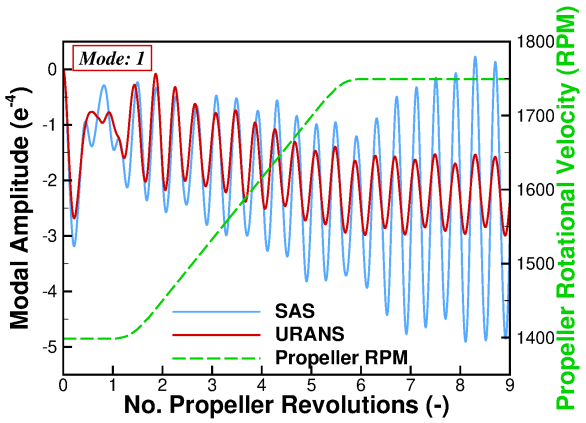

(a) Mode 1.

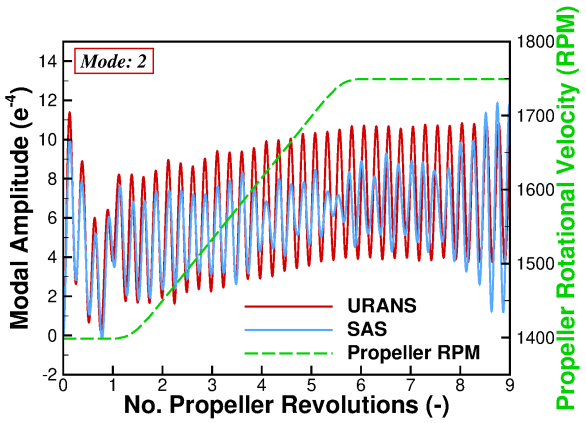

(b) Mode 2.

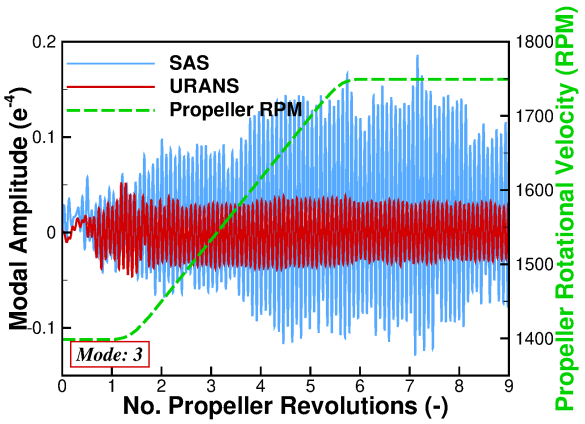

(c) Mode 3.

Figure 4.5: Modal amplitude response for the Commander blade in static conditions at a pitch angle of $27^{o}40'$ through a rotational velocity acceleration.

As previously described within Chapter 2, the modal amplitudes are calculated based upon the modal forces and these modal forces are a projection of the nodal point pressure onto the interpolated mode shape. Therefore, a decrease in modal amplitude indicates a decrease in modal force, and as a result a potential increase in detached flow due to the use of *SAS* . This is highlighted in the flow-field visualsation of Figures 4.7 to 4.10. Once the *SAS* simulation reaches the final rotational velocity, the periodic amplitude gradually increases to 66% of the transition value.

During the experiments of DOWTY, it was found that the first torsional mode was excited prior to the onset of the stall flutter. This, in no doubt, contributed to the eventual blade discruction with the combination of excited torsional mode and stall flutter response amplifying the deformations. From Figure 4.5(c) a significant difference is found between the *URANS* and *SAS* response. For the *URANS* simulation, the modal amplitude oscillates at a frequency of 11.3 $/revolution$ around a constant mean value with a constant periodic amplitude. For the *SAS* computation, the periodic amplitude grows during the transition phase, with a significant step change seen during the 4^{th} propeller revolution. During this step change, the periodic amplitude

increases by a factor of 2. The rotational velocity at this point is 1600 (rpm) and this correlates to the step change in torsional stress seen during the experiment. Once the acceleration is complete, the periodic amplitude continues to increase to 3 times the original transition value.

For the frequency response of the modal amplitudes, a Fast-Fourier-Transform is conducted on each signal, and this is presented in Figure 4.6 for the *URANS* and *SAS* simulations. As can be seen for both computations, non-integer harmonics are present for all modes. This gives an indication of the presence of stall on the blade. Larger amplitudes are observed for the *SAS* simulation with additional noise also appearing around the main frequency peaks. The obtained frequencies for the three modes relate to the observed natural frequencies seen in the Spoke diagram in Figure 4.3(b). From the Spoke diagram: Mode 1 is observed to have a response between 2^{nd} and 3^{rd} order; Mode 2 has a 4^{th} order response; and Mode 3 is found to have a 11^{th} order response. This is what is seen from the FFT of the modal amplitudes.

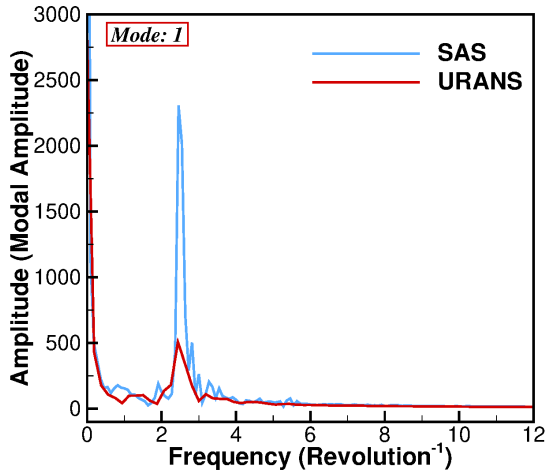

(a) Mode 1.

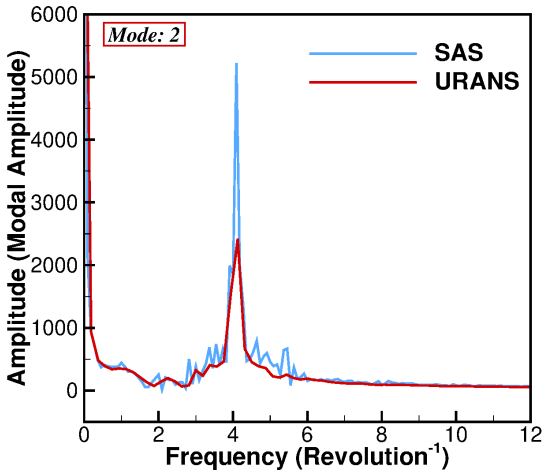

(b) Mode 2.

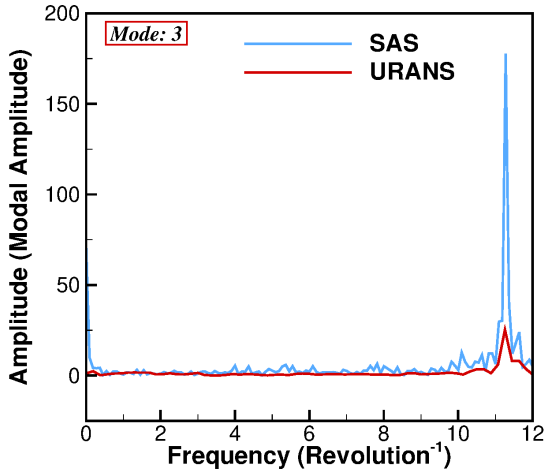

(c) Mode 3.

Figure 4.6: FFT of the modal amplitude response for the Commander blade.

Presented in Figures 4.7 & 4.8 is the flow visualisation of the non-dimensional tangential velocity for the *URANS* and *SAS* calculations, respectively, using radial slices at 90%R across several azimuthal positions at the maximum torsional stress point. For the *URANS* simulation (Figure 4.7), a stable velocity profile is observed, with recirculating flow present across the full station. The stable velocity profile is determined due to the nature of the statistical *URANS* model, where no shedding occurs. As a result, the stall bubble remains essentially fixed to the blade surface.

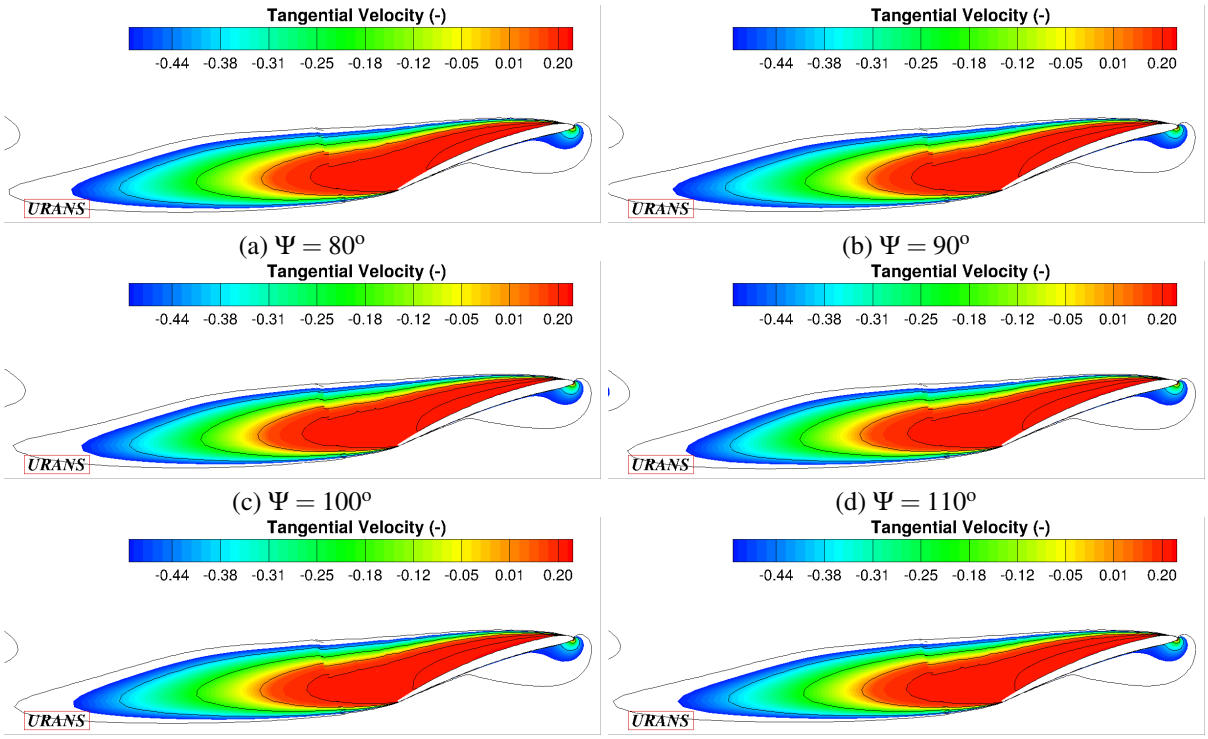

(a) $\Psi = 80^o$ (b) $\Psi = 90^o$

(c) $\Psi = 100^o$ (d) $\Psi = 110^o$

(e) $\Psi = 120^o$ (f) $\Psi = 130^o$

Figure 4.7: Flow visualisation of the non-dimensional tangential velocity using radial slices for the accelerating blade *URANS* calculation.

The *SAS* results (Figure 4.8) provide much greater variations in unsteady content compared to the *URANS*. Focusing on the first time-step (Figure 4.8(a)), approximately five vortex structures are present. These are located on the blade surface at $\sim 0.25\ c_{ref}$, $\sim 0.6\ c_{ref}$ and $\sim 0.9\ c_{ref}$, and off the blade above the surface bubble at $\sim 0.9\ c_{ref}$ and between $\sim 0.9\ c_{ref} - \sim 0.6\ c_{ref}$. As the solution is marched in time, the off body vorticies detach. Initially it is the larger $\sim 0.9\ c_{ref}$ in Figure 4.8(b), before the remaining trailing edge and mid-chord vorticies in Figure 4.8(c). At this point (Figure 4.8(c)), the flow has attempted to reattach, however the leading edge vortex ($\sim 0.25\ c_{ref}$ in Figure 4.8(a)) has grown in size and results in a much larger vortex shedding in Figure 4.8(d). After this (Figure 4.8(e)), the overall bubble is at its smallest and the multiple vorticies found at the start begin to develop. These are then present in Figure 4.8(f).

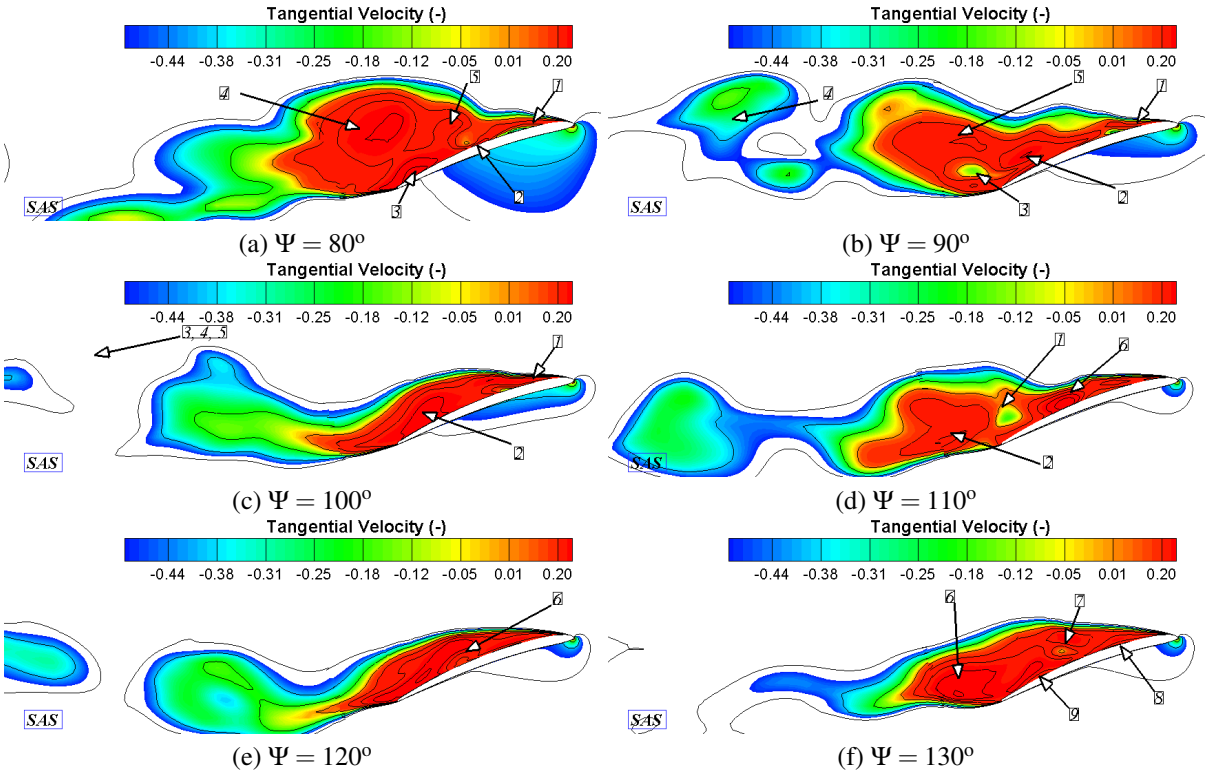

(a) $\Psi = 80^o$ (b) $\Psi = 90^o$

(c) $\Psi = 100^o$ (d) $\Psi = 110^o$

(e) $\Psi = 120^o$ (f) $\Psi = 130^o$

Figure 4.8: Flow visualisation of the non-dimensional tangential velocity using radial slices for the accelerating blade *SAS* calculation.

In terms of the entire flow-field, a visualisation of the vorticity magnitude iso-surfaces of value 1.0 is presented in Figures 4.9 & 4.10 for the *URANS* and *SAS* simulations, respectively. The presented figures correspond to the same time-steps as Figures 4.7 & 4.8, and thus is looking at the flow-field solution across the point at which the maximum stress occurs.

Looking at the *URANS* solution (Figure 4.9), the detached flow bubble present towards the tip of the blade is clearly present. This projects inboard until the 70% station. Towards the blade root, a detached flow bubble is present towards the trailing edge. During the blade acceleration, the inboard detached flow begins to project along the blade and interact with the tip bubble creating an additional bubble around mid span. This is present here, with two distinct bubbles. Additionally and as expected from the tangential velocity profiles (Figure 4.7), very little change to the flow-field is found individual time-step to time-step due to the lack of vortex shedding.

For the *SAS* results (Figure 4.10), the flow is fully detached at the trailing edge across almost the entire blade radius. Several individual vorticies are present across the span which vary in size. All of these vorticies interact and shed from the surface, unlike the *URANS* solution. As the blade is accelerated, the iso-surfaces shed at an increasing rate. Additionally, the detaching-reattaching process results in increased vorticies towards the leading edge, adjusting the active moments. This is particularly evident towards the tip, where the greatest variation occurs. These fluctuations in detached flow content results in increased fluctuations of the surface loads causing variations in the periodic amplitude of the *SAS* modal response.

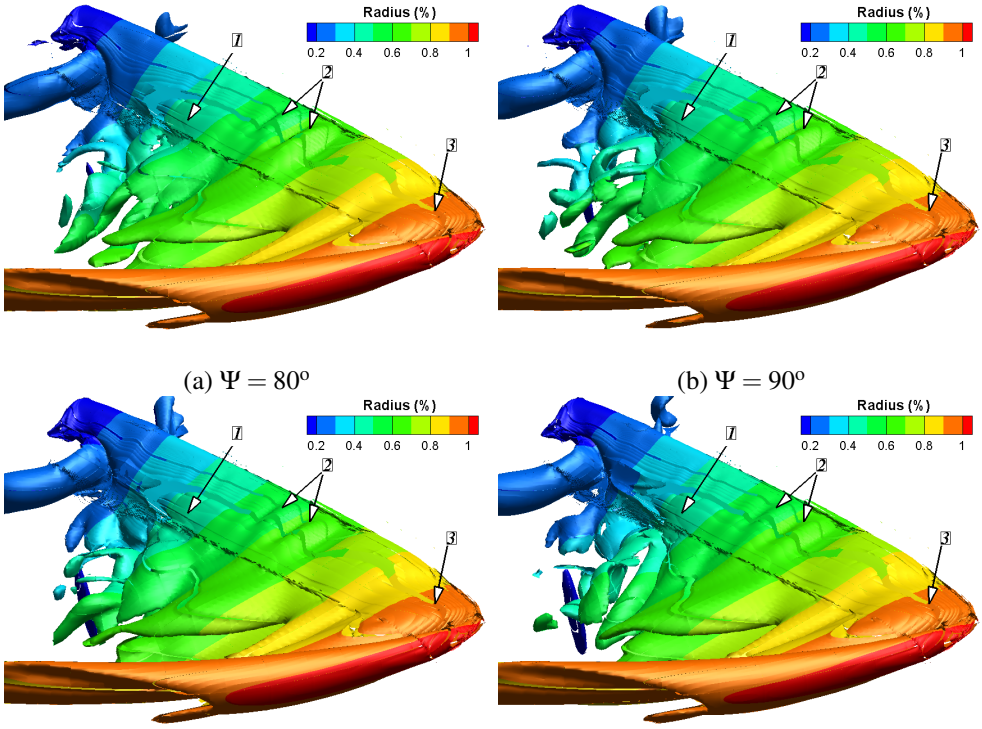

(a) $\Psi = 80^o$ (b) $\Psi = 90^o$

(c) $\Psi = 100^o$ (d) $\Psi = 110^o$

Figure 4.9: Flow visualisation using vorticity magnitude iso-surface of $|\omega| = 1.0$ for the accelerating blade *URANS* calculation.

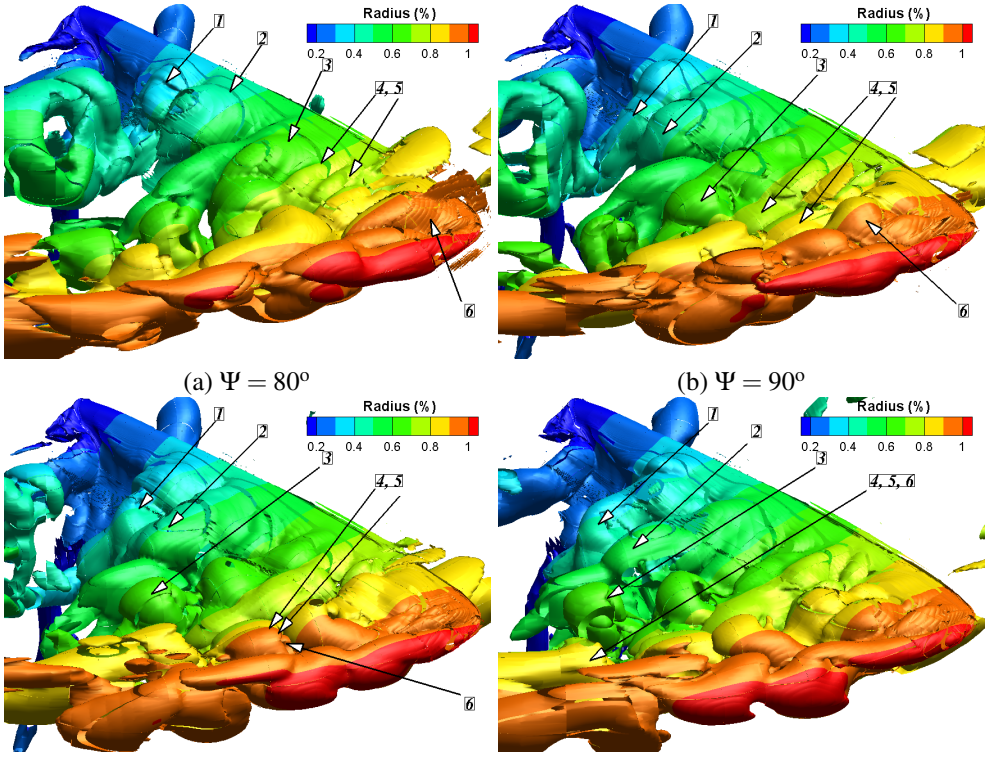

(a) $\Psi = 80^o$ (b) $\Psi = 90^o$

(c) $\Psi = 100^o$ (d) $\Psi = 110^o$

Figure 4.10: Flow visualisation using vorticity magnitude iso-surface of $|\omega| = 1.0$ for the accelerating blade *SAS* calculation.

Presented in Figures 4.11 and 4.12 is the instantaneous surface pressure coefficients contours along the upper surface of the blade through the transition period for the *URANS* and *SAS* simulations, respectively. Focusing on the *URANS* simulation (Figure 4.11), two clear stations indicate the presence of stall, via the flat pressure contours, following the acceleration period and these are found at the blade mid-span and tip. At the start of the transition (Figure 4.11(a)), only the tip bubble was present. This tip bubble slowly increases in size until the end of the 4th revolution (Figure 4.11(c)). As the blade reaches the higher rotational velocity (Figure 4.11(d)), the secondary bubble develops around the mid-span. This evidentually splits in two once at the final stage (Figure 4.11(f)) and this double stall bubble can be observed within the vorticity magnitude iso-surfaces of Figure 4.9 (highlighted via marker 2).

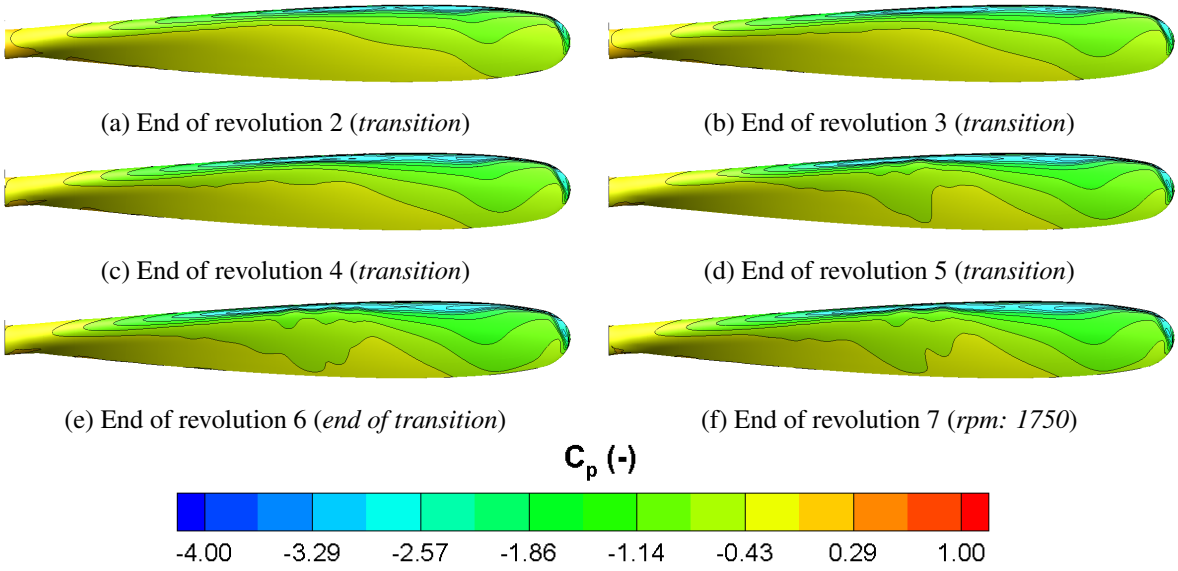

(a) End of revolution 2 (*transition*)

(b) End of revolution 3 (*transition*)

(c) End of revolution 4 (*transition*)

(d) End of revolution 5 (*transition*)

(e) End of revolution 6 (*end of transition*)

(f) End of revolution 7 (*rpm: 1750*)

Figure 4.11: Visualisation of the surface pressure coefficients for the *URANS* simulation through the transition period.

For the *SAS* simulation result (Figure 4.12), significant variation in the pressure profile is observed. At the start of the acceleration (Figure 4.12(a)), similarities between the *URANS* and *SAS* results can be observed with a similar flat contour at the tip of the blade. As the blade is transitioned from the lower to higher rotational velocity, an increase is found in the fluctuations of the pressure contours with pockets of lower and higher pressure. This is driven by detached flow at the root being projected outwards towards the tip, interacting with the stalled flow. These variations, and fluctuations, peak at the end of the acceleration (Figures 4.12(e) & (f)), where high pressure pockets are observed. This is a result of the attempted reattachment of the flow to that section, as the vortex is shed from the blade.

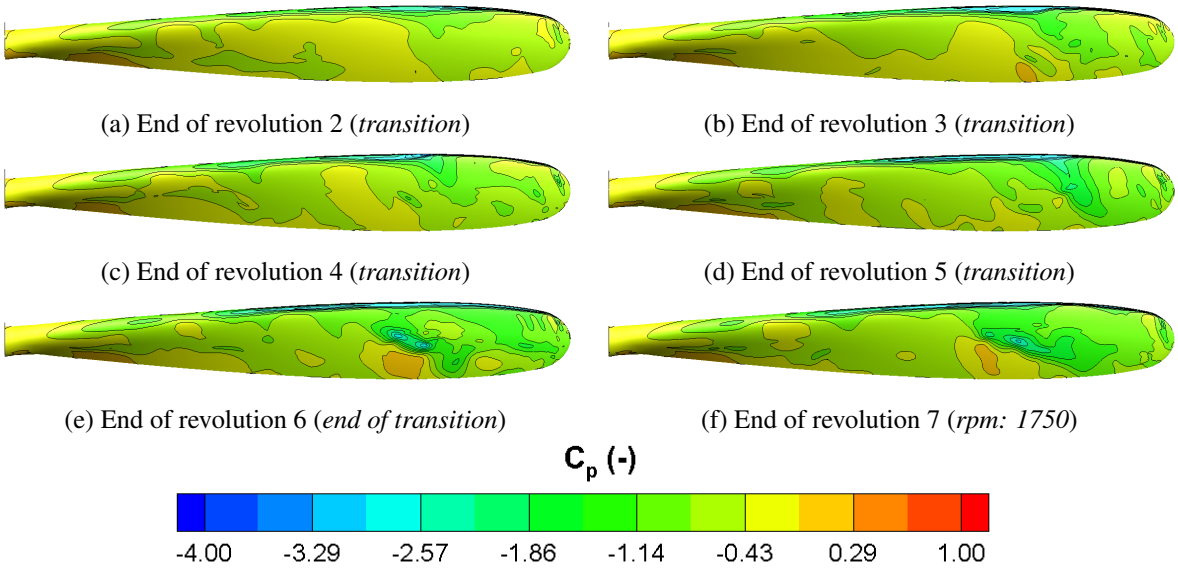

(a) End of revolution 2 (*transition*)

(b) End of revolution 3 (*transition*)

(c) End of revolution 4 (*transition*)

(d) End of revolution 5 (*transition*)

(e) End of revolution 6 (*end of transition*)

(f) End of revolution 7 (*rpm: 1750*)

Figure 4.12: Visualisation of the surface pressure coefficients for the *SAS* simulation through the transition period.

To determine the overall fluctuation in surface pressure, a Fast-Fourier Transform was conducted on selected block faces of the propeller upper surface. This is shown in Figure 4.13 for the *URANS* and *SAS* simulations. As can be seen, a larger amount of frequency content is captured via the *SAS* simulation, with almost no significant peaks captured using *URANS* .

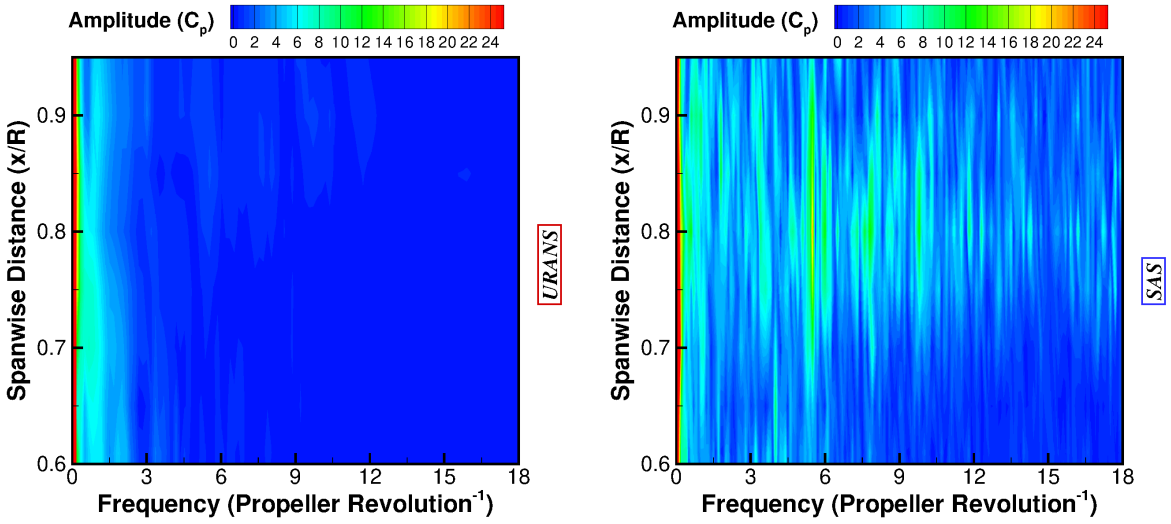

(a) *URANS*

(b) *SAS*

Figure 4.13: FFT of the surface pressure coefficient along the upper surface of the blade.

4.3 Investigating the effect of the blade acceleration

To determine the effect of the blade acceleration, a simulation at a fixed rotational velocity of 1750 (rpm) using the *SAS* model was conducted. For this simulation, the mode shapes and frequencies were updated to correlate with the current rotational velocity. A rigid solution at 1750 (rpm) was produced from which to start this calculation.

In a similar manner to the accelerating blade simulation, a comparison of the maximum relative torsional stress can be seen in Figure 4.14, with the trends extracted during the point of maximum torsional stress for both accelerating and fixed rpm simulations. For the fixed rpm simulation, a linear trend in the torsional stress is observed across the blade. This varies significantly from the experimental and accelerating blade simulations where a quadratic response is seen. The change in response is a result of the greater fluctuations in modal force seen for the fixed rpm modes during the aeroelastic simulation start up. As previously described, high levels of structural damping are used to control the initial oscillation of the aeroelastic blade. This level of damping is kept constant, combine this with the fact greater levels of force are seen during the initial revolutions of the fixed rpm simulation compared to the accelerating blade, greater oscillations are observed impacting the final deformation results. Based upon this and in order to capture the same physics as the experiment, it is observed that the acceleration of the blade is critical.

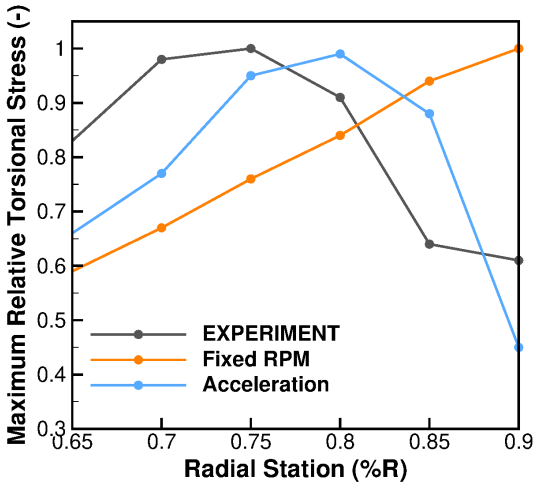

Figure 4.14: Comparison of the maximum relative torsional stress, along the blade radius, between the accelerating and fixed *rpm* simulations.

Presented in Figure 4.15 is the comparison of the modal amplitude between the fixed rpm and accelerating blade simulations. For the accelerating blade, the comparison is focused on the last revolution of the acceleration and the five revolutions at the final state. Focusing on Mode 1 and for the fixed rpm simulation, there is a slight increase in mean value of 15%. The response

of both simulations, however, remain similar. The frequency response of Mode 1 is presented in Figure 4.16(a). A reduction of 0.6 $/revolution$ in frequency for the fixed simulation is found, with a reduction in periodic amplitude of 12%.

For Mode 2, the periodic amplitude of the fixed rpm simulation is found to be 130% greater than the accelerating blade during the initial two revolutions. As the accelerating blade modal amplitude begins to diverge, this difference is reversed with the fixed rpm simulation periodic amplitude found to be 23% smaller than the accelerating blade during the final two revolutions of comparison. Overall, there is an 8% reduction in periodic amplitude for the fixed rpm simulation, with a 20% reduction in the frequency response, as is shown in Figure 4.16(b).

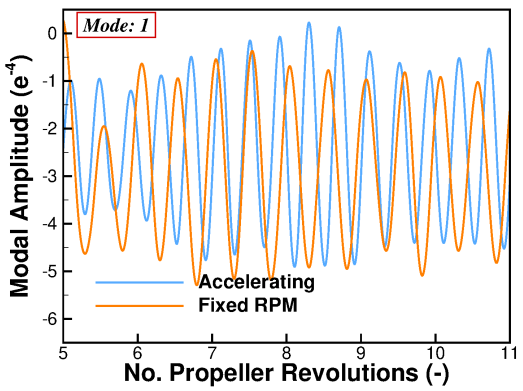

(a) Mode 1.

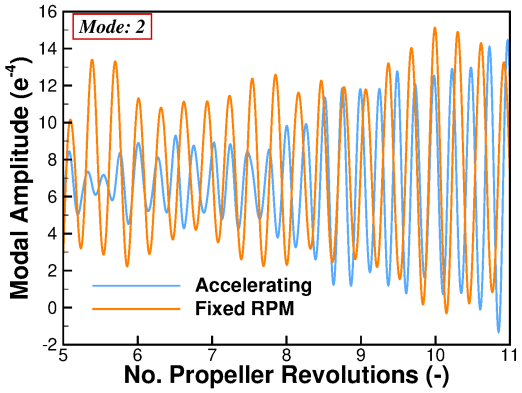

(b) Mode 2.

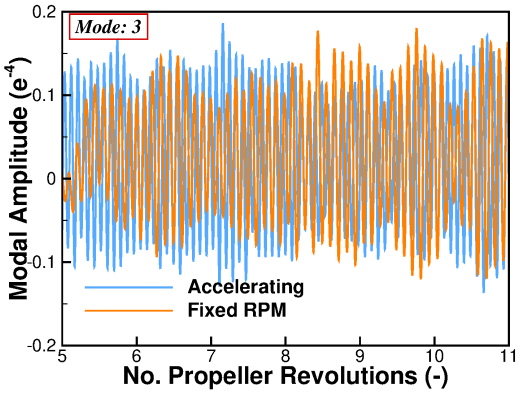

(c) Mode 3.

Figure 4.15: Comparison of the modal amplitude response between the accelerating blade and fixed *RPM* simulations.

For the final mode, similar profiles are observed between the accelerating blade and fixed rpm simulations. Due to the significant varation of this mode found in the accelerating *SAS* results of Section 4.2, the difference in periodic amplitude fluctuates between the simulations. For the initial two revolutions of comparison, the accelerating blade simulation is seen to have a periodic amplitude 20% greater than the fixed rpm. This reverses during revolutions 8 to 10, where the fixed rpm simulation is seen to have a periodic amplitude 73% greater than the accelerating blade. Overall, a 20% reduction in periodic amplitude is observed for the fixed rpm

simulation with a reduction in frequency of 20%.

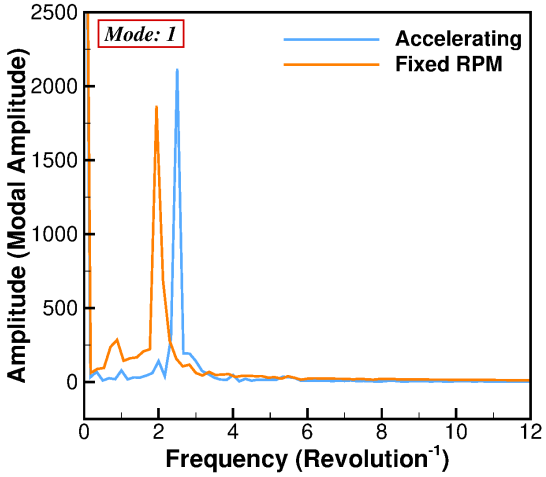

(a) Mode 1.

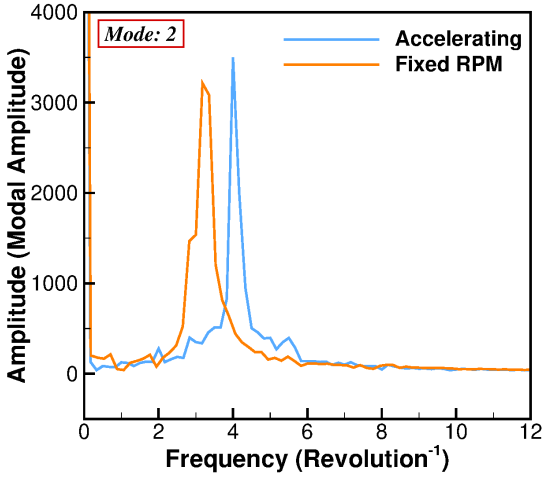

(b) Mode 2.

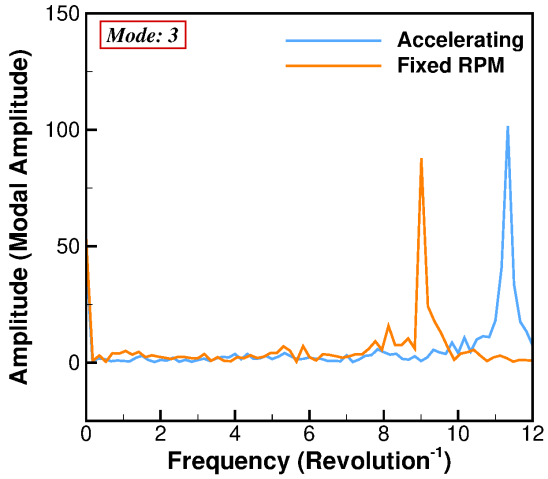

(c) Mode 3.

Figure 4.16: A comparison of the modal amplitude frequency response for the accelerating and fixed *RPM* simulations.

To summarise, regardless of ramping or fixed rpm, all *SAS* simulations show blade excitation via the oscillations of the modal amplitudes. This qualitatively agrees with the test, particularly the increase in modal amplitude magnitude for the third mode during the blade acceleration. However, in order to capture the physics of the torsional stress trend through the blade radius seen during the experiments, the acceleration of the blade is required as the fixed rpm results did not capture the required trend.

4.4 Aeroelastic response with reduced blade stall

Previous simulations involved the acceleration of the Commander propeller blade at a fixed rigid pitch of $27^{o}40'$. This pitch angle was selected based upon the details of the experimental investigation and focuses on a blade suffering from stall. In order to ensure the effect of the previous blade deflection was the result of stall, an investigation was conducted at lower rigid pitch angles to determine the attached flow angles and the subsequent modal response.

4.4.1 Examination of stall through rigid computations

In order to examine the effect of blade pitch on the rigid blade, several hover formulation simulations where conducted at 1400 (rpm). This formulation was used in Section 3.1 for the JORP propeller validation and includes an additional source term to the *RANS* equations to account for the rotational effects. A pitch reduction of 10^{o}, 15^{o} and 20^{o} was investigated using *RANS-hover* with the $k-\omega$ turbulence model. For reference, this results in a reference pitch angle at $70\%R$ of $\sim 17^{o}$, $\sim 12^{o}$ and $\sim 7^{o}$, respectively.

Presented in Figure 4.17 is the vorticity magnitude iso-surfaces of the rigid hover formulation simulations for the range of pitch angles. As previous presented for the *URANS* baseline pitch simulation, three destinct stall bubbles are present on the blade. These form from the blade mid-span to the tip. With a reduction in pitch of 10^{o} (Figure 4.17(b)), such bubbles are removed. Detached flow can be seen towards the root of the blade, however, this is expected due to the higher pitch angle and increased thickness aerofoil shapes. A further reduction of 5^{o} (Figure 4.17(c)) finds a reduction in the size of the root stall bubble. Although a reduction in detached flow is seen across the blade, the reduction in pitch, and subsequently thrust, sees a closer passing of the blade tip vortex. This is highlighted at 20^{o} (Figure 4.17(d)) where a significant blade vortex interaction is seen around $85\%R$. Through these simulations, it is shown that the 15^{o} pitch reduction is the cleanest solution as the blade stall has been reduced without introducing secondary consequences.

Following on from the rigid hover-formulation simulations, the 15^{o} blade was simulated in an unsteady manner using the standard *URANS* compared to the *SAS* method. Presented in Figure 4.18 is the normalised thrust coefficients for the *URANS* and *SAS* standard and reduced pitch simulations. As observed, aside from the expected drop in thrust coefficient for the reduced pitch simulation, a reduction in the load oscillations is also captured due to the reduction in detached flow. For the standard pitch simulations average values of 1.094 and 1.0 are seen for the *URANS* and *SAS* simulations, respectively. All thrust values have been normalised with respect to the average rigid *SAS* simulation, hence the average value of 1.0. These values drop to 0.716 and 0.684, respectively, with the reduction in pitch. The influence of the *SAS* modelling is seen via the average values. At the higher pitch angle where signficant stall is present, the thrust value is reduced by 9.4%. This reduces to 3.3% with the lower pitch.

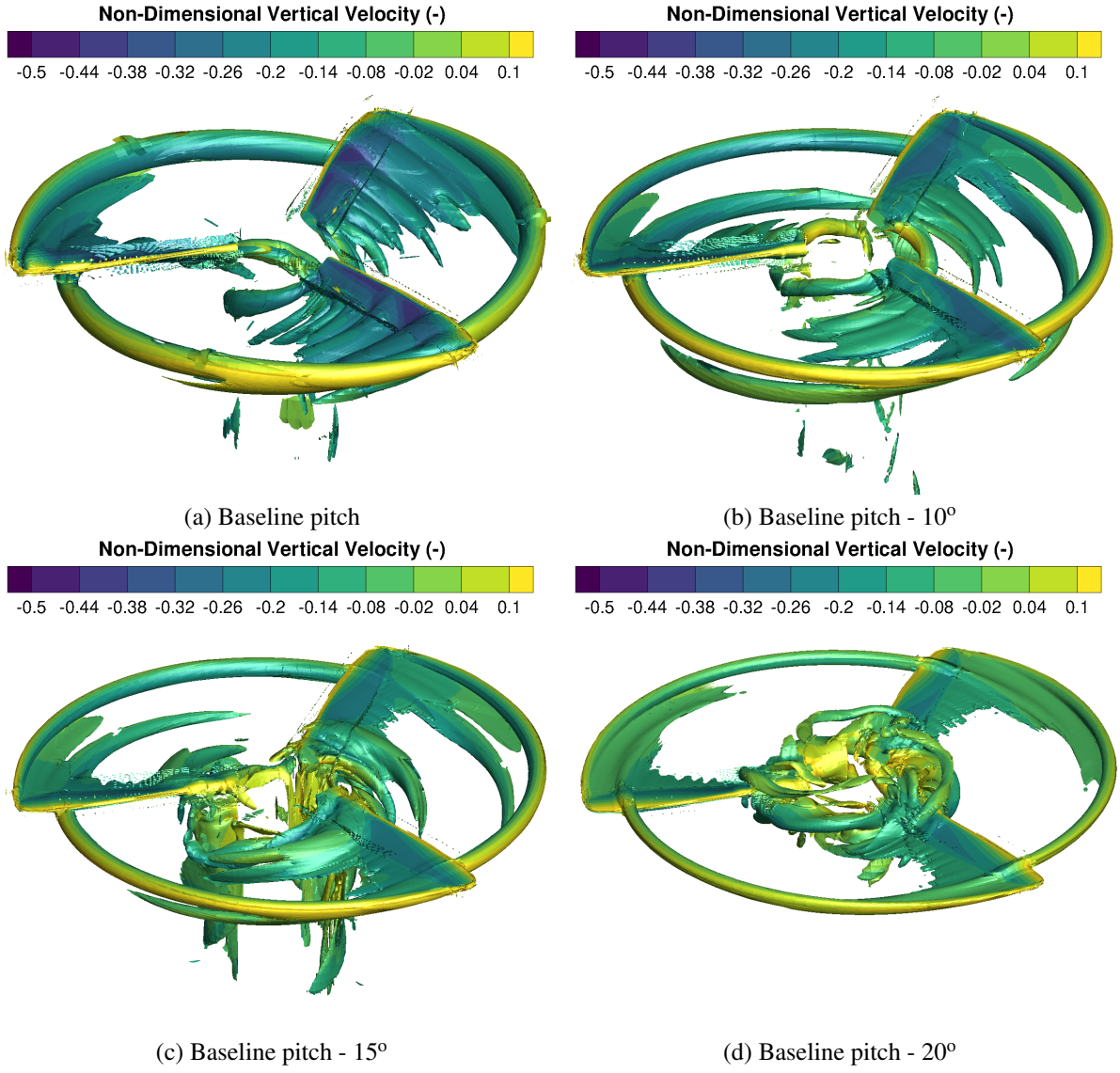

(a) Baseline pitch

(b) Baseline pitch - 10^{o}

(c) Baseline pitch - 15^{o}

(d) Baseline pitch - 20^{o}

Figure 4.17: Vorticity magnitude iso-surfaces of the rigid hover formulation solutions over a range of blade pitch angles at 1400 (rpm)

In addition to the average values, the reduction in detached flow content, and influence of the *SAS* modelling, is also seen in the fluctuations around these normalised thrust averages. For the standard pitch, normalised thrust oscillations of ± 0.038 and ± 0.090 are seen for the *URANS* and *SAS* simulations, respectively. These drop to ± 0.006 and ± 0.013, representing an $\sim 85\%$ drop in detached flow content for both methods.

With the reduction in detached flow and influence of the *SAS* method, the 15^{o} reduced pitch blade was selected for an aeroelastic investigation. The blade was accelerated from 1400 to 1750 (rpm) using both the *URANS* and *SAS* techniques. All structural properties remain unchanged as was simulated in Section 4.2.

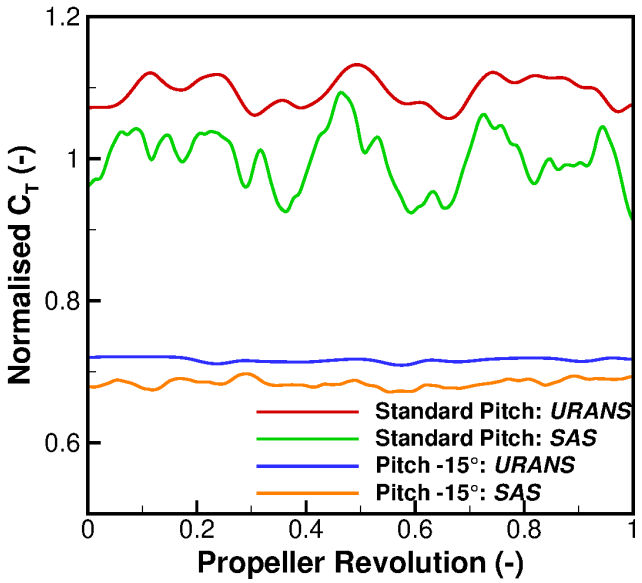

Figure 4.18: Unsteady normalised thrust coefficients for the standard and reduced pitch *URANS* and *SAS* rigid solutions

4.4.2 Aeroelastic results

Presented in Figure 4.19 is the modal amplitude comparison between the standard and reduced pitch simulations. As observed, a signifcant reduction in all modal amplitudes is seen. With the reduction in pitch angle, the linear increase in both the first and second modes is not seen with a constant oscillation throughout the simulation. In terms of the fluctuation around the average, the reduced pitch simulations are slightly higher than the standard *URANS* with values of $\sim \pm 0.90$ and ± 0.73, respectively, for the first mode. However, the standard pitch *URANS* simulation has a signficantly higher average due to the linear increase, relative to the change in rpm. The standard pitch *SAS* simulation has a fluctuation value of ± 2.56.

For the second mode, a similar trend is observed. Subtracting the average values from the results, the standard pitch *URANS* and both reduced pitch simulations have similar fluctuation values. These are ± 3.60 for the standard pitch *URANS* , ± 3.09 for the reduced pitch *URANS* and ± 2.95 for the reduced pitch *SAS* . The standard pitch *SAS* results indicate a significantly higher fluctuation value of ± 7.87 based upon the derived detached flow.

With the same trend captured across all simulations for the third mode, the reduction in blade pitch has reduced the fluctuation values. For the reduced pitch sulations, similar values of ± 0.0162 and ± 0.018 are seen for the *URANS* and *SAS* solutions, respectively. These are signifcantly lower than the standard pitch values of ± 0.038 and ± 0.162 for the *URANS* and *SAS* , respectively.

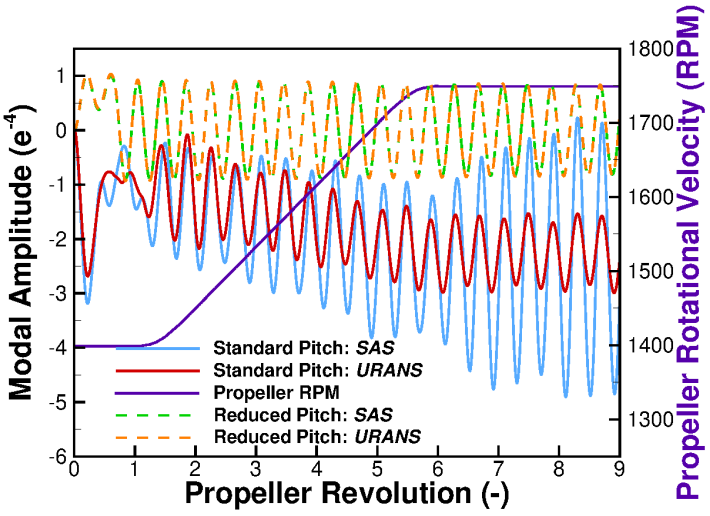

(a) Mode 1.

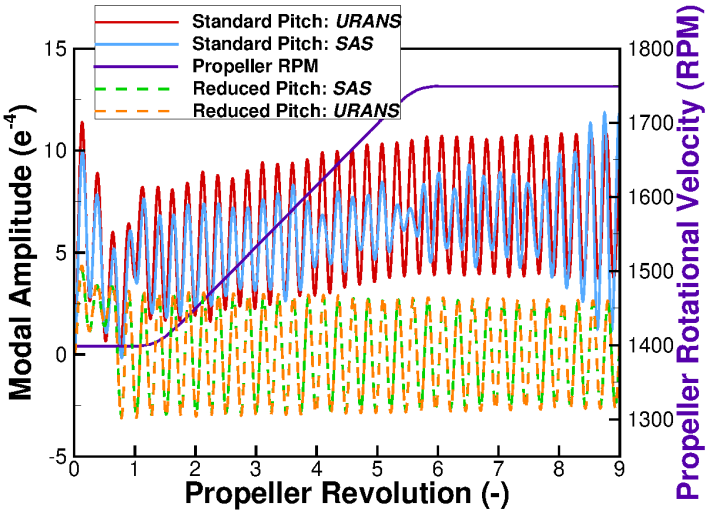

(b) Mode 2.

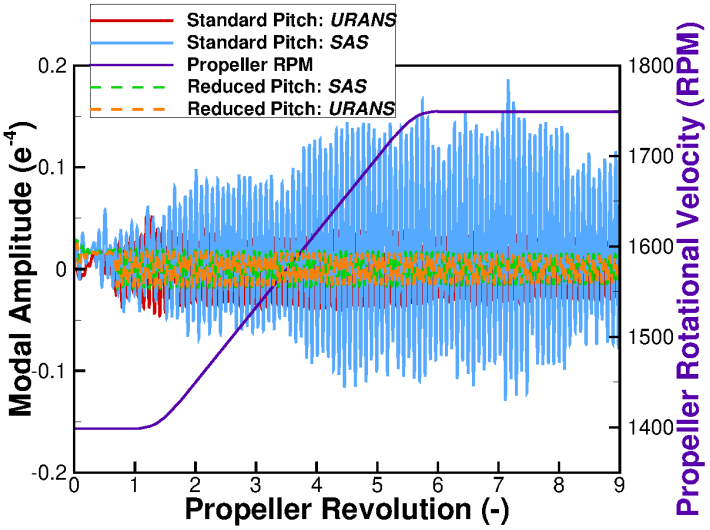

(c) Mode 3.

Figure 4.19: Comparison of the modal amplitude response for the reduction in propeller blade stall

Overall, the reduction in pitch angle reduced the overall blade deflection via the reduction of average and fluctuation modal amplitude values. With the removal of blade stall, a minute difference is observed between the *URANS* and *SAS* simulations thus indicating the influence of the detached flow on the modal amplitude values.

4.5 Influence of supplied mode shape

The original structural model, presented in Section 4.1.2, was derived based upon the assumption of a solid material blade with a comparison made to the active mode shape and frequency. In order to assess the influence of the mode shape on the aeroelastic prediction, a structural model based upon a bungee test was derived.

4.5.1 Bungee Structural Modelling

DOWTY Propellers conducted a modal test on the Commander propeller in order to understand its structural response [113]. A single blade was suspended from a steel beam via bungee chords with the blade excited using a step input in force. A NASTRAN equivalent was derived with four spring elements (CELAS2) used to represent the bungee chords and these are connected to the structural CBEAM elements using rigid bars at the blade root section. This is visualised in Figure 4.20(a). For this model, the linear real eigenvalue analysis (SOL 103) was used with a gravitational force added.

In order to match the mode shapes and frequencies, and based upon the previous assumption of a solid material blade, the inertial properties were adjusted and these are presented in Figure 4.20(b). This includes an increase in chordwise inertia across the mid-span of the blade, a reduction in flapwise inertia and an increase in torsion towards the root with a reduction towards the tip.

The adjustments made to the properties had a significant impact on the derived mode shapes and frequencies. Although the general order of the mode shape remained the same, i.e. bending-bending-torsion, the increase in chordwise inertia resulted in two pure flapwise bending modes followed by a pure torsional mode. The comparison between the bungee test and NASTRAN model is presented in Table 4.5 with a close match found between the two studies.

There was also a significant decrease in modal frequency for the tuned model with the Spoke diagram presented in Figure 4.21. The tuned modes found a closer match to the experimental excitation for the first mode compared to the standard model with a reduction away from the experiment for the second and third modes. The effect of the change in mode shape and frequency was analysed via the simulation of the accelerating blade using the *SAS* model.

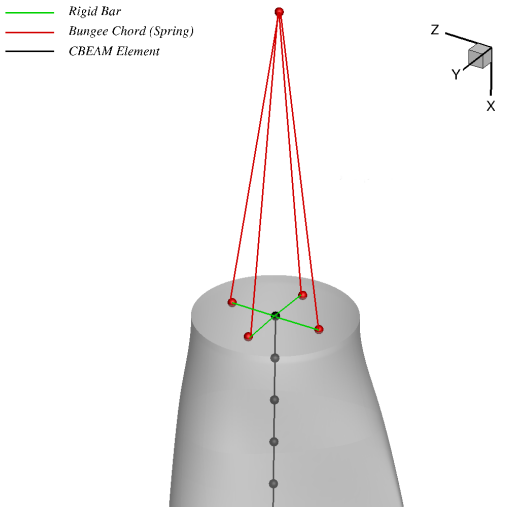

(a) Bungee NASTRAN Model

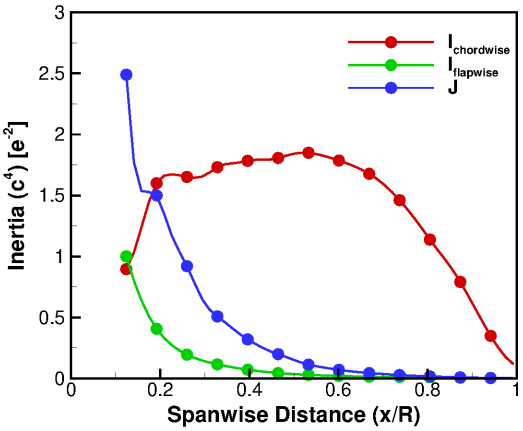

(b) Tuned updated structural properties

Figure 4.20: Commander propeller blade bungee structural model and tuned properties

Table 4.5: Comparison of the mode shapes and frequencies of the experimental and computational bungee model

	Bungee Test		**NASTRAN tuned Model**	
Mode	*Mode*	*Frequency*	*Mode*	*Frequency*
1	Flapwise Bending	62.49 Hz	Flapwise Bending	62.94 Hz
2	Flapwise Bending	160.17 Hz	Flapwise Bending	165.10 Hz
3	Torsion	290.78 Hz	Torsion	291.67 Hz

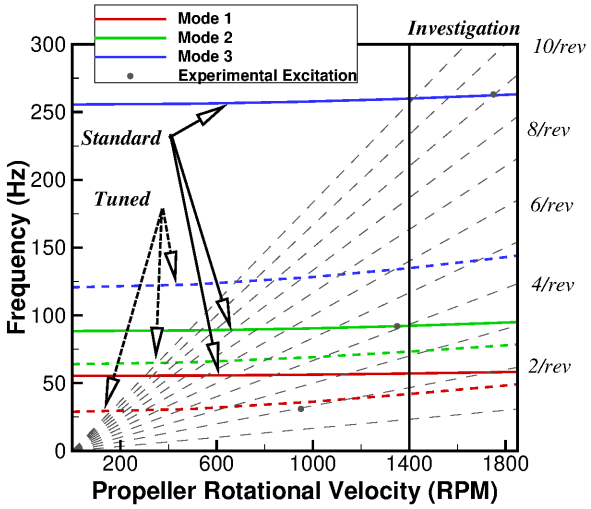

Figure 4.21: Commander propeller blade tuned model spoke diagram

4.5.2 Aeroelastic Results

Due to the change in mode shape and frequency, significant alterations in the model amplitudes were found with the amplitudes presented in Figure 4.22. Looking at the 1st mode, and examining the profile in Figure 4.5(a), the linear increase in modal amplitude for the standard modes is not seen in the tuned modes, hence there is a reduction in average amplitude of 81.4%. There is, however, a significant increase in amplitude fluctuation. Examing the profiles after the acceleration, the standard model has a fluctuation value of ± 2.58 around the average with the tuned modes increasing by 240% to a fluctuation value of ± 62.0. This change in response is dominated by the adjustment in mode shape with an alteration from chordwise to flapwise bending. This shows that a significant increase in energy is applied to the flapwise bending mode as opposed to the chordwise.

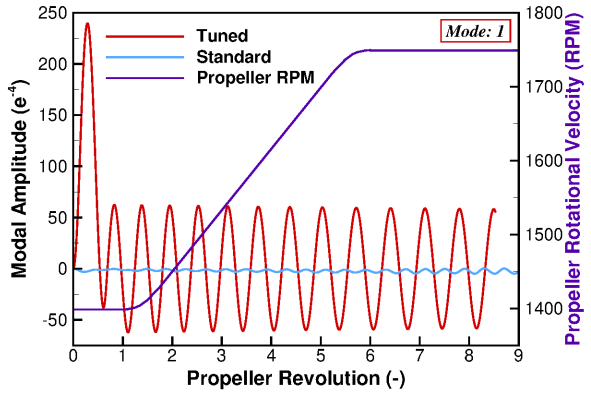

(a) Mode 1.

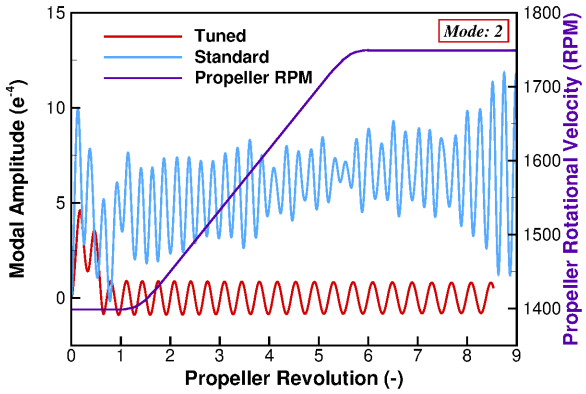

(b) Mode 2.

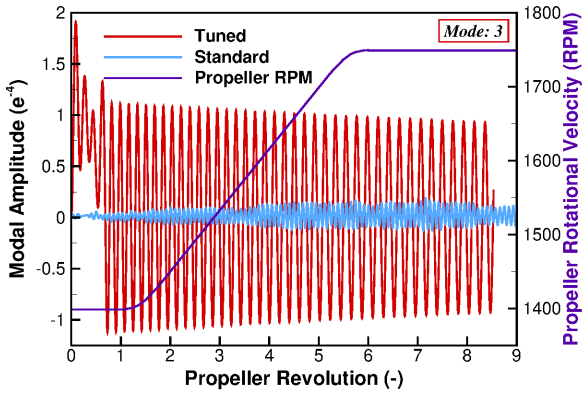

(c) Mode 3.

Figure 4.22: Comparison of the modal amplitude response for the change in structural model for the Commander blade using *SAS*

Due to the same mode shape being present in the second mode, a true comparison between the modal amplitudes can be conducted. As observed from Figure 4.22(b) and in a similar manner to the first mode, the linear increase in modal amplitude is not seen in the tuned modes. This results in a reduction of the average value from 6.15 to 0.01. The fluctuation around this

average has also been reduced by 84.3%. This is dominated by the increase in standard mode fluctuation towards the end of the simulation.

The change in third mode from bending-torsion to pure torsion is seen in the modal amplitudes of Figure 4.22(c). Again, the change in modal amplitude trend through the simulation is not seen for the tuned mode and although the linear increase is minimal (Figure 4.5(c)), it has an effect on the average values. The introduction of the tuned modes reduces the average value by 70.4%. However, as was seen in the first mode, the change in shape results in an increase in fluctations from ± 0.16 to ± 1.11.

As previously stated, the combination of all modal amplitudes results in the final blade deformation. Presented in Figure 4.23 is the non-dimensional torsional stress values seen across the blade radius and through the simulation with the difference between the tuned and standard models also shown. The stress values were non-dimesionalised with respect to the maximum value seen during the quasi-steady portion of the experimental trends.

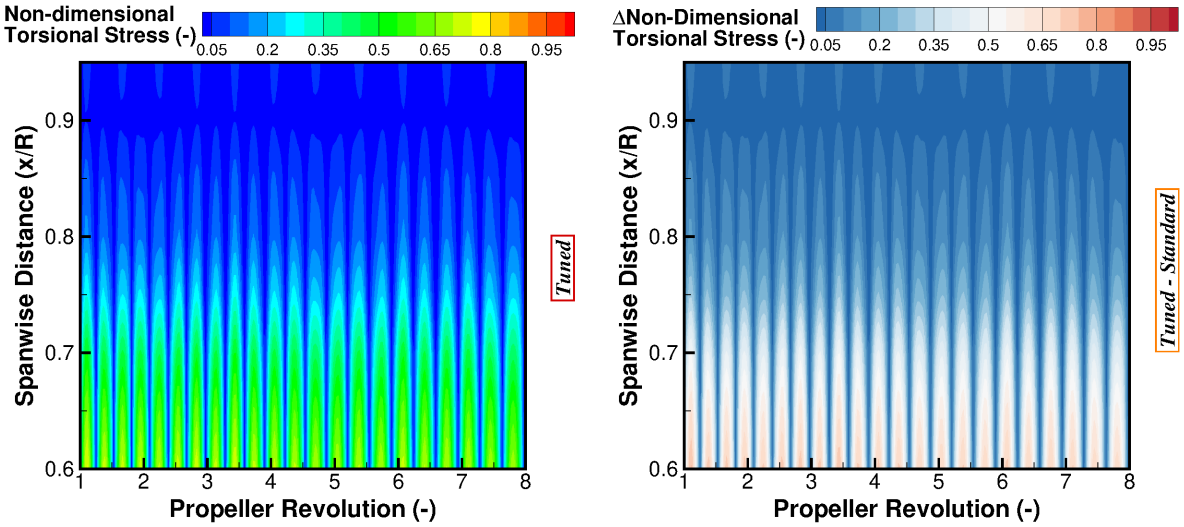

(a) Tuned model

(b) Difference with baseline

Figure 4.23: Comparison of the non-dimensional torsional stress results for the change in structural model for the Commander blade

With the adjustment in mode shapes, a significant increase in torsional stress is observed. A non-dimensional average value of 0.18 is seen across the radius and simulation, with a maximum value of 0.76 captured. This represents a 91% difference between the standard and tuned simulations with the significant difference a result of the increased fluctuation in modal amplitudes.

Presented in Figure 4.24 is the difference between the bending and torsion oscillations of the standard and tuned mode simulations, along with an extract from the 70%R station of the raw results. Looking at the difference in blade twist (Figure 4.24(a)), a significant increase in pitch oscillations is seen with maximum values of $\pm 0.33^{o}$ with the flucuations occuring around an average value of 0.003^{o}. These oscillations occur at a frequency of 1.5/revolution and this

correlates with the modal amplitude frequency for the first mode. The first tuned mode is a pure flapwise bending mode, hence the bending oscillations, shown in Figure 4.24(b), due to the first mode result in the fluctuations in pitch. A maximum bending oscillation of $\pm 0.02 c_{ref}$ is seen throughout the simulation with a frequency of 1.5/revolution . These results are additionally highlighted within the 70%R extract, where very small oscillations in pitch and bending are found for the baseline simulation.

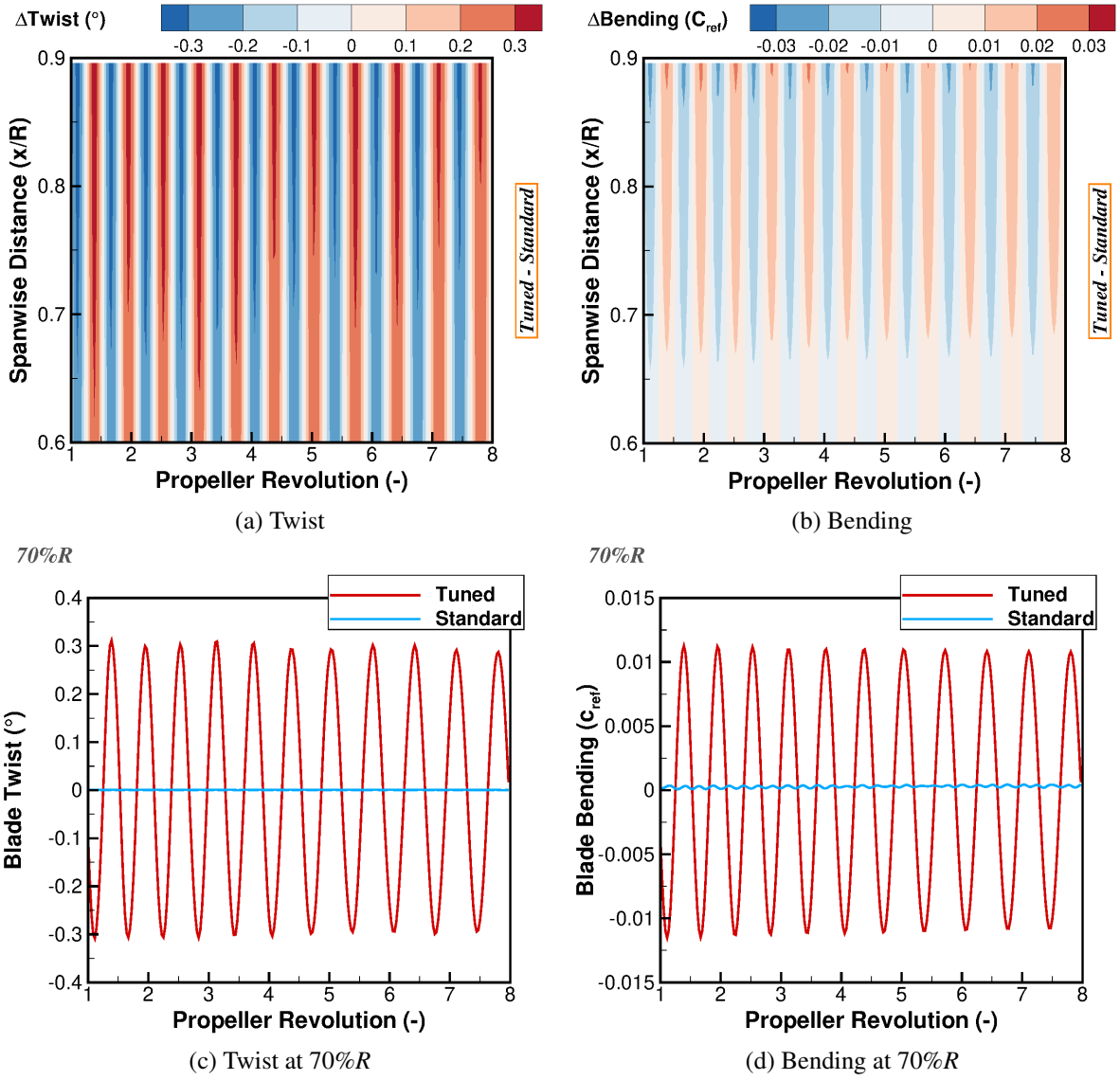

(a) Twist

(b) Bending

(c) Twist at 70%R

(d) Bending at 70%R

Figure 4.24: Difference in bending/torsion for the change in structural model for the Commander blade

Presented in Figure 4.25 is the full propeller normalised thrust coefficient for the tuned and standard structural model simulatons. The true thrust coefficients have been scaled by the average rigid value at 1400 (*rpm*). A similar profile is seen between both simulations. After the initial peak due to the aeroelastic start-up, the thrust coefficient linearly increases to a value 1.8$\times$ the rigid average value. Following the completion of the acceleration, the oscillations in thrust start to increase. This is clear in Figure 4.25(b) where the difference between the two simula-

tions is presented. Ignoring the final revolution of the acceleration where the rotational velocity is closest to the final value, differences in thrust of ± 0.17 are seen and this increases to ± 0.32 during the final steady-state revolutions. This is a combination of the blade bending/torsion and the flow-field excitation at the maximum velocity.

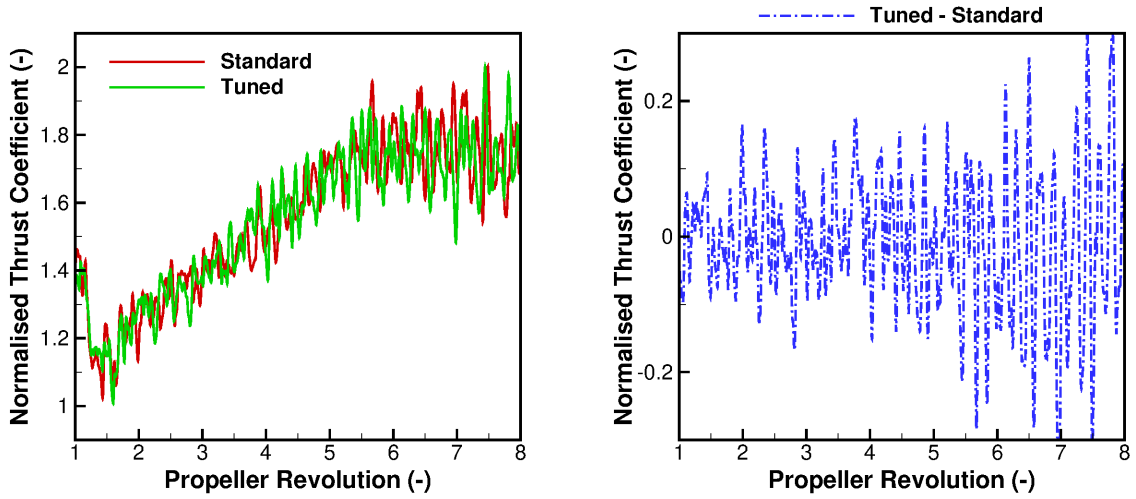

(a) Normalised C_T

(b) Difference between tuned and standard models

Figure 4.25: Resultant propeller thrust coefficient for the tuned and standard model simulations

4.6 Interpolated Modal Response

As described in Section 2.2.5, the modal response of the structure alters depending on the given conditions. In order to quantify the effects of this change in modal response during the blade acceleration, the tuned model is used with the interpolation function to simulate the propeller blade.

4.6.1 Supplied Modes

For this simulation the original tuned modes at 1400 (*rpm*) will be compared to the interpolation function with four and two stages supplied. This includes modes given at 1400, 1500, 1650 and 1750 (*rpm*) for the four stage. Only the starting (1400 (rpm)) and final (1750 (rpm)) modes are used for the two stage simulation. Figure 4.26 presents the interpolation schedule for the four and two stage simulations. This details the blending coefficient used to multiply the modal amplitude result for the supplied modes with the final deformation a combination of all stages. Due to the nature of the coefficient, at the select stages specific modes are fully active with the subsequent modes of no influence. During a period between stages, an inverse distance interpolation combines the nearest modes.

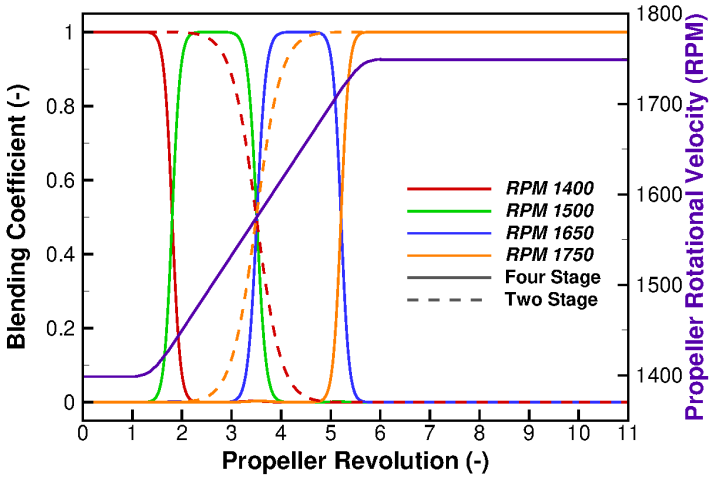

Figure 4.26: Interpolation scaling factor schedule for the tuned model acclerated blade simulation

In terms of the modal response, no signficant change was found in the mode shape with an alteration only found in the frequencies. The frequencies of each of the three modes at the four stages is presented in Table 4.6. As shown and expected based upon the Spoke diagram in Figure 4.21, an increase in frequency is seen for modes and hence an adjustment in the modal amplitude frequency is expected through the acceleration.

Table 4.6: Frequencies of each mode for every supplied stage of the interpolated simulation

	Rotational Velocity Stage			
Mode	*1400*	*1500*	*1650*	*1750*
1	41.96	43.50	45.87	47.78
2	73.25	74.38	76.12	77.30
3	134.84	136.74	139.75	141.88

4.6.2 Interpolated Four Stage Aeroelastic Results

Presented in Figure 4.27 is the modal amplitude results for the fixed and interpolated tuned modes. For the first mode (Figure 4.27(a)), very similar trends are seen between the two simulatons where a constant oscillation around a negligible average value is seen. The introduction of the interpolation function has resulted in an increase in modal amplitude for the first mode. The oscillations increase from ± 0.0062 to ± 0.0096, a 54.8% increase. The use of the interpolation function has very little impact on the full profile of the first mode.

Focusing on the second mode (Figure 4.27(b)), a decrease in the modal amplitude fluctuation of 41.6% is found. The interpolation function has a greater impact on the second mode profile

and as a result, the amplitude fluctuation reduces to 38.2% of the fixed tuned mode oscillations. A similar trend is captured across the third mode, where a minimum reduction of 24.55% is seen at the start of the acceleration with this increasing to 57.27% towards the end.

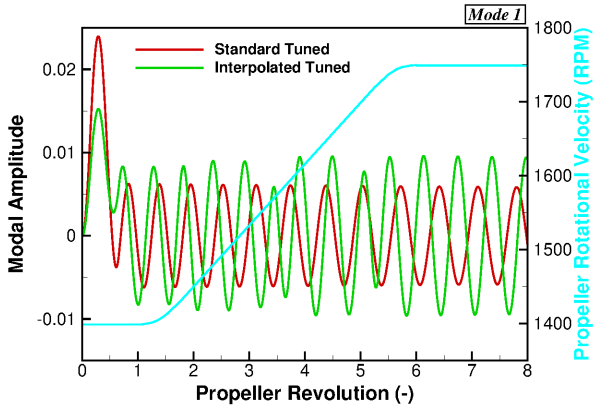

(a) Mode 1.

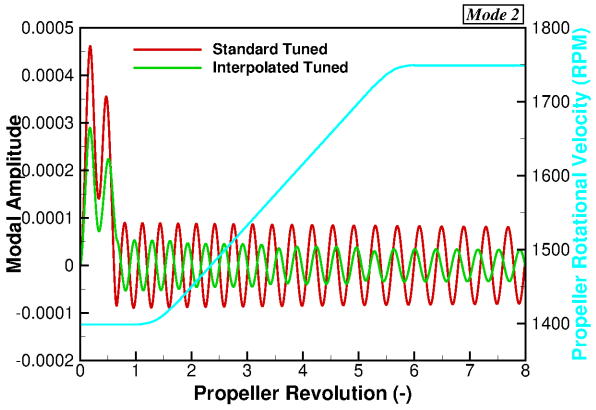

(b) Mode 2.

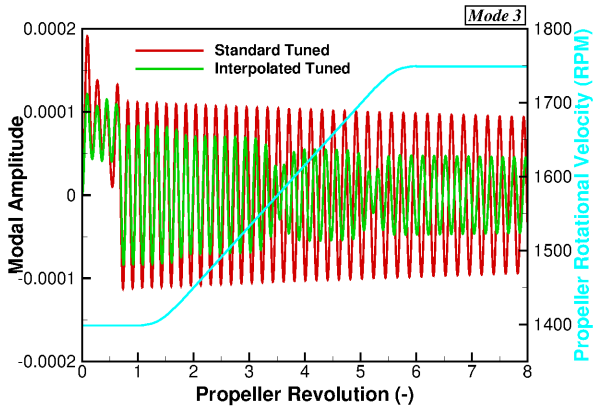

(c) Mode 3.

Figure 4.27: Comparison of the modal amplitude response for the introduction of interpolated modes to the Commander blade simulation

Presented in Figure 4.28 is the modal amplitude frequency response for the static and interpolated tuned mode simulations, across the full time-history. In addition to the alterations in amplitudes where the time-history results are mirrored, a slight shift in all modal amplitude frequencies are observed. For the static tuned mode simulation, the first mode oscillates at a frequency of 1.76/revolution . This increases by 5.7% to 1.86/revolution with the introduction of the interpolated modes. For the second mode, the largest amplitude frequency decreases from 3.05/revolution to 2.95/revolution . This equates to a difference of 3.12%. An increase in the third mode frequency is observed with an adjustment from 5.51/revolution to 5.68/revolution . The percentage shift in mode three (3.2%) is thus simular to the shift in mode two.

Presented in Figure 4.29 is the non-dimensional torsional stress results for the interpolated modes, with the difference take between the static (Figure 4.23(a)) and interpolated simulation also shown. As observed from both figures, an increase in torsional stress is found as a result of the introduction of the interpolation function. The average value has increased from 0.18 to 0.22,

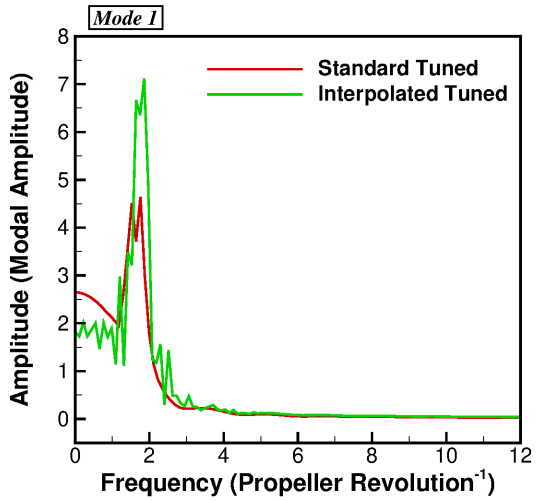

(a) Mode 1.

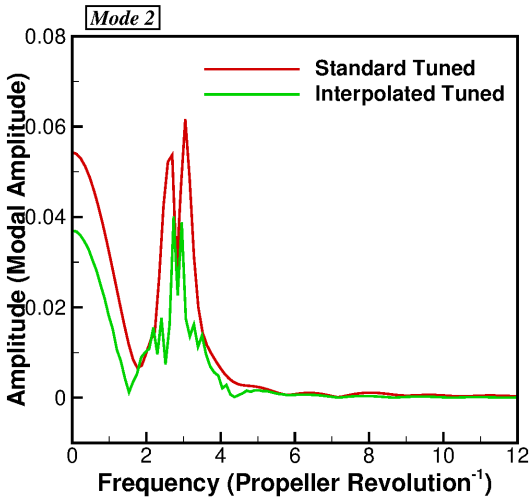

(b) Mode 2.

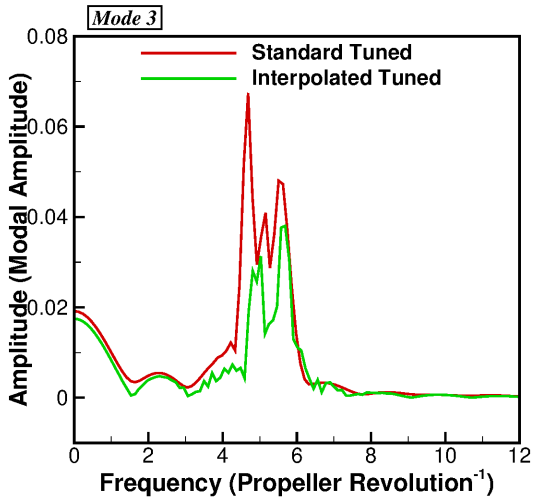

(c) Mode 3.

Figure 4.28: Comparison of the modal amplitude frequency response, across the full time-history, for the introduction of interpolated modes to the Commander blade simulation

an increase of 22%. In addition to this, the maximum value has increased from 0.76 to 1.04. The introduction of the interpolation function therefore correlates closer to the experimental results.

Examining the difference between the fixed and interpolated tuned mode simulations (Figure 4.29(b)), an average value of 0.044 is observed, thus indicating an overall increase in stress. The difference in stress results fluctuates around this average value with a maximum increase of 0.98 and reduction of 0.67, with the greatest fluctuation between the $0.6R$ and $0.7R$ stations. Between $0.6R$ and $0.7R$ an average value of 0.1247 is observed. This reduces to 0.0246 at the $0.7R$ to $0.8R$ station with a further reduction to 0.0015 outwards of $0.8R$.

Presented in Figure 4.30 is the difference in blade bending and torsion between the fixed and interpolation simulations. As expected based upon the torsional stress fluctuations, an increase of 50% in both bending and torsion is seen. This is driven by the increase in periodic fluctuation

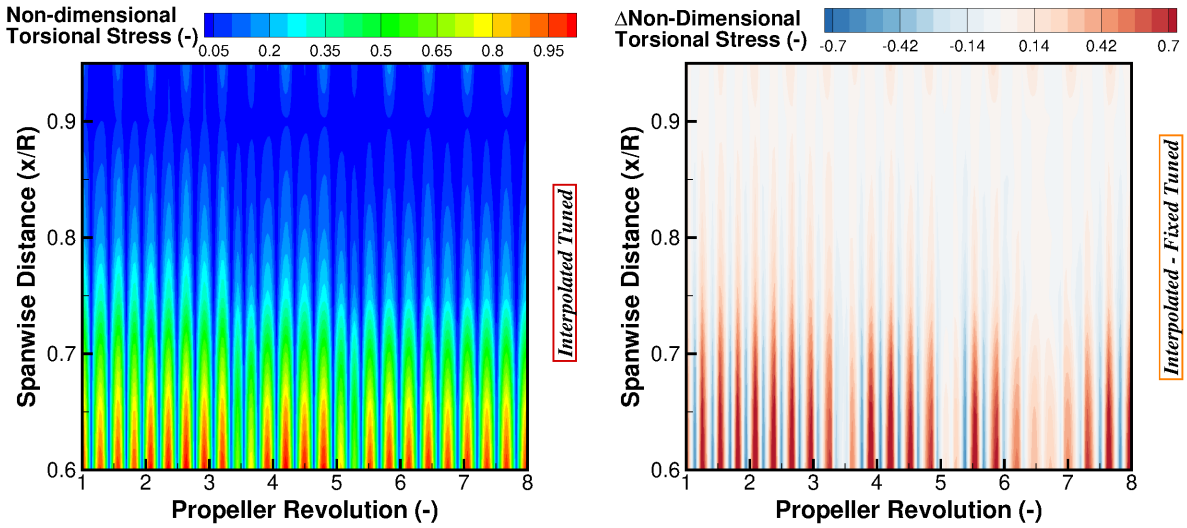

(a) Interpolation model

(b) Difference with baseline

Figure 4.29: Comparison of the non-dimensional torsional stress results for the introduction of interpolated modes to the Commander blade simulation

of the first modal amplitude. The introduction of the interpolation has also altered the pattern of the blade deflection through the acceleration. As the blade travels through the acceleration, a second order quadratic response of the maximum and minimum profiles is seen with the greatest peak occuring at the third revolution. This correlates to a rotatonal velocity of 1500 (rpm). As the blade nears the completion of the transient phase, the difference between the fixed and tuned simulations are seen to be minimal. The blade then follows a secondary quadratic response at the final state with the peak occuring at a faster rate.

In addition to the difference in bending/twist between the fixed and interpolated tuned model simulations, the raw bending and twist profiles at $70\%R$ are presented in Figure 4.30(c) and (d). The increase in deformation due to the introduction of the interpolated function is clear, with the bending and twist profiles following the trend of the first modal amplitude.

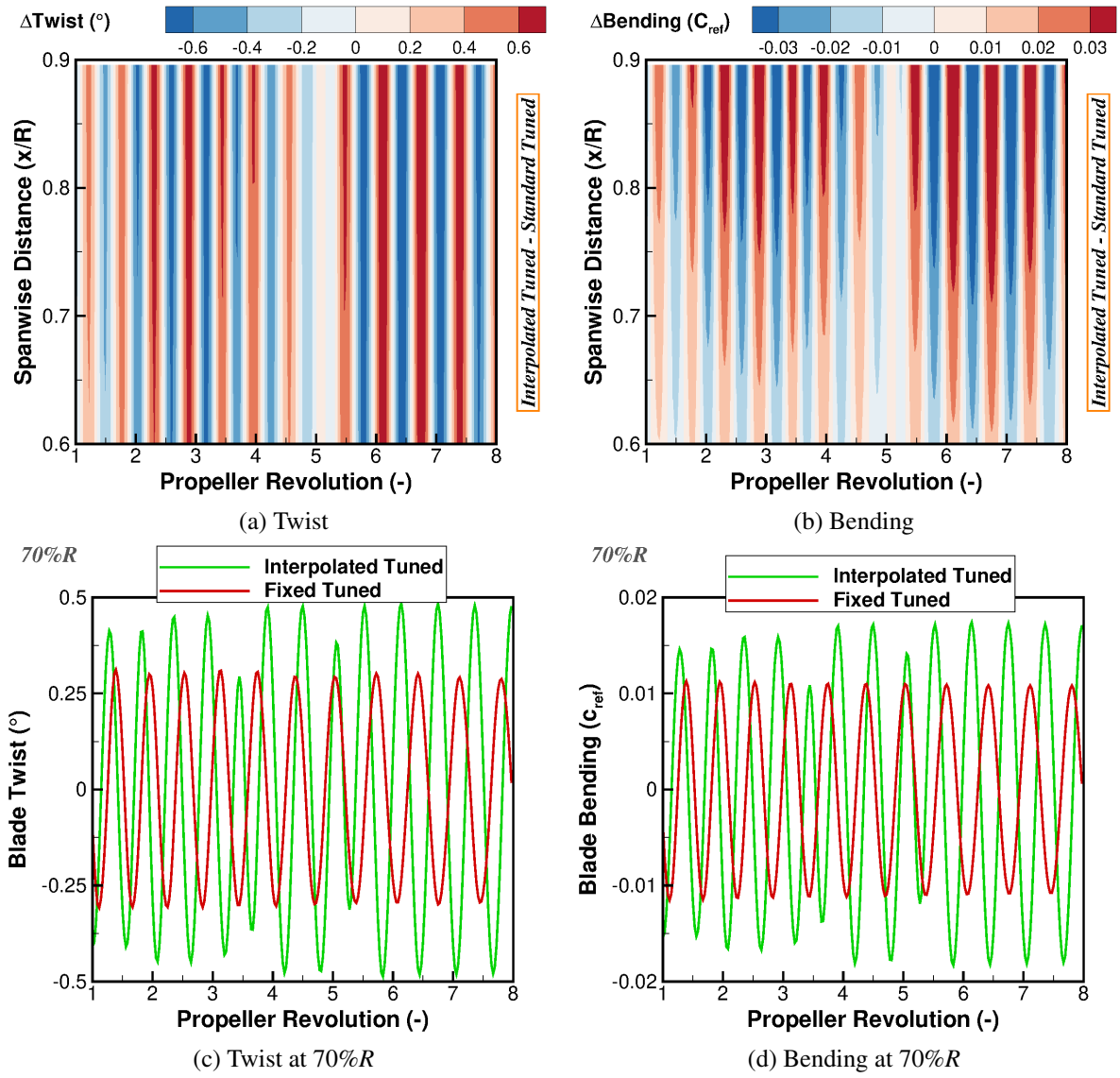

(a) Twist

(b) Bending

(c) Twist at 70%R

(d) Bending at 70%R

Figure 4.30: Difference in bending/torsion for the introduction of interpolated modes to the Commander blade simulation, along with raw results for the 70%R station

The introduction of the interpolated modes has a significant effect on the overall blade load. Presented in Figure 4.31 is the overall propeller thrust coefficient for the fixed and interpolated tuned mode simulations. The thrust values have again been normalised with respect to the average rigid value at 1400 (rpm). As observed, a sizable reduction in the overall force is seen across the full simulation with an average reduction of 16%. This is highlighted in Figure 4.31(b) where all differences are negative, with respect to the interpolated modes. A key observation of the difference in thrust coefficient is the increase in fluctuation following the transition. Between revolutions 2-5, fluctuation magnitude of ± 0.1 are observed. This increases to ± 0.2 after the 5th revolution. Similar responses are also found in the comparison of the standard and tuned models (Figure 4.25(b)) and is driven by the increased pressure fluctuations at the maximum rotational velocity.

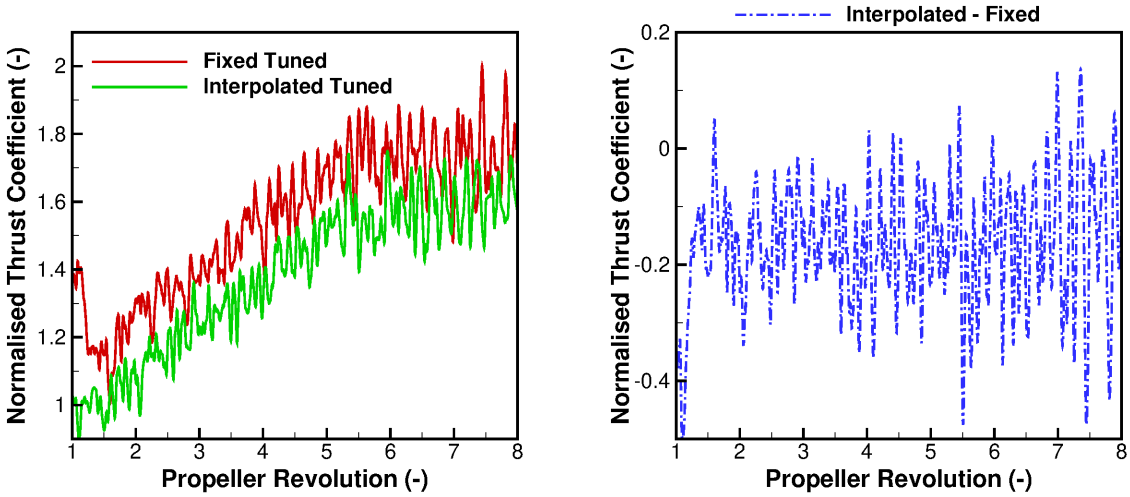

(a) Normalised C_T

(b) Difference between the fixed and interpolated tuned modes

Figure 4.31: Resultant propeller thrust coefficient for the fixed and interpolated tuned mode simulations

4.6.3 Interpolated Two Stage Aeroelastic Results

Presented in Figure 4.32 is the time-history of the two and four stage interpolated simulations using the tuned modes. The modes supplied for the two stage simulation were at the start and end of the transition, hence, the modal amplitude response is the same between the simulations at these stages. Only a slight reduction of 17.65% in the modal amplitude fluctuation magnitudes is observed for the second mode during the final revolutions.

As expected, the key changes in modal amplitudes are observed during the acceleration. For the first mode, the magnitude of the fluctuations remain fairly constant throughout the acceleration for both two and four stages. A change in frequency is observed at the start and end of the transition, and this is a result of the higher and lower frequencies at 1500 and 1650 (rpm), respectively, to the 1400 and 1750 (rpm) two stage results. A similar response is observed for the second and third modes.

Presented in Figure 4.33 is the non-dimensional torsional stress results for the two stage interpolated simulation with a comparison between the four stage also shown. The use of two stages has a minimal effect on the stress results with an increase in average from 0.22 to 0.23 and reduction in the maximum value from 1.04 to 1.03. As shown from the modal amplitude results, the greatest changes comes during the two stage interpolation phase. Here, an oscillation of the stress of ± 0.6 is seen.

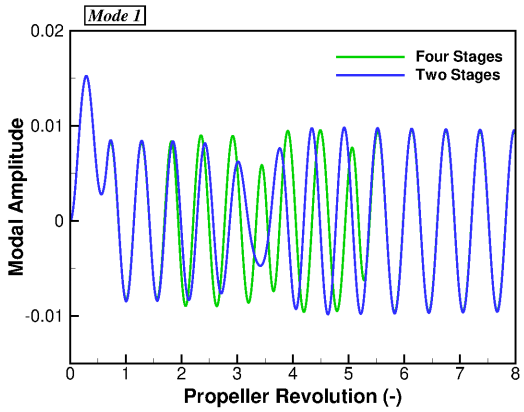

(a) Mode 1.

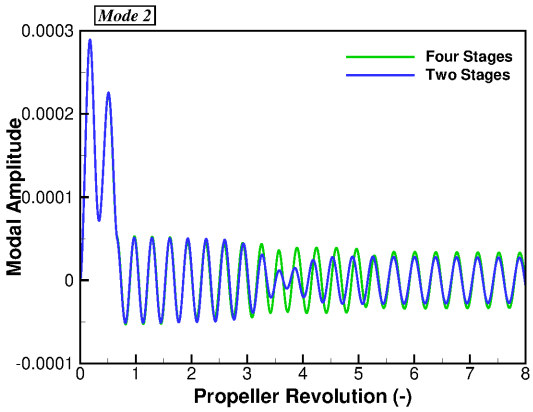

(b) Mode 2.

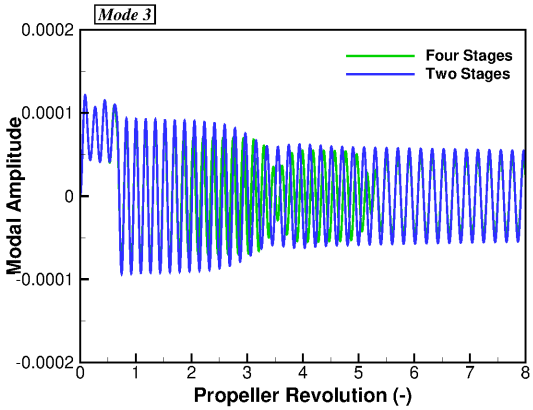

(c) Mode 3.

Figure 4.32: Comparison of the modal amplitude response between the two and four stage interpolated modes

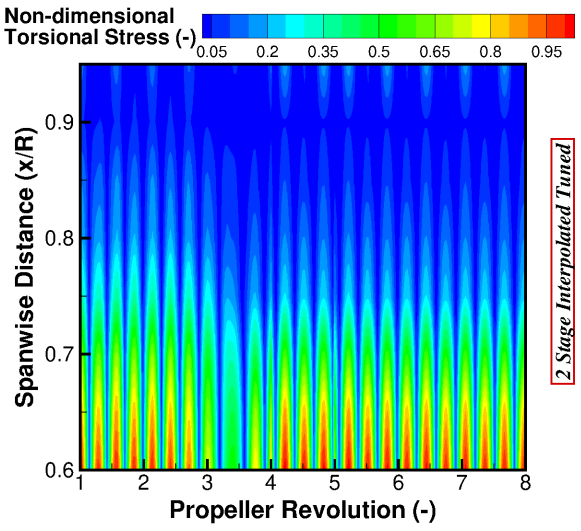

(a) Two stage interpolation

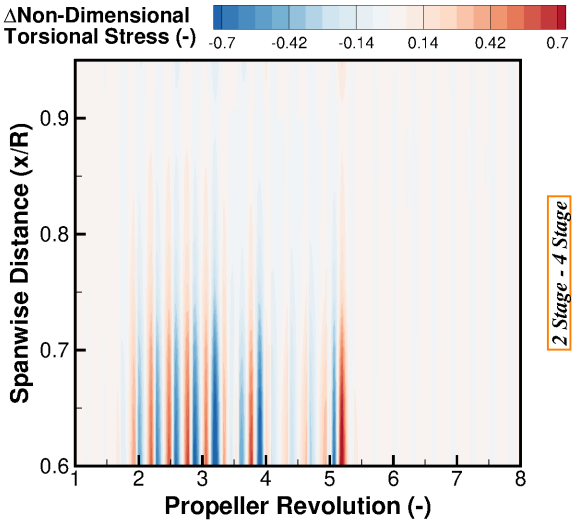

(b) Difference with four stage interpolation

Figure 4.33: Comparison of the non-dimensional torsional stress results between the two and four stage interpolated simulations

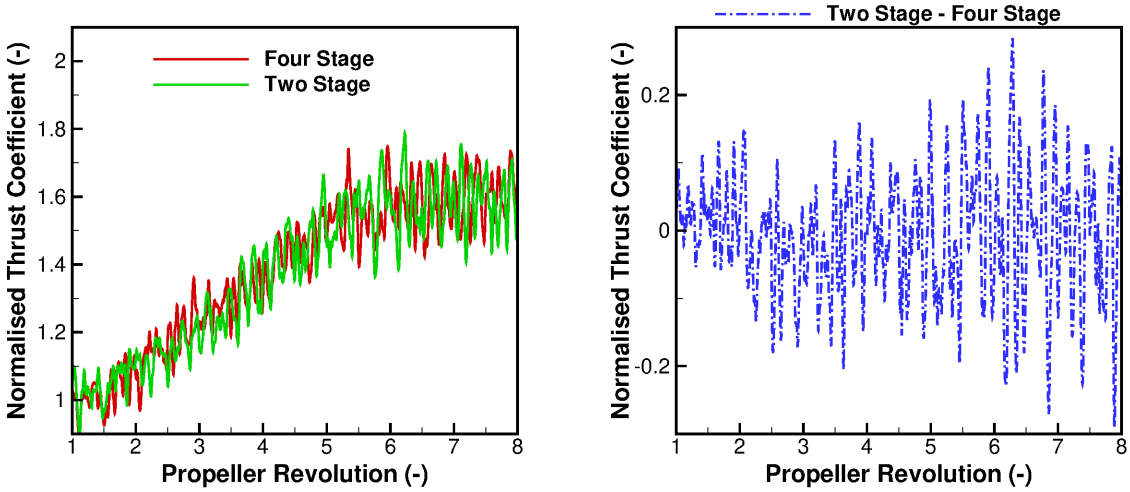

(a) Normalised C_T

(b) Difference between the two and four staged interpolation

Figure 4.34: Resultant propeller thrust coefficient for the two and four staged interpolation

In terms of the overall blade load, in a similar manner to the modal amplitude and stress results, very little change is oberved with the normalised thrust coefficient presented in Figure 4.34. Filtering out the high frequency detached flow content, the difference in average between the simulations is 0.0026. Due to the nature of the stalled flow, fluctuations in the instantaneous thrust of ± 0.2 is seen with the greatest fluctuation seen after the blade acceleration.

As observed from the two stage results, very little difference is observed for this simulation. Due to the test conditions being limited to the given velocity range, this is expected based upon the almost negligible change in mode shape and frequency for this model. Greater consideration of the amount of interpolated stages would be required across a larger velocity range or with a structural model that signficantly changed. It is shown from the interpolated simulations that the influence is significant with a closer approximaton to the experimental value seen for both interpolated simulations.

4.7 Transient Phase Effect

The previous simulations have all been conducted with an accelerating blade. The introduction of the interpolation function indicated a variation in the blade response. In order to assess this further, the direction of change in blade rotational velocity is switched. This section will determine the differences found between an accelerating and decelerating blade using the interpolation function with the tuned model derived mode shapes and frequencies.

4.7.1 Deceleration Computational Setup

For this simulaton the Commander propeller blade was decelerated from 1850 to 1400 (rpm). As per the reference accelerating case, four stages are supplied for the interpolation feature. This includes mode shapes at 1400, 1550, 1700 and 1850 (rpm) with the changes in frequency shown in Table 4.7. The interpolation schedule, along with the rpm profile, is presented in Figure 4.35 with the deceleration taking place over six propeller revolutions. The number of transient revolutions was increased to account for the higher velocity.

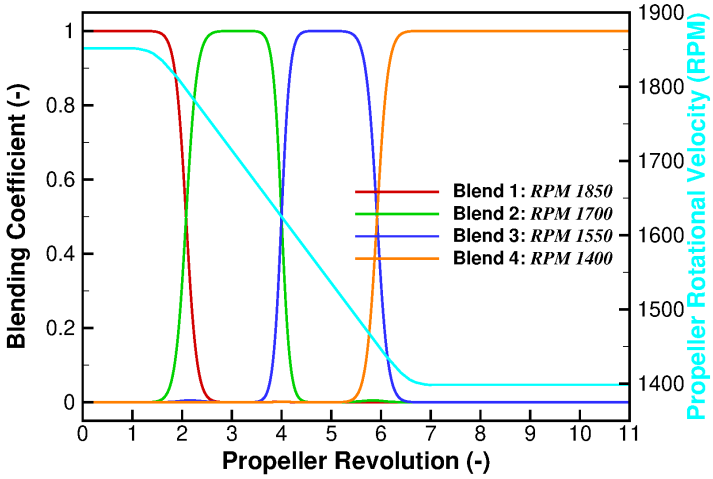

Figure 4.35: Interpolation scaling factor schedule for the tuned model decelerated blade simulation

Table 4.7: Frequencies of each mode for every supplied stage of the declerating interpolated simulation

	Rotational Velocity Stage			
Mode	*1850*	*1700*	*1550*	*1400*
1	49.11	46.67	44.28	41.96
2	78.50	76.71	74.95	73.25
3	144.08	140.80	137.72	134.84

4.7.2 Deceleration Aeroelastic Results

Presented in Figure 4.36 is the modal amplitude results for the decelerating and accelerating blades. As observed, significant alterations to the to the modal amplitude results are found with changes in both trend and magnitude. Looking at the first mode, the accelerating simulation

produces an amplitude profile which remained stable throughout the calculation. The decelerating blade, however, results in a profile which signficantly alters its magntiude through the transient phase. Oscillations of ± 0.0096 are observed throughout the simulation for the accelerating blade. At the start of the blade deceleration, the magntiude of the oscillation is found to be 47% smaller, a value of ± 0.0051 during the first to fourth propeller revolution. Towards the end of the transient phase, revolutions four to six, this increases by 33% to ± 0.0068. The final oscillation magntiude reaches values of ± 0.011 after the sixth revolution, taking it above the accelerating blade value by 14.6%. Due to the first mode having the highest modal amplitude values, this change in profile has a signficant effect on the blade deformation.

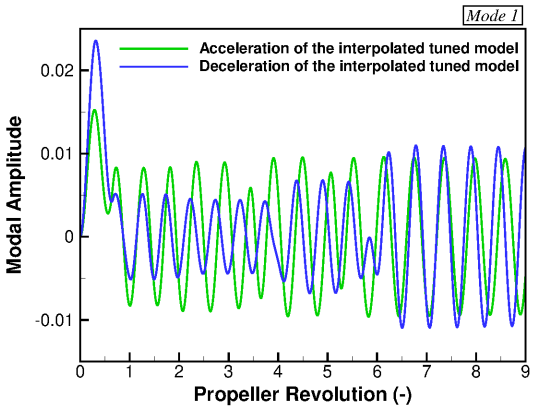

(a) Mode 1.

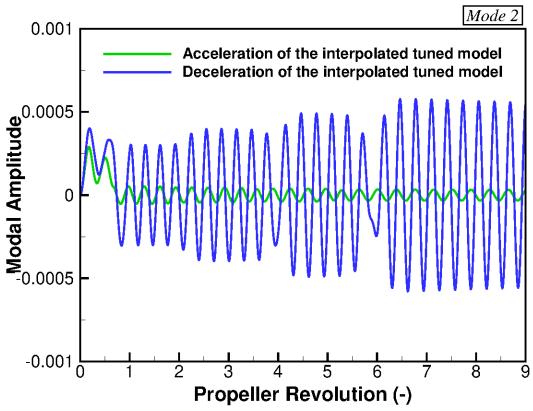

(b) Mode 2.

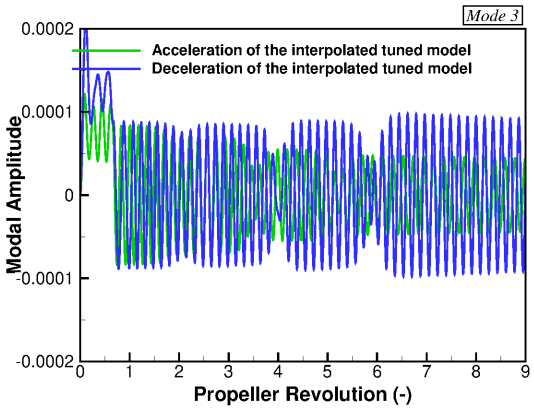

(c) Mode 3.

Figure 4.36: Difference between the accelerating and decelerating interpolated modal response for the Commander propeller

The shift in magnitude for the first mode results in a 115% increase. Such an increase is not observed in the second or third mode, with more stable profiles seen through the transition. The accelerating and decelerating results for the second mode mirror each other through the transient, however the values are an order of magnitude apart. For the accelerating blade, the magnitude of the oscillation starts of at $\pm 5.24 \times 10^{-5}$, decreasing to $\pm 3.4 \times 10^{-5}$. For the declerating blade, the magnitude starts at $\pm 3.97 \times 10^{-4}$ before increasing to $\pm 5.77 \times 10^{-4}$. This represents a 35%

and 45% shift in magnitude, respectively, from start to finish.

The smallest shift in magntiude is observed in the third mode for the decelerating blade. For the decelerating blade, the third mode starts oscillating at a value of $\pm 8.77 \times 10^{-5}$ increasing to $\pm 9.76 \times 10^{-5}$ through the deceleration. An 11% increase. The accelerating blade, however, follows the opposite trend with a far greater change in magntiude. The acclerating blade third mode starts at a similar value to the decelerating blade, $\pm 8.28 \times 10^{-5}$. This value decreases by 43%, following the increase in velocity, to a value of $\pm 4.73 \times 10^{-5}$.

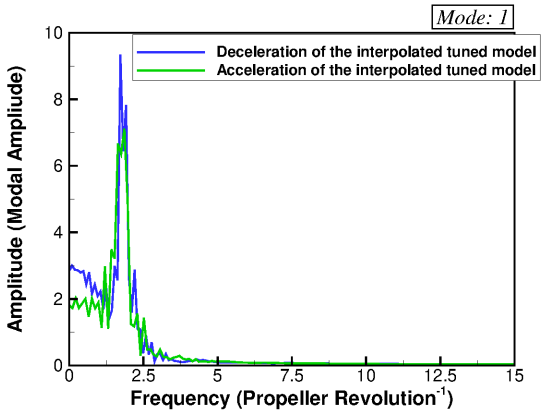

(a) Mode 1.

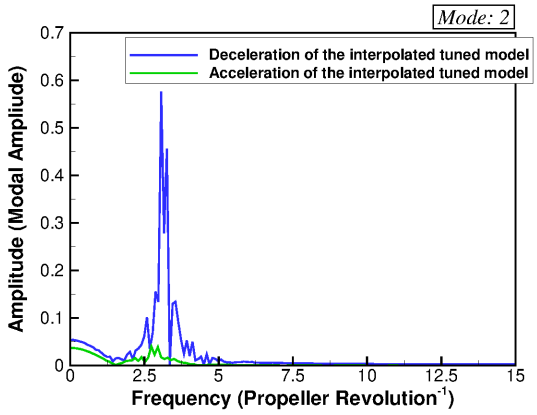

(b) Mode 2.

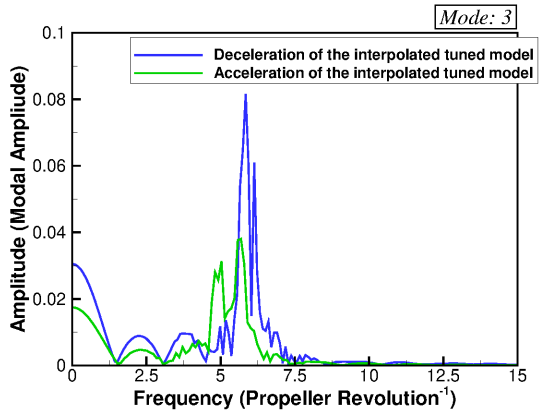

(c) Mode 3.

Figure 4.37: Comparison of the accelerating and decelerating interpolated modal frequency response for the Commander propeller

Presented in Figure 4.37 is the frequency response of the accelerating and decelerating simulations. For the first mode, a similar profile is observed between the two. In line with the modal amplitude results, an increase in amplitude is observed with a slight increase in frequency. The accelerating blade results in a peak frequency of 1.75/revolution with the decelerating blade peak occuring at 1.82/revolution . Two subsequent peaks are seen either side of this average with the a smaller band of 0.19/revolution seen for the decelerating blade compared to 0.22/revolution for the accelerating simulation. A similar response is seen for the second mode where an increase in frequency and magnitude is observed. The greatest change in frequency

response comes from the third mode. Two peaks are again observed for the decelerating simulation, however, the lower peak occurs at a frequency 0.81/revolution higher than the accelerating. This shift also has a signficant effect on the secondary peak where the band range is decreased by 56.2%.

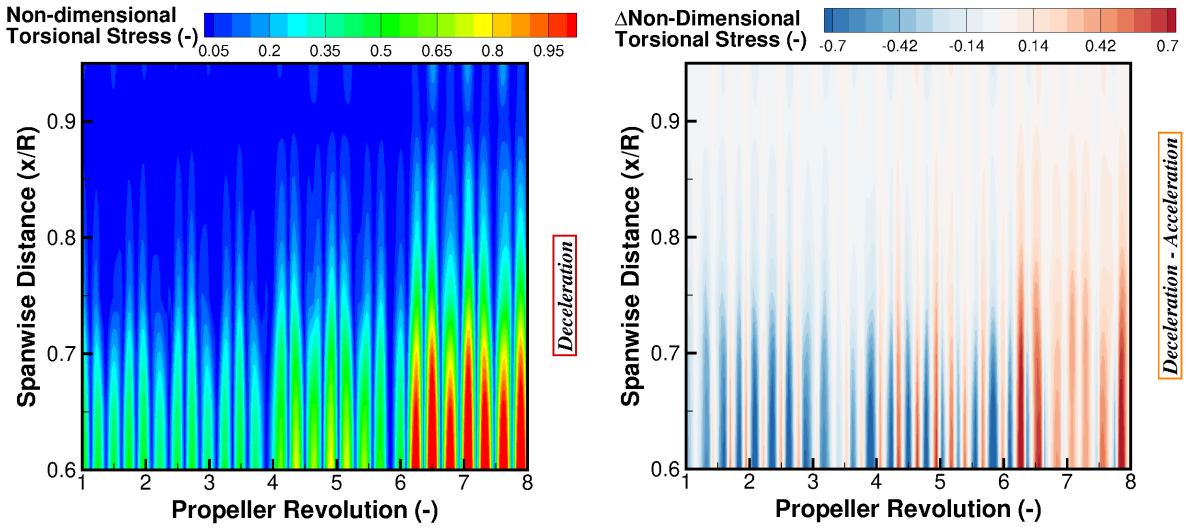

(a) Deceleration

(b) Difference with baseline

Figure 4.38: Difference between the accelerating and decelerating interpolated non-dimensional torsional stress response for the Commander propeller

Presented in Figure 4.38 is the non-dimensional torsional stress response for the decelerating blade with the difference between the simulations shown. The stress response follows the same trend as seen in the first modal amplitude (Figure 4.36(a)). From revolutions one to four, a reduction in torsion stress is seen when compared to the accelerating blade. The overall average response during this phase is a reduction of 0.134, where 67.6% of the response is dominated by a significant reduction in stress. This negative response results in an average reduction of 0.208 and maximum value of 1.0.

The second phase encompasses an increase in torsional stress content for the decelerating blade and ranges from revolutions four to six. From the first to second phase, the average stress value for the decelerating blade increased from 0.1088 to 0.1172, a 7.72% increase, with a larger increase of 45.4% seen in the maximum value. Although the stress values have risen, the accelerating blade stress values are seen to be higher at this stage. The average difference during this phase is of a 0.030 reduction.

The third phase represents a significant increase in torsional stress for the decelerating blade. Between revolutions six to eight, the average stress value has increased by over 300% to 0.4970, with the maximum value increasing by a further 73.2% to 1.362. This is a significant increase in torsional content and takes it above the reference value seen in the experiment.

Presented in Figure 4.39 is the difference in blade bending and torsion between the accelerating and decelerating simulations, along with plots of the twist and bending at 70%R for both

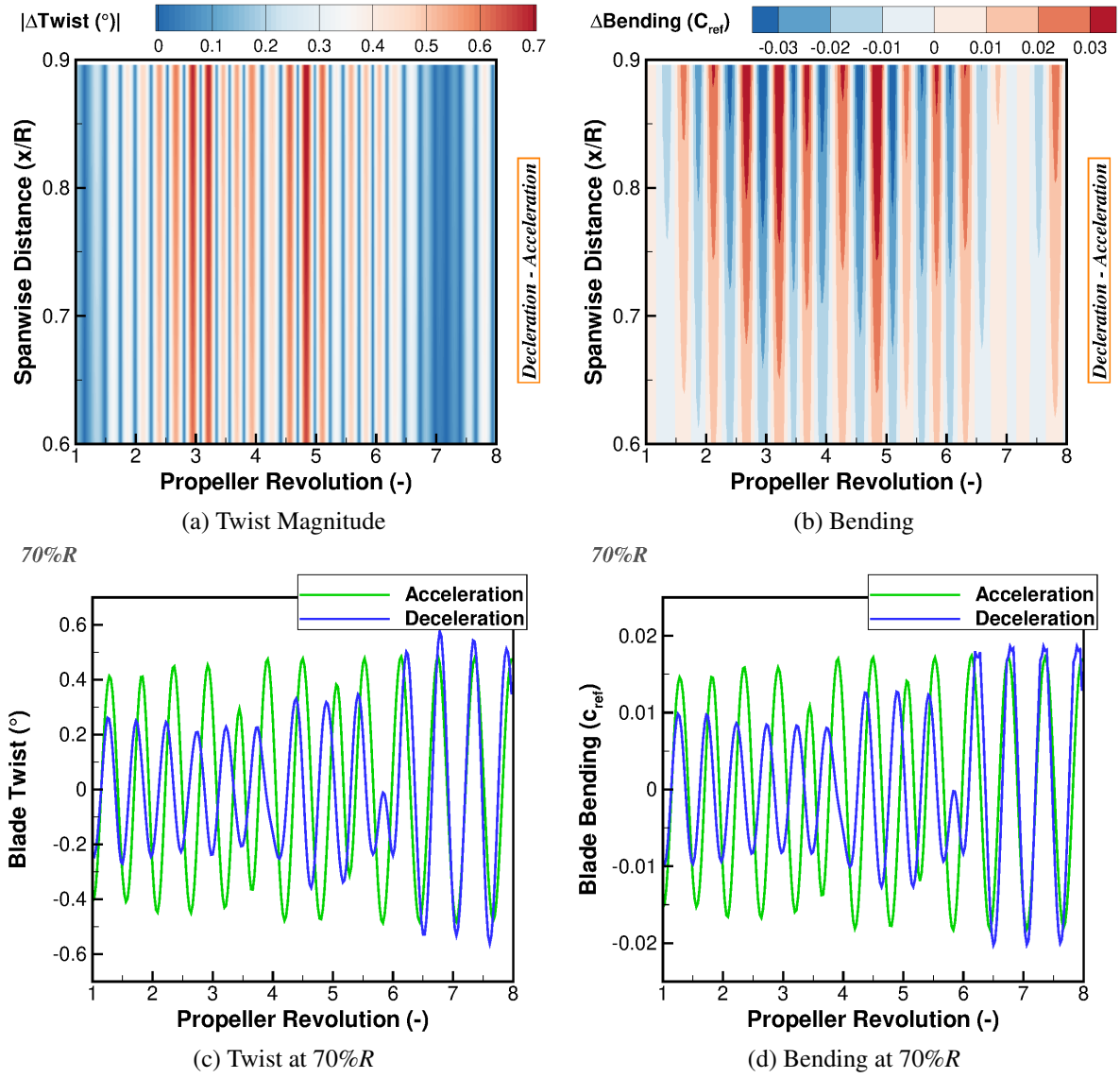

(a) Twist Magnitude

(b) Bending

(c) Twist at 70%R

(d) Bending at 70%R

Figure 4.39: Difference in the bending/torsion of the Commander blade between the accelerating and decelerating simulations

simulations. The change in blade twist is presented as the magntiude of the difference in order to show the oscillation trends through the simulation with no significant variation found along the blade radius. The twist oscillations gradually increase from revolution one through to a maximum of $\pm 0.7^{o}$ around revolution three. This oscillation quickly decreases during this revolution before increasing again around revolution five. This secondary peak has increased in magnitude to $\pm 0.73^{o}$. Following this, the magnitude of the twist oscillations decline towards the end of the deceleration.

These trends of twist difference are driven by the differences in modal amplitude for the first mode (Figure 4.36(a)) and are highlighted via the raw twist results at 70%R presented in Figure 4.39(c). The increase in difference magnitude between revolutions 1 to 3 is found as a result of the decrease in pitch for the decelerating blade and increase in pitch for the accelerating

blade. As the simulation transitions from one interpolation stage to the other, a phase difference between the simulatations occurs resulting in the maximum difference magnitude of $\pm 0.73^{o}$ at the second peak. As per the modal amplitude results, the final revolutions see very similar twist values and as a result the difference between the two is at its lowest.

A similar trend in terms of two distinct peaks is captured across the change in bending (Figure 4.39(b)) and raw bending results (Figure 4.39(d)). A greater difference is found along the radial direction with the maximum values captured at the tip and virtually no bending occuring inward of $0.6R$.

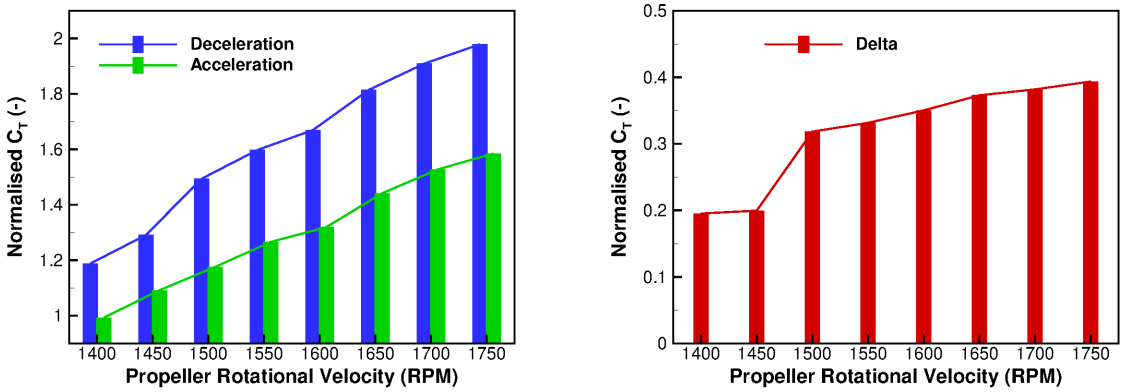

(a) Normalised C_T

(b) Difference between the acclerating and decelerating

Figure 4.40: Resultant propeller averaged thrust coefficients for the decelerating and accelerating simulations

Presented in Figure 4.40 is the propeller averaged normalised thrust coefficients for the decelerating and accelerating simulations at selected rotational velocities, with the difference between the simulations also shown. Starting with the accelerating blade, the initial value at 1400 (rpm) is seen to be slightly less than the average rigid value and this is expected based upon the fact the accelerating simulation starts from this rigid solution. The accelerating thrust value then gradually increases to 60% above the starting value. For the decelerating blade, a significant increase in thrust is observed across the velocity range with an average difference of 32% of the rigid value. The difference between the decelerating and accelerating simulations is fairly constant across the range except at 1400 and 1450 $(rpm)$where the difference drops below 20%. This drop at the lower velocity range is a result of the higher value fluctuations being filtered out in the average calculation as a greater amount of time is spend around these values.

4.8 Conclusions

A time-marching aeroelastic method using CFD has been derived, with the quality of the computational mesh preserved throughout the calculation. For the Commander propeller blade, qualitative agreement can be found between the simulation results and experiments, whilst using the

SAS simulation model for the accelerating blade with the standard mode shapes provided at a single state. An absolute correlation between the torsional stress levels was not seen, however the trend of stress across the blade radius are predicted well for the *SAS* simulation. A qualitative comparison of the modal amplitude response is presented with an unstable solution achieved for the *SAS* computation. The *URANS* calculation did not provide such a response, and therefore, this highlights the need for scale-resolving CFD methods for stall flutter predictions.

A comparison was also made between the accelerating blade and fixed rpm simulations. In terms of the modal response, similar profiles are observed between the simulations with a reduction in frequency seen for all modes. However, the response seen in terms of the torsional stress distribution across the blade radius for the fixed rpm simulation did not correlate to the experiment. As a result, to mirror the response seen in the experiment, the acceleration of the blade is seen as critical to the evaluation of torsional stress.

The setup of the Commander propeller blade simulations focused on a pitch angle of $27^{o}40'$ where significant stall was present. In order to ensure the aeroelastic excitation were a result of the detached flow, simulations were conducted at a pitch angle of $12^{o}40'$ (reducton of 15^{o}). As indicated from the modal amplitude results, a significant reduction of the aeroelastic magnitudes were observed. Thus, contributing the oscillations to stall.

The validation of the structural model is seen as critical to the modelling response. For the standard model, general shape and active frequencies were known for the blade and, hence, the inertias were adjusted to match these results. In addition to this, a bungee test of the propeller blade was conducted and this focused on the extraction of the free mode shapes and frequencies. The differences in frequency were not too dissimilar, however, greater detail on the shape became available and hence, the inertias were again tuned to match such shapes. The influence of these new modes shapes were investigated and found a significant increase in the torsional stress and blade deformation. The removal of the chordwise response from the standard modes resulted in a greater level of flapwise bending and therefore, torsion. This change in mode shape resulted in a closer stress result to the experiment with a maximmum non-dimensional value of 0.76.

As the blade accelerates through the velocity range, a change in modal response would be seen across the blade. In order to mirror this, the effect of the interpolation function was computed against the single stage tuned modes. With a total of four stages supplied through the acceleration, an increase in torsional stress was achieved. The maximum was increased to 1.04 taking the result above the reference experimental value. Due to the increase in blade deformation, a reduction in overall thrust was observed using the interpolated modes.

The setup of the interpolation function was analysed via the comparison of the four and two stage simulation results. As was seen, very little difference was observed between the two simulations in terms of maximum and average stress results. Therefore, all remaining simulations with modal interpolation utilise four stages. Such an influence must be examined depending on

the transient range and structural response.

The focus of the simulations was on an acceleraing blade and this was selected to mirror the physical experiment. This transient phase has a significant influence on the modal amplitudes and this was demonstrated via the simulation of a decelerating blade. Starting from a higher rotational velocity state, and using the interpolated tuned modes, a greater variation in the response was seen through the transient phase. Looking at the stress results, such values gradually increased through this phase reaching a maximum value of 1.362. Although all accelerating blade simulations were shown to suffer from stall flutter, via the oscillations of modal amplitudes, the decelerating blade has shown a sharper response to the conditions. The decrease in velocity results in the detached vorticies remaining enclosed around the blade for longer. This results in a greater amount of positive pressure fluctuations acting on the blade.

Chapter 5

Estimation of Three-Dimensional Aerodynamic Damping*

Aeroelastic phenomena of stall flutter is the result of the negative aerodynamic damping associated with separated flow. From this basis, an investigation was conducted to estimate the aerodynamic damping from a time-marching aeroelastic computation. An initial investigation is conducted on the NACA 0012 aerofoil section, before transition to 3D propellers and full aeroelastic calculations. Estimates of aerodynamic damping are presented, with a comparison made between *URANS* and *SAS* . Use of a suitable turbulence closure to allow for shedding of flow structures during stall is seen as critical in predicting negative damping estimations. From this investigation, it has been found that the *SAS* method is able to capture this for both the aerofoil and 3D test cases.

5.1 Two-Dimensional Aerodynamic Damping

Very few 2D cases have been conducted for specific propeller sections to allow for the introduction of the *SAS* approach for the calculation of aerodynamic damping. As a result, the NACA 0012 section was selected due to the amount of experiment data available at different pitching conditions. The 70%R and 90%R Commander aerofoils were also investigated to provide a comparison with the NACA 0012 for a specific propeller section.

5.1.1 2D Aerodynamic Damping Calculation

To fully determine the stability of the aerofoil section, the amount of aerodynamic damping within the system can be computed via the integration of the pitching moment coefficient with respect to the pitching angle. Such a method was described by Corke in 2015 [33] with the

*The results presented in this chapter is published in R.J. Higgins *et al.* "Estimation of Three-Dimensional Aerodynamic Damping using CFD", *The Aeronautical Journal*, Vol. 124, Issue 1271, doi: 10.1017/aer.2019.135, 2020

derivation of the aerodynamic damping shown in Equation 5.1, where C_m^D and C_m^U are the pitching moment coefficients on the downstroke and upstroke, respectively, and α_h is the harmonic pitching angle.

$$\theta_{cycle} = \frac{1}{\pi \alpha_h^2} \int \left(C_m^D - C_m^U \right) d\alpha \tag{5.1}$$

5.1.2 Computational Setup

NACA 0012 Section

The topology of the grid follows a traditional C-grid type with a downstream far-field boundary applied at 15 chords from the trailing edge. In terms of the mesh, 650 cells were distributed around the aerofoil with 85 cells distributed via an exponential law, clustering to $1 \times 10^{-6}\, C_{ref}$, outward of the aerofoil surface. This is shown in Figure 5.1.

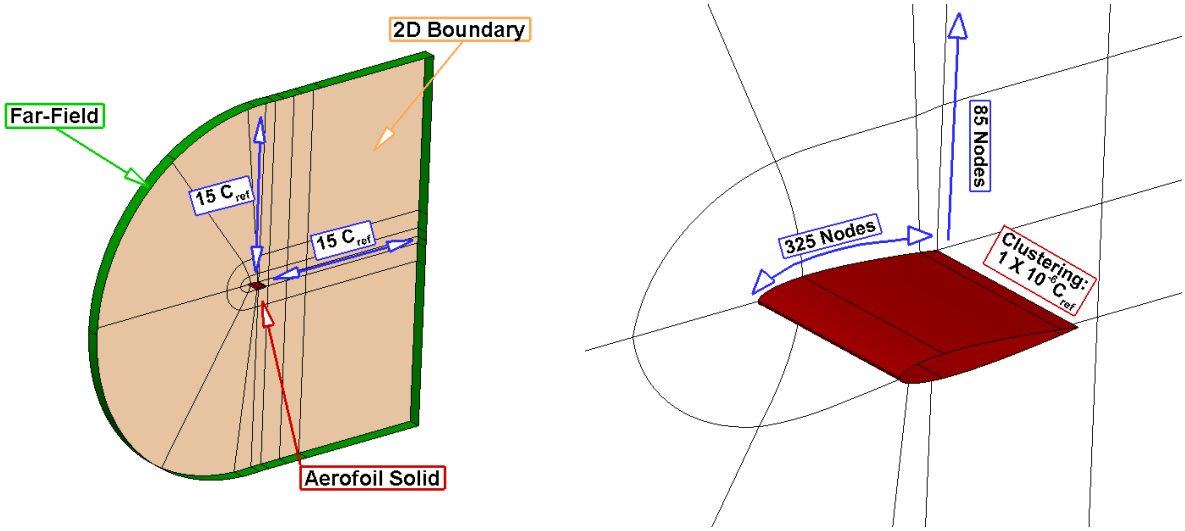

(a) Domain

(b) Solid wall detail

Figure 5.1: Computational grid for the 2D NACA 0012 aerofoil

Standard two-dimensional boundary conditions were applied to the spanwise boundary faces for an initial verification (Section 5.1.3) of the mesh quality and CFD setup, with a single computational cell in the spanwise direction of length 1 chord. A single chord spanwise length was selected due to the ease of non-dimensional load scaling within HMB3. Following this, the two-dimensional conditions were replaced with periodic boundary conditions. This allows for quasi-3D simulations where scale-resolving turbulence modelling can be implemented. For this investigation standard *URANS* closed with the $k-\omega$ shear-stress-transport (SST) turbulence model was compared to SST-*SAS* . No difference in aerofoil loads was observed between the 2D and quasi-3D simulations using the standard *URANS* formulation, hence, only the 2D *URANS* loads are presented. For the quasi-3D simulations, the spanwise length was set to a quarter of the chord, with a quarter chord selected based upon the findings of the LESFOIL project [94].

This project was sponsored by the European Union and involved seven partners looking into the feasibility of Large-Eddy-Simulation (LES) for the computation of flow around an aerofoil. One of the findings found that for accurate turbulence production from scale-resolving methods, the spanwise extent of the aerofoil must not be greater than a quarter of the chord.

The test conditions for this calculation are presented in Table 5.1 and correspond to experiments by McAlister in 1982 [91]. These test conditions were selected as they represent typical flow conditions found during the dynamic stall of a helicopter rotor in forward flight and based upon the experimental report, these test conditions were found to have negative aerodynamic damping.

Commander Aerofoil Section

In a similar manner to the NACA 0012 investigation, a matched grid was derived for the Commander $70\%R$ and $90\%R$ sections with similar topology, number of grid points and points distribution used. Subtle modifications to the NACA 0012 mesh are required to account for the blunt trailing edge on the Commander sections.

For the Commander sections, the same computational setup, in terms of time-step, pseudo steps, CFL and turbulence modelling, as the NACA 0012 case is selected. Standard 2D and quasi-3D simulations were conducted. The selected test conditions for the Commander sections are presented in Table 5.1. These test conditions were selected based upon the Mach number and pitch angle seen by the 3D blade, with a harmonic pitch angle of 5° selected to determine its response. All *SAS* simulation results were phased averaged over 4 revolutions before comparing to standard *URANS* .

Table 5.1: Test Conditions for the Dynamic Stall Computations

Parameter	*NACA 0012*	*70%R*	*90%R*
Reynolds Number	2.42×10^6	1.8×10^6	2.0×10^6
Mach Number	0.184	0.44	0.57
Reduced Frequency	0.149	0.18	0.12
Pitching Motion	$15^{\circ} \pm 10^{\circ} \sin(2k\tau)$	$12^{\circ} \pm 5^{\circ} \sin(2k\tau)$	$8^{\circ} \pm 5^{\circ} \sin(2k\tau)$
Steps per Revolution	1600		
Pseudo-Steps	200		
Modelling	*URANS* $k-\omega$ SST & *SAS*		

5.1.3 NACA 0012 2D Verification

In order to verify the two-dimensional grid, the following parameters were altered: grid size, number of unsteady pseudo-steps, unsteady time-step, and CFL number. The range of tested parameters are presented in Table 5.2. The datum values, as additionally highlighted in the test conditions of Table 5.1, are 196,716 volume cells, 200 pseudo-steps, 1600 steps per revolution and a CFL value of 10.0. For all parameters, a comparison in terms of experimental moment coefficient was made.

Table 5.2: Range of tested parameters for the NACA 0012 2D verification

Parameter	**Value Range**		
Grid size	48,720	196,716	447,488
Pseudo-steps	100	200	400
Steps per revolution	800	1600	3200
CFL	5.0	10.0	25.0

Presented below in Figure 5.2 is the comparison between the NACA 0012 verification simulations and the experimental data for the pitching moment coefficient. With an increase in the pseudo-steps, time-step and CFL number, the secondary stall event occurs earlier. Thus, moving the simulation results further from the experiments.

This difference is mimimal and the greatest change comes from the grid size. The experimental results present a two loop profile with the crossing point occuring around 12^{o}. For the coarse grid, complete different physics is seen with a three loop profile captured. The initial stall during the upstroke occurs early. The aerofoil then recovers quickly resulting in a positive damping loop (anti-clockwise moment loop). The secondary event due to the detached flow increases the pitching moment before recovering around 15^{o}.

With the increase in grid size to the baseline and fine mesh, similar profiles are observed. The simulations now mirror the experimental result during the upstroke with an earlier recovery in comparison to the coarse and experimental results. The difference between the baseline and fine simulations are minimal during the downstroke.

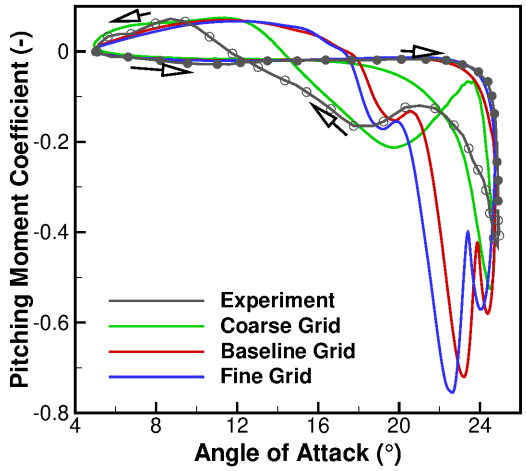

(a) Grid size

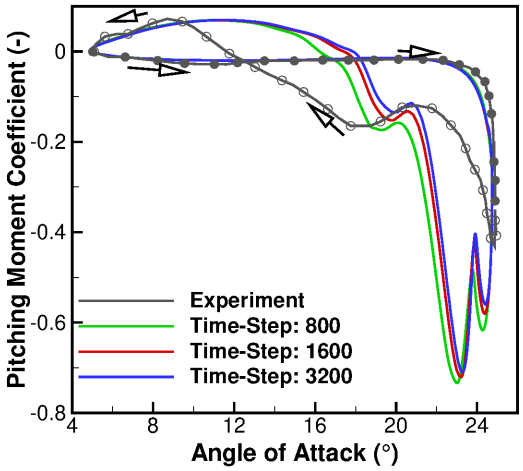

(b) Time-step

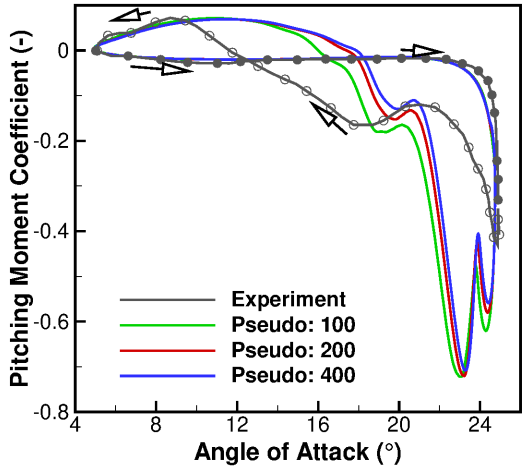

(c) Pseudo-steps

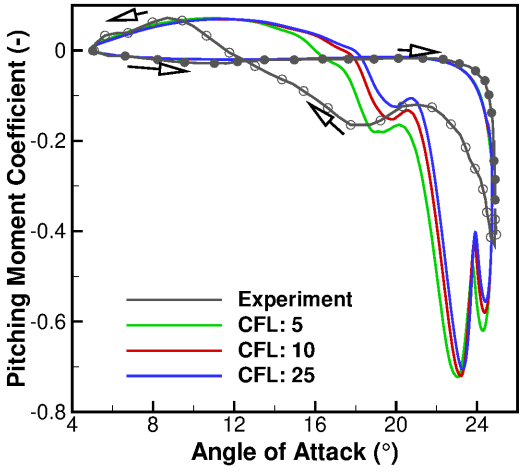

(d) CFL

Figure 5.2: Pitching moment comparison to the experimental values for the NACA 0012 verification, where the datum case is selected as the middle value for each investigated parameter

5.1.4 NACA 0012 Quasi-3D Results

Presented in Figure 5.3 is the pitching moment coefficient results for the NACA 0012 test case, comparing 2D *URANS* and phase-averaged quasi-3D *SAS* , to experiments.

In the experimental results, the pitching moment remains almost constant up until 22°, where it starts to increase, with the peak pitching moment coefficient observed at the maximum angle of 25°. A similar response is found with the 2D *URANS* simulation, however, the peak pitching moment is found to be greater. Based upon the 2D *URANS* results, this response is seen to be based upon the development of stalled flow across the aerofoil trailing edge. This is observed in the flow visualisation results of Figures 5.5(a,c,e). The negative pitching moment for the quasi-3D *SAS* simulation is found to increase earlier at 18°, and this correlates with an increase in the developed detached flow. Figures 5.5(b,d,f) highlight the earlier development of detached flow,

particularly at 22^o where the stalled flow is seen to be further upstream towards the leading edge for the quasi-3D *SAS* result in comparison to the 2D *URANS* .

The recovery of the pitching moment during the experiment is found to occur over a range of 13^o, eventually recovering and crossing the upstroke profile around 12^o. During the downstroke, the 2D *URANS* is found to have a significant secondary stall event, resulting in two pitching moment peaks. The 2D *URANS* then quickly recovers, crossing the upstroke profile 6^o earlier than experiments at 18^o. This indicates that the 2D *URANS* simulation develops a closed stall bubble. This sheds from the section quickly, allowing the flow to attach at an earlier pitch angle than seen during the experiment. This is observed in the flow-field visualisation results for the *URANS* simulation in Figures 5.6(a,c,e). For the quasi-3D *SAS* , following the peak, the pitching moment then recovers to similar values as the experiment. The experimental pitching moment, during the downstroke, is seen to increase around 18^o. This indicates the development of further separated flow between the $22 - 18^o$ range, as observed in Figures 5.6(b,d,f). This is also present in the quasi-3D *SAS* simulation, however, the magnitude of this secondary event is found to be larger. The quasi-3D *SAS* simulation then begins to recover crossing the upstroke profile at the same angle as experiments. An average variation of $\pm 0.5^o$ is found for the recovery angle, thus resulting in the closer estimation to the experimental recovery angle for the phased-averaged quasi-3D *SAS* than the 2D *URANS* simulations.

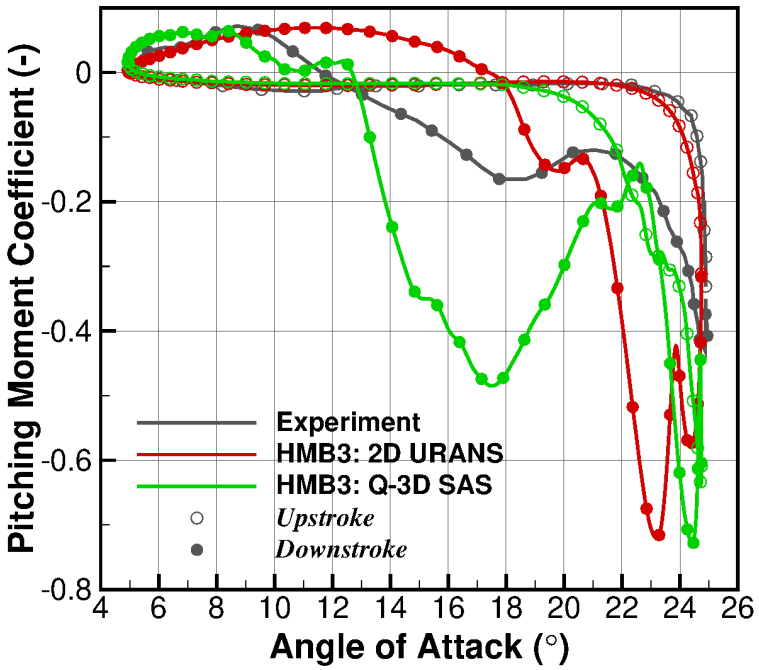

Figure 5.3: Comparison of the NACA 0012 pitching moment coefficient for the 2D and quasi-3D simulations to the experiment, with the flow conditions presented in Table 5.1.

This variation in recovery angle is the result of cycle-to-cycle differences in the pitching moment coefficient for the quasi-3D *SAS* simulation, with this variation presented in Figure 5.4. Here, three revolutions are examined next to the phase-averaged solution across the full time-history and a focused region across the recovery angle of attack range. Looking at the time-history (Figure 5.4(a)), several points of cycle-to-cycle variation are found and highlighted, with these mainly confined to the downstroke phase. The first point occurs at approximately the mid-point during the initial build-up of the first pitching moment peak. It is small and related to a small detachment of flow as the larger dynamic stall vortex develops. The second variation point occurs at the moment peaks and these variations are a result of the cycle-to-cycle differences in vortex volume. No vortex of significant unsteadiness, such as those found within this test case, could be re-created with the exact volume and this is evident via this variation point. Following the pitching moment peak, the detached flow is shed from the aerofoil and the recovered moment varies depending upon the shedding process and final vortex volume. A larger vortex at the second point would have a greater amount of detached flow to shed, thus resulting in the slight differences in moment. This third stage is fairly small, when the individual curves are compared. However, they have a significant effect on the fourth varation which is due to the second build up of vorticity. A recovery moment which occurs earlier allows the secondary vortex to develop earlier. Additionally, in this case, the earlier recovery results in a larger secondary peak, thus delaying the final recovery angle.

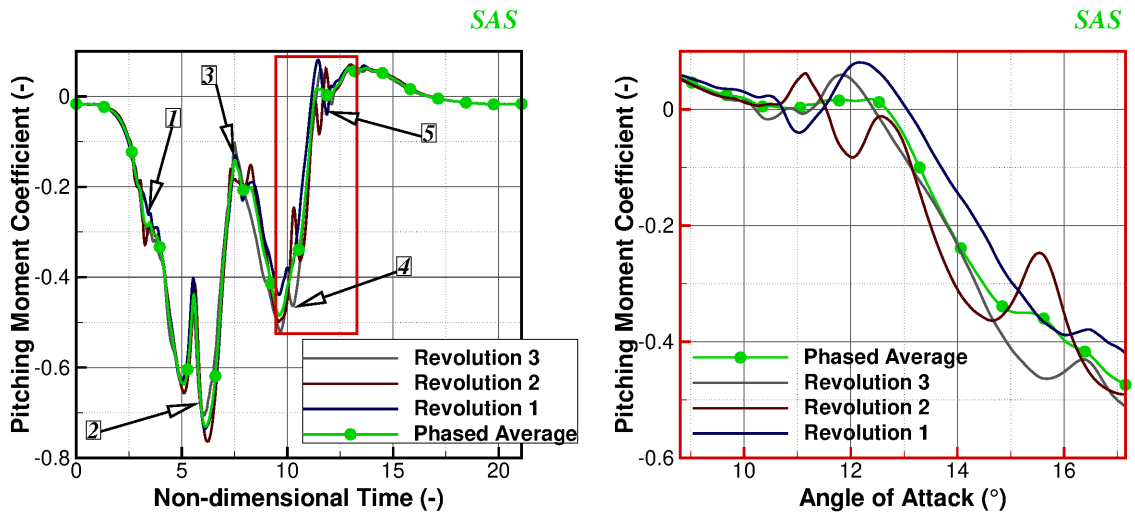

(a) Full time-history

(b) Focused angle of attack

Figure 5.4: Cycle-to-cycle variations of the NACA 0012 pitching moment coefficient for the quasi-3D *SAS* simulation

The final variation point is seen at the recovery angle and this is highlighted within Figure 5.4(b) with respect to the aerofoil angle of attack. Focusing on revolutions 1 and 3, the smaller secondary peak/vortex of revolution 1 sees the pitching moment recover at $\sim 13^{o}$ with the larger secondary peak of revolution 3 recovering later at $\sim 12.5^{o}$. Revolution 2 is seen

to recover the latest ($\sim 11.5^{o}$) and this is a result of an additional shedding/detachment event occuring during the downstroke around 15.5^{o}.

Such cycle-to-cycle variations in dynamic stall experimental data has been discussed recently by Ramasamy *et al.* [107]. They analysed two sets of experimental data and found that traditional phase-average filtering is not effective enough to represent dynamic stall load measurements. As a result, two new data-driven algorithms were developed to cluster the load results based upon the developed flow phenomena. Significant differences were found in the aerodynamic damping and load results between the two new clusters and the traditional phased-averaged solutions. From this study it is clear that an improvement in the analysis of experimental results is required to ensure the correct flow physics is captured.

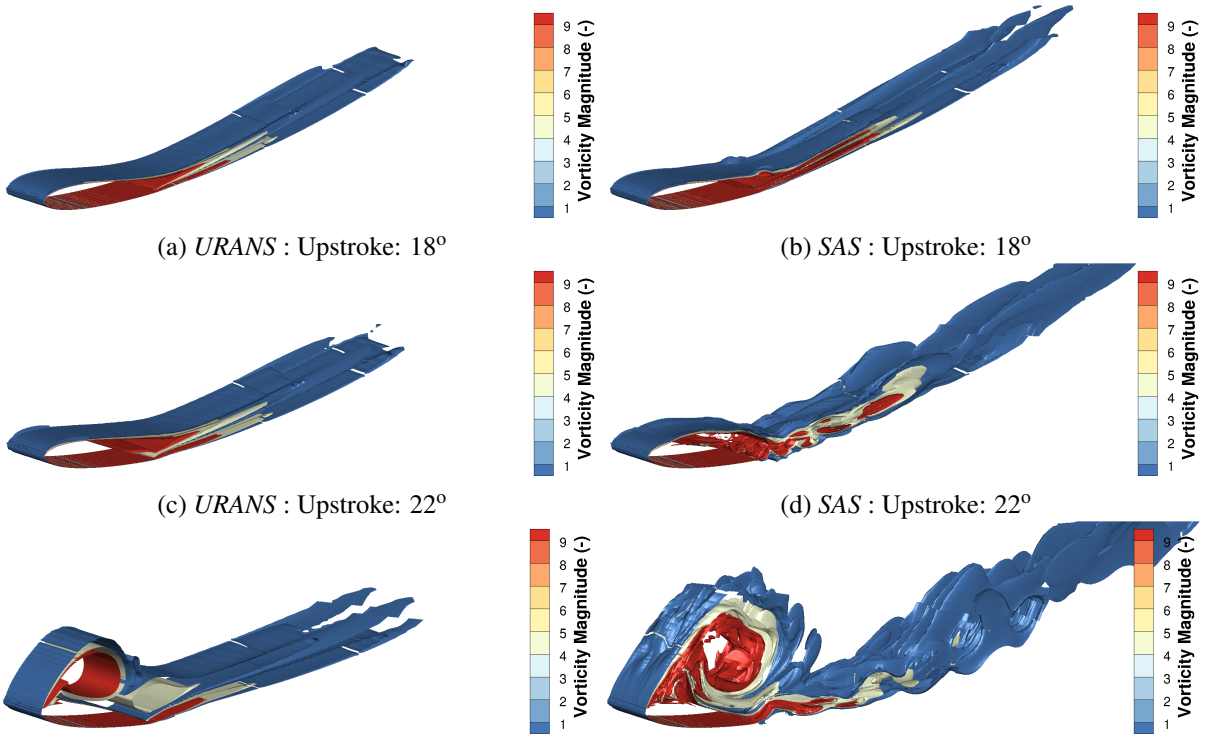

(a) *URANS* : Upstroke: 18^{o} (b) *SAS* : Upstroke: 18^{o}

(c) *URANS* : Upstroke: 22^{o} (d) *SAS* : Upstroke: 22^{o}

(e) *URANS* : Upstroke: 25^{o} (f) *SAS* : Upstroke: 25^{o}

Figure 5.5: Flow visualisation of $|\omega| = [1.0, 5.0, 10.0]$ iso-surfaces during the aerofoil upstroke

Using the pitching moment curve, the aerodynamic damping of the system is estimated and presented in Table 5.3. As expected from the experimental report, a negative damping value is seen for both 2D *URANS* and quasi-3D *SAS* simulations. However, due to the sharp recovery of the 2D *URANS* simulation, the positive anti-clockwise moment loop is greater than seen from the experiment, therefore the damping estimation is below the experiment. The quasi-3D *SAS* simulation provides a larger negative damping value for the phased average solution, at a closer percentage to the experiment than the 2D *URANS* . In addition, a scatter in the estimated aerodynamic damping of $\pm 37\%$ is observed per revolution, thus resulting in a closer estimation to the experimental results.

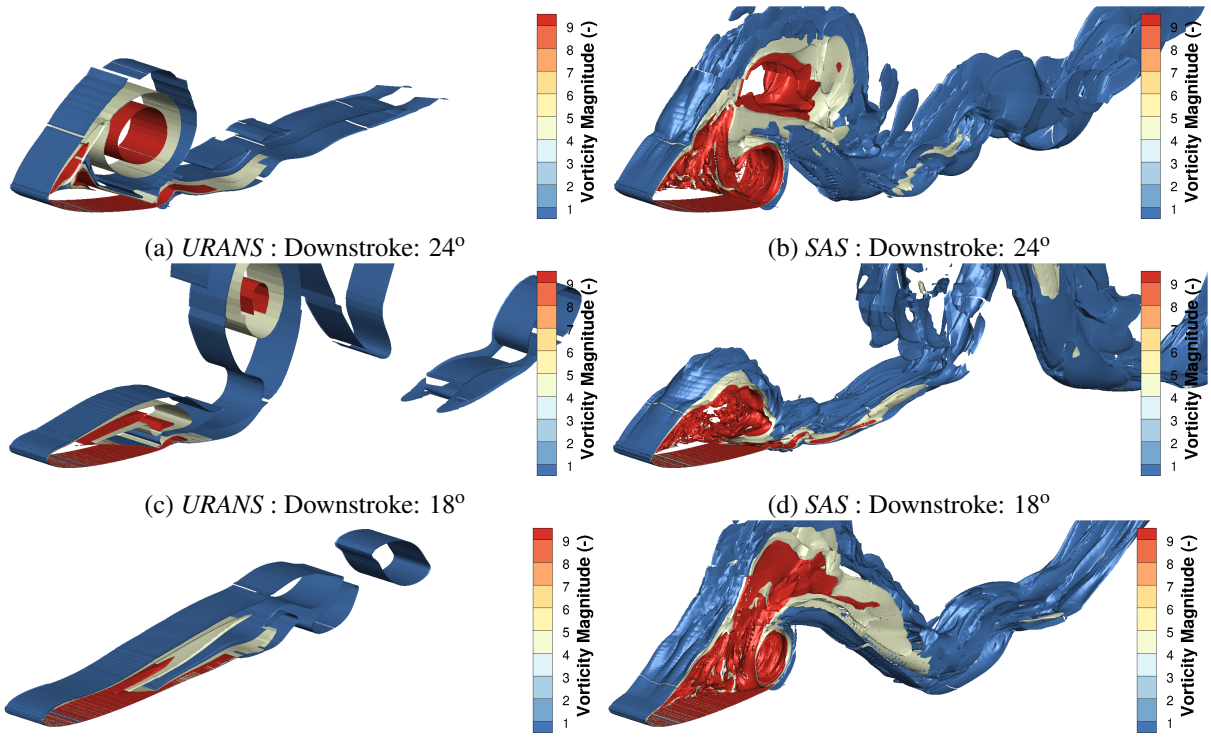

(a) *URANS* : Downstroke: 24°

(b) *SAS* : Downstroke: 24°

(c) *URANS* : Downstroke: 18°

(d) *SAS* : Downstroke: 18°

(e) *URANS* : Downstroke: 12°

(f) *SAS* : Downstroke: 12°

Figure 5.6: Flow visualisation of $|\omega| = [1.0, 5.0, 10.0]$ iso-surfaces during the aerofoil downstroke

Table 5.3: NACA 0012 Aerodynamic Damping

Section	**Modelling Method**	**Aerodynamic Damping**
NACA 0012	Experiment	-0.350
	2D *URANS*	-0.204
	Quasi-3D *SAS*	-0.457

One of the objectives of this investigation was to determine which method, 2D *URANS* or quasi-3D *SAS* , best captures the characteristics associated with stall flutter. Based upon the aerodynamic loads, the 2D *URANS* achieves closer correlation to the experiment during the upstroke with the pitching moment coefficient increasing at the same position. However, it is the downstroke segment of the oscillation that has the greatest effect on the level of aerodynamic damping due to the amount of unsteady flow features present during this stage. On this basis, the quasi-3D *SAS* simulation provides closer correlation as the levels of aerodynamic damping better represent what was seen in the experiment. Overall, neither *URANS* or *SAS* are perfect for dynamic stall predictions, though the *SAS* appears to be more representative of the separated flow and this is important in the present investigation.

5.1.5 Commander Aerofoil 2D Aerodynamic Damping Estimation

70% Radial Station

Presented in Figure 5.7(a) is the pitching moment coefficient of the Commander propeller section of the 70% radial station. As can be seen from the 2D *URANS* simulation results, a stable pitching moment profile is derived. During the upstroke, an almost constant negative pitching moment of -0.1 is seen up until 15^{o}. Following this, the aerofoil section separates causing the increase in negative pitching moment. Following the shedding of the developed closed stall bubble, the pitching moment recovers within 1^{o}. As a result of this sharp recovery, the pitching moment loops do not cross, and hence, a stable anti-clockwise loop is derived.

Table 5.4: 70%*R* Aerodynamic Damping

Section	Modelling Method	Aerodynamic Damping
RC070	*2D: URANS*	0.614
	Quasi-3D: SAS	-0.045

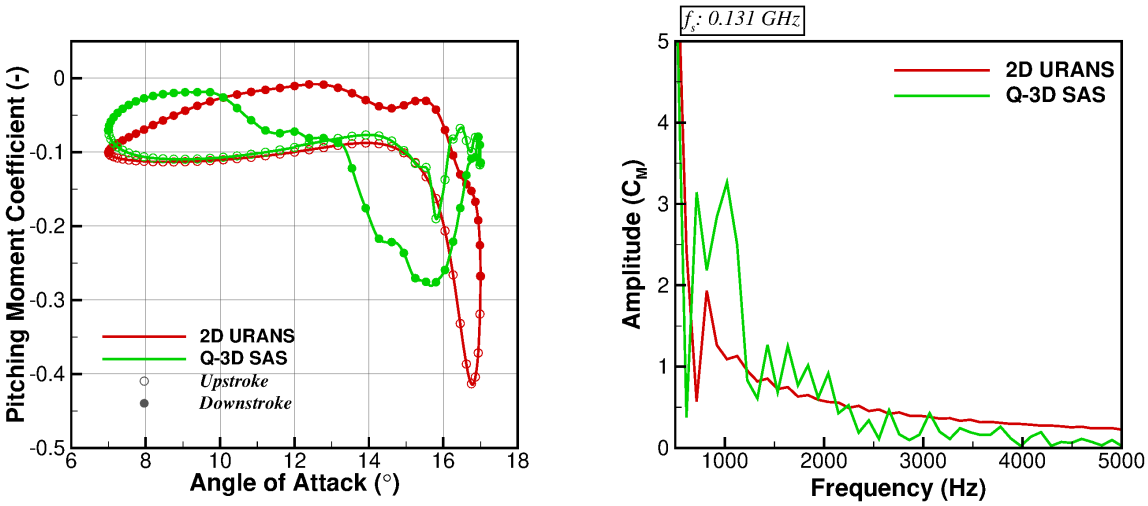

(a) Moment Coefficient

(b) Frequency response above the mean pitch angle.

Figure 5.7: Pitching moment response of the 70%*R* Commander aerofoil section.

For the quasi-3D *SAS* simulation, similar values of pitching moment are found during the upstroke, with the same stall angle of 15^{o}. Following the initial stall, the detached flow is shed resulting in a small recovery/reattachment of the flow-field. As the angle of attack is increased further, detached flow again develops and vortices are shed from the aerofoil, accumulating during the peak pitching moment. The quasi-3D *SAS* simulation recovers around 12^{o}. Due to this initial recovery on the upstroke, a negative clockwise moment loop is derived, resulting in negative aerodynamic damping, as shown in Table 5.4. The 2D *URANS* shows a stable solution.

A Fast-Fourier-Transform was conducted on the pitching moment coefficient results above the mean angle of attack of 12^o, with the results presented in Figure 5.7(b). For these simulations, a sampling frequency of 0.131 GHz is used, thus resulting in a maximum available frequency of 0.066 GHz. The Nyquist theorem is therefore satisfied for these comparisons. For the 2D *URANS* result, a single peak at 1 kHz is found and this corresponds to the peak moment coefficient. A similar peak is found in the quasi-3D *SAS* simulation, however, due to the double stall event, a double peak is observed from the frequency response with the frequency band ranging from 0.7 kHz to 1.4 kHz. At higher frequencies, several oscillations from the quasi-3D *SAS* simulation are observed. This is expected to due to the resolution of scales not captured via *URANS* and the oscillations in pitching moment coefficient seen at the maximum pitch angle. Some small oscillations are present at higher frequencies for the 2D *URANS* case, however, these are negligible in comparison to the quasi-3D *SAS* response.

90% **Radial Station**

Similar responses are found between the 2D *URANS* and quasi-3D *SAS* simulations. A full anti-clockwise moment loop is found, and presented, in Figure 5.8(a) for the 2D *URANS* simulation. The pitching moment begins to increase around 11^o. This is 3^o above the mean angle of attack. The pitching moment recovers almost instantly resulting in a stable moment loop.

In a similar manner to the 70% station, after the pitching moment begins to increase and the detached flow develops, the flow-field is shed from the station resulting in a recovery of the pitching moment for the quasi-3D *SAS* simulation. Several vortices from the detached flow are shed and this gives an oscillating pitching moment as the section reaches the maximum angle of attack. During the downstroke, the pitching moment increases producing an unstable clockwise moment loop. The moment recovers around the mean angle of attack. The resultant anti-clockwise moment loop causes a reduction in the aerodynamic damping, presented in Table 5.5.

Table 5.5: Aerodynamic Damping

Section	**Modelling Method**	**Aerodynamic Damping**
RC090	*2D: URANS*	0.497
	Quasi-3D SAS	0.104

The frequency response for the pitching moment curve above the mean angle of attack of 8^o is presented in Figure 5.8(b). The sampling frequency was reduced to 0.113 GHz due to the increase in sample time-step. This sampling frequency still satisfies the Nyquist theorem in order for a comparison to be made. For the 2D *URANS* simulation, several peaks are observed below 1 kHz, with the highest amplitude seen at 0.6 kHz. The quasi-3D *SAS* simulation produces a two high amplitude peaks at 0.75 kHz and 1.2 kHz, corresponding to the two stall events.

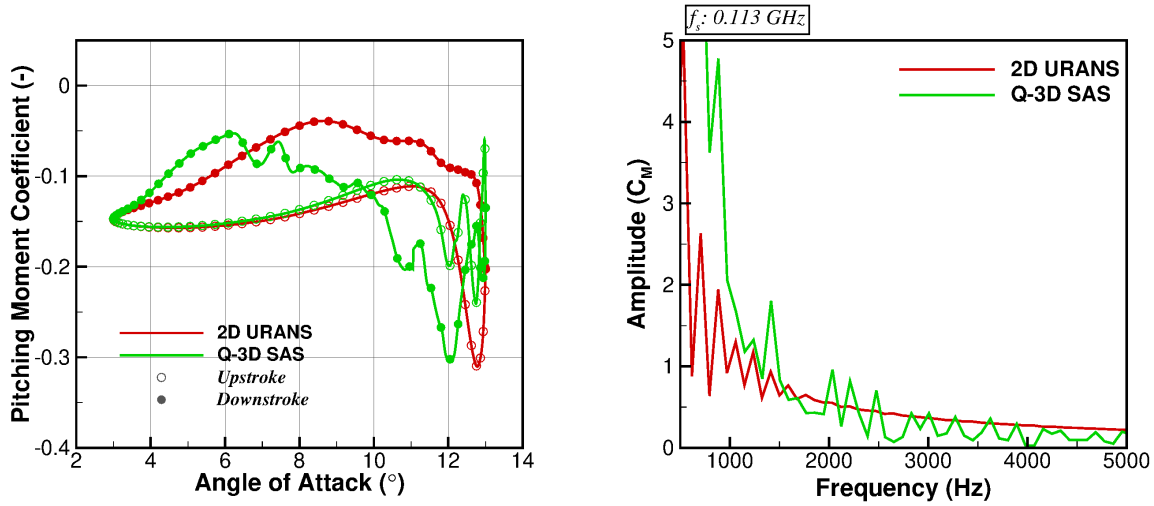

(a) Moment Coefficient

(b) Frequency response above the mean pitch angle.

Figure 5.8: Pitching moment response of the 90%R Commander aerofoil section.

5.1.6 Summary of the Two-Dimensional Aerodynamic Damping Investigation

It is concluded that the use of the *SAS* method provides a more realistic representation of the negative aerodynamic damping associated with stall flutter, as seen from the NACA 0012 damping estimations. Therefore, to conduct a stall flutter investigation, it is vital that scale-resolving aerodynamics are used which captures the fluctuations in surface pressure associated with vortex shedding.

5.2 Three-Dimensional Aerodynamic Damping

Using the time-marching aeroelastic method derived in Chapter 2, an attempt is made to estimate the aerodynamic damping values from the time-marching simulations of Chapter 4. A description of the damping equations are given with this correlated against the values for aerodynamic work.

5.2.1 3D Aerodynamic Damping Calculation

To determine the stability of the propeller blade, the amount of aerodynamic work (W_{aero}) can be used. This involves the integration of the unsteady surface pressure ($\tilde{p}$) and local displacement velocity ($\vec{u}$) over time (Equation 5.2). A test case which has a negative aerodynamic damping value, i.e. a destabilising flow, will have positive aerodynamic work. This method is used to determine the stability of the entire blade.

$$W_{aero} = \int (\tilde{p} \cdot (\vec{u} \cdot \vec{n}))\, d\tau \tag{5.2}$$

To relate the three-dimensional calculation to the two-dimensional aerofoils, as per the two-dimensional aerofoil calculations, the moment curve of a propeller blade section is used to determine the stability of the section. For the two-dimensional calculations, a sinusoidal rigid motion is applied to the aerofoil and this determines the change in angle of attack. For a full three-dimensional aeroelastic simulation, a test case which is active in torsion is required to obtain this change in angle of attack for the estimation of the aerodynamic damping coefficient.

Due to the employed multi-block mesh, selected block faces along the propeller blade surface can be used to determine the current pitch angle and pitching moment. The instantaneous pitch angle is calculated based upon reference leading edge and trailing edge node positions from the rigid blade. Presented in Figure 5.9 are the selected block faces for the Commander propeller blade from the 50% to 90% radial station. For this investigation, and as per the dynamic stall study, focus will remain on the 70% and 90% radial stations.

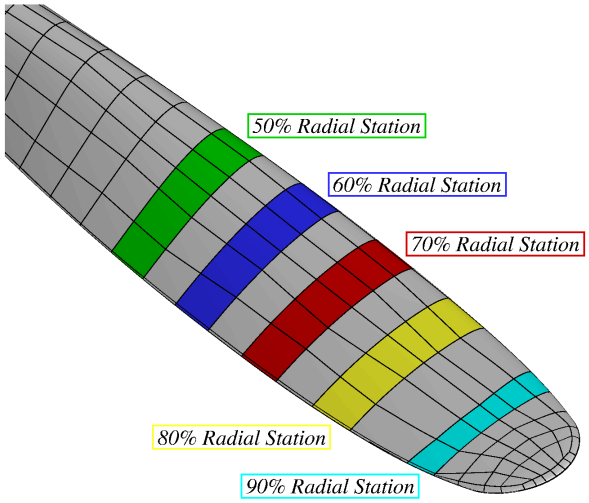

Figure 5.9: Commander propeller sections used for the damping calculations.

Based upon the derived pitching moment and pitch angle, the aerodynamic damping is estimated via equation 5.3:

$$\theta_{cycle} = \int \left(C_m^{D*} - C_m^{U*}\right) \partial\alpha, \tag{5.3}$$

where C_m^{D*} and C_m^{U*} are the pitching moment coefficients along the radial station minus the mean value observed for that section, with superscripts ^{D} and ^{U} indicating downstroke and upstroke, respectively. To determine the aerodynamic damping based upon a change in pitching moment, and therefore relate such aerodynamic damping estimations to the two-dimensional study, the mean value of the pitching moment is subtracted from the instantaneous to ensure the blade

rotational effects become less influential and the remaining moment values are respective to the aerofoil section.

5.2.2 Computational Setup

The main focus of this analysis is the standard structural model *URANS* and *SAS* calculations from Section 4.2. This includes the standard structural model described in Section 4.1.2 with no modal interpolation function and an accelerating blade. Results are calculated for the fixed and interpolated tuned modes, along with the decelerating blade, for reference.

5.2.3 Commander Propeller Blade 3D Aerodynamic Damping Estimation

Presented in Table 5.6 is the aerodynamic damping estimation from the 3D aeroelastic test case for the *URANS* and *SAS* simulations. As can be seen, and as expected from the dynamic stall study, positive damping values are observed for the *URANS* results, with reduced damping estimations seen for the *SAS* . At the 70% station, the damping estimation reduces by 50%, with the 90% station reducing further and producing a negative damping estimation. This reduction in aerodynamic damping for the *SAS* result is also found within the amount of aerodynamic work derived from the entire blade. As observed from Table 5.6, the *URANS* result produces a negative work estimation with the *SAS* solution producing positive work. From experiments [28], it is known that this propeller blade is found to suffer from stall flutter. Analysis of the modal amplitudes from the simulation data found the *SAS* results to significantly increase in torsional content with the trend in terms of torsional stress observed across the blade. This is presented in Figures 4.4 and 4.5(c). Through the use of the *SAS* method, the negative aerodynamic damping value associated with stall flutter is achieved.

Table 5.6: Comparison three-dimensional aerodynamic damping estimates for the 3D *URANS* and *SAS* simulations over the entire simulation.

Modelling	***Aerodynamic Damping****		***Aerodynamic Work****
	0.70	0.90	Whole Blade
URANS	0.010	0.035	-2.947
SAS	0.005	-0.004	0.733
Tuned Structural Model	-0.002	-0.009	73.171
Interpolated Tuned Modes	-0.023	-0.043	284.869
Decelerating blade	-0.026	-0.072	192.948
		*Equation 5.3	**Equation 5.2

In addition to the standard structural model simulations, the aerodynamic damping and work results for the subsequent calculations conducted in Chapter 4 are also presented in Table 5.6. The introduction of the tuned modes resulted in a signficant increase in torsional stress and

deflection. Subsequently, an increase in the negative damping associated with stall flutter is seen for the two examined radial stations with a significant increase in positive aerodynamic work. This instability is progressed further with the use of the modal interpolation function for the tuned modes where the largest workdynamic work value is seen. This increase is also observed in the radial damping results.

Switching the nature of the simulation from an accelerating to decelerating blade had a significant effect on the torsional stress trend through the transient phase. A reduction in the blade stress was seen during the decelerating with an eventual increase at the final state. This has an effect on the damping and work results. Like the accelerating modal interpolation simulation, high values of unstable damping and work are observed. For the work which takes into account the full blade, a reduction in the magnitude is seen when compared to the modal interpolation. This is a result of the reduction in content observed during the deceleration.

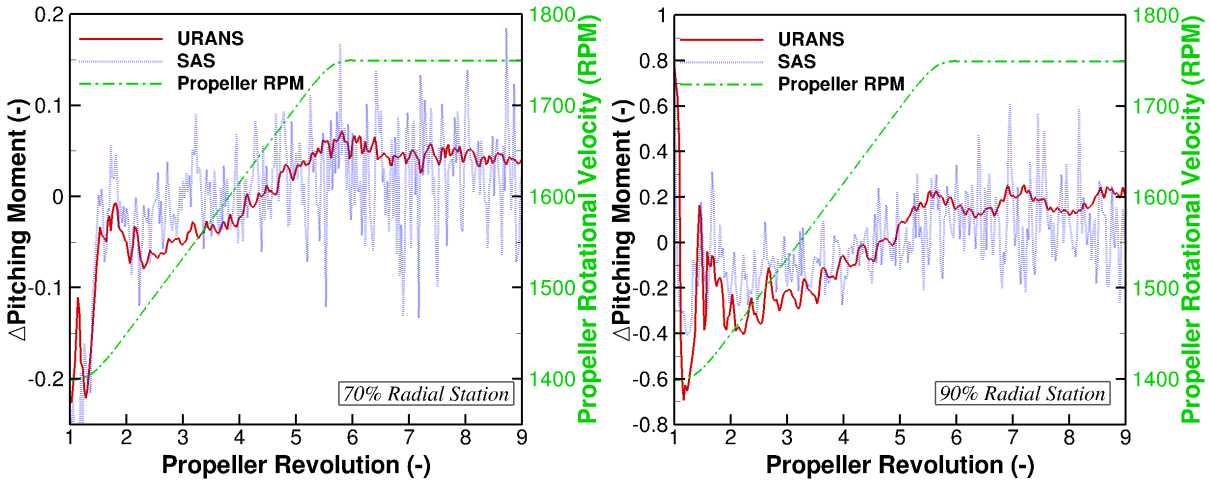

(a) $\frac{x}{R}$: 0.7 (b) $\frac{x}{R}$: 0.9

Figure 5.10: Comparison of the change in pitching moment for the *URANS* and *SAS* simulations.

As previously stated, the 3D aerodynamic damping is estimated using the changes in pitching moment. This is presented in Figure 5.10 for the 70% and 90% radial stations. As observed from both *URANS* and *SAS* simulations, there is a significant shift in pitching moment at the start of the first revolution. This is a result of the start-up of the aeroelastic deformations. Following this, oscillations in both *URANS* and *SAS* simulations settle, with a linear increase in the pitching moment found during the transition phase for both radial stations. Examining the profiles for the 70% station, an order of magnitude larger variations in pitching moment are observed during the transition phase for the *SAS* simulation when compared to the *URANS* . This increases to two orders of magnitude following the completion of the acceleration. For the 90% station, a linear trend in pitching moment is also observed during the transition for the *URANS* and *SAS*

simulations, however, once the acceleration is complete, significant fluctuations of ± 0.4 in C_m, are captured by the *SAS* .

Shown in Figure 5.11 is the flow visualisation, using radial slices, of the non-dimensional tangential velocity at the 90% radial station around the maximum change in pitching moment for the *URANS* (a,b,c) and *SAS* (d,e,f) simulations. The time-steps corresponding to the maximum change in pitching moment were selected as these would highlight the key changes that occur in the flow during the given oscillation. Additionally, the tangential velocity is the dominant component across the aerofoil section, therefore, its fluctuations highlight the alterations in detached flow. As can be seen from both the *URANS* and *SAS* results, the 90% station is fully stalled. This results in an entire stall bubble predicted by *URANS* . Very slight changes are observed around the peak value for the *URANS* simulation, in which the detached flow moves towards the leading edge, thus changing the pressure distribution. The change in pressure distribution on the upper surface, for the *URANS* simulation, is shown in Figure 5.12(a). There is a reduction in pressure towards the leading edge at the peak moment location due to the increase in the stalled flow. This detached flow then travels further downstream causing an increase in pressure which reduces the pitching moment. These changes in surface pressure coefficient, and hence pitching moment, for the *URANS* simulations are small in comparison to the *SAS* .

Looking at the *SAS* flow visualisation results, the structure of the detached flow is significantly different when compared to the *URANS* . For the *URANS*, one singular vortex is produced, whereas the *SAS* method is able to capture the smaller vortex structures which combine to create the entire section wake. Looking at the pre-peak station (Figure 5.11(d)), at least five vortical structures can be observed for the *SAS* result. There are three small pockets of detached flow on the blade surface, with two larger structures beginning to shed. As peak pitching moment is reached (Figure 5.11(e)), the two larger vortices have shed from the station. This shedding causes a significant reduction in pressure, as observed from Figure 5.12(b). Following the shedding of the two larger vortices, the flow attempts to recover post-peak resulting in a positive shift in pressure. It is this process of vortex shedding which causes the larger fluctuations in pitching moment and hence reduced stability in terms of the aerodynamic damping.

5.3 Conclusions

To summarise, using the change in pitching moment from its mean and the aeroelastic blade pitch angle, the aerodynamic damping of a given propeller section can be estimated. A comparison of the aerodynamic damping is made of the Commander propeller blade, which is found to be active in torsion, using *URANS* and *SAS* methods. Both observed radial stations, with the *SAS* simulation were found to produce lower levels of aerodynamic damping. This is due to the fact that greater amounts of flow features, such as shedding open stall bubbles, are produced, and therefore cause greater variation in loads and blade deflections. This correlates to the dy-

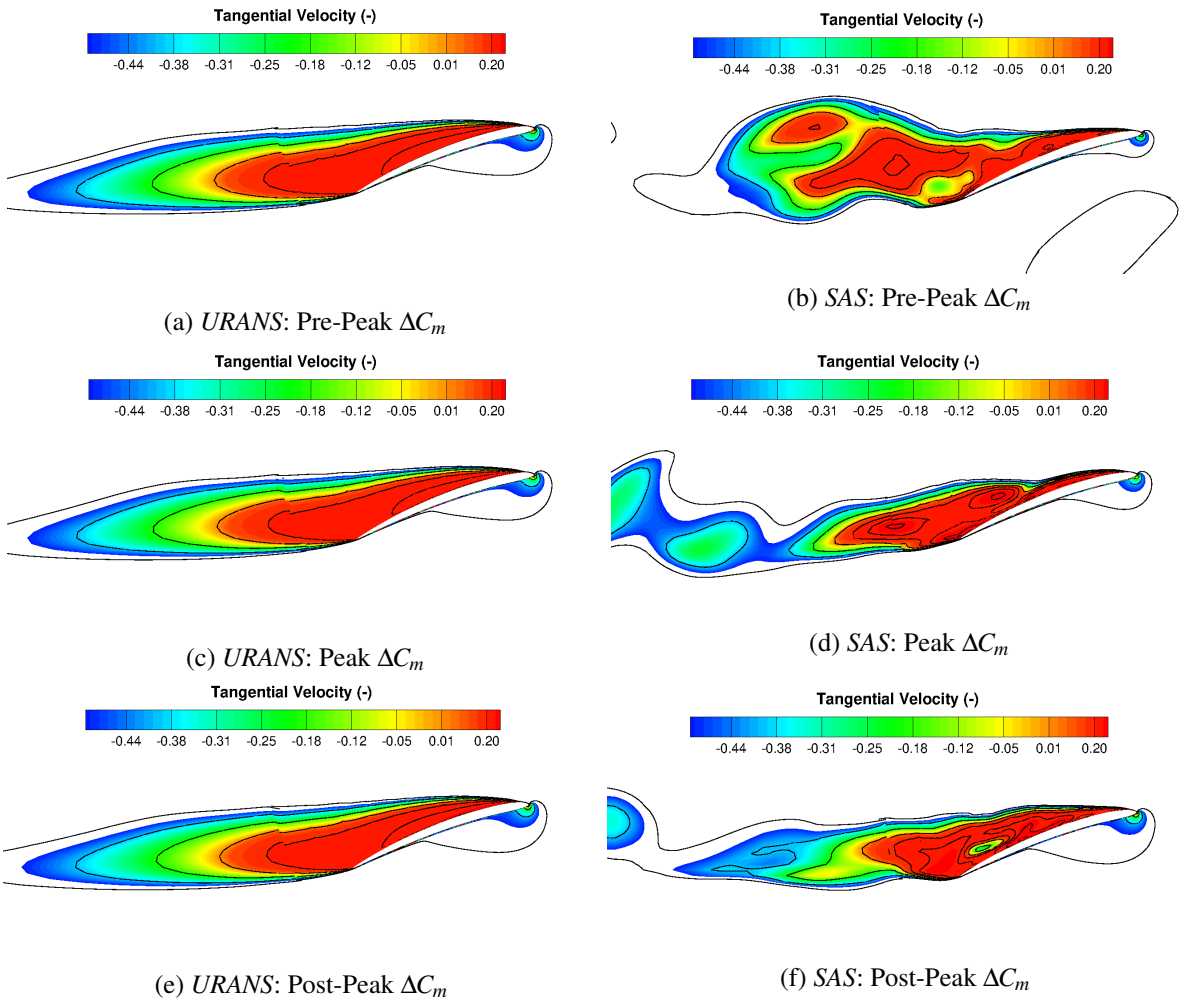

(a) *URANS*: Pre-Peak ΔC_m

(b) *SAS*: Pre-Peak ΔC_m

(c) *URANS*: Peak ΔC_m

(d) *SAS*: Peak ΔC_m

(e) *URANS*: Post-Peak ΔC_m

(f) *SAS*: Post-Peak ΔC_m

Figure 5.11: Flow visualisation at $\frac{x}{R}$: 0.9 of the tangential velocity profile for the *SAS* and *URANS* simulations at maximum ΔC_m.

namic stall investigations in which the aerodynamic damping is reduced for the quasi-3D *SAS* solutions, and to the model validation in which the full 3D aeroelastic simulation using *SAS* was found to flutter, with the *URANS* producing a stable result.

The use of the *SAS* method achieves closer correlation to the experiments, thus approximates the physics associated with stall flutter more closely. As this investigation was conducted over a select deep stall test case, the effect of this uncertainty between *URANS* and *SAS* would need to be examined further with a combination of deep, light and stall onset test cases. Additionally, a combination of different methods could also be used in the future to examine scale-resolving, such as LES and DES. However, based upon both the aerofoil dynamic stall and full 3D aeroelastic investigations, the *SAS* method is able to capture negative aerodynamic damping estimations. Using the aerodynamic damping estimated from three-dimensional simulations and *SAS* , stall flutter was explored.

It has been found that for two-dimensional and three-dimensional test cases, the *SAS* method

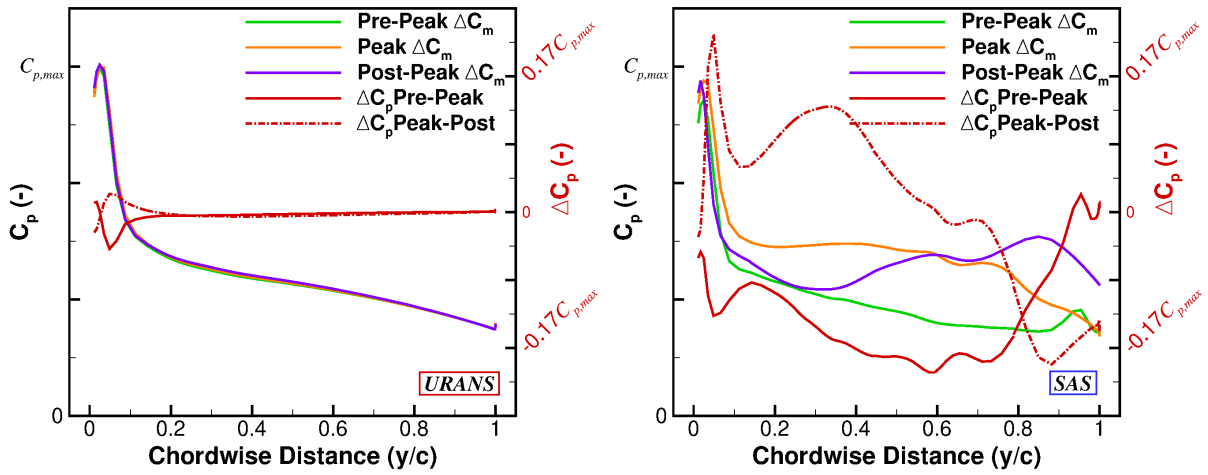

(a) *URANS* (b) *SAS*

Figure 5.12: Surface pressure coefficient on the blade upper surface at the 90% radial station through the peak ΔC_m for the *URANS* and *SAS* simulations.

provides a reduction in the aerodynamic damping, showing clearly the lack of stability for the examined flow conditions. This was in line with the experiment.

In addition, the use of improved turbulence modelling improved the correlation between simulation and experiments during the downstroke. This was one of the key factors discussed by Ekaterinaris and Platzer [46], with this investigation highlighting the improvement in modelling during this phase. The match between the results are not exact whilst using *SAS* and further study would be required.

Chapter 6

Parametric Study of the Commander Propeller Blade

With the validation of the Commander blade for stall flutter, a study was conducted on the structural and aerodynamic conditions in order to better understand the blade response. The structural changes involved the introduction of a greater level of torsion to the blade mode shapes. This is achieved with the adjustment of the blade centre of gravity along the chord, the inclusion of additional mass at the blade tip and the adjustment of the blade material torsional stiffness.

In terms of aerodynamic conditions, the aim of the study was to understand the change in blade structural response which could be easily determined from a similar wind tunnel study and additionally gain greater insight via the use of the derived method. This includes the change in blade pitch angle and the introduction of a freestream inflow, both of which have been shown in the past to influence the stall flutter response. All simulations involved the acceleration of the blade through the 1400 (rpm) to 1750 (rpm) velocity range.

6.1 Structural Study

With the focus of the structural parametric study on the introduction of greater torsion, a study of the tuned model was conducted to obtain the magnitude of the changes. As such a study of the NASTRAN structural model is described for each section before the analysis of the aeroelastic simulations.

6.1.1 Centre of Gravity

The placement of the aerofoil centre of gravity is historically seen as critical to it's aeroelastic stability. It is the distance between the aerofoil elastic axis and the centre of gravity which can have a significant effect on the level of instability. Increasing this distance, in turn increases the moment arm between the aerodynamic centre, elastic axis and the centre of gravity. For a

condition in which the aerofoil is unstable in pitch, increasing the moment arm of the pitching moment will potentially increase the oscillation amplitudes.

The previous simulations of the Commander propeller blade were conducted with the centre of gravity in line with the neutral axis. With the movement of the centre of gravity rearward, this introduces an additional element of instability. In order to assess the effect of the change in centre of gravity position, a study was conducted on the NASTRAN bungee model. Presented in Figure 6.1 is the change in modal frequencies with the adjustment in centre of gravity position. The change in centre of gravity position has the smallest effect on the first blade mode frequency. From 0% to 25%, the frequency remains within 15% of the original model. A greater change is observed with a 50% adjustment in the centre of gravity with a 22% difference between 25% and 50%.

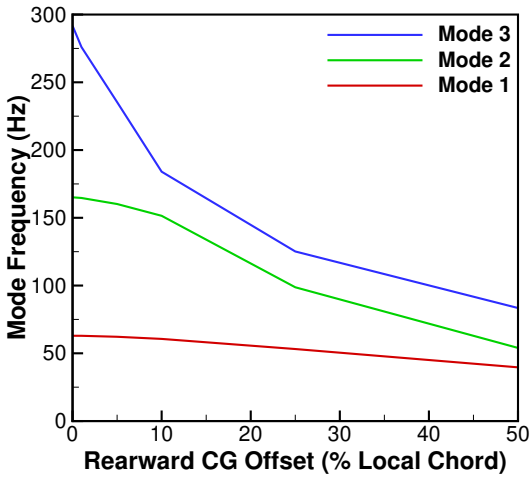

Figure 6.1: Change in the modal frequencies with the adjustment in centre of gravity position for the Commander propeller blade

The greatest changes in modal frequency are contained to the second and third modes. With the third mode being of pure torsion, the rearward offset of the centre of gravity has a signficant effect on the frequency. For a 10% change in centre of gravity position, the frequency of the mode drops by 37%. This is compared to the first mode where only a 4% reduction in frequency is observed. A greater than 10% adjustment in the centre of gravity position forms a coupling of the second and third modes as the frequencies remain parallel to one another.

This is also mirrored in the modal shape results presented in Figure 6.2. As observed from the second mode, a complete change in shape is found for a shift of 25%. The baseline shape is seen as the second flapwise bending mode with a change to pure torsional mode. The mode shape is mirrored in the third mode and further confirms the coupling of the second and third modes. Although the magnitude of the first mode has changed, the overall profile remains the same.

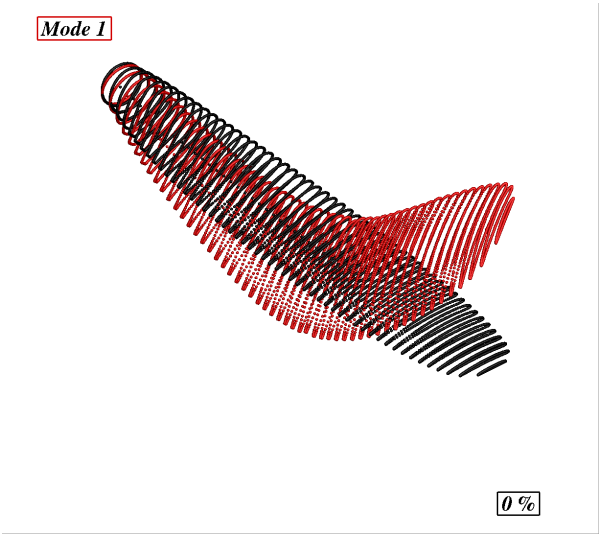

(a) Mode 1: 0% Offset

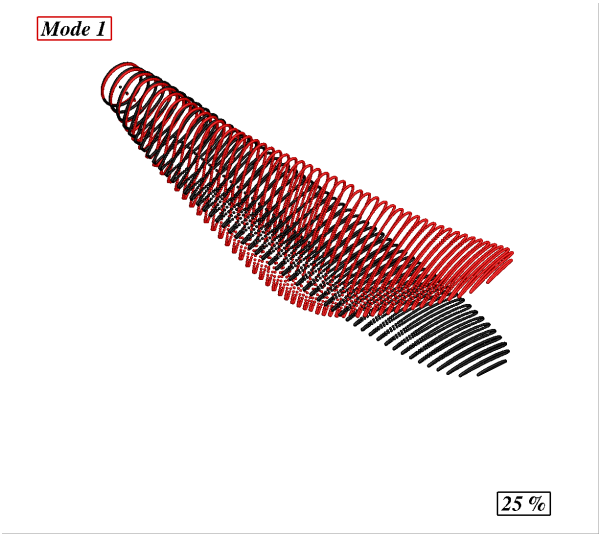

(b) Mode 1: 25% Offset

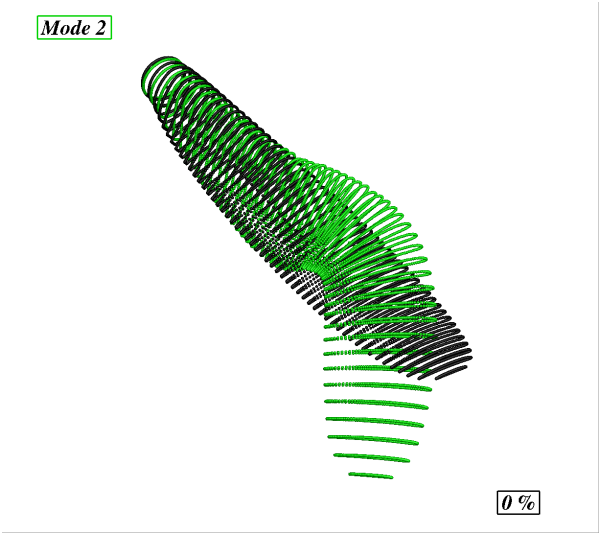

(c) Mode 2: 0% Offset

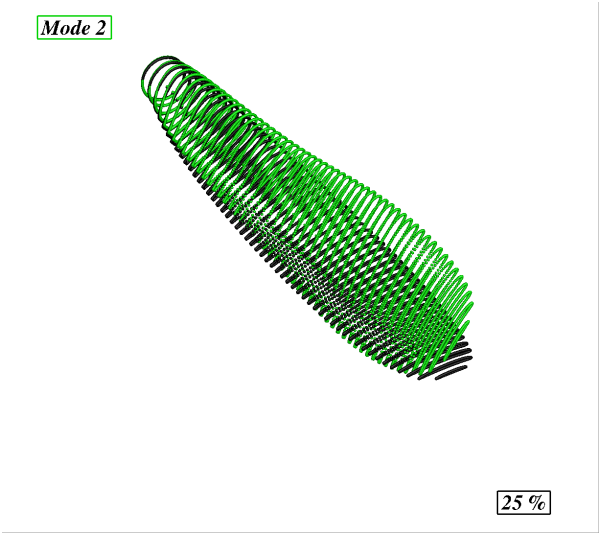

(d) Mode 2: 25% Offset

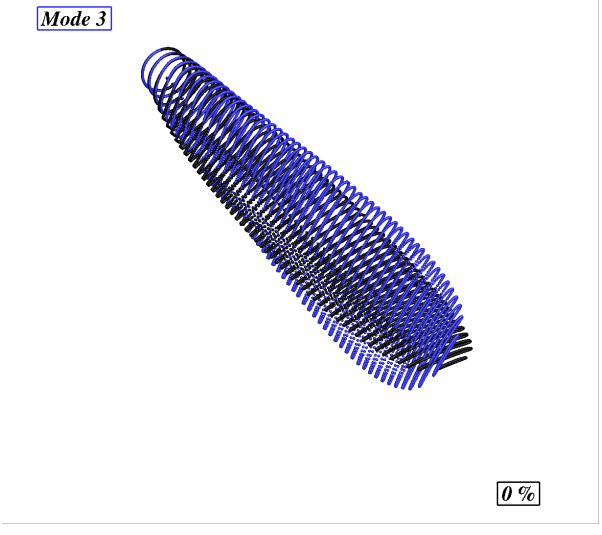

(e) Mode 3: 0% Offset

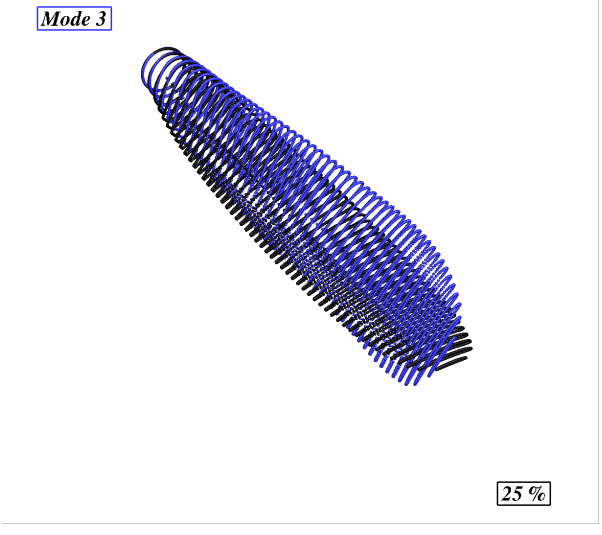

(f) Mode 3: 25% Offset

Figure 6.2: Change in the mode shape for adjustment in blade centre of gravity

Supplied Modes

As seen from both frequency and mode shape results for the tuned structural model, a greater introduction of torsion is found with a 25%, of the local chord, rearward offset in the centre of gravity, hence this condition will be used for the CG parametric study. As found from Section 4.6, the use of the tuned structural model with the interpolation function found the closet approximation to the torsional stress experimental results. These are therefore used for this simulation.

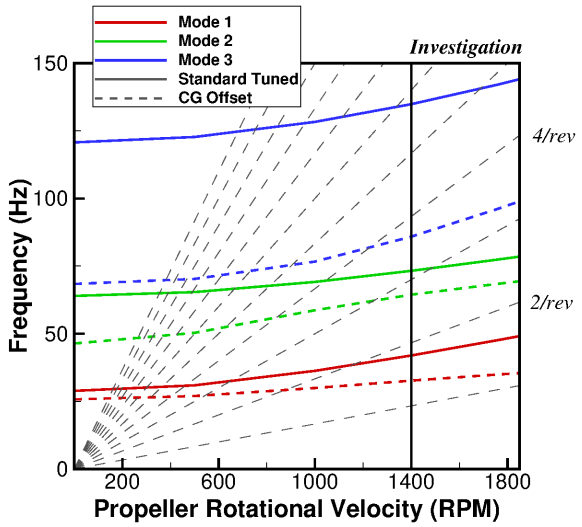

Figure 6.3: Influence of the centre of gravity offset on the Commander propeller blade spoke diagram

Presented in Figure 6.3 is the comparison between the standard tuned and the tuned model with the centre of gravity offset for the spoke diagram. A reduction in the frequencies is observed for all modes, with the greatest reduction coming for the third mode. From the start to end of the investigation region, the frequency rate is lower for the centre of gravity offset in comparison to the standard tuned for the first mode. For the standard tuned model, the first mode frequency increases by 7.14 Hz (17%). This is significantly lower than the difference in the centre of gravity offset model which increases by 2.75 Hz (8%). This indicates a reduction in the influence of the interpolation function. The frequencies for each stage of the interpolation function are presented in Table 6.1, along with evaluations of the new shape.

Aeroelastic Results

Presented in Figure 6.4 is the modal amplitude comparison between the standard interpolated tuned model simulation and with the change in centre of gravity. Due to the change in mode shape for the first and second mode, a direct comparison of the amplitude is difficult, however, they are presented to give context to the overall deflection results.

For the first mode, a significant reduction in the modal amplitude is seen. The standard

Table 6.1: Frequencies and shape of each mode for the centre of gravity parametric study for every supplied stage of the interpolated simulation

		Rotational Velocity Stage			
Mode	**Shape**	*1400*	*1500*	*1650*	*1750*
1	T	32.67	33.34	34.29	34.88
2	T+FB	64.43	65.62	67.28	68.34
3	T+FB	85.87	88.62	92.92	95.89

T: Torsion, FB: Flapwise Bending

model produces an oscillation of ± 0.0096. This reduces by 98% to ± 0.00012. An additional insert into Figure 6.4(a) is provided to examine the trend of the first mode for the centre of gravity offset. As observed, a gradual decrease in the modal amplitude for the centre of gravity offset is seen. The value of ± 0.00012 is seen at the start of the acceleration with the oscillation value dropping to ± 0.000017 by the final state.

This significant drop in modal amplitude for the first mode results in a change in the active mode. For this case, this is now the second mode (Figure 6.4(b)) where amplitude values increase from ± 0.000052 for the standard model to ± 0.0011 with the rearward shift in centre of gravity. This significant increase in modal amplitude for the second mode is determined by a variety of factors. The change in mode shape for the first mode now allows for greater energy to be tranferred to the second mode, due to the increase in modal amplitude associated with a flapwise bending mode. In addition to the change in mode shape, the reduction in mode frequency has an impact on the amplitudes.

A direct comparison of the modal amplitude values can be conducted for the third mode (Figure 6.4(c)) due to the fixed shape. A similar profile is observed between the two simulations with a gradual decrease in amplitude as the blade accelerates through the stages. The difference in amplitude between the start and end of the simulation reduces from 42.4% for the standard model to 36.2% with the change in centre of gravity. As observed and expected based upon the reduction in frequency for mode 3, an increase of an order of magnitude in the modal amplitude values is found. For the standard simulation at the end of the acceleration, a fluctuation value of 0.48×10^{-4} is captured. This increases to 2.68×10^{-4} with the centre of gravity offset.

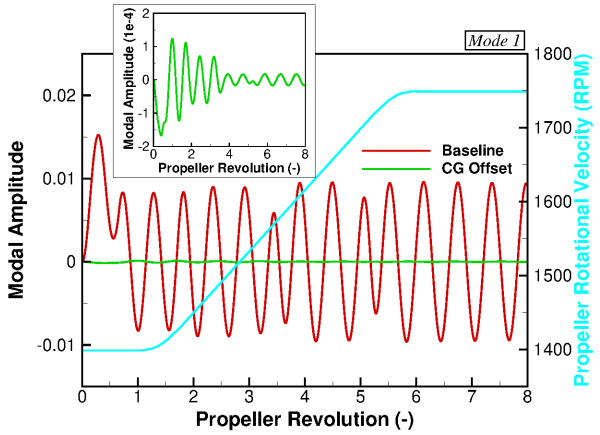

(a) Mode 1.

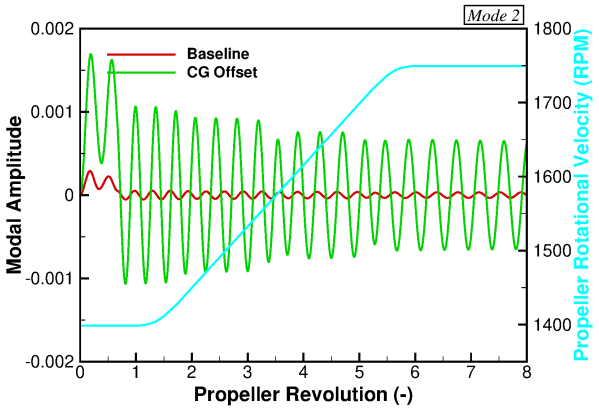

(b) Mode 2.

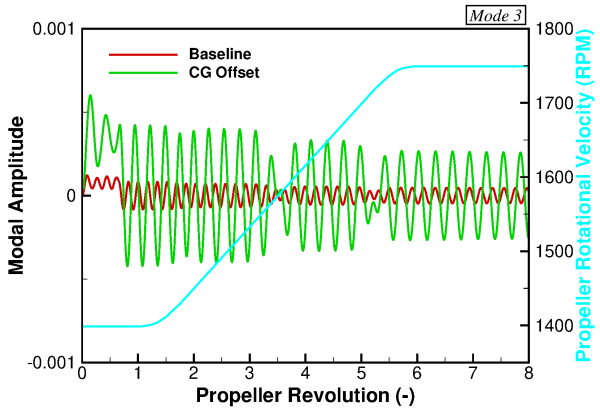

(c) Mode 3.

Figure 6.4: Comparison of the modal amplitude response for the change in centre of gravity for the Commander blade

Presented in Figure 6.5 is the non-dimensional torsional stress results for the rearward offset in centre of gravity. Due to the change in active mode shape and the reduction in modal amplitude for the first mode, a significant reduction in torsional stress is observed. The average value has reduced from 0.22 to 0.03, a decrease of 86%. For the maximum value, this reduces from 1.04 to 0.13, a reduction of 88%. In addition to the overall reduction, the position of maximum stress has also shifted. The standard simulation finds the maximum value at the inner most section of the examined region (60%R). This shifts outwards towards 72%R.

Due to this shift and overall reduction, the difference between the two simulations (Figure 6.5(b)) results in a significantly reduced profile towards the mid-span of the blade. Towards the mid-span, a maximum decrease of 0.98 is observed with an average decrease across the entire negative profile of 0.24. The shift in maximum stress location results in some small increases in stress towards the tip of the blade with a maximum value of 0.075.

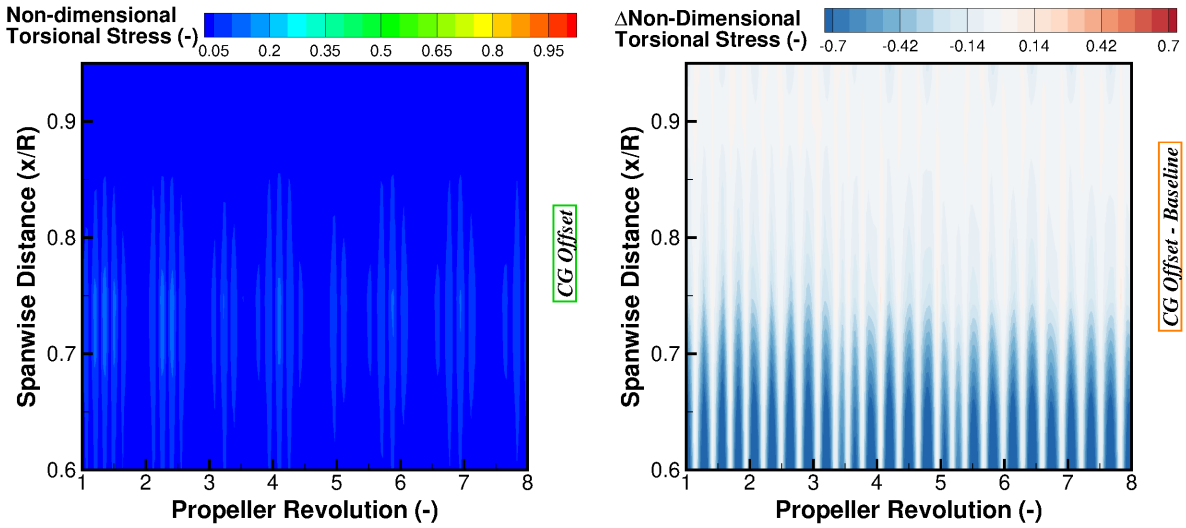

(a) CG Offset

(b) Difference with baseline

Figure 6.5: Comparison of the torsional stress results for the change in centre of gravity for the Commander blade

Presented in Figure 6.6 is the comparison between the two simulations for the difference in bending and torsion, along with the raw bending and torsion plots for the offset in centre of gravity simulation. With the raw data contours plotted with respect to the values of the standard simulations, line contours are added to give an indication of the deformation for this parametric simulation. As observed (Figures 6.6(a) & (c)), the offset in centre of gravity results in a signficant reduction in bending/torsion. For the standard simulation, fluctuation values of $\pm 0.03 c_{ref}$ and $\pm 0.45^{o}$ are captured for the bending and twist, respectively. This significantly reduces to $\pm 0.0002 c_{ref}$ and $\pm 0.03^{o}$. Such small values result in an almost constant deformation throughout the entire simulation. As a result, the difference in bending and torsion plots (Figures 6.6(b) & (d)) show the profile for the standard interpolated tuned mode simulation.

Due to the offset in centre of gravity, signficant change to the mode shape was produced. This change in mode shape results in a secondary torsional mode contribution. As a result, there was a potential for the modal amplitude results to balance out the contributions from each mode and this occured during the simulation. Focusing on the second and third modes (Figures 6.4(b) & (c)), the peaks and troughs of the amplitudes are found to occur out of phase. This results in the positive contribution from one mode being reduced by the negative pitch contribution from the second. As the second and third modes are the dominant modes (based upon the higher modal amplitude oscillations), this balancing results in a significantly reduced blade deformation. Future assessment of such an offset may require the reduction of the supplied modes to two as this will ensure the contribution of a single pure torsion mode.

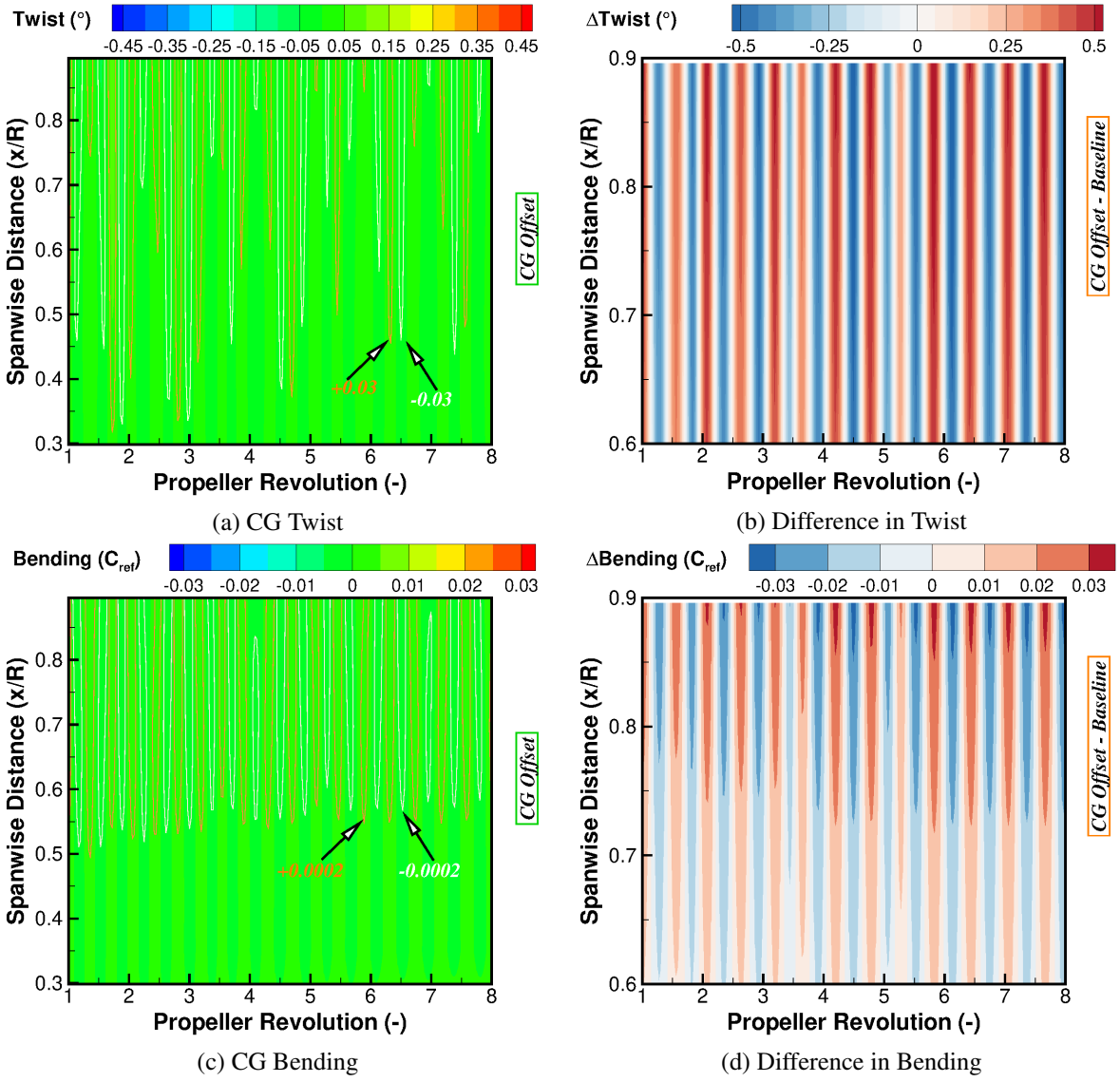

(a) CG Twist

(b) Difference in Twist

(c) CG Bending

(d) Difference in Bending

Figure 6.6: Difference in bending/torsion for the change in centre of gravity for the Commander blade

6.1.2 Tip Mass

In a similar manner to the position of the centre of gravity, the placement of mass is historically seen as critical to the overall stability of an aeroelastic surface. The example of a cantilever wing under the influence of a concentrated mass highlights such an influence. This was demonstrated experimentally by Runyan and Sewall in 1948 [117] and investigated numerically by Gern and Librescu in 1998 [56]. The experiment highlighted the reduction in flutter velocity as the concentrated mass was positioned away from the wing root, with a minimum velocity achieved around mid-span. This minimum value is related not only to the position of the store but the subsequent modal response. The modal response with the addition of a concentrated mass can be highlighted via the use of the assumed shapes methodology. Although a reduction in the deformation of the first bending mode is seen, the use of additional mass towards the tip

introduces an element of twist to the second bending mode. This is potentially critical in terms of stall flutter with the introduction of greater torsion. As a result and for the second structural parametric study, the introduction of a concentrated mass to the blade tip was investigation.

Through the use of the CONM2 NASTRAN element for a concentrated mass, additional weight was added to the blade tip. The blade tip was selected based upon the observations of the cantilever wing where the greatest amount of twist was added to the second bending mode at the tip. In addition, the second bending mode for the standard tuned model has a maximum deflection point at the tip and any additional mass will therefore alter the overall magnitude.

The positioning of the mass along the chord length is also important. From the cantilever study, divergence of the wing was found to occur for all masses forward of the wing centre of gravity. No divergence was seen rearward of the centre of gravity, however, depending on the position along the span, a reduction is flutter velocity was achieved and is related to the mass position with respect to the wing nodal points. As a result of this, the concentrated mass was positioned $27\%c_{local}$ rearward of the centre of gravity on one of the rigid bar grid points on the upper surface of the blade.

With the position defined based upon previous theory, the magnitude of the mass had to be defined along with an understanding of its effect. Presented in Figure 6.7 is the change in modal frequencies for the first three modes of the Commander propeller blade for the change in mass weight. As observed, the greatest change in modal frequency comes through the initial introduction of the concentrated mass. Between 0% and 5%, the gradient for each mode is seen to be the highest within this region with a gradual reduction as the mass exceeds 10%.

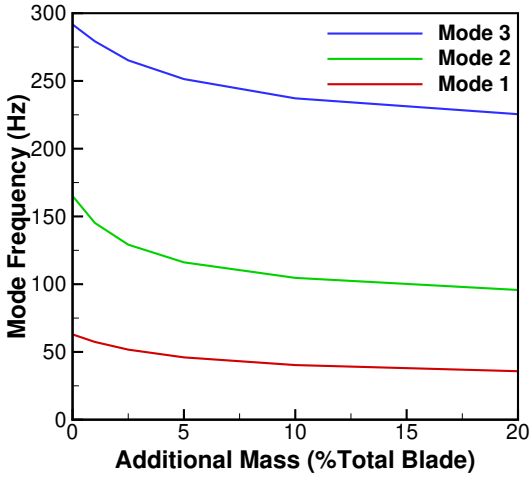

Figure 6.7: Change in the modal frequencies with the adjustment in additional mass weight for the Commander propeller blade

Presented in Figure 6.8 is the mode shape comparison between the standard model and the structural model with an additional mass of $20\%m_b$ at the blade tip. As expected based upon theory, the introduction of the concentrated mass results in the second mode changing from a

second bending mode to a coupled torsion-bending mode with torsion dominating.

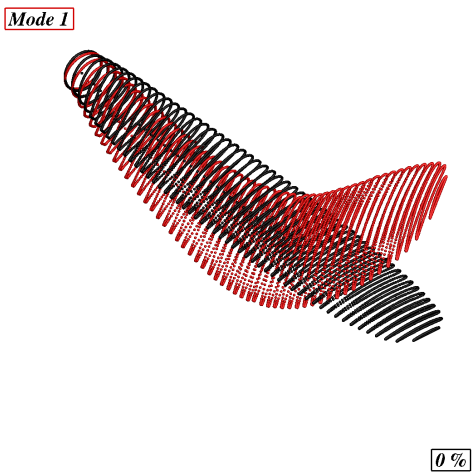

(a) Mode 1: 0% Mass

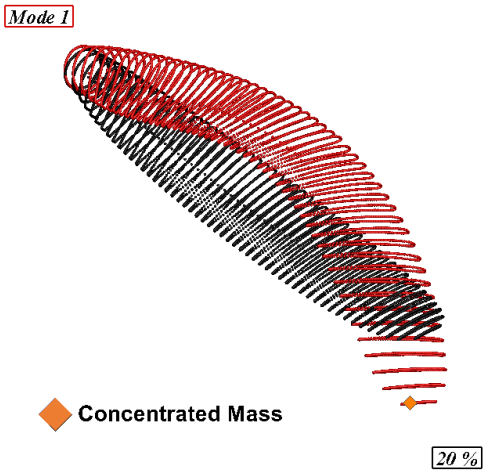

(b) Mode 1: 20% Mass

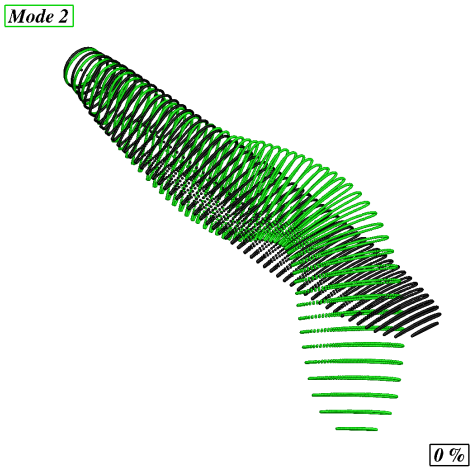

(c) Mode 2: 0% Mass

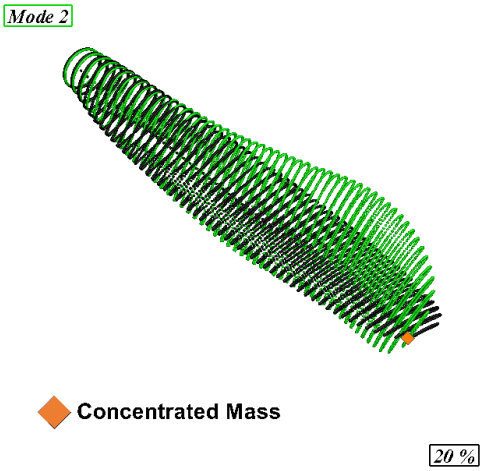

(d) Mode 2: 20% Mass

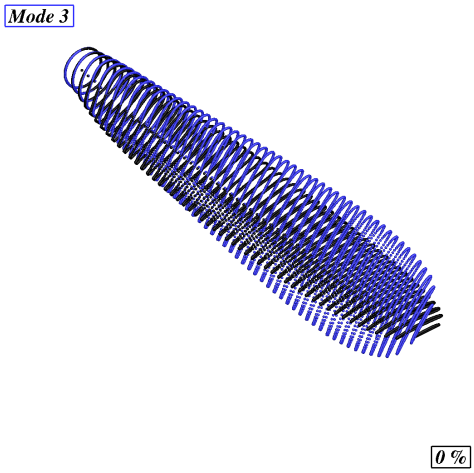

(e) Mode 3: 0% Mass

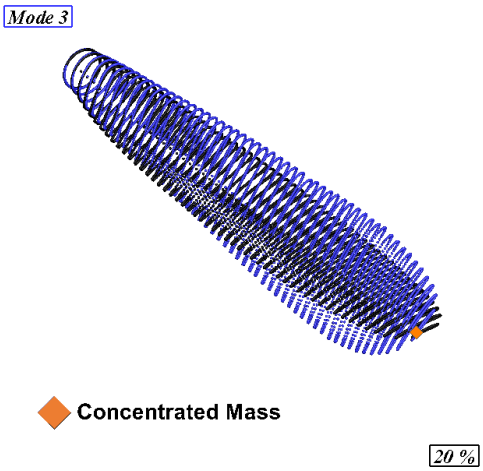

(f) Mode 3: 20% Mass

Figure 6.8: Change in the mode shape for introduction of a 20%m_b mass to the blade tip

The profiles of the first and third modes do not change significantly, however, the direction of the offset for the first mode has shifted from a positive bending to negative due to the additional weight at the tip. Due to these findings, the $20\%m_b$ mass was selected for the study.

Supplied Modes

The previous results are found using the bungee springs and as such, the addition of the $20\%m_b$ must be evaluated for the rotating blade. Presented in Figure 6.9 is the spoke diagram comparing the standard tuned model to the additional mass model for the first three modes. All modes see a reduction in the frequencies. For the first mode, a reduction in frequency of 22% is seen with a similar gradient through the investigation region. The second mode for the additional mass model follows closely the frequencies of the first mode for the standard model. This results in a reduction of 39% for the second mode frequencies. The third, and final, mode sees a significant change in the gradient of the frequencies. Going from static to the final velocity condition, the reduction in frequency reduces from 23% to 5%. This change in gradient is minimised during the investigation region with a starting velocity difference of 9%. Although this gradient change is minimised, the difference in starting and final frequencies increases by 76%, hence a greater change in the modal amplitudes is expected through the interpolation sequence.

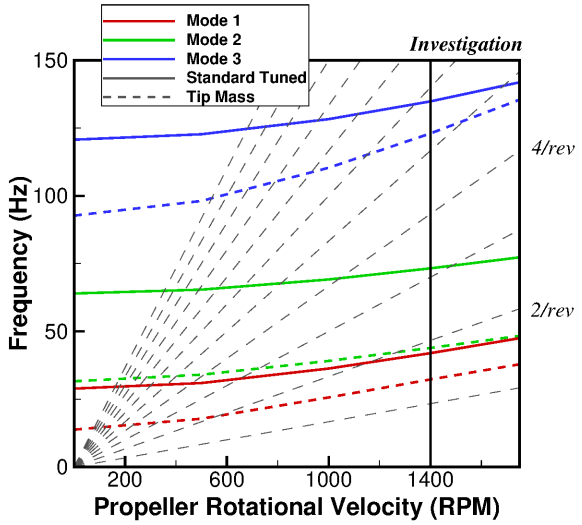

Figure 6.9: Influence of the additional tip mass on the Commander propeller blade spoke diagram

As per the centre of gravity parametric study, the interpolation function with four stages was used and compared to the standard tuned model with four stages. The frequencies and shape for each stage of the interpolation function are presented in Table 6.2.

Table 6.2: Frequencies and shape of each mode for the tip mass parametric study for every supplied stage of the interpolated simulation

		Rotational Velocity Stage			
Mode	**Shape**	*1400*	*1500*	*1650*	*1750*
1	FB	32.25	33.89	36.29	37.86
2	T	43.90	45.15	47.05	48.34
3	FB	123.04	126.49	131.82	135.46

T: Torsion, FB: Flapwise Bending

Aeroelastic Results

Presented in Figure 6.10 is the modal amplitude comparison for the addition of the concentrated mass at the blade tip. Due to the difference in mode shape, an exact comparison of the values may not be representative to the full blade deformation but does give an indication as to the energy supplied to the mode. Focusing on the first mode (Figure 6.10(a)), a change in the profile and magnitude is observed. With no additional mass, the profile through the acceleration is fairly constant with little change in the fluctuation values. This constant oscillation is removed with the introduction of the tip mass. At the start of the simulation (between revolution 1 and 2), an increased amplitude magnitude of 55% is seen for the tip mass simulation. This increase gradually reduces quickly through the acceleration with similar values between revolutions 2 and 3.5, and continues to decrease until the end of the acceleration. The final fluctuation value for the tip mass simulation reaches 47% of its original starting value and this equates to a 37% reduction in comparison to the no mass simulation.

For the second mode (Figure 6.10(b)), the significant change in mode shape results in a significant increase in modal amplitude. For the standard simulation with no mass, an average fluctuation value of 4.27×10^{-5} is observed. This average value increases by more than an order of magnitude to 8.49×10^{-4}. This is a result of the change in mode shape and the decrease in modal frequency. As was observed from Figure 6.9, the greatest change in frequency came from the second mode with a large reduction. The combination of these changes results in the increase in energy supplied to the second mode.

A comparison between the modal amplitudes for the third mode is presented in Figure 6.10(c). Due to the overall reduction in frequency, an increase in modal amplitude is found. Although the increase between the two simulations is significant, the increase is not as large as observed in the second mode. In terms of average fluctuation values, this changes from 6.38×10^{-5} with no mass to 2.76×10^{-4} with mass. An increase of an order of magnitude. From the spoke diagram (Figure 6.9), an increase in third mode gradient was observed during the acceleration region. This was expected to result in an increasing change in modal amplitude through the acceleration and this is observed. The starting to final fluctuation value for the no additional mass simulation

decreases by 43%. This percentage increased to 53% for simulations with additional mass.

Looking at the modal amplitude plots in full, an overall increase in blade deformation is expected. This is based upon the average fluctuation results of mode one being similar for the two simulations and the overall increase in magnitude for the second and third modes.

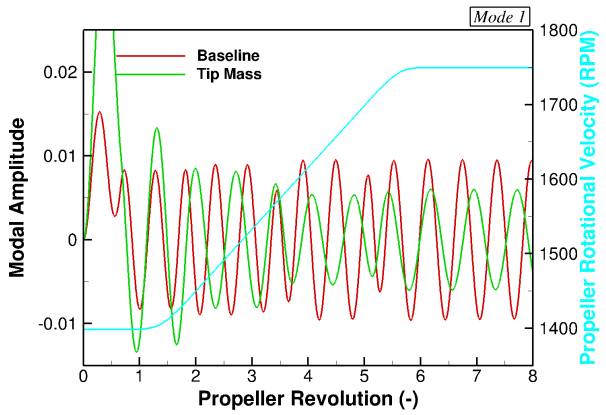

(a) Mode 1.

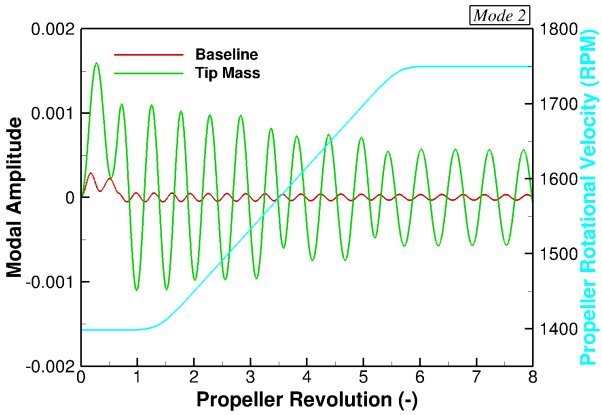

(b) Mode 2.

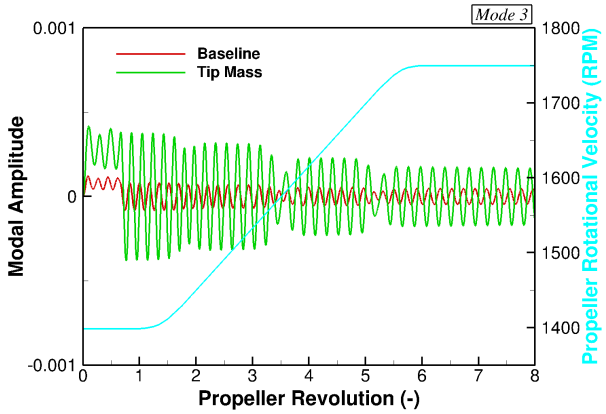

(c) Mode 3.

Figure 6.10: Comparison of the modal amplitude response for the inclusion of a tip mass on the Commander blade

Presented in Figure 6.11 are the torsional stress results for the additional mass simulation. An increase in both the average and maximum values is observed with the introduction of a concentrated mass. For the average value, this increases by 11% to 0.248, with the maximum value almost doubling from 1.04 to 2.03 (a 95% increase).

To assess the stuctural design, such figures will be used as a baseline from which to aim for, however, for this configuration, such values do not give the full picture. The greatest change comes from the change in profile along the radius and through the simulation. Looking through the acceleration, the profile mirrors the trend captured in the first mode (Figure 6.10(a)), with the largest values found towards the start of the simulation and lowest values at the end.

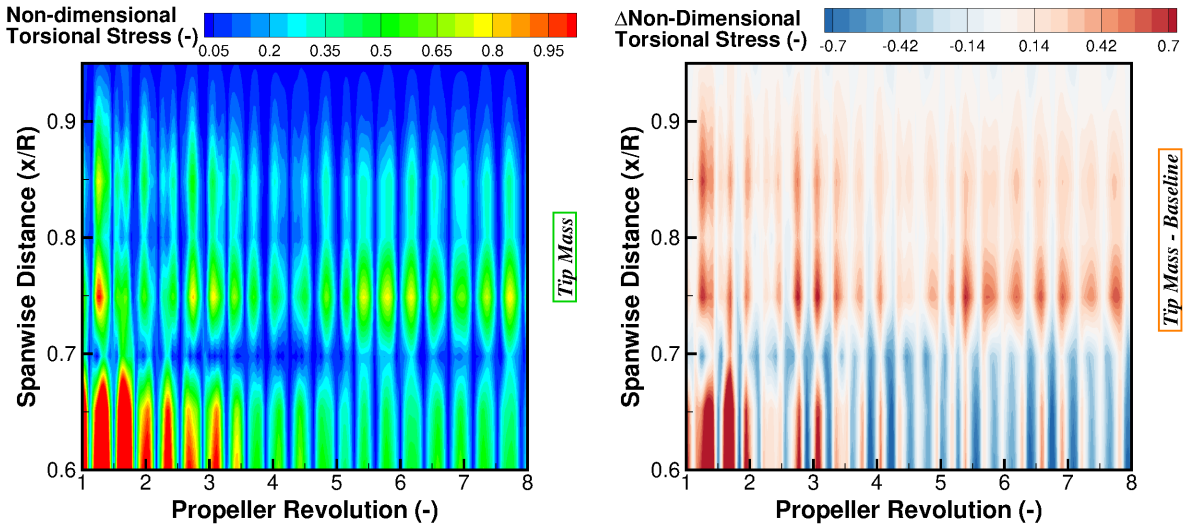

(a) Tip mass

(b) Difference from baseline

Figure 6.11: Comparison of the torsional stress results for the the inclusion of a tip mass on the Commander blade

For the simulation with no concentrated mass (Figure 4.29(a)), an almost linear distribution of stress is observed from mid-span to tip. Such linearity is not seen from the concentrated mass simulation with a quadratic response seen across the blade. Looking at the start of the simulation, three distrinct peaks are seen at 65%R, 75%R and 85%R. The trend for each of these peaks are presented in Figure 6.12. The linearity between the radial station is again present from the no mass simulation (Figure 6.12(b)), along with the constant profile throughout the simulation which follows its modal amplitudes. The same can be said for the 65%R in the concentrated mass simulation (Figure 6.12(a)) where its peak follows the modal amplitude trend for the first mode (gradually decreasing at the start of the simulation before leveling off). Aside from the higher values, greater variation in the peak values are seen for the 75%R and 85%R stations in the concentrated mass calculation. Such variation allows for higher values of stress to be captured at the 75%R station post revolution four.

Positive contributions are found across 60% of the difference plot presented in Figure 6.11(b). Of this 60%, the contribution is dominated by the increases outwards of 75%R with this region equaling 60% of the positive values. Across the positive values, an average of 0.21 is seen. Although less of the plot is found to have a negative contribution, the average magnitude is larger with a value of -0.33. Balancing these out and mirroring the average stress value, a small increase in the average difference between the two simulations is found to be 0.0245.

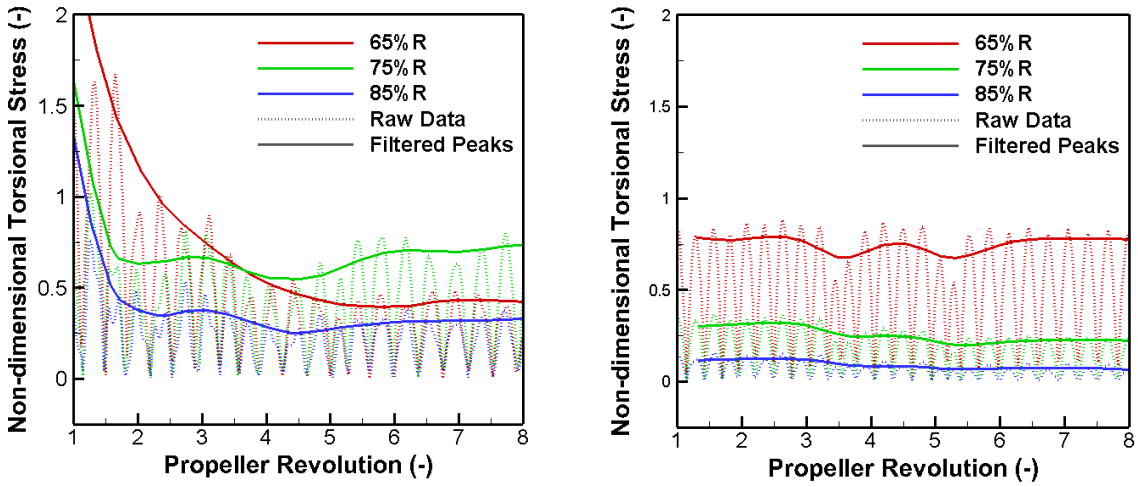

(a) Concentrated tip mass

(b) No mass

Figure 6.12: Comparison of the filtered peak torsional stress results for the the inclusion of a tip mass on the Commander blade at select radial stations

Presented in Figure 6.13 is the bending and torsion results for the simulation with a concentrated mass and the difference from the baseline result. The baseline result, presented in Figure 4.30, represents the profile of the baseline bending and torsion and as such indicates a tip heavy profile. This is also true for the tip mass bending result, shown in Figure 6.13(c), with the maximum bending of $\pm 0.06 c_{ref}$. This maximum, as per the stress, is contained towards the start of the simulation and as such gradually reduces through the acceleration reaching a final maximum value of $\pm 0.02 c_{ref}$. Due to the large bending oscillations at the start of the acceleration, the difference plot (Figure 6.13(d)) indicates an increase in the magnitudes. After the fourth revolution, the tip mass profile is almost constant and therefore the increases in the magnitudes towards the end of the simulation are a result of the baseline calculation.

This time-wise profile, shown in the torsional stress, is present in the bending and twist results, however, the maximum twist magnitude is contained towards the root of the blade (Figure 6.13(a)). The opposite profile of the bending. In terms of the maximum value, a starting value of $\pm 0.66^{o}$ is seen and this gradually reduces to $\pm 0.26^{o}$. This change in maximum location from tip to root results in an almost constant oscillation across the radius in the difference plot (Figure 6.13(b)). As a result, the inclusion of the concentrated mass can be said to minimise the blade torsion whilst amplifying the bending.

This difference in maximum locations for the bending and torsion results in the multi-peak oscillations in stress across the radius. Therefore, the key finding from this parametric study is the alteration of the stress profile across the blade radius.

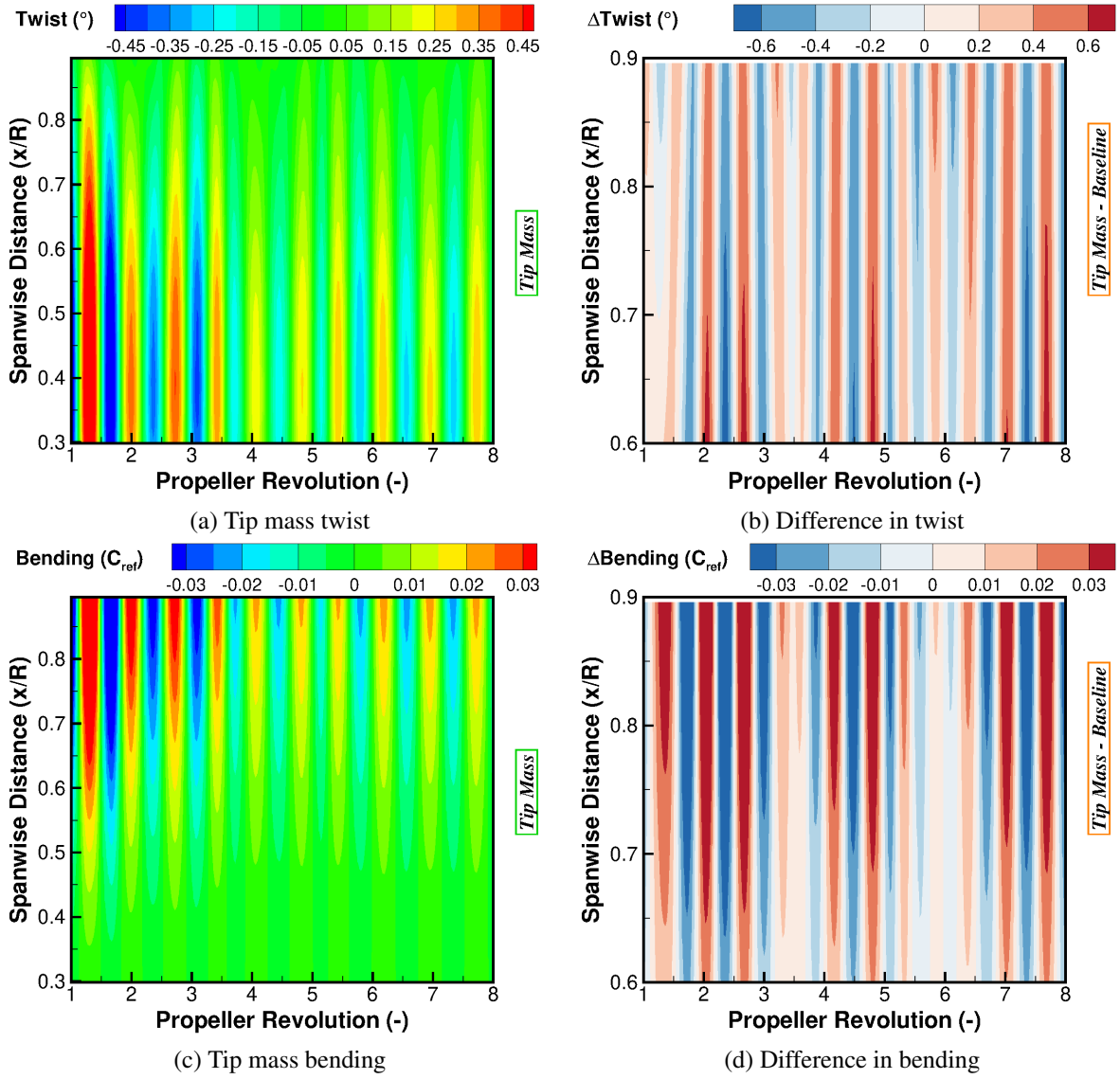

(a) Tip mass twist

(b) Difference in twist

(c) Tip mass bending

(d) Difference in bending

Figure 6.13: Difference in bending/torsion for the inclusion of a tip mass on the Commander blade

6.1.3 Torsional Stiffness

The third and final structural parametric study involves the investigation of the blade torsional stiffness. Rather than focusing on an specific change, such a study encompasses the entire blade on a more global scale. Changes in torsional stiffness can occur in an operational propeller and could involve damage or loosening of the root connection. For this reason, and due to the fact that any adjustment in torsional stiffness will result in a change in the torsional modal response, the reduction of the torsional stiffness is investigated.

In order to assess the change in blade response as a result of the reduction in torsional stiffness, the spring-bungee model is used. The reduction in stiffness is achieved by altering the shear modulus value in the `MAT1` isotropic material parameter. With a baseline shear modulus of $26GPa$, reductions to $2.7GPa$ are examined and the change in resultant frequency is pre-

sented in Figure 6.14. Up to a reduction of 40%, very little change is observed within the first and second modes. This is expected based upon the fact that both modes are flapwise bending and hence the torsional influence is minimal. It is only at reductions below 25% where larger changes in frequency are seen. For the torsion mode (mode 3), an almost linear reduction in the modal frequency is captured.

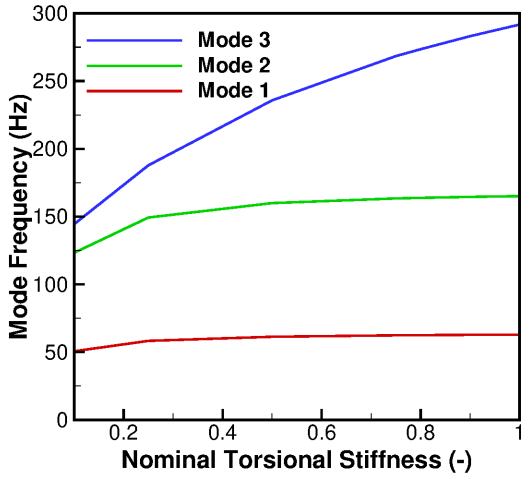

Figure 6.14: Change in the modal frequencies with the reduction in torsional stiffness for the Commander propeller blade

A reduction in the torsional stiffness by 50% sees a reduction in third mode frequency of 20%. For this configuration, the mode shapes are presented in Figure 6.15. There is a reduction in the flapwise bending deflection for the first mode. This, in line with a reduction in frequency, should result in a reduced modal amplitude response. For the third mode, as expected from the previous parametric studies, almost no change to the shape is observed. The response remains a torsional mode with the significant change coming from the frequency. The second mode has the potential to introduce a greater amount of variation within the simulation due to the increased amount of torsion included within the shape. The magnitude of the shape change from bending to torsion is not as prevalent as the previous studies, however, is noticible. Particularly around the blade root where the stall is seen to propagate from during the simulation.

Supplied Modes

Presented in Figure 6.16 is the spoke diagram comparison for the standard torsional stiffness and the 50% reduction. As per previous parametric simulations, the standard model involves the tuned validated model with the rotating blade configuration. As observed, small reductions in the modal frequencies are found with an average reduction of 4.5%, 11%, and 3% seen for the first, second and third modes, respectively. Such differences are smaller in comparison to the spring-bungee result and previous parametric simulations, however, remain sufficient enough to cause an effect. A substantial event would have to occur to result in a reduction in the torsional stiffness

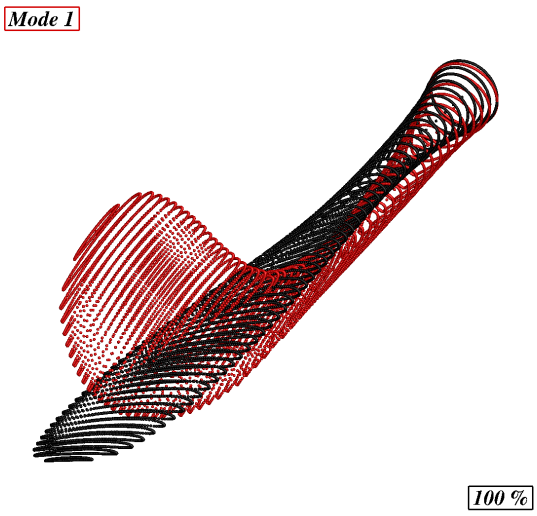

(a) Mode 1: 100% G

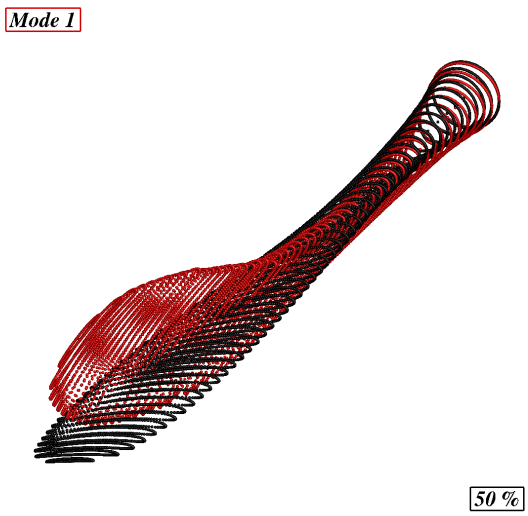

(b) Mode 1: 50% G

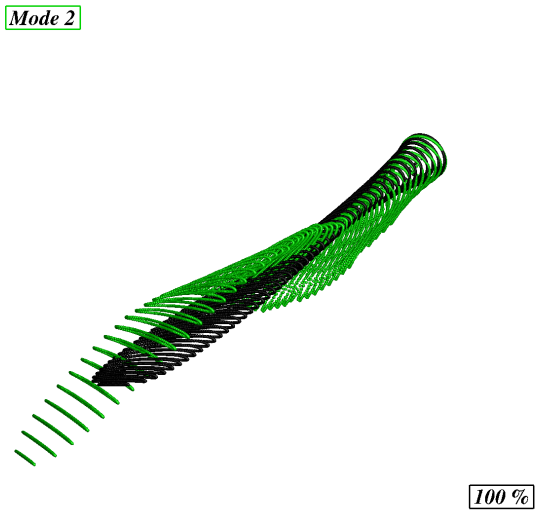

(c) Mode 2: 100% G

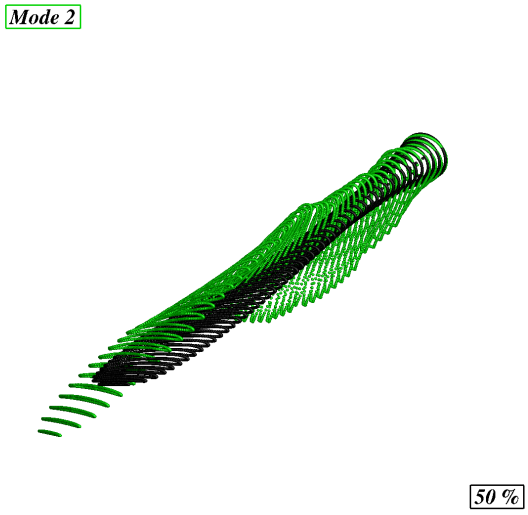

(d) Mode 2: 50% G

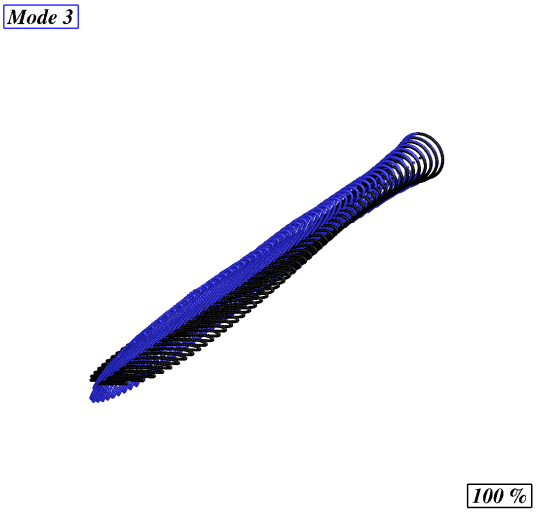

(e) Mode 3: 100% G

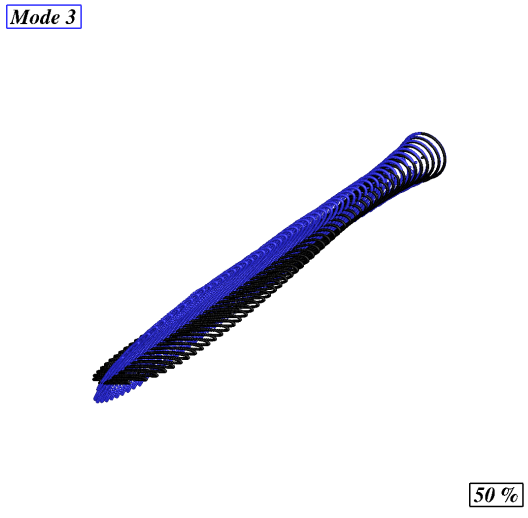

(f) Mode 3: 50% G

Figure 6.15: Change in the mode shape for reduction in torsional stiffness by 50%

by 50% and therefore, such a study strikes a balance between feasibility and the examination of the boundary.

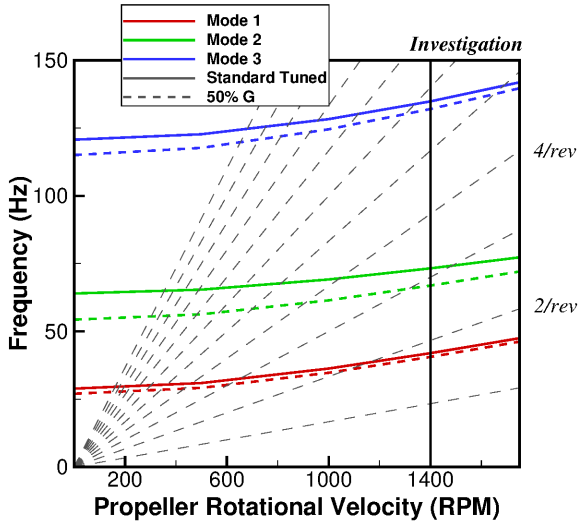

Figure 6.16: Influence of a 50% reduction in torsional stiffness on the Commander propeller blade spoke diagram

As per the previous parametric studies, the interpolation function with four stages was used and compared to the standard tuned model with four stages. The frequencies and shape for each stage of the interpolation function are presented in Table 6.3.

Table 6.3: Frequencies and shape of each mode for the reduction in torsional stiffness parametric study for every supplied stage of the interpolated simulation

		Rotational Velocity Stage			
Mode	**Shape**	*1400*	*1500*	*1650*	*1750*
1	FB	40.58	42.15	44.57	46.21
2	FB+T	66.89	68.35	70.57	72.07
3	T	132.02	134.11	137.40	139.69

T: Torsion, FB: Flapwise Bending

Aeroelastic Results

Presented in Figure 6.17 is the modal amplitude results for the full and reduced torsional stiffness simulations. All modes show similar profiles with slight changes in magnitude. For mode 1 (Figure 6.17(a)), the reduction in torsional stiffness sees a reduction in the first mode magnitude. This reduction is found to be $\sim 30\%$ with an overall fluctuation of ± 0.0067 for the stiffness reduction. In terms of the influence of the interpolation, an increase in percentage change is observed from the reduction in torsional stiffness. For the standard model, the modal amplitude increases by 15.4% through the acceleration. This percentage more than doubles to 33.5% for

the reduced stiffness calculation. Such an effect may become more influential over a larger acceleration range.

The greatest change in supplied frequencies is found for the second mode (Figure 6.17(b)) and as such, the greatest difference in modal amplitude magnitude is found here. Looking at the maximum fluctuation values, for the standard stiffness a value of $\pm 5.2 \times 10^{-5}$ is achieved and this increases by more than 100% to $\pm 10.9 \times 10^{-5}$. In terms of the change in magntiude through the acceleration, a greater reduction is observed for the reduced stiffness simulation with a reduction of 47% compared to 35%.

In a similar manner to the second mode, the third mode (Figure 6.17(c)) sees an increase in modal amplitude magnitude with the reduction in torsional stiffness. This is expected based upon the reduction in frequency and stability in mode shape. Looking at the maximum fluctuation values, the change in torsional stiffness sees an increase in magnitude of 19.5%. This percentage increase in magnitude grows through the acceleration with a final magnitude value 39% higher for the reduced stiffness simulation. This increase in ratio sees a reduction in the influence of the interpolation with the magntiude dropping less for the parametric simulation.

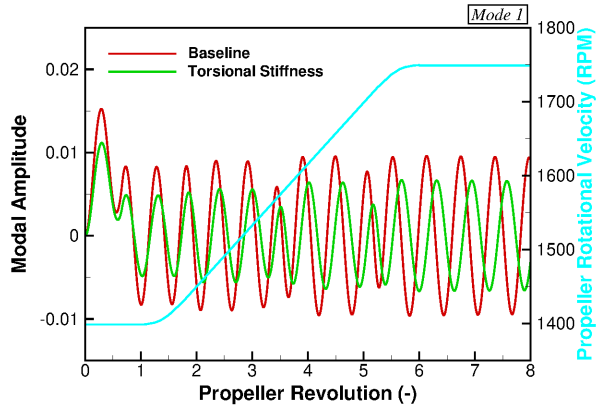

(a) Mode 1.

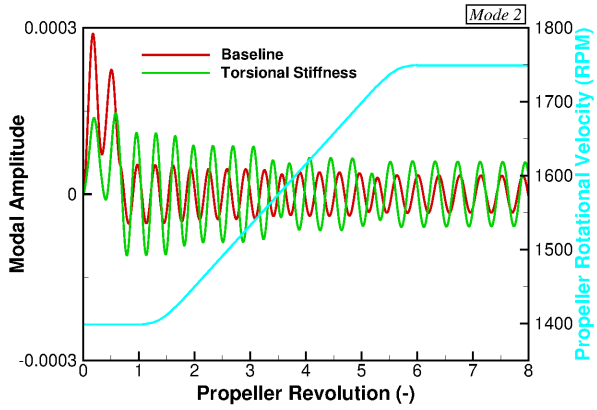

(b) Mode 2.

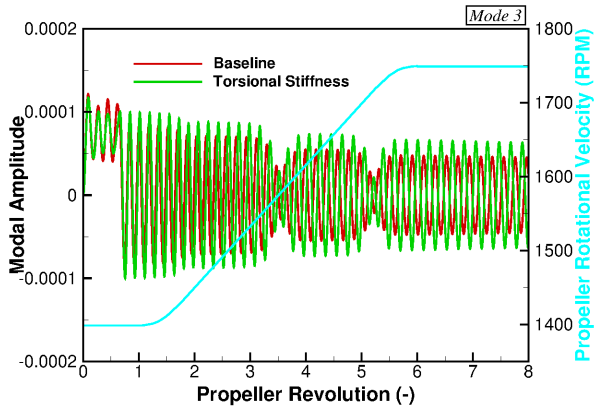

(c) Mode 3.

Figure 6.17: Comparison of the modal amplitude response for the reduction in torsional stiffness of the Commander blade

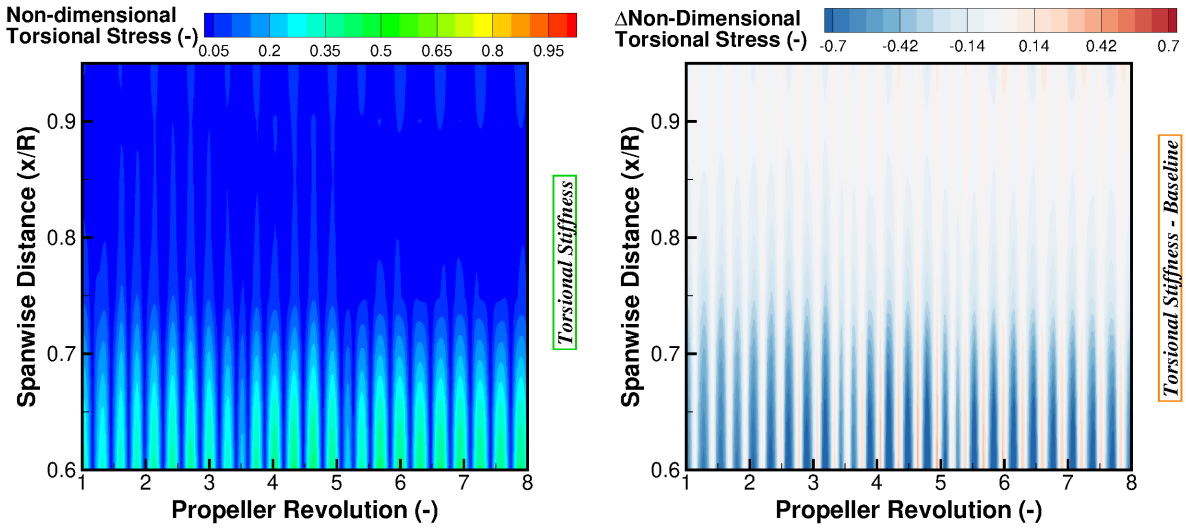

(a) Stiffness reduction

(b) Difference from baseline

Figure 6.18: Comparison of the torsional stress results for the reduction in torsional stiffness of the Commander blade

Presented in Figure 6.18 is the torsional stress results for the reduced stiffness calculation and the difference from the baseline. Due to the influence of the first mode, a reduction in the torsional stress results is found. The average value reduces from 0.22 to 0.09, equating to a percentage change of $\sim 60\%$. The maximum value also reduces by $\sim 28\%$ to 0.75. The overall profile of the stress results mirror the standard stiffness simulation, and thus, such a reduction in stiffness does not result in a significant change to the radial profile.

In a similar manner to the torsional stress, a reduction in both bending and twist is found. This is presented in Figure 6.19. For the standard simulation, maximum values of $\pm 0.033 c_{ref}$ and $\pm 0.52^{o}$ is found for the bending and torsion, respectively. With a reduction in stiffness, the bending maximum value reduces by 55% to $\pm 0.015 c_{ref}$ with the torsion maximum value reducing by 31% to $\pm 0.36^{o}$. In addition to the reduction in magntiudes, a shift is phase is found. This results in an amplification of the difference plot shown in Figures 6.19(b) & (d). Such a trend, as observed in the modal amplitude results, is also captured in the stress results, however is minimised due to the relative difference.

6.1.4 Key Findings

Following the conclusion of the structural parametric study, it was observed that all structural changes investigated influenced the stall flutter excitation for the given condition, with changes in torsional stress, blade deformation and modal amplitude results. The study is not exhaustive, but does give an indication as to the potential influence of the changes. A full parameter sweep would be required to determine the stall flutter boundary for this propeller blade. In lieu of such a study, the following findings can be drawn based upon this parametric investigation.

Both the offset in centre of gravity and reduction in torsional stiffness was found to reduce

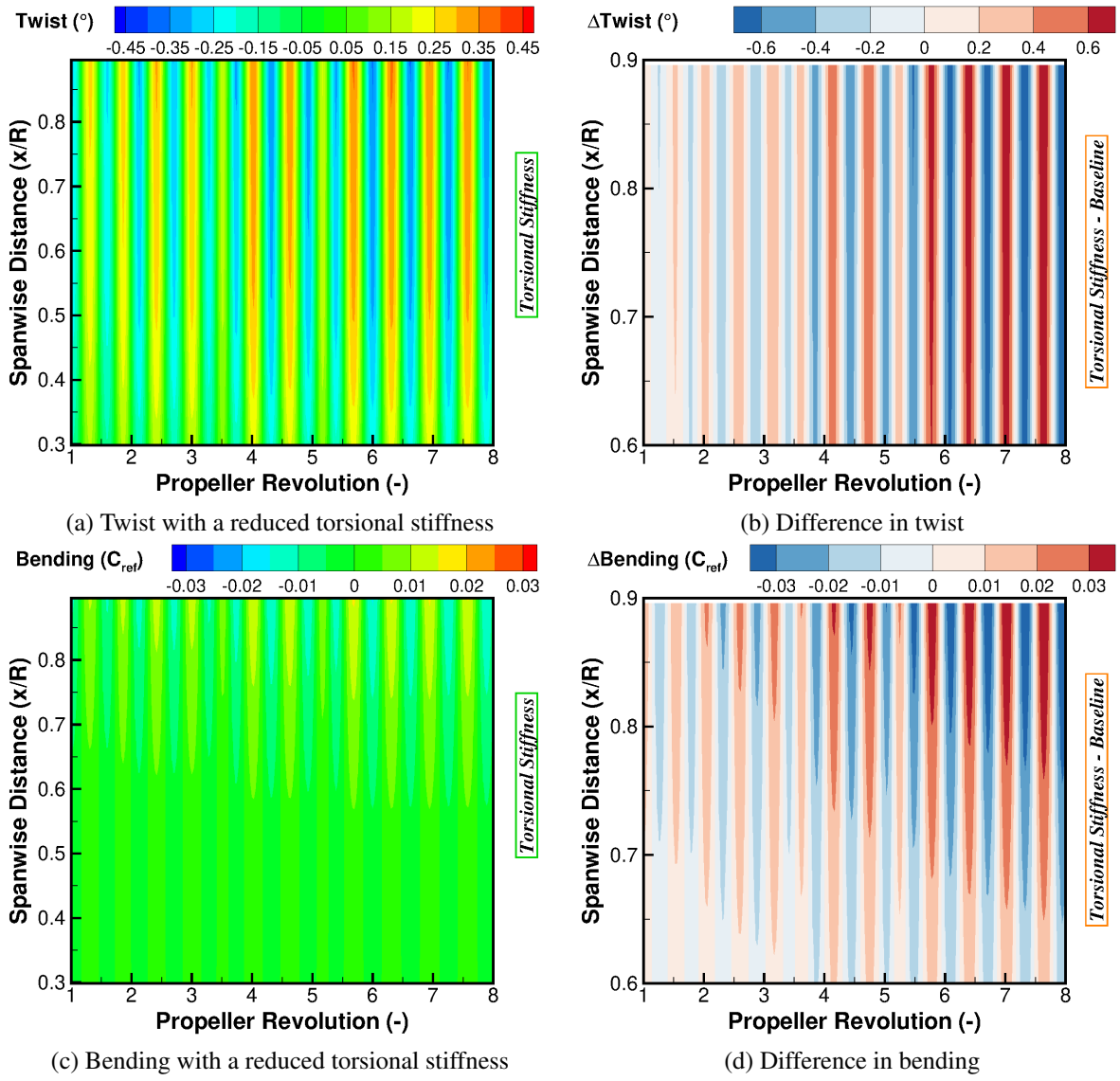

(a) Twist with a reduced torsional stiffness

(b) Difference in twist

(c) Bending with a reduced torsional stiffness

(d) Difference in bending

Figure 6.19: Difference in bending/torsion for the reduction in torsional stiffness for the Commander blade

the stress acting on the blade. In addition to the reduction in torsional stress, the overall loads acting on the blade did not change significantly, as shown in Figure 6.20. This result indicates a potential optimisation path and, combined with smart blade technology, could result in significant stall flutter mitigation throughout the flight regime.

The greatest change in torsional stress profile comes from the introduction of the concentrated mass. The centre of gravity and torsional stiffness simulations found the profile to be similar to the standard modal interpolated-tuned modes simulation. The highest stress is found towards the mid-span with an almost constant profile through the acceleration. With the introduction of a tip mass, additional peaks along the radius are generated. The $75\%R$ station is found to be fairly constant through the acceleration and subsequently results in a higher stress value towards the tip. The structural design of the blade must therefore be able to cope with such a change and could be exacerbated depending on the conditions. Although such an increase

($20\%m_b$) is unlikely, an increase tip mass can be generated through propeller damage, debris pickup, and/or ice build up. This simulation indicates the potential for such an alteration and a full sweep of the mass value would be required to understand the full boundary effect.

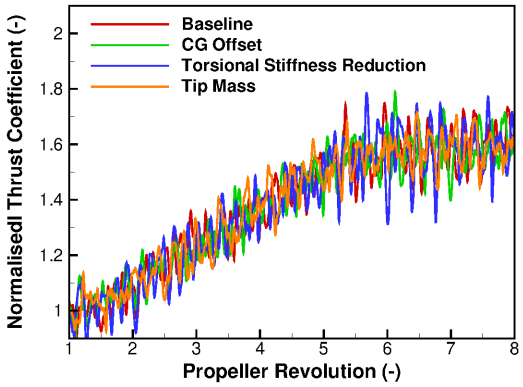

Figure 6.20: Comparison of the normalised thrust coefficient for all structural parametric studies

For all simulations, the overall deformation is dominated by the first mode with a fairly consistant flapwise bending profile. Parametric investigations involving the bending modes is required to understand how this first mode effects the blade response. This could involve a forward offset in centre of gravity, increase in torsional stiffness, or decrease in bending stiffness.

6.2 Aerodynamic Study

All structural parametric simulatons involved the acceleration of the Commander propeller blade in static conditions at a reference pitch angle. The reference pitch angle and static conditions have a significant affect on the stall conditions and subsequent blade loads. A drastic decrease in blade pitch angle was investigated in Section 4.4 and found a large reduction in blade deformation. A similar effect in reducing the amount of stall can be captured via the introduction of a freestream axial velocity. With this in mind, these affects are investigated to determine their effects on the blade stall flutter response.

6.2.1 Increase in blade pitch

The following parametric study involves the increase in blade pitch angle to understand its effect on the blade response. An increase in blade pitch could result in an increase in blade loads and detached flow, subsequently changing the response. Such a response change was seen during the Dowty experiment with a large increase in stress captured up to the stall angle [28], and also historically through the experiments of Baker [14] and Smith [125]. The historical studies found a significant reduction in stall flutter boundary at low pitch angles before slowly increasing at high pitch. The slow increase following the minimum value is a result of the blade being fully

stalled and hence, any increase in pitch is likely to reduce blade loads and thus reduce blade deformation.

Due to these factors, and the fact the reference simulation is conducted at the stall flutter angle of the experiment, care must be taken in choosing the correct angle. Too high an increase may result in a reduction in stress, in line with the historical studies, and also become unrealistic as to what to expect from an operational point-of-view. A slight increase, within a single degreee, could be possible due to an incorrect maintenance procedure, slight damage within the blade pitch controller, or simple mis-calibration. If the increase is too low, the expected change may be too small to distinguish between the simulations and therefore not provide any insight.

As a result, for this parametric study, the propeller blade was investigated at an increased pitch angle of 2^{o}. The pitch change was applied via the blade grid and a subsequent rigid solution was required before introducing the aeroelastic module. As per the previous simulations, the *SAS* model is used for the accelerating blade between 1400 and 1750 (rpm). This result was compared to the interpolated tuned model simulation of Section 4.6 in which the same structural setup was used.

Aeroelastic Results

Presented in Figure 6.21 is the modal amplitude comparison between the standard and increased pitch simulations. Due to the increase in pitch, a small change in magnitude is observed with a constant profile seen between the two simulations. This is optitimised by the first mode where a reduction in the fluctuation magnitude of 7.8% is found. As this is the critical mode, a subsequent reduction in stress and deformation is expected.

A similar small change in magnitude is observed for the third mode. Here an increase in fluctuation magntiude is found with the average value increasing from $\pm 6.38 \times 10^{-5}$ to $\pm 6.83 \times 10^{-5}$. Equating to a 7.1% increase in magnitude. Both the second and third modes were found to increase, with the greatest change captured in the second mode. The second mode increases in fluctuation magntiude by 125% to $\pm 9.62 \times 10^{-5}$.

Looking at the differences between the two simulations for all modes, greater insight into the resultant change can be observed. As previously discussed, the percentage change over the current modes are -7.8%, $+125\%$ and $+7.1\%$ for the first, second and third modes, respectively. For the overall change, with respect to the first mode difference, this results in a 7.1% and 0.6% increase for the second and third modes, respectively. As expected, the first mode dominates, however, some slight changes may be expected across the blade due to the other modes.

Due to the consistancy of structural models, the difference in modal amplitude is driven by the modal force results and these, along with the difference from the reference, are presented in Figure 6.22. Presented for the increased pitch simulation (Figure 6.22(a)) is the 90^{o} rolling averaged results. Due to the acceleration of the blade, a gradual increase in all modes is observed with larger values seen for the first mode.

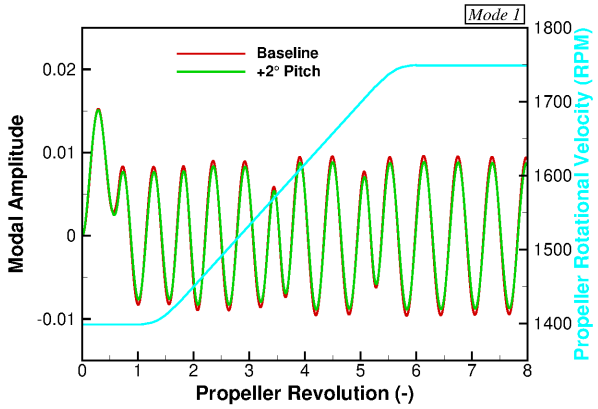

(a) Mode 1.

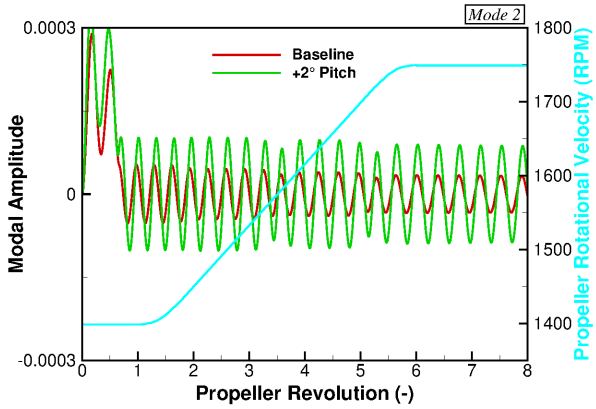

(b) Mode 2.

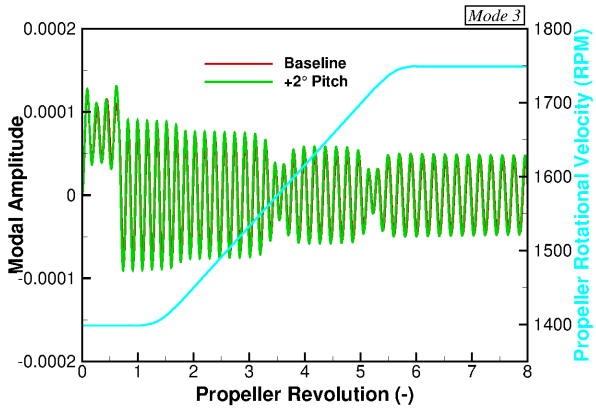

(c) Mode 3.

Figure 6.21: Comparison of the modal amplitude response for the increase in blade pitch of the Commander blade

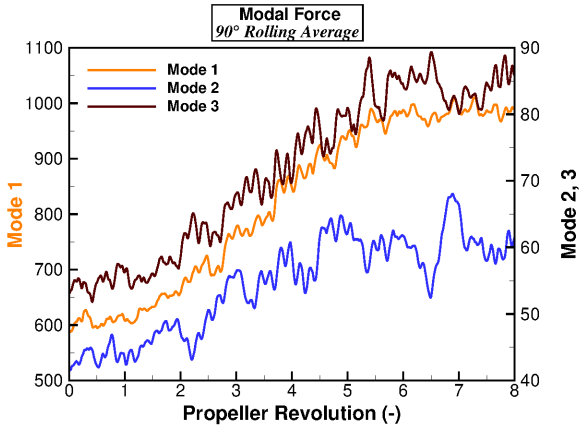

(a) Increased pitch rolling average

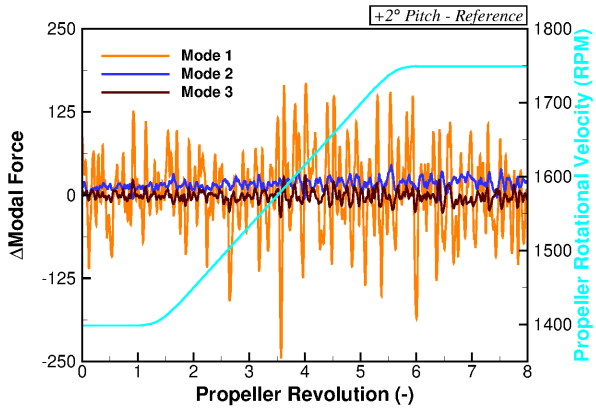

(b) Difference from reference

Figure 6.22: Modal force results for the increased pitch simulation, with the difference from the reference, for the Commander propeller blade

With similar trends between both simulations, the difference in modal force is shown in Figure 6.22(b). Average differences of 1.85, 16.52 and -1.72 are found for the first, second and third modes, respectively, however, the nature of the stalled conditions results in the fluctuations driving the differences in amplitudes. Removing such averages, the mean fluctuations are found to be ± 50.8, ± 6.6 and ± 7.3, respectively.

Presented in Figure 6.23 is the torsional stress results for the increased pitch simulation. With the stress results mirroring the first modal amplitude, very similar profiles and values are found. The maximum value has reduced by 2% from 1.04 to 1.02, with the same average value of 0.224 for both simulations. The reduction in maximum value is highlighted in the difference plot shown in Figure 6.23(b), where the high stress regions at the mid-span indicate small decreases in stress.

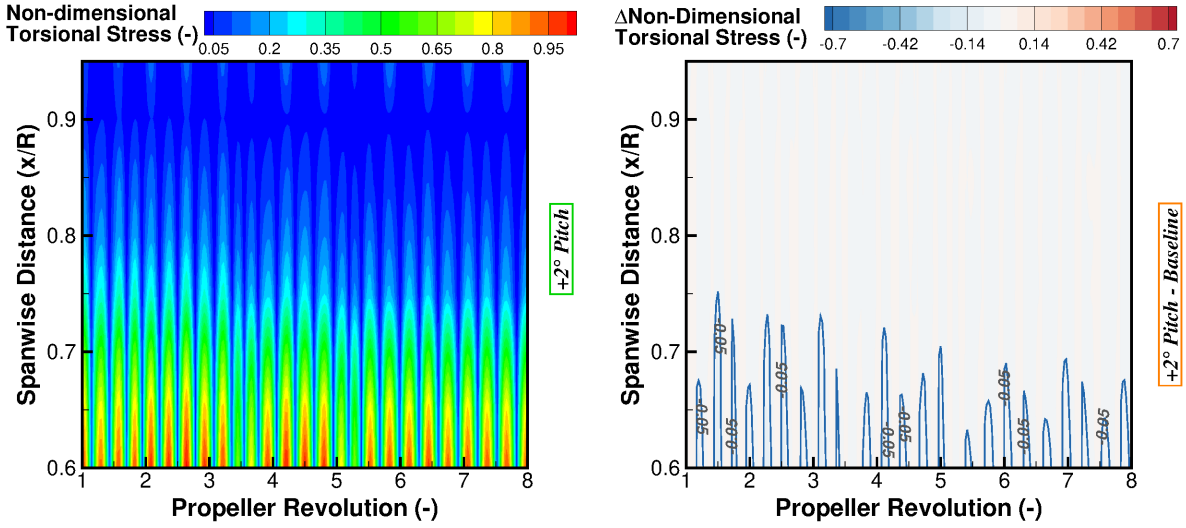

(a) Increased pitch

(b) Difference with baseline

Figure 6.23: Comparison of the torsional stress results for the the increase in blade pitch of the Commander blade

In a similar manner to the torsional stress results, very small differences in bending and torsion are also shown in Figure 6.24, with the twist results taking into account the increase in blade pitch. With the contour kept constant as per the previous parametric simulations, small magnitudes in both parameters are found. For the blade torsion, an average reduction of -0.171° is seen and this is highlighted in Figure 6.24(a). The maximum and minimum values are found to be -0.39° and -0.06°, respectively, and thus finding an overall reduction throughout the blade and simulation. In terms of the difference profile for the blade torsion, larger changes in twist are present towards the mid-span section with the lower magntiude values towards the tip.

In terms of bending (Figure 6.24(b)), an average reduction of $-0.0048c_{ref}$ is found with reductions seen across the entire plot. The maximum and minimum values are $-0.0082c_{ref}$ and $-0.0013c_{ref}$, respectively. An opposite bending profile is captured with respect to the torsion with the highest bending differences found towards the tip.

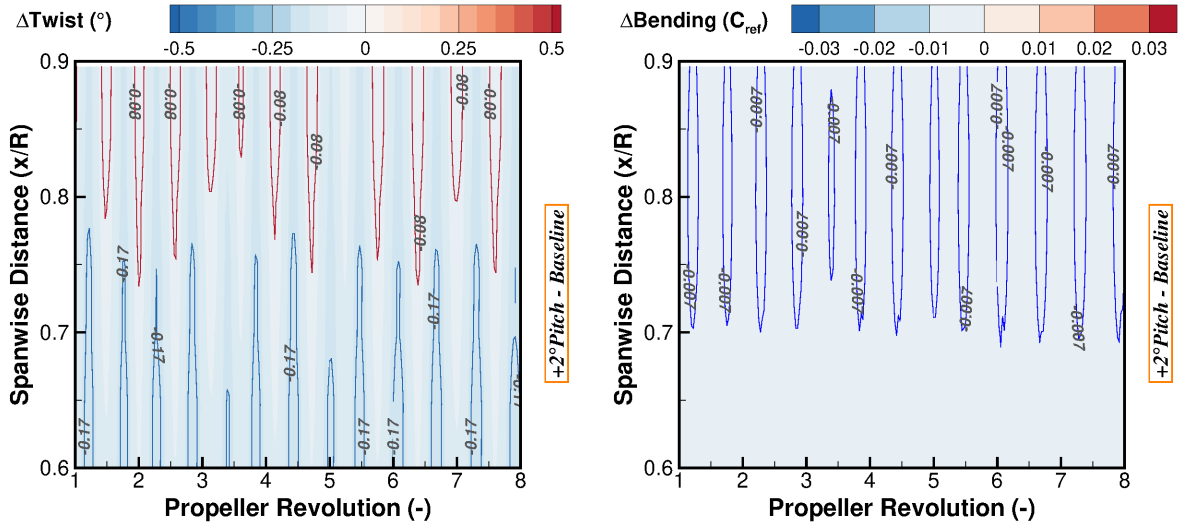

(a) Twist (b) Bending

Figure 6.24: Difference in bending/torsion for the increase in blade pitch of the Commander blade

In order to assess the change in aerodynamic conditions due to the increase in pitch, the frequency response of the blade surface pressure coefficient, and the difference from the reference, is presented in Figure 6.25. Due to the broadly similar conditions, similar profiles (Figure 6.25(a)) between the two simulations are captured with the greatest fluctuations in pressure found around 80%R. The similar profiles are expected with the differences anticipated in terms of magnitude, and this is found for the increased pitch simulation. The largest magnitudes come above a frequency value of 3/revolution , with the maximum frequency occuring at 5.37/revolution . In addition to an increase in magnitude around this frequency, an increase in content at higher frequencies up to 18/revolution is found towards the blade tip. This gives an indication of an increased frequency of the blade shedding.

Focusing on the difference plot (Figure 6.25(b)), the average change in amplitude is found to be an increase of 1.214. This represents an increase of 29% from the average reference value, with a maximum increase of 77% and reduction of 50%. In terms of the area comparison, 65% of the difference plot is found to have a positive contribution, hence the positive average.

Due to the change in surface pressure coefficient, a slight variation in the propeller loads were expected and these are shown in Figure 6.26. In addition to the 90^{o} rolling average thrust and pitching moment coefficients, the frequency response of the raw data is inserted into each plot. Focusing on the thrust coefficient (Figure 6.26(a)), very similar results are found for the rolling average profiles with an average change of $+0.04\%$. Some small pockets of decreased and increased load is captured throughout the simulation, for example, around revolution 2.75 and 4.0, respectively.

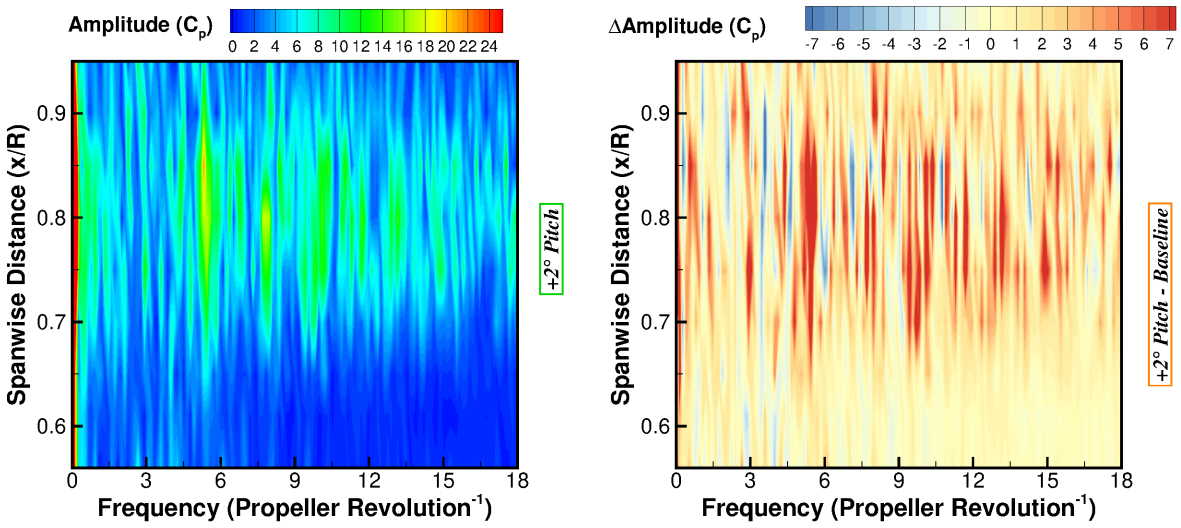

(a) Increased pitch frequency response

(b) Difference from reference

Figure 6.25: Surface pressure coefficient frequency response for the increased pitch simulation of the Commander blade

In terms of the frequency response for the thrust coefficient, the highest amplitude is found around 5/revolution . This is true for both thrust and pitching moment. It is found that the increased pitch simulations results in increased amplitudes around this frequency. This is expected based upon the surface pressure coefficient results and further afirms the increase in detached flow.

For the pitching moment (Figure 6.26(b)), a reduction in the coefficient is found throughout the entire simulation. This results in an average reduction of $\sim 10\%$. Such a result mirrors the change in twist results (Figure 6.24(a)) where an overall reduction in torsion was found.

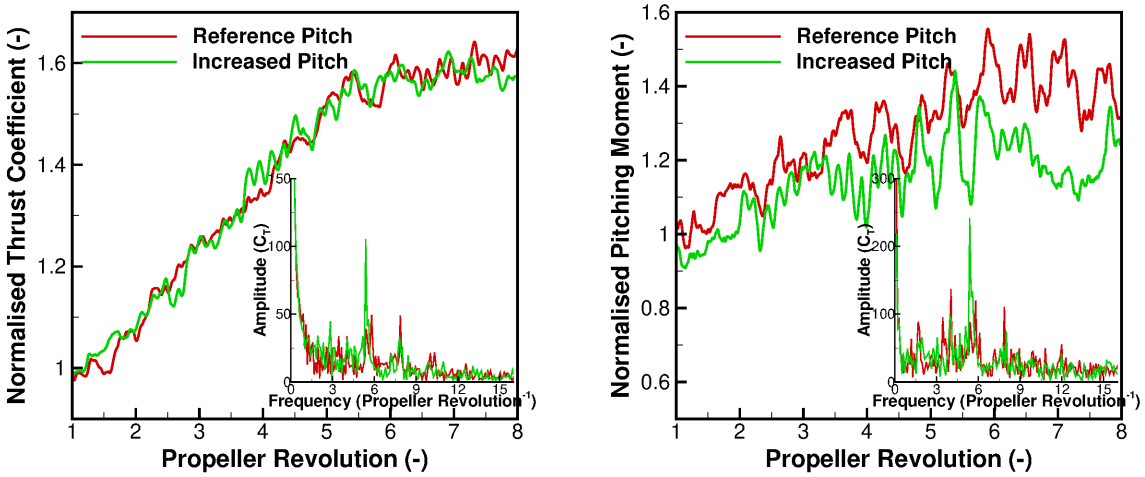

(a) Thrust coefficient

(b) Pitching moment

Figure 6.26: Rolling average normalised load comparison for the increased pitch simulation of the Commander blade

Presented in Figure 6.27 is the centre of pressure comparison for the increased pitch simulation of the Commander propeller blade. Due to the shift in pitching moment, a suspected change in the blade centre of pressure was expected and this is seen in Figure 6.27(a). Almost all examined radial stations see a shift forward in centre of pressure and this shift varies from $+0.06\%$ to -0.27%. As observed from Figure 6.27(b). The greatest change is found at the $70\%R$ station, where an average shift of -0.21% is seen. In terms of the profile along the radius, this does not change between the simulations with the profile for the increased pitch shown in Figure 6.27(c). From the root, the centre of pressure gradually shifts rearward towards the tip with one single change in direction at $80\%R$.

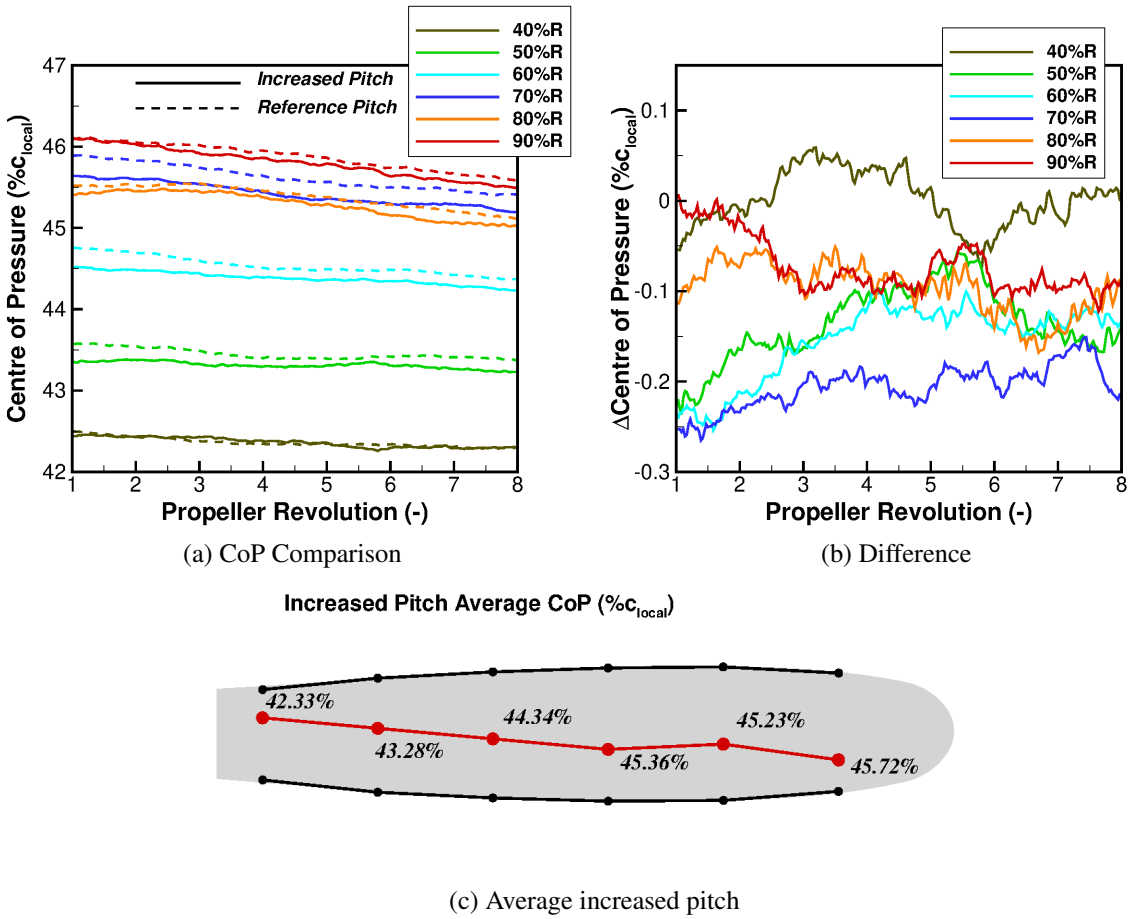

(a) CoP Comparison

(b) Difference

(c) Average increased pitch

Figure 6.27: Rolling average centre of pressure comparison for the increased pitch simulation of the Commander blade

6.2.2 Introduction of Inflow

All of the simulations conducted for this propeller have been in static conditions. This is selected based upon the experimental conditions but also due to the fact an inflow velocity can stabilise any detached flow with stall flutter likely to occur in low inflow conditions, such as during take-off. With this in mind, a parametric study was conducted with an inflow velocity introduced.

In order to assess the effect of the change in aerodynamic condition, rigid simulations using the hover formulation were conducted. The hover formulation was used in Section 4.4 to assess the change in pitch and was similarily used to assess the introduction of an inflow of 2.5%, 5% and 10% of the blade tip velocity at $1400(rpm)$. This equates to an inflow velocity of 10, 20 and 40 knots, respectively, corresponding to advance ratios of 0.082, 0.164 and 0.328. For this rigid simulation, the *RANS* formulation is used with the $k-\omega$ turbulence model.

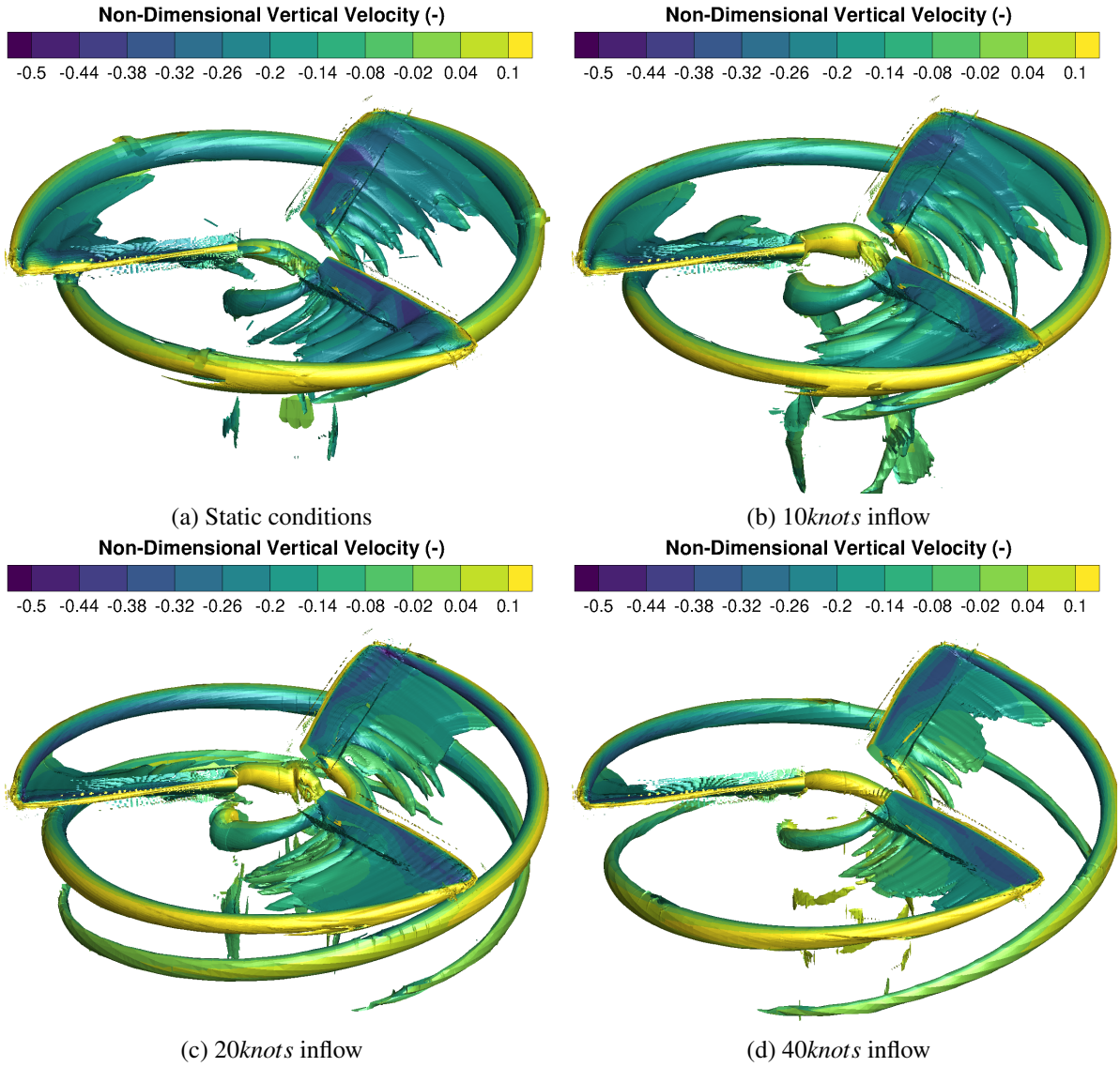

(a) Static conditions

(b) 10*knots* inflow

(c) 20*knots* inflow

(d) 40*knots* inflow

Figure 6.28: Flow visualisation using iso-surface of vorticity magnitude for the introduction of an inflow velocity to the Commander blade

Presented in Figure 6.28 is the vorticity magntiude iso-surfaces of the rigid hover formulation simulations for the introduction of an inflow velocity. The static simulation (Figure 6.28(a)) was previous described and found the detached flow across the entirity of the blade. The level of detached flow is gradually reduced each inflow velocity increment. A similar stall profile is seen at 10 knots (Figure 6.28(b)) with a reduction in the stall bubble size. This is highlighted towards

the tip where two distinct bubble merge.

Increasing the velocity further to 20 knots (Figure 6.28(b)) almost fully attaches the flow across the blade. This creates a more refined wake profile with the inflow velocity propagating the tip vortex further downstream. Some small pockets of detached flow are seen across the blade, specifically, towards the blade tip at the leading edge and at the trailing edge inwards of mid-span. As found from the static aeroelastic simulation, the detached flow at the root propagates towards the tip and thus the detached flow for the inflow case is likely to follow a similar path.

The final inflow velocity of 40 knots (Figure 6.28(c)) presents a completely attached flow profile. The small vorticies at the leading edge of the tip and trailing edge of the root have now been mitigated. Such a condition, although it would improve the overall blade performance, does not fit the criteria to investigate propeller stall flutter due to the lack of detached flow. Thus, based upon the hover formulation simulations, the 20 knots inflow is seen as the best condition from which to base the parametric study.

Following the hover simulations, the introduction of the 20 knots inflow velocity was studied in an unsteady manner. This would allow for the detached flow to be propagated in time and thus, gaining further insight into the condition. With this in mind, the normalised thrust results are presented in Figure 6.29. Along with the standard *URANS* simulation with the $k-\omega$ turbulence model, the *SAS* method was employed to refine the detached flow modelling. As prevous, the thrust coefficient results are normalised with respect to the average static *SAS* result, hence an average normalised value of 1.0 is found. The introduction of the *SAS* model results in an increased amount of detached flow and vortex shedding due to the modelling refinement. As a result, the *URANS* static simulation produces a higher average value of 1.09 and a reduced amount of fluctuation. A similar trend is seen between the inflow calculations. The *URANS* result produces an almost constant thrust value throughout a propeller revolution with the highest average value of 1.26. This is expected based upon the reattachment of the flow shown in the hover formulation results and the expected lack of vortex shedding. As per the static simulations, the use of the *SAS* model reduces the average load value to 1.14 with an increase in load fluctuations. These fluctuations are driven by the shedding of vorticies from the detached flow regions highlighted in the hover formulation simulations.

From both the hover formulation and unsteady simulations, the introduction of the 20 knots inflow reduces the amount of detached flow without fully reattaching. With this in mind, the introduction of 20 knots inflow to the model was simulated using the aeroelastic model and the *SAS* formulation. Such an inflow provides a balance between mitigating the stall and pushing the boundary towards what would be expected during take-off. For this aeroelastic simulation and as per the increased pitch parametric study, the tuned verified structural model is used with the four-stage interpolation function.

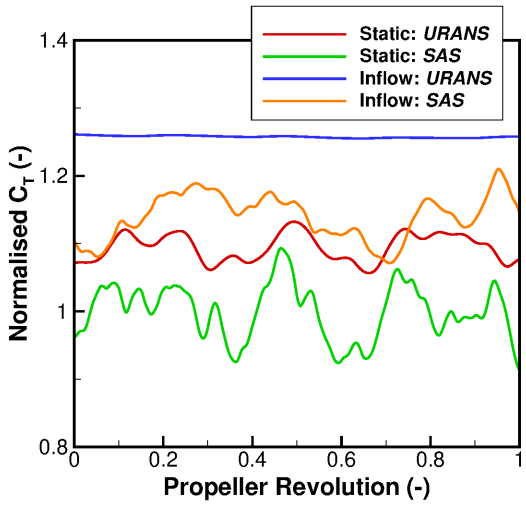

Figure 6.29: Unsteady normalised thrust results for the introduction of 20 knots inflow to the Commander blade

Aeroelastic Results

Presented in Figure 6.30 is the modal amplitude comparison between the static and inflow simulations for all supplied modes. Due to the fact the same mode shapes and frequencies are supplied, similar profiles are captured between the amplitudes. The greatest change in the each mode comes from the fluctuation magnitudes.

With the trend between each stage the same, an average amplitude across the simulations are taken and compared. All modes see an increase in fluctutation magnitude and this is potentially expected due to the increase in thrust observed from the unsteady simulations (Figure 6.29). For each individual mode, an increase of 13.4%, 162.5% and 14.7% is seen for the first, second and third modes, respectively. Due to the fact the largest amplitudes are observed for the first mode, these differences are scaled with respect to this and subsequently the percentage differences for the second and third mode drop to 8.78% and 0.1%. Such a result shows that the overall blade deformation change is effected by the first and second modes.

As with the increased pitch simulation, the shift in modal amplitude is driven by the modal force results. These are presented in Figure 6.31 for the introduction of inflow. Similar profiles between the reference static, increased pitch and inflow simulations are found for all modes. Focusing on Figure 6.31(a), the modal force gradually increases through the acceleration with larger forces observed for the first mode.

The differences between the static and inflow simulations are presented in Figure 6.31(b). As expected, increases in all modes are found with the greatest increase coming in the first mode. Average increases of 47.5, 4.18 and 8.9 are seen for the first, second and third modes, respectively.

Due to the slight change in modal force driving an increase in modal amplitude, a slight change in torsional stress is also found. This is presented in Figure 6.32 for the inflow simulation.

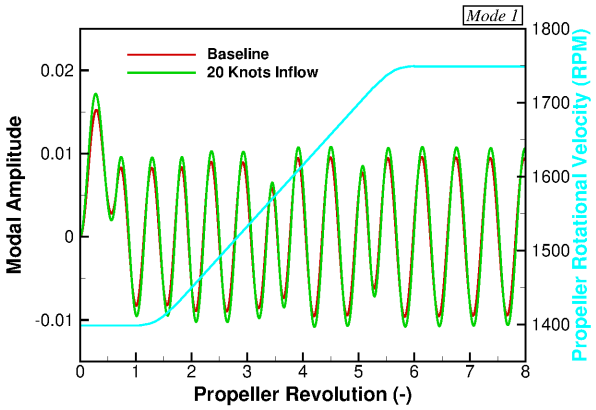

(a) Mode 1.

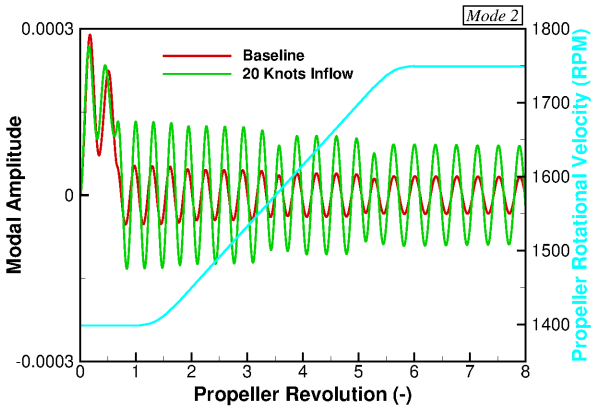

(b) Mode 2.

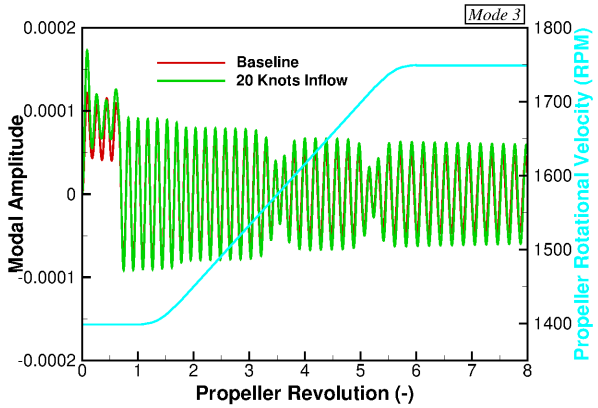

(c) Mode 3.

Figure 6.30: Comparison of the modal amplitude response for the introduction of a 20 knots inflow to the Commander blade

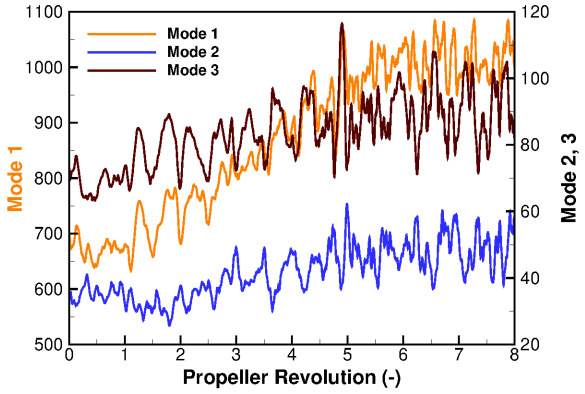

(a) Inflow

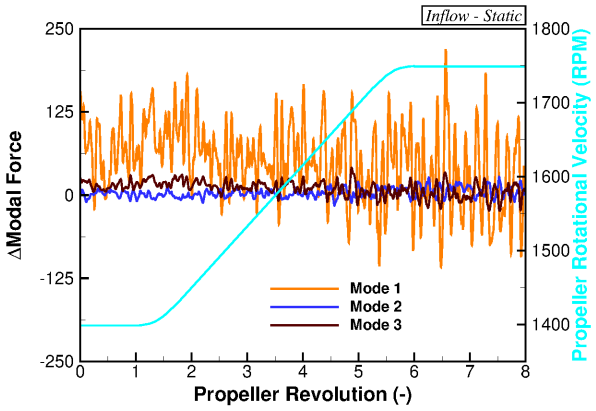

(b) Difference from reference

Figure 6.31: Modal force results for the 20 knots inflow simulation, with the difference from the reference, for the Commander propeller blade

Focusing on the inflow result (Figure 6.32(a)), the same trend between the static (Figure 4.29(a)) and inflow simulations are found. An almost linear profile from mid-span to tip is seen along the radius with a constant trend through the transition. Looking at the average and maximum values,

increases in both are found. As previously reported for the static simulation, values of 0.224 and 1.04 are captured for the average and maximum values, respectively. With the introduction of a 20 knots inflow, the average value increases by 10.5% to 0.2475 and the maximum increases by 15.2% to 1.12. Such values correlate to the percentage increases in the modal amplitudes.

The difference between the two simulations is presented in Figure 4.29(b), where the profile is dominated by an increase in stress. In terms of the area, 74.2% of the profile finds an increase in stress with an overall average value of $+0.030$. The increase in stress is dominated by the change towards the mid-span section of the blade. Between the $60\%R$ and $75\%R$ station, an average value of $+0.056$ is found and this reduces by 80% to $+0.011$ outwards of $75\%R$.

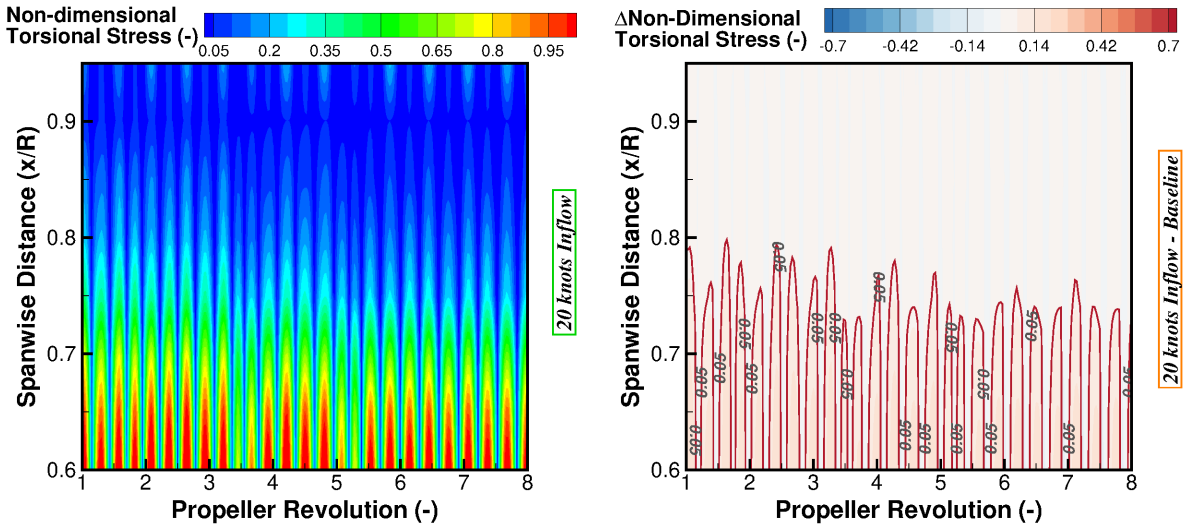

(a) 20 knots inflow

(b) Difference with baseline

Figure 6.32: Comparison of the torsional stress results for the introduction of a 20 knots inflow to the Commander blade

Presented in Figure 6.33 is the change in bending and torsion between the two simulations. Due to the similarities in modal amplitude and stress, the deformation profile is also similar with some slight increases in the magnitude of the fluctuations. With the introduction of the inflow, the blade torsion increases in magnitude by $\pm 0.05^{o}$ with the bending also increasing in fluctuation magnitude to $\pm 0.003 c_{ref}$.

The increase in overall blade deformation is driven by the increase in loads being applied to the blade. This is presented in Figure 6.34 and shows the normalised thrust and moment coefficients with inserts showing the frequency response. The time-history results are rolling averaged over 90^{o} of the revolution with the raw data used for the fast fourier transform. As observed from the thrust coefficient (Figure 6.34(a)), an increase in thrust is found with this expected based upon the rigid solution. At the start of the simulation, an almost 20% difference between the two simulations is found. This is contained to within the first propeller revolution. After this initial peak, the difference between the two simulations stablise with an average increase of 6.4%. A similar frequency response is observed in Figure 6.34(a). Some lower frequency peaks

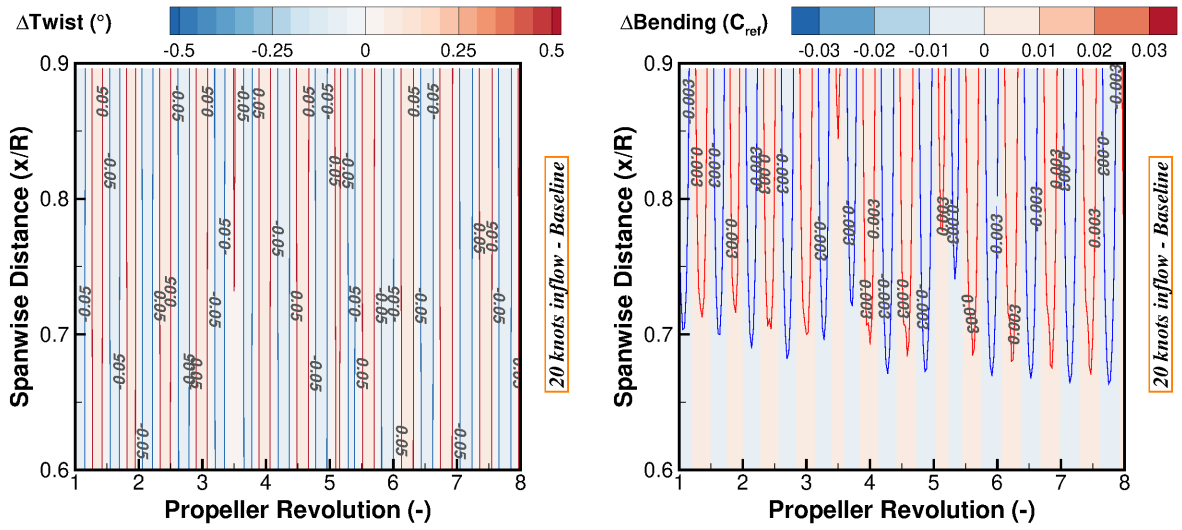

(a) Twist (b) Bending

Figure 6.33: Difference in bending/torsion for the introduction of a 20 knots inflow to the Commander blade

are observed for the inflow simulation with peaks around 1.7/revolution and 3.1/revolution . For both simulations, higher frequency peaks are observed at 4/revolution , 5.6/revolution and 7.8/revolution . Each of these indicate a reduction in amplitude for the inflow simulation, and hence a reduced fluctuation in the thrust results.

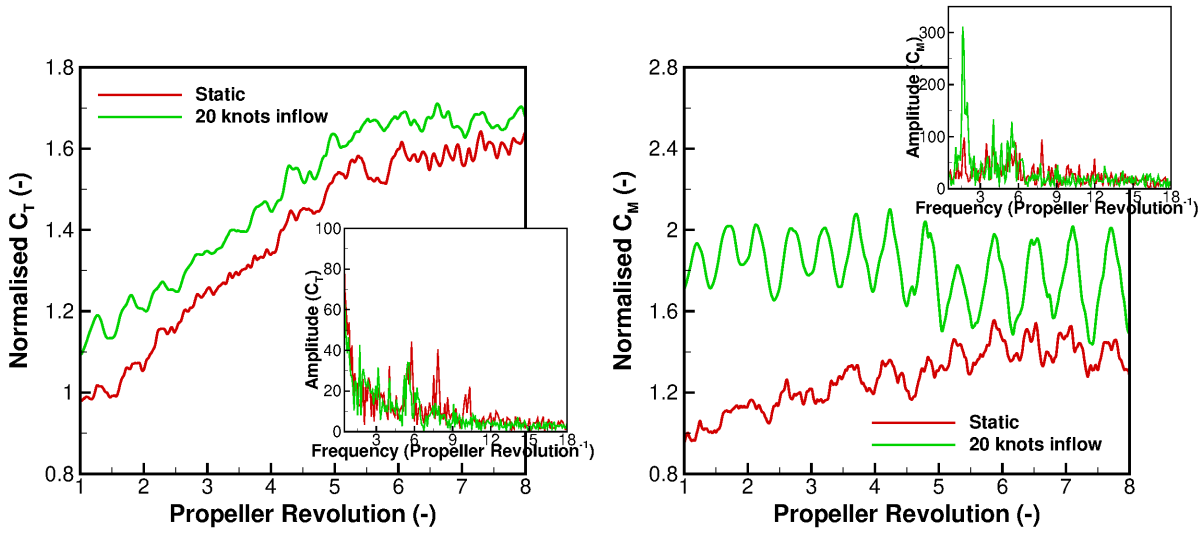

(a) Thrust coefficient (b) Pitching moment

Figure 6.34: Rolling average normalised load comparison for the 20 knots inflow simulation of the Commander blade

In addition to the thrust coefficient, the time and frequency response of the blade pitching moment is presented in Figure 6.34(b). Differing responses are found between the two simulations in terms of the blade pitching moment. For the static simulation, a gradual increase in moment is observed through the acceleration with the response stabilising after revolution 5. An almost stable oscillating response is found for the inflow simulation with the fluctuation mag-

nitude increasing as the blade accelerates. Before revolution 5, the moment oscillates around the average value at ±0.21 with this increasing to ±0.33. Due to the almost constant average value for the inflow simulation, the difference between the simulations follows the inverse trend of the static plot. From the start to end of the acceleration, the inflow result drops from an peak increase of 99% to an average increase of 23%. Due to the change in moment response, a differing frequency plot is observed with the greatest peak found from the inflow simulation at a lower frequency value of 1.6/revolution .

One of the key discoveries from the thrust coefficient results is the reduction in amplitude of the frequency response. This is driven by the detached flow and subsequently, the surface pressure coefficient. The surface pressure coefficient frequency response for the inflow simulation, and the difference from the static, is presented in Figure 6.35. With the static response similar in trend to the increased pitch simulation (Figure 6.25(a)), a significant change in surface pressure response is found. For the static simulation, high magnitude and frequency fluctuations were dominant around the 80%R station. Such a response is not seen in Figure 6.35(a) with all content above 6/revolution small in terms of amplitude and no significant peak seen around 80%R. Essentially a single peak around 90%R is found at a low frequency value of 1.7/revolution . This frequency is found within both the thrust and pitching moment response, and is the primary frequency driving the oscillation in moment. These differences are highlighted in Figure 6.35(b).

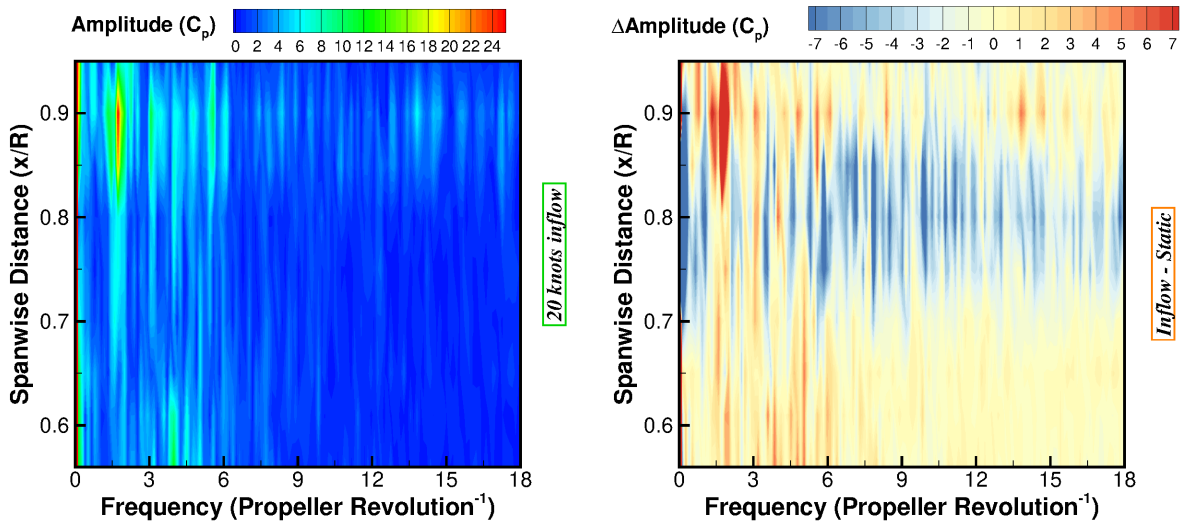

(a) Inflow frequency response

(b) Difference from reference

Figure 6.35: Surface pressure coefficient frequency response for the 20 knots inflow simulation of the Commander blade

Due to the significant change in thrust and pitching moment coefficient, a shift in the centre of pressure profile is expected and this is presented in Figure 6.36. Around the blade mid-span, from 40%R to 60%R, very small changes are found with an almost constant offset in pressure from the static conditions seen. The 40%R station results in an average rearward offset of 0.18%, with the 50%R and 60%R stations shifting forward by 0.13% and 0.18%, respectively.

Outwards of these sections, significant changes in average offset and profile is found. For both the 70%R and 80%R stations, a change in profile through the acceleration is observed between the start and end of the simulation. Focusing on the 70%R station in the first four propeller revolutions, very little difference is found in the centre of pressure result between the inflow and static conditions. At this stage, an average difference of 0.04% is seen. Following the fourth revolution, the inflow profile shifts forwards at a rate 165% higher than the gradient observed across the full static profile resulting in an average forward offset of 0.28%. A similar change is seen in the 80%R station with a significant increase in gradient around the fourth revolution, however, the greatest shift in centre of pressure is found at the start of the simulation rather than the end. At the start, a maximum rearward offset in centre of pressure of 0.64% is found with this value dropping to an average of 0.24% after the fourth revolution. This large rearward offset at the 80% station produces a linear trend in centre of pressure across the blade with the introduction of the inflow velocity. The final station (90%R) produces the largest average offset in centre of pressure with a value of 0.57% towards the rear.

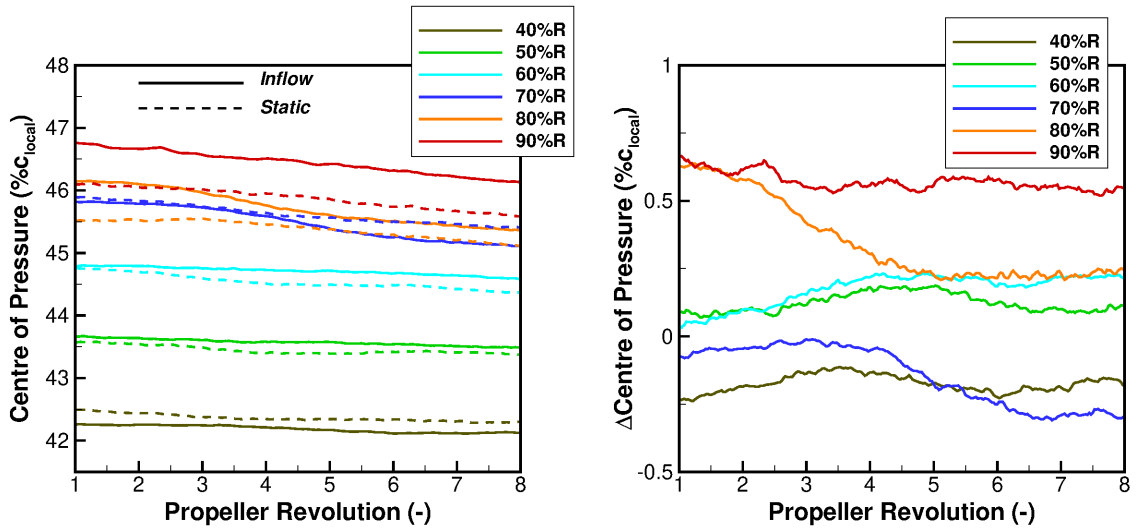

(a) CoP Comparison

(b) Difference

Figure 6.36: Rolling average centre of pressure comparison for the 20 knots inflow simulation of the Commander blade

6.2.3 Key Findings

Following the conclusion of the aerodynamic parametric study, it has been observed that all changes investigated influenced the stall flutter excitation for the given structural model. The study is not exhaustive, but does give an indication as to the potential influence of the changes. A full parameter sweep would be required to determine the stall flutter boundary for this propeller blade. In lieu of such a study, the following findings can be drawn based upon this parametric investigation.

From the increase in blade pitch, the amount and level of shedding from the blade increased. This in turn resulted in a slight decrease in overall load acting on the blade, reducing in the dominant modal amplitude and therefore reducing the overall magnitude of the blade deformation. At this condition, it is observed that the stall flutter boundary has been reached in terms of blade pitch angle at the reference pitch. Increases in stall flutter boundary is historically seen following the peak pitch angle and correlates what was found in the experimental investigation. A further analysis of the pitch angle effect may be required with a reduced level of detached flow, e.g. when an inflow velocity is present.

The introduction of an inflow velocity mitigated the level of stall acting on the blade. The use of the *SAS* model continued to provide vortex shedding, however, the magnitude was significantly reduced. This resulted in an overall increase in loads and therefore blade deformation. The retachment of the flow resulted in the blade pressure fluctuations to occur further towards the tip and this resulted in an oscillating pitching moment. With the blade now acting in a more design like condition, a linear distribution of the centre of pressure across the radius is found with a significant shift found during the blade acceleration. From this simulation, it is found that a blade can be excited from stall with an inflow velocity and in turn, making the convergence of the simulations easier.

Chapter 7

Conclusions and Future Work

7.1 Research Performed and Conclusions

The objectives of this investigation is split over four key factors. These include the examination of the current literature, the development of a modern understanding of the modelling requirements for a propeller stall flutter investigation, the development of a reduced computational cost method which can be use to determine stability and the investigation of key factors associated with propeller stall flutter.

A thorough examination of the current works has been studied and discussed in Chapter 1. This included a range of experimental and numerical investigations which focused on propeller stall flutter. Additional works focusing on aerofoil sections have been conducted with a range of stability insights gleaned. However, such studies lack the full complexities of three-dimensional propeller stall flutter and, therefore, the discussed literature was confined to propellers.

A range of experimental investigations have been carried out over the years. Due to the heavy use of propeller driven aircraft between 1945 and 1960, a high number of experiments were conducted to understand blade flutter. This started off with wooden blades, however, manufacturing advancements allowed for the introduction of alloys in the 1950's. It was during this period that the greatest understanding of the phenomena was gained. This was due to the reduction in manufacturing uncertainty that came with an alloy design and the need to improve propeller performance. Furthermore, the conversion from propeller-driven aircraft to turbofan engines resulted in a loss of interest and subsequently, no propeller stall flutter experimental investigation has been conducted post 1980.

The fact that no experimental investigation has been conducted since the 1980's is a fact that must be resolved. With the motivation of propeller efficiency improvements, acoustic mitigations and eVTOL development, there is a need for a modern physical propeller stall flutter test that utilises the improved, non-intrusive techniques currently available. Such a test would not only provide knowledge, but also allow for a greater validation of numerical techniques.

In terms of the numerical propeller stall flutter investigations, interest only began with the

development of the SR propfans in the 1980's. These studies involved both time-marching and eigenvalue stability analysis with semi-empirical aerodynamic models. The use of eigenvalue analysis was selected to ensure fast calculations of the stability boundaries and this trend continues today. However, with the availability of faster computing power in recent times, more complex finite element models could be used alongside a greater amount of time-marching simulations. Despite this, focus still remained on the use of semi-empirical aerodynamic models with these shown to perform well up until the point of deep stall. It is this fact that requires the need for an investigation into the current modelling requirements for a propeller stall flutter study.

The construction of an aeroelastic model is hinged on two key factors: the aerodynamic and structural modelling. In order to correctly obtain the propeller stall flutter response, the accurate capture of the non-linear aerodynamics is critical. A range of structural models have been shown to provide an accurate response from the past numerical studies presented in Chapter 1. Therefore, for this study the aeroelastic model includes Navier-Stokes based Computational Fluid Dynamics with a loosely/weakly coupled structural modal method with the novel ability to interpolate between different phases of a transient test case. The full model is described in Chapter 2 and the use of this model brings novelty to the investigation. The inclusion of Navier-Stokes based CFD allows for the use of statistical and resolved flow modelling, something which has not been attempted in a full propeller stall flutter study. Resolving certain length-scales can improve the accuracy of detached flow modelling, however, can also include an increase in computational cost. Therefore, a balance of these techniques may be required and was examined through this investigation. For the structural modelling, a time-marching modal method is utilised. This was selected based upon past studies due to the accuracy of response and reduced computational cost. The modal method requires the supply of accurate mode shapes and frequencies. In this investigation, these are obtained via a rotating NASTRAN non-linear beam model, with the effect of such models investigated.

The validation of the Commander propeller stall flutter response was presented in Chapter 4. The blade was modelled in isolation with periodic boundary conditions. In order to verify the computational setup, certain aerodynamic and structural parameters were investigated. This included the following: the comparison of the standard *URANS* with $k-\omega$ modelling to the *SAS* formulation; the comparison of the accelerated, decelerated and fixed rotational velocity setups; the comparison of high and low pitch angles to ensure excitation via detached flow; the effect of validated structural models via the standard and tuned derived responses; and the effect of changing modal response through the acceleration via the modal interpolation function.

Based upon this validation procedure, the following factors are deemed critical to a propeller stall flutter investigation:

- The need for resolved flow modelling is critical and this was highlighted here via the use of the *SAS* model. A propeller stall flutter response is driven by the detached flow

and it is the processes associated with such flow features that must be captured. This includes the extend of the stall vortex and the shedding from the blade. Although statistical models, such as *URANS* , are able to develop similar stall features, the process of the vortex shedding from the blade results in oscillations of the pressure profile which adjust the active moments and, hence, the deformations.

- The simulation setup must mirror the experiment. This is often a given when comparing two sets of data, however, the influence of this was highlighted via the comparison of the fixed rpm and accelerating blade simulations. The fixed rpm results did not match the experimental trends, despite the accelerating blade finishing on the same velocity. It is therefore critical that both experiment and simulation setup the in same fashion in terms of pitch, rotational velocity and inflow.

- The requirement for a well validated structural model is shown via the use of the tuned model. This required an accurate bungee test from which the mode shapes and frequencies could be compared. The tuned model was shown to achieve significantly greater levels of deflection with a closer comparison to the experimental results. Additionally, the change in modal response must be taken into account when conducting a transient simulation. This investigation used the modal interpolation function to update the active mode and this provided the closest comparison to the experiment.

Following the validation of the Commander propeller test case, a method is required which can provide stall flutter information at a reduced computational cost and additionally, the utilisation of the three-dimensional simulations to enhance the modelling fidelity. For this, the study of aerodynamic damping is assessed in Chapter 5. Aerodynamic damping defines the amount of energy supplied to a structure from the airflow, with negative values indicating instability and a dominating flow-field. It was previously used for the understanding of potential stall flutter boundaries, due to this indication of stability, when examining two-dimensional aerofoil sections. With this in mind, an investigation is conducted on quasi-three-dimensional aerofoil sections to assess the need for resolved flow modelling in simplified test cases and, also, a method is derived to obtain the aerodynamic damping values from the time-marching aeroelastic simulations. This derived three-dimensional method is novel with such extractions never attempted before. This extraction from fully three-dimensional simulations allows for the inclusion of three-dimensional aerodynamic effects and can assist in lower-fidelity modelling.

From the quasi-3D investigation and as per the results from Chapter 4, the use of *SAS* modelling is seen as beneficial to the correlation, between experiment and calculation, of airloads from a pitching NACA 0012 aerofoil section. Although both *URANS* and *SAS* do not track the loads perfectly, with a validation case defined within the deep stall range of dynamic stall, the *SAS* formulation improves the downstroke agreement due to the capture of the vortex shedding process. Previous aerofoil studies with semi-empirical aerodynamics have shown lower agree-

ment during the downstroke/reattachment phase due to the inability to capture the non-linearity. Using such methods improved the airload correlation during this phase and therefore the aerodynamic damping estimations.

In order to compare the quasi-3D aerofoil simulations to a fully three-dimensional elastic simulation, a method was derived to extract aerodynamic damping data. This method is similar in format to the aerofoil damping estimates, however, with adjustments made to the pitching moment integration to only include the effects of the detached flow. The method was applied on all simulations from Chapter 4, with damping estimates taken from the 70%R and 90%R blade sections (same sections as per the aerofoil study). Negative, or low, values were observed across both sections for all simulations whilst using the *SAS* method. The highest magnitude values are observed for the simulation which yielded the closest agreement to the experimental data (modal interpolated tuned mode simulation), thus indicating the potential to use such damping extractions for lower-fidelity modelling or the use of quasi-3D aerofoil studies for stability insights.

The final objective was to look into some of the key factors associated with propeller stall flutter using the validated test case and setup. For this, a parametric study was conducted in Chapter 6. This parametric study involved the adjustment of several structural and aerodynamic factors associated with the validated modal interpolated tuned mode, accelerated blade, *SAS* calculation. The structural factors included: the adjustment in sectional centre-of-gravity; the inclusion of additional tip mass; and the reduction in material torsional stiffness. The idea behind such adjustments was to include greater twist within the mode shapes and, therefore, assess the response. The aerodynamic factors included the introduction of a freestream velocity and increase in blade pitch angle. Such changes were geared towards the adjustments expected within a wind-tunnel study and were also seen as some of the most influential parameters in the literature survey. Although some of the final results may be expected, such as the reduction of stall flutter response with the introduction of an inflow velocity, the insight gleaned into each parameter's effect is novel due to the use of the derived method.

For each structural parametric study, the change in structural model was access from the bungee model setup with a comparison made to the baseline model. With the simulations utilising the accelerated blade conditions, comparisons were made in terms of torsional stress, modal amplitudes, blade deformation and thrust coefficient. It was observed that all structural changes investigated influenced the stall flutter excitation for the given condition. The study is not exhaustive, but does give an indication as to the potential influence of the changes. A full parameter sweep would be required to determine the stall flutter boundary for this propeller blade. In lieu of such a study, the following findings can be drawn based upon this parametric investigation.

Both the rearward chordwise offset in centre of gravity and reduction in torsional stiffness were found to reduce the stress acting on the blade. In addition to the reduction in torsional stress, the overall loads acting on the blade did not change significantly. This result indicates a

potential optimisation path and, combined with smart blade technology, could result in significant stall flutter mitigation throughout the flight regime, due to the reduction in stress for the same thrust.

The greatest change in torsional stress profile comes from the introduction of the concentrated mass. The centre of gravity and torsional stiffness simulations found the profile to be similar to the standard modal interpolated-tuned mode simulation. The highest stress is found towards the midspan with an almost constant profile through the acceleration. With the introduction of a tip mass, additional stress peaks along the radius are generated. The 75%R station is found to be fairly constant through the acceleration and subsequently results in a higher stress value towards the tip. The structural design of the blade must therefore be able to cope with such a change and could be exacerbated depending on the flow conditions, such as those found here within the baseline simulations which include significant stall. Although such an increase is unlikely additional tip mass can be generated through propeller damage, debris pickup, and/or ice build up. This simulation indicates the potential for such an alteration and a full sweep of the mass value would be required to understand the full boundary effect.

From the increase in blade pitch, the amount and level of shedding from the blade increased. This in turn resulted in a slight decrease in overall load acting on the blade, reducing in the dominant modal amplitude and therefore reducing the overall magnitude of the blade deformation. At this condition, it is observed that the stall flutter boundary was reached in terms of blade pitch angle at the reference pitch. Increases in the stall flutter boundary have been seen following the peak pitch angle via past studies. This parametric study therefore correlates to what has been previously found. A further analysis of the pitch angle effect may be required with a reduced level of detached flow.

The introduction of an inflow velocity mitigated the level of stall acting on the blade. The use of the *SAS* model continued to provide vortex shedding, however, the magnitude was significantly reduced. This resulted in an overall increase in loads and therefore blade deformation. The reattachment of the flow resulted in the blade pressure fluctuations to occur further towards the tip and this resulted in an oscillating pitching moment. With the blade now acting in a more design like condition (i.e. in axial flight), a linear distribution of the centre of pressure across the radius is found with a significant shift found during the blade acceleration. From this simulation, it is found that a blade can be excited from stall with an inflow velocity and in turn, making the convergence of the simulations easier.

7.2 Future Work

One of the clear take-aways from the propeller stall flutter review in Chapter 1 is the lack of definitive propeller stall flutter data. The experimental investigations are historic and often lacking in clear boundary assessment. This minimises the range of validation that can be conducted

for the range of numerical methods. Therefore, a modern set of experiments is required to extract greater datasets from non-intrusive techniques for enhanced validation of numerical methods.

Although sufficient validation has been conducted in Chapter 4 for the selected test case, a number of factors that were unable to be fully examined in the given time frame still require some examination. These are as follows:

- The rotational velocity range between 1400 and 1750 (rpm) was kept fixed for all accelerating blade simulations. This remained the case in order to correlate with the experimental report. However, the ability lies within the computational method to survey a wider range of velocities to understand its effect on the stall flutter response. This would also be at a much reduced cost compared to an experiment, hence a variety of factors associated with the acceleration could be studied. This could include a staggered acceleration approach and an increase or decrease of the gradient of acceleration.

- This investigation focused on two key aerodynamic models: the statistical *URANS* with $k-\omega$ turbulence model and the hybrid resolving *SAS* . In order to provide further confidence with the *SAS* approach, a comparison is required against additional models including LES and DES. Such models were not examined within this thesis due to time constraints related to the finer grids and time-steps required for LES and DES. Such a comparison should also be made for the quasi-3D aerofoil simulations of Chapter 5. Here, both the *URANS* and *SAS* do not agree fully with the experimental data with both achieving closer comparison at different stages. However, the examination of LES and/or DES could provide a clearer insight into the requirements for resolved flow.

- For the majority of simulations, approximately ten full revolutions were simulated with five of these revolutions incorporating the acceleration. This range of revolutions should be examined further to test for any low frequency responses. Although such responses would not appear to majorly influence the deformation, as a good agreement is found with the current setup, such low frequencies may vary over time and become more influential.

- During Chapter 4, the examined pitch angle focused on the baseline and a reduction from this of 15^{o}. This was mainly to ensure that the deformations of the blade were influenced by the detached flow. For a fuller understanding, the pitch angle should be examined further. This is likely an extension of the parametric study conducted in Chapter 6. Such a study would not only look into the effects of attached/detached flow but also secondary effects such as tip vortex interactions.

- In Chapter 4, the effect of the modal interpolation function was examined. This included a two-stage and four-stage approach. Although the closest correlation was made to the experimental report via the four-stage simulation, the full effect of this requires further analysis. This involves the total number of stages (i.e. three-/five-/six-staged approach)

and the blending coefficient power parameter. This power parameter is in reference to the inverse distancing weighting interpolation used to calculate the blending coefficients. Currently this is fixed, however an examination of this and as a result the interpolation procedure would be required.

In Chapter 5, a method is derived to extract aerodynamic damping data from three-dimensional simulations. This is an improvement on the traditional aerofoil damping estimates as the propeller simulations include three-dimensional effects. The aim of such extractions would be to enhance lower-fidelity modelling which utilise aerodynamic damping values. Such an enhancement is not conducted within this thesis and is therefore something which must be investigated.

Additionally in Chapter 5, a comparison is made between quasi-3D simulations and experimental dynamic stall data for the NACA 0012 aerofoil. The selected test case was a deep stall solution and was selected to link to the negative damping associated with stall flutter. The use of the quasi-3D method should be examined further for a range of dynamic stall test cases, including further deep stall, light stall and stall onset profiles. It would also be beneficial to conduct a validation study against a known propeller aerofoil profile, further linking the aerofoil damping studies to the full propeller.

Finally, in Chapter 6 a parametric study is conducted on the validated propeller test case to examine certain aerodynamic and structural effects. The list of examined effects are not exhaustive with the selected parameters only studied in a binary fashion. Firstly, further simulations of the selected aerodynamic and structural changes must be conducted over a greater range. This would help to improve the insight gained and achieve an overall picture of the flutter boundary. Secondly, the number of parameters investigated must be increased. This can include a propeller at yaw, altitude, blade sectional mass and sectional bending inertia. Certain planform parameters, such as camber and thickness ratio, are fixed due to the selected blade. However, these could also be examined in a model blade if linked to an accompanying experiment.

Bibliography

[1] Impacta - improving the propulsion aerodynamics of turboprop aircraft.

[2] Finding optimal rotation and translation between corresponding 3d points. http://nghiaho.com/?page_id=671, 2013. Last accessed 8th February 2021.

[3] Rolls-royce unveils evtol air taxi concept at farnborough airshow. https://www.theengineer.co.uk/rolls-royce-evtol-air-taxi/, 2018. Last accessed 8th February 2021.

[4] Rolls-royce unveils 'flying taxi' at farnborough airshow. https://www.cityam.com/rolls-royce-unveils-flying-taxi-farnborough-airshow/, 2018. Last accessed 8th February 2021.

[5] Air history - gulfstream american 695a jetprop 1000. https://www.airhistory.net/photo/135248/N695MM, 2019. Last accessed 22nd February 2021.

[6] Gulfstream aerospace jetprop & turbo commander. https://www.airliners.net/aircraft-data/gulfstream-aerospace-jetprop-turbo-commander/344, 2020. Last accessed 8th February 2021.

[7] Twin commander aircraft history. https://twincommander.com/about-us/, 2020. Last accessed 22nd February 2021.

[8] A.E. Allis and J.M. Swihart. The effect of blade-section camber on the stall-flutter characteristics of three naca propellers at zero advance. Research Memorandum L53B17, National Advisory Committee for Aeronautics, 1956.

[9] A. Arena, W. Lacarbonara, and P. Marzocca. Nonlinear aeroelastic formulation and post-flutter analysis of flexible high-aspect-ratio wings. *Journal or Aircaft*, 50(6), 2013. DOI: https://doi.org/10.2514/1.C032145.

[10] P. Arguelles, M. Bischoff, P. Busquin, B. Droste, Sir R. Evans, W. Kroll, J. Lagardere, A. Lina, J. Lumsden, D. Ranque, S. Rasmussen, P. Reutlinger, Sir R. Robins, H. Terho,

and A. Wittlov. European aeronautics: A vision for 2020: Meeting society's needs and winning global leadership. Technical report, European Commission, 2001.

[11] H. Ashley and M. Landahl. *Aerodynamics of wings and bodies*. Dover Publications, 1965.

[12] O. Axelsson. *Iterative Solution Methods*. Cambridge University Press, 1994.

[13] S.V. Babu, G.J.M. Loupy, F. Dehaeze, G.N. Barakos, and N.J. Taylor. Aeroelastic simulations of stores in weapon bays using detached-eddy simulation. *Journal of Fluids and Structures*, 66:207–228, October 2016. doi:10.1016/j.jfluidstructs.2016.07.014.

[14] J.E. Baker. The effects of various parameters, including mach number, on propeller-blade flutter with emphasis on stall flutter. Technical report, National Advisory Commitee for Aeronautics, 1955.

[15] G. Barakos and C. Johnson. Acoustic comparison of propellers. *International Journal of Aeroacoustics*, 15(6-7):575–594, 2016. DOI: 10.1177/1475472X16659214.

[16] T. Beddoes. Application of indicial aerodynamic functions. Technical report, AGARD, 1980.

[17] T.S Beddoes. A synthesis of unsteady aerodynamic effects including stall hysteresis. *Vertica*, 5(1), 1976.

[18] J. Beedy, G.N. Barakos, K.J. Badcock, and B.E. Richards. Non-linear analysis of stall flutter based on the onera aerodynamic model. *The Aeronautical Journal*, 107(1074), 2003. DOI: 10.1017/S0001924000134001.

[19] D. Beeman. Some multistep methods for use in molecular dynamics calculations. *Journal of Computational Physics*, 20(2), 1976. DOI: 10.1016/0021-9991(76)90059-0.

[20] M. Biava and G.N. Barakos. Optimisation of ducted propellers for hybrid air vehicles using high-fidelity cfd. *The Aeronautical Journal*, 120(1232):1632–1657, 2016. doi:10.1017/aer.2016.78.

[21] R.L. Bielawa. *Rotary Wing Structural Dynamics and Aeroelasticity*. American Institute of Aeronautics and Astronautics, 2002.

[22] R.L. Bielawa, S.A. Johnson, R.M. Chi, and S.T. Gangwani. Aeroelastic analysis for propellers: Mathematical formulations and program user's manual. Contractor Report 3729, National Aeronautics and Space Administration, 1983.

[23] M.N. Bismarck-Nasr. *Structural Dynamics inAeronautical Engineering*. American Institute of Aeronautics and Astronautics, 1999.

[24] R.L. Bisplinghoff and H. Ashley und R.L. Halfman. *Aeroelasticity*. Addison-Wesley Publishing Company, Inc., 1955.

[25] J. Bonet and J. Peraire. An alternating digital tree (adt) algorithm for 3d geometric searching and intersection problems. *International Journal for Numerical Methods in Engineering*, 31(1):1–17, 1991. doi:10.1002/nme.1620310102.

[26] N. Bown and A. Knepper. Aircraft and propulsion design requirements for the impacta project institution = Dowty Propellers (GE Aviation Systems Ltd), year = 2013, number = ITS 01675, Issue 3,. Technical report.

[27] M. Bryant, J.C. Gomez, and E. Garcia. Reduced-order aerodynamic modeling of flapping wing energy harvesting at low reynolds number. *AIAA Journal*, 51(12), 2013. DOI: https://doi.org/10.2514/1.J052364.

[28] P.E. Burton. Straingauge Test Report on a Spin Test Carried out on a Type (c) R.305/3-82-F/6 Propeller on the Spinning Tower at the R.A.E. Farnborough, Hants. Technical Report 093.1.592, DOWTY ROTOL LTD., 1979.

[29] F.O. Carta and P.F. Lorber. Experimental study of the aerodynamics of incipient torsional stall flutter. *Journal of Propulsion and Power*, 3(2), 1987.

[30] F.O. Carta and C.F. Niebanck. Prediction of Rotor Instability at High Forward Speeds. Technical Report 68-18C, US Army Aviation Material Laboratories, 1969.

[31] G. Chirico, G.N. Barakos, and N. Bown. Numerical aeroacoustic analysis of propeller designs. *The Aeronautical Journal*, 122(1248):283–315, 2018. DOI: 10.1017/aer.2017.123.

[32] G. Chirico, G.N. Barakos, and N. Bown. Propeller installation effects on turboprop acoustics. *Journal of Sound and Vibration*, 424, 2018. DOI: 10.1016/j.jsv.2018.03.003.

[33] T.C. Corke and F.O. Thomas. Dynamic Stall in Pitching Airfoils: Aerodynamic Damping and Compressibility Effects. *Annual Review of Fluid Mechanics*, 47, 2015.

[34] C.C. Critzos, H.H. Heyson, and Jr R.W. Boswinke. Aerodynamic characteristics of naca 0012 airfoil section at angles of attack from 0 to 180. Technical Report 3361, National Advisory Committee for Aeronautics, 1955.

[35] C. Crozon, R. Steijl, and G.N. Barakos. Coupled flight dynamics and cfd - demonstration for helicopters in shipborne environment. *The Aeronautical Journal*, 122(1247):42–82, 2018. DOI: https://doi.org/10.1017/aer.2017.112.

[36] E.C.E. Culler, C. Fagley, J. Seidel, T.E. McLaughlin, and J.A.N. Farnsworth. Developing a reduced order model from structural kinematic measurements of a flexible finite span wing in stall flutter. *Journal of Fluids and Structures*, 71, 2017. DOI: https://doi.org/10.1016/j.jfluidstructs.2017.03.010.

[37] E.C.E. Culler and J.A.N. Farnsowrth. Higher frequencies in stall flutter moment development. *Journal of Fluids and Structures*, 85, 2019. DOI: https://doi.org/10.1016/j.jfluidstructs.2019.01.007.

[38] T. M. Darecki, C. Edelstenne, T. Enders, E. Fernandez, P. Hartmanand J.P. Herteman, M. Kerkloh, I. King, P. Ky, M. Mathieu, G. Orsi, G. Schotman, C. Smith, and J.D. Worner. Flightpath 2050: Europes vision for aviation. report ofthe high level group on aviation research. Technical report, ACARE (Advisory Councilfor Aeronautics Research in Europe), 2011.

[39] F. Dehaeze and G.N. Barakos. Mesh deformation method for rotor flows. *Journal of Aircraft*, 49(1):82–92, 2012. DOI: https://doi.org/10.2514/1.C031251.

[40] D. Delamore-Sutcliffe. *Modelling of Unsteady Stall Aerodynamics and Prediction of Stall Flutter Boundaries for Wings and Propellers*. PhD thesis, University of Bristol, 2007.

[41] D.W. Delamore-Sutcliffe and D.I. Greenwell. A model for the fast prediction of propeller stall flutter. In *25th AIAA Applied Aerodynamics Conference*, 2006. DOI: 10.2514/6.2006-3477.

[42] D.W. Delamore-Sutcliffe, R.J. Whiting, and D. Greenwell. Experimental and Numerical Study of Stall Flutter. In *23rd AIAA Applied Aerodynamics Conference*, 2005. DOI: 10.2514/6.2005-5096.

[43] E.H. Dowell. A simple approach of converting frequency domain aerodynamics to the time domain. Technical Memorandum 81844, National Aeronautics and Space Administration, 1980.

[44] E.H. Dowell. *A Modern Course in Aeroelasticity*. Springer International Publishing, Switzerland, 5th edition, 2015.

[45] P. Dunn and J. Dugundji. Nonlinear stall flutter and divergence analysis of cantilevered graphite/epoxy wings. *AIAA Journal*, 30(1), 1992. DOI: 10.2514/3.10895.

[46] J.A. Ekaterinaris and M.F. Platzer. Computational prediction of airfoil dynamic stall. *Progress in Aerospace Sciences*, 33(11-12), 1997. DOI: 10.1016/S0376-0421(97)00012-2.

[47] L.E. Ericsson and J.P. Reding. Fluid dynamics of unsteady separated flow. part ii. lifting surfaces. *Progress in Aerospace Sciences*, 24(4), 1987. DOI: 10.1016/0376-0421(87)90001-7.

[48] H.G. Ewing, J. Kettlewell, and D.R. Gaukroger. Comparative flutter tests on two, three, four and five-blade propellers. Technical Report 2634, Aeronautical Research Council, 1952.

[49] R. Steijl F. Rovere and G.N. Barakos. Cfd analysis of a micro rotor in ground effect. In *AIAA SciTech Forum*, Orlando, Florida, USA, 2020. AIAA. DOI: 10.2514/6.2020-1793.

[50] R. Fanti, F.O. Carta, and W.R. Pitt. Stall-flutter characteristics of several 16-series cantilevered airfoil models. Technical Report R-23624-2, United Aircraft Corporation Research Department, 1954.

[51] F.O.Carta. An experimental investigation of gapwise periodicity and unsteady aerodynamic response in an oscillating cascade: I - experimental and theoretical results. Contractor Report 3513, National Aeronautics and Space Administration, 1982.

[52] J.N. Franklin. On the numerical solution of characteristic equations in flutter analysis. *Journal of the Association for Computing Machinery*, 5(1), 1958. DOI: 10.1145/320911.320917.

[53] Y.C. Fung. *An introduction to the theory of aeroelasticity*. Dover Publications, 3rd edition, 1993.

[54] S.T. Gangwani. Prediction of dynamic stall and unsteady airloads for rotor blades. *Journal of the American Helicopter Society*, 27(4), 1982. DOI: 10.4050/JAHS.27.57.

[55] S.T. Gangwani. Synthesized Airfoil Data Method for Prediction of Dynamic Stall and Unsteady Airloads. Contractor Report 3672, National Aeronautics and Space Administration, 1983.

[56] F.H. Gern and L. Librescu. Effects of externally mounted stores on aeroelasticity of advanced swept cantilevered aircraft wings. *Aerospace Science and Technology*, 2(5), 1998. DOI: https://doi.org/10.1016/S1270-9638(98)80008-4.

[57] B.W. Goepner. Static flutter tests of hsd prop-fan models. Technical Report R81-335414, United Technologies Research Center, 1982.

[58] S. Goldstein. On the vortex theory of screw propellers. In *In proceedings of the Royal Society of Aviation*, 1929.

[59] M. Goman and A. Khrabrov. State-space representation of aerodynamic characteristics of an aircraft at high angles of attack. *Journal of Aircraft*, 31(5), 1994. DOI: 10.2514/3.46618.

[60] A. Gomariz-Sancha, M. Maina, and A.J. Peace. Analysis of propeller-airframe interaction effects through a combined numerical simulation and wind-tunnel testing approach. In *AIAA SciTech Forum, 53rd AIAA Aerospace Sciences Meeting*, pages 1–19, Kissimmee, Florida, 2015. AIAA.

[61] R.E. Gormont. A Mathematical Model of Unsteady Aerodynamics and Radial Flow for Application to Helicopter Rotors. Technical Report 72-67, USAAMRDL, 1973.

[62] D.W. Gross and F.D. Harris. Prediction of inflight stalled airloads from oscillating airfoil data. In *25th Annual National Forum*. American Helicopter Society, 1969.

[63] R.L. Halfman, H.C. Johnson, and S.M. Haley. Evaluation of high-angle-of-attack aerodynamic derivative data and stall-flutter prediction techniques. NACA TN 2533, National Advisory Committee for Aeronautics, 1951.

[64] H.D. Ham. Helicopter blade flutter. Technical report, AGARD, 1973.

[65] D. Han, C. Dong, and G.N. Barakos. Performance improvement of variable speed rotors by gurney flaps. *Aerospace Science and Technology*, 81:118–127, 2018. DOI: 10.1016/j.ast.2018.07.044.

[66] C. W. Hirt, A. A. Amsten, and J. L Cook. An arbitrary lagrangian-eulerian computing method for all flow speeds. *Journal of Computational Physics*, 14(3):227–253, 1974. DOI: 10.1016/0021-9991(74)90051-5.

[67] D.H. Hodges and G.A. Pierce. *Introduction to Structural Dynamics and Aeroelasticity*. Cambridge University Press, 2011.

[68] J.C. Houbolt and G.W. Brookes. Differential equations of motion for combined flapwise bending, chordwise bending, and torison of twisted nonuniform rotor blades. Technical Report 1346, National Advisory Commitee for Aeronautics, 1957.

[69] E.L. Houghton, P.W. Carpenter, S. Collicott, and D. Valentine. *Aerodynamics for Engineering Students*. Elsevier Butterworth-Heinemann, 7th edition, 2016.

[70] G.W. Housner and T. Vreeland-Jr. *The analysis of stress and deformation*. The MacMillan Co., New York, 6th edition, 1965.

[71] H.H. Hubbard, M.F. Burges, and M.A. Sylvester. Flutter of thin propeller blades, including effects of mach number, structural damping, and vibratory-stress measurements

near the flutter boundaries. Technical Report 3707, National Advisory Commitee for Aeronautics, 1956.

[72] G. Iosilevskii, Ya.A. Iosilevskii, and A. Rosen. Asymptotic aerodynamic theory of oscillating rotary wings in axial flight. *SIAM Journal on Applied Mathematics*, 59(4), 1999.

[73] A. Jameson, W. Schmidt, and E. Turkel. Numerical solutions of euler equations by finite volume methods using runge-kutta time-stepping schemes. In *Proceedings of the Fourteenth Fluid and Plasma Dynamic Conference*, pages 1–19, Palo Alto, California, 1981. AIAA.

[74] M. Jarkowski, M.A. Woodgate, G.N. Barakos, and J. Rokicki. Towards Consistent Hybrid Overset Mesh Methods for Rotorcraft CFD. *International Journal for Numerical Methods in Fluids*, 74(8):543–576, 2014. doi:10.1002/fld.3861.

[75] W.P. Jones and J.A. Moore. Aerodynamic theory for a cascade of oscillating airfoils in subsonic flow. *AIAA Journal*, 14(5), 1976. DOI: 10.2514/3.7129.

[76] E.J. Jumper, S.J. Schreck, and R.L. Dimmick. Lift-curve characteristics for an airfoil pitching at constant rate. *Journal of Aircraft*, 24(10), 1987. DOI: 10.2514/3.45507.

[77] K.R.V. Kaza, O. Mehmed, G.V. Narayanan, and D.V. Murthy. Analytical flutter investigation of a composite propfan model. *Journal of Aircraft*, 26(8), 1989. DOI: 10.2514/3.45838.

[78] A. Khrabrov and M. Ol. Effect of flow separation on aerodynamic loads in linearised thin airfoil theory. *Journal of Aircraft*, 41(4), 2004. DOI: 10.2514/1.5524.

[79] A. Knepper and N. Bown. IMPACTA Wind-tunnel Instrumentation Specification. Technical Report ITS 01777, Issue 3, Dowty Propellers (GE Aviation Systems Ltd), 2014.

[80] R.M. Kufield and W.G. Bousman. High load conditions measured on a uh-60a in maneuvering flight. In *In proceedings of the Vertical Flight Society 52nd Annual Forum*, Fort Worth, TX, USA, 1995.

[81] T.E. Lee, G.J. Leishman, and R. Manikandan. Fluid dynamics of interacting blade tip vortices with a ground plane. *Journal of the American Helicopter Society*, 55(2), 2010. DOI: 10.4050/JAHS.55.022005.

[82] J.G. Leishman. Validation of approximate indicial aerodynamic functions for two-dimensional subsonic flow. *Journal of Aircraft*, 25(10), 1988. DOI: 10.2514/3.45680.

[83] J.G. Leishman. Indicial lift approximations for two-dimensional subsonic flow as obtained from oscillatory measurements. *Journal of Aircraft*, 30(3), 1993. DOI: 10.2514/3.46340.

[84] J.G. Leishman. *Principles of Helicopter Aerodynamics*. Cambridge University Press, 2nd edition, 2016.

[85] J.G. Leishman and T.S. Beddos. A semi-empirical model for dynamic stall. *Journal of the American Helicopter Society*, 34(3), 1989. DOI: 10.4050/JAHS.34.3.3.

[86] A.Z. Lemnios. Aerodynamic damping tests of propeller blade airfoil sections. Technical Report R-0997-1, United Aircraft Corporation Research Department, 1957.

[87] A.H. Lind and A.R. Jones. Unsteady airloads on static airfoils through high angles of attack and in reverse flow. *Journal of Fluids and Structures*, 63, 2016. DOI: 10.1016/j.jfluidstructs.2016.03.005.

[88] Z. Liu and Y.L. Young. Static divergence of self-twisting composite rotors. *Journal of Fluids and Structures*, 26(5), 2010. DOI: 10.1016/j.jfluidstructs.2010.05.002.

[89] R.G. Loewy. A two-dimensional approximation to the unsteady aerodynamics of rotary wings. *Journal of the Aeronautical Sciences*, 24(2):81–92, 1957.

[90] E. Madenci and I. Guven. *The Finite Element Method and Applications in Engineering Using ANSYS*. Springer International Publishing, Boston, MA, 2nd edition, 2015. DOI: 10.1007/978-1-4899-7550-8.

[91] K.W. McAlister, S.L. Pucci, W.J. McCroskey, and L.W. Carr. An Experimental Study of Dynamic Stall on Advanced Airfoil Sections Volume 2: Pressure and Force Data. Technical Report TM-84245, National Aeronautics and Space Administration, 1982.

[92] B.W. McCormick. *Aerodynamics, aeronautics and flight mechanics*. John Wiley & Sons, Ltd., 2nd edition, 1926.

[93] W.J. McCroskey. The Phenomenon of Dynamic Stall. Technical Memorandum 81264, National Aeronautics and Space Administration, 1981.

[94] C.P. Mellen, J. Frohlich, and W. Rodi. Lessons from lesfoil project on large-eddy-simulation of flow around an airfoil. *AIAA Journal*, 41(4), 2003.

[95] F.R. Menter. Two-equation eddy-viscosity turbulence models for engineering applications. *AIAA Journal*, 32(8):1598–1605, 1994. DOI: 10.2514/3.12149.

[96] F.R. Menter and Y. Egorov. A Scale Adaptive Simulation Model using Two-Equation Models. In *43rd AIAA Aerospace Sciences Meeting and Exhibit*, 2005.

[97] F.R. Menter and Y. Egorov. The Scale-Adaptive Simulation Method for Unsteady Turbulent Flow Predictions. Part 1: Theory and Model Description. *Flow, Turbulence and Combustion*, 85(1), 2010. DOI: 10.1007/s10494-010-9264-5.

[98] R.H. Miller and C.W. Ellis. Helicopter blade vibration and flutter. *Journal of the American Helicopter Society*, 1(3), 1956. DOI: 10.4050/JAHS.1.19.

[99] MSC Software. *MSC.Nastran 2004*, 2003.

[100] W. Ng and A. Datta. Hydrogen fuel cells and batteries for electric-vertical takeoff and landing aircraft. *Journal of Aircraft*, 56(5):1765–1782, 2019. DOI: 10.2514/1.C035218.

[101] V. Ognev and A. Rosen. Influence of using various unsteady aerodynamic models on propeller flutter prediction. *Journal of Aircraft*, 2011.

[102] S. Osher and S. Chakravarthy. Upwind schemes and boundary conditions with applications to euler equations in general geometries. *Journal of Computational Physics*, 50(3):447–481, 1983. DOI: 10.1016/0021-9991(83)90106-7.

[103] D.A. Peters. Toward a unified lift model for use in rotor blade stability analyses. *Journal of the American Helicopter Society*, 30(3), 1985. DOI: 10.4050/JAHS.30.3.32.

[104] R.A. Piziali. 2-d and 3-d oscillating wing aerodynamics for a range of angles of attack including stall. Technical Memorandum 4632, National Aeronautics and Space Administration, 1994.

[105] A. Pope. The forces and pressures over an naca 0015 airfoil through 180 degrees angle of attack. Technical report, Georgia Institute of Technology, 1947.

[106] S.B. Pope. *Turbulent Flows*. Cambridge University Press, New York, USA, 10th edition, 2000.

[107] M. Ramasamy, A. Sanayei, J.S. Wilson, P.B. Martin, T. Harms, P. Nikoueeyan, and J. Naughton. Data-driven optimal basis clustering to characterize cycle-to-cycle variations in dynamic stall measurements. In *In proceedings of the Vertical Flight Society 75th Annual Forum and Technology Display*, Philadelphia, PA, USA, 2019.

[108] D.C. Rapaport. *The Art of Molecular Dynamics Simulation*. Cambridge University Press, 2nd edition, 2004. DOI: 10.1017/CBO9780511816581.

[109] N.A. Razak, T. Andrianne, and G. Dimitriadis. Flutter and stall flutter of a rectangular wing in a wind tunnel. *AIAA Journal*, 49(10), 2011. DOI: https://doi.org/10.2514/1.J051041.

[110] T.S.R. Reddy and K.R.V. Kaza. A comparative study of some dynamic stall models. Technical memorandum, National Aeronautics and Space Administration, 1987.

[111] T.S.R. Reddy and K.R.V. Kaza. Analysis of an unswept propfan blade with a semiempirical dynamic stall model. Technical report, National Aeronautics and Space Administration, 1989.

[112] R.J. Renka. Multivariate interpolation of large sets of scattered data. *ACM Trans. Math. Softw.*, pages 139 – 148, 1988. doi:10.1145/45054.45055.

[113] Ian Roberts. Dowty modal test: Commander blade results. Technical Report 1, DOWTY/AeroTex UK LLP, 2017.

[114] V.L. Rogallo and P.F. Yaggy. A wind-tunnel investigation of the stall-flutter characteristics of a supersonic-type propeller at positive and negative thrust. Technical Memorandum 3-9-59A, National Aeronautics and Space Administration, 1959.

[115] J.P. Rogers. Applications of an analytic stall model to time-history and eigenvalue analysis of rotor blades. *Journal of the American Helicopter Society*, 29(1), 1984. DOI: 10.4050/JAHS.29.25.

[116] J.C. Rotta. *Ü*ber eine Methode zur Berechnung turbulenter Scherstr*ö*mungen. Technical Report 69A 14, Aerodynamische Versuchsanstalt G*ö*ttingen, 1968.

[117] H.L. Runyan and J.L. Sewall. Experimental investigation of the effects of concentrated weights on flutter characteristics of a straight cantilever wing. NACA TN 1594, National Advisory Committee for Aeronautics, 1948.

[118] M.S. Ryerson and M. Hansen. The potential of turboprops for reducing aviation fuel consumption. *Transportation Research Part D: Transport and Environment*.

[119] R.H. Scanlan and R. Rosenbaum. *Introduction to the Study of Aircraft Vibration and Flutter*. Macmillan and Co., London, 1951.

[120] N. Scrase and M. Maina. The Evaluation of Propeller Aero-acoustic Design Methods by Means of Scaled-Model Testing Employing Pressure Tapped Blades and Spinner. In *19th ICAS Congress*, 1994.

[121] W.R. Sears. Some aspects of non-stationary airfoil theory and its practical application. *Journal of the Aeronautical Sciences*, 8(3):104–108, 1941.

[122] D. Shepard. A Two-dimensional Interpolation Function for Irregularly-spaced Data. In *Proceedings of the 1968 23rd ACM National Conference*, New York, NY, USA, 1968.

[123] M. Smirti and M. Hansen. The potential of turboprops to reduce aviation fuel consumption. `https://escholarship.org/uc/item/5131891j`, 2009. Last accessed 8^{th} February 2021.

[124] A.F. Smith. Analysis and test evaluation of the dynamic response and stability of three advanced turboprop models at low forward speeds. Contractor Report 175026, National Aeronautics and Space Administration, 1985.

[125] A.F. Smith. Analysis and Test Evaluation of the Dynamic Stability of Three Advanced Turboprop Models at Zero Forward Speeds. Contractor Report 175025, National Aeronautics and Space Administration, 1985.

[126] M.J. Smith, N.D. Liggett, and B.C.G. Koukol. Aerodynamics of airfoils at high and reverse angles of attack. *Journal of Aircraft*, 48(6), 2011. DOI: 10.2514/1.C031428.

[127] S.N. Smith. Discrete frequency sound generation in axial flow turbomachines. Technical Memoranda 3709, National Advisory Commitee for Aeronautics, 1973.

[128] R. Steijl, G.N. Barakos, and K. Badcock. A framework for cfd analysis of helicopter rotors in hover and forward flight. *International Journal for Numerical Methods in Fluids*, 51(8), 2006. DOI: 10.1002/fld.1086.

[129] L.H.G. Sterne. Spinning Tests on Fluttering Propellers. *Aeronautical Research Council: Reports and Memoranda*, (2022), 1945.

[130] H.L. Stüder. Experimentelle untersuchungen uber flugelschwingungen. *Eidgenossischen Tech. Hochschule Zurich*, 1946.

[131] T. Theodorsen. General theory of aerodynamic instability and the mechanism of flutter. Technical Report 496, National Advisory Commitee for Aeronautics, 1934.

[132] T. Theodorsen. General theory of aerodynamic instability and the mechanism of flutter. Technical Report 496, National Advisory Commitee for Aeronautics, 1949.

[133] T. Theodorsen and I.E. Garrick. Mechanism of flutter: a theoretical and experimental investigation of the flutter problem. Technical Report 685, National Advisory Commitee for Aeronautics, 1940.

[134] T. Theodorsen and A.A. Regier. Effect of lift coefficient on propeller flutter. Technical Report L5F30, National Advisory Commitee for Aeronautics, 1945.

[135] C.T. Tran and D. Falchero. Application of the ONERA Dynamic Stall Model to a Helicopter Blade in Forward Flight. *Vertica*, 6, 1982.

[136] J. Turnberg. Classical flutter stability of swept propellers. In *In proceedings of the 24th Structures, Structural Dynamics and Materials Conference*, Lake Tahoe, NV, U.S.A., 1983. AIAA.

[137] G. D. van Albada, B. van Leer, and W. W. Roberts. A comparative study of computational methods in cosmic gas dynamics. *Astronomy and Astrophysics*, 108(1):76–84, 1982.

[138] B. van Leer. Towards the ultimate conservative difference scheme. v. a second-order sequel to godunov's method. *Journal of Computational Physics*, 32(1):101–136, 1979. DOI: 10.1016/0021-9991(79)90145-1.

[139] E. Verstraelen, G. Habib, G. Kerschen, and G. Dimitriadis. Experimental passive flutter suppression using a linear tuned vibration absorber. *AIAA Journal*, 55(4), 2017. DOI: https://doi.org/10.2514/1.J055397.

[140] M.R. Visbal and D.J. Garmann. Investigation of spanwise end effects on dynamic stall of a pitching wing section. *Journal of Aircraft*, 56(6), 2019.

[141] D.S. Whitehead. Force and moment coefficients for vibrating airfoils in cascades. Technical Memoranda 3254, National Advisory Commitee for Aeronautics, 1960.

[142] R. Whittle. The demand for on-demand mobility. *Vertiflite*, January/February:34–38, 2017.

[143] D.C. Wilcox. Multiscale model for turbulent flows. *AIAA Journal*, 26(11), 1988.

[144] D.C. Wilcox. Simulation of Transition with a Two-Equation Turbulence Model. *AIAA Journal*, 32(2), 1994.

[145] E.L Wilson and K.J. Bathe. *Numerical methods in finite element analysis*. Prentice-Hall, Englewood Cliffs, N. J., 1976.

[146] J.H. Wood and J.M. Swihart. The effect of blade-section camber on the stati c characteristics of three naca propellers. Research Memorandum L51L28, National Advisory Committee for Aeronautics, 1952.

[147] M.A. Woodgate and G.N. Barakos. Implicit computational fluid dynamics methods for fast analysis of rotor flows. *AIAA Journal*, 50(6), 2012. DOI: 10.2514/1.J051155.

[148] L.C. Woods. *The Theory of Subsonic Plane Flow*. Cambridge University Press, 1961.

[149] J.R. Wright and J.E. Cooper. *Introduction to Aircraft Aeroelasticity and Loads*. John Wiley & Sons, Ltd., 2nd edition, 2015.

[150] M. Yamasaki, K. Isogai, T. Uchida, and I. Yukimura. Shock-stall flutter of a two-dimensional airfoil. *AIAA Journal*, 42(2), 2004. DOI: https://doi.org/10.2514/1.9088.